

Springer Proceedings in Materials

Andrei Victor Sandu · Petrica Vizureanu ·
Mohd Mustafa Al Bakri Abdullah ·
Marcin Nabialek ·
Che Mohd Ruzaidi Ghazali ·
Ion Sandu *Editors*

Selected Papers from ICIR EUROINVENT - 2023

International Conference on Innovative
Research

 Springer

Series Editors

Arindam Ghosh, *Department of Physics, Indian Institute of Science, Bengaluru, India*

Daniel Chua, *Department of Materials Science and Engineering, National University of Singapore, Singapore, Singapore*

Flavio Leandro de Souza, *Universidade Federal do ABC, Sao Paulo, São Paulo, Brazil*

Oral Cenk Aktas, *Institute of Material Science, Christian-Albrechts-Universität zu Kiel, Kiel, Schleswig-Holstein, Germany*

Yafang Han, *Beijing Institute of Aeronautical Materials, Beijing, Beijing, China*

Jianghong Gong, *School of Materials Science and Engineering, Tsinghua University, Beijing, Beijing, China*

Mohammad Jawaid , *Laboratory of Biocomposite Technology, INTROP, Universiti Putra Malaysia, Serdang, Selangor, Malaysia*

Springer Proceedings in Materials publishes the latest research in Materials Science and Engineering presented at high standard academic conferences and scientific meetings. It provides a platform for researchers, professionals and students to present their scientific findings and stay up-to-date with the development in Materials Science and Engineering. The scope is multidisciplinary and ranges from fundamental to applied research, including, but not limited to:

- Structural Materials
- Metallic Materials
- Magnetic, Optical and Electronic Materials
- Ceramics, Glass, Composites, Natural Materials
- Biomaterials
- Nanotechnology
- Characterization and Evaluation of Materials
- Energy Materials
- Materials Processing

To submit a proposal or request further information, please contact one of our Springer Publishing Editors according to your affiliation:

European countries: **Mayra Castro** (mayra.castro@springer.com)

India, South Asia and Middle East: **Priya Vyas** (priya.vyas@springer.com)

South Korea: **Smith Chae** (smith.chae@springer.com)

Southeast Asia, Australia and New Zealand: **Ramesh Nath Premnath** (ramesh.premnath@springer.com)

The Americas: **Michael Luby** (michael.luby@springer.com)

China and all the other countries or regions: **Mengchu Huang** (mengchu.huang@springer.com)

This book series is indexed in **SCOPUS** database.

Andrei Victor Sandu · Petrica Vizureanu ·
Mohd Mustafa Al Bakri Abdullah ·
Marcin Nabialek · Che Mohd Ruzaidi Ghazali ·
Ion Sandu
Editors

Selected Papers from ICIR EUROINVENT - 2023

International Conference on Innovative
Research

Editors

Andrei Victor Sandu
Gheorghe Asachi Technical University of Iasi
Iasi, Romania

Petrica Vizureanu
Gheorghe Asachi Technical University of Iasi
Iasi, Romania

Mohd Mustafa Al Bakri Abdullah
Universiti Malaysia Perlis
Perlis, Malaysia

Marcin Nabialek
Czestochowa University of Technology
Czestochowa, Poland

Che Mohd Ruzaidi Ghazali
Universiti Malaysia Terengganu
Kuala Nerus Terengganu, Malaysia

Ion Sandu
Alexandru Ioan Cuza University of Iasi
Iasi, Romania

ISSN 2662-3161

ISSN 2662-317X (electronic)

Springer Proceedings in Materials

ISBN 978-3-031-45963-4

ISBN 978-3-031-45964-1 (eBook)

<https://doi.org/10.1007/978-3-031-45964-1>

© The Editor(s) (if applicable) and The Author(s), under exclusive license
to Springer Nature Switzerland AG 2023

This work is subject to copyright. All rights are solely and exclusively licensed by the Publisher, whether the whole or part of the material is concerned, specifically the rights of translation, reprinting, reuse of illustrations, recitation, broadcasting, reproduction on microfilms or in any other physical way, and transmission or information storage and retrieval, electronic adaptation, computer software, or by similar or dissimilar methodology now known or hereafter developed.

The use of general descriptive names, registered names, trademarks, service marks, etc. in this publication does not imply, even in the absence of a specific statement, that such names are exempt from the relevant protective laws and regulations and therefore free for general use.

The publisher, the authors, and the editors are safe to assume that the advice and information in this book are believed to be true and accurate at the date of publication. Neither the publisher nor the authors or the editors give a warranty, expressed or implied, with respect to the material contained herein or for any errors or omissions that may have been made. The publisher remains neutral with regard to jurisdictional claims in published maps and institutional affiliations.

This Springer imprint is published by the registered company Springer Nature Switzerland AG
The registered company address is: Gewerbestrasse 11, 6330 Cham, Switzerland

Paper in this product is recyclable.

Foreword

This volume contains selected peer-reviewed articles presented at the International Conference on Innovative Research ICIR EUROINVENT 2023 Conference. The event was held in Iași, România, from the 11th to the 12th of May 2023.

The organizers are the Romanian Inventors Forum; Faculty of Materials Science and Engineering, The “Gheorghe Asachi” Technical University of Iasi, Romania; ARHEOINVEST Platform, Alexandru Ioan Cuza University of Iasi; Centre of Excellence Geopolymer and Green Technology (CEGeoGTech), Universiti Malaysia Perlis (UniMAP) and Department of Physics, Czestochowa University of Technology, Czestochowa, Poland, with the support of University Malaysia Terengganu.

The ICIR Conference is organized under the auspices of EUROINVENT. This is a joint event promoting creativity in a European context, by displaying the contributions of consecrated schools from higher education and academic research and also of individual inventors and researchers.

The EUROINVENT International Conference on Innovative Research (ICIR) brings together leading researchers, engineers and scientists who will present actual research results in the field of Materials Science and Engineering.

The conference aims to provide a high-level international forum for researchers, engineers and scientists to present their new advances and research results in the field of materials science and engineering.

The volume covers all the aspects of materials science, from synthesis and characterization of materials to procedures and technologies for materials engineering, as well as materials application and their involvement in the life sciences.

All the papers have been reviewed by at least two expert referees in their relevant topic disciplines, and only 18 were accepted. The papers selected for the volume depended on their quality and relevancy to the conference. All articles were checked with plagiarism software.

The conference was very dynamic with many questions and replies from the participants. At the conference closure ceremony, on the decision of the Scientific Board, Best Oral Presentation Award was presented next to two Best Poster Awards.

The editors hope that this volume will provide the reader with a broad overview of the latest advances in the field of materials science and engineering and that they will be a valuable reference source for further research.

The editors would like to express their sincere appreciation and thanks to all the committee members of the ICIR 2023 for their tremendous efforts.

Finally, the editors would like to thank all the authors for their contribution to this valuable volume.

Contents

State-of-the-Art and Future Trends of Thermoelectric Generation Systems in Automotive Industry	1
<i>George Achitei, Andrei Ionut Dontu, Bogdan Chiriac, and Aristotel Popescu</i>	
Tribological Characterization of Phosphate Coatings Deposited on Ti6Al4V	9
<i>Diana-Petronela Burduhos-Nergis, Andrei Victor Sandu, Dumitru-Doru Burduhos-Nergis, Nicanor Cimpoesu, Marcelin Benchea, Mihai Popa, and Costica Bejinariu</i>	
Flow Characteristics in Subsurface Storm Water Perforated Pipe for Drainage System Application	22
<i>Junaidah Abdullah, Mohd Remy Rozainy Mohd Arif Zainol, Mohd Sharizal Abdul Aziz, Mohd Fazly Yusof, Nor Ariza Azizan, Siti Fairuz Juiani, and Khairul Rahmah Ayub</i>	
XRD and TG-DTA Analysis of Fly Ash Based Geopolymer Composite Reinforced with Recycled Glass Fibers	31
<i>Dumitru-Doru Burduhos-Nergis, Petrica Vizureanu, Andrei Victor Sandu, and Bogdan Istrate</i>	
The Potential of Hybrid Polymer in Treating Textile Wastewater: Optimization of pH and Dosage Using Response Surface Methodology	45
<i>Siti Aisyah Ishak, Mohamad Fared Murshed, Mohd Remy Rozainy Mohd Arif Zainol, and Mohd Mustafa Al Bakri Abdullah</i>	
A Study of Flow Pattern and Sedimentation in Hydraulic Physical Model	62
<i>Muhammad Nasri Nasehir Khan, Mohd Remy Rozainy Mohd Arif Zainol, Mohd Azmier Ahmad, Nazirul Mubin Zahari, Mohd Hafiz Zawawi, Mohd Rashid Mohd Radzi, Nurhanani Abd Aziz, Farah Nurhikmah Che Ghazali, and Mohamad Aizat Abas</i>	
Effect of Different Foaming Temperature on Properties of NaHCO ₃ – Natural Rubber Latex Foam	77
<i>Mohammad Syahrin Smail, Zunaida Zakaria, Hakimah Osman, Abdulkhakim Masa, and Anusha Leemsuthep</i>	

Mapping of Geological Structures: Potential Geohazards in Tropical Highlands	89
<i>Nurfirdaus Sapawie, Afikah Rahim, Nazri Ali, Hamzah Hussin, Nor Shahidah Mohd Nazer, Agus Winarno, Deddy Tanggara, and Asmawi Hisham</i>	
A Review on Concrete Performance Towards Incorporation of Recycled Material - Coal	100
<i>Syuhaidah Azam, Afikah Rahim, Nazri Ali, Hamzah Hussin, Nor Shahidah Mohd Nazer, Agus Winarno, Deddy Tanggara, and Asmawi Hisham</i>	
Assessment of Hydrogen-Rich Syngas From Biogas Using Aspen HYSYS	116
<i>Adlina Alia Nofal Firhat, Muhammad Zulfaiz Hilmi Riduan, Hanafiah Zainal Abidin, Normadyzah Ahmad, Norhasyimi Rahmat, and Mohd Mustafa Al Bakri Abdullah</i>	
Physical Properties Characterization of Ceramic Waste Particles Used as Filler in Boat Hull Production: A Proposed Study	134
<i>Fakhrurrazi Rahman, Che Mohd Ruzaidi Ghazali, Mat Jusoh Suriani, Ahmad Fitriadhy, Nor Aieni Mokhtar, and Aminnudin</i>	
Yield of Biochar from Shrimp Shell Torrefaction and its Characterization: Proximate, Ultimate, and FTIR Spectroscopy Analyses	145
<i>Nurul Iffah Farhah Mohd Yusof, Alia Syafiqah Abdul Hamed, Aminnudin, Che Mohd Ruzaidi Ghazali, and Nur Farizan Munajat</i>	
Hybrid Fiber/Filler Reinforced Vegetable Oil-Based Composites: A Short Review	152
<i>Rohani Mustapha, Azrul Nazif Adnan, Siti Noor Hidayah Mustapha, Che Mohd Ruzaidi Ghazali, and Mohamad Awang</i>	
A Review on the Effect of Extrusion Parameter on 3D Printing Filament Diameter	163
<i>Krishna Kumar Nitiyah, Musa Luqman, Mohamad Rasidi Mohamad Syahmie, Ahmad Khairul Rafezi, Abd Rahim Shayfull Zamree, Rozyanty Rahman, and Ahmad Azrem Azmi</i>	
Mechanical Performance of Coal Ash - Mine Tailings Blended Geopolymer Designed by Taguchi Method	170
<i>Petrica Vizureanu, Dumitru-Doru Burduhos-Nergis, Andrei Victor Sandu, Dragos-Cristian Achitei, Diana-Petronela Burduhos-Nergis, Madalina-Simona Baltatu, and Manuela-Cristina Perju</i>	

Densification Behavior and Mechanical Performance of Nepheline Geopolymer Ceramics: Preliminary Study	184
<i>Nur Bahijah Mustapa, Romisuhani Ahmad, Mohd Mustafa Al Bakri Abdullah, Wan Mastura Wan Ibrahim, Andrei Victor Sandu, Christina Wahyu Kartikowati, Puput Risdanareni, and Wan Hasnida Wan Mohamed Saimi</i>	
The Properties of Crumb Rubber Loading on Fly Ash Based Geopolymer Mortar	193
<i>Reshikesan Ravi, Ahmad Azrem Azmi, Mohd Mustafa Al Bakri Abdullah, Lokman Hakim Ibrahim, Romisuhani Ahmad, and Che Mohd Ruzaidi Ghazali</i>	
Phosphate Conversion Coatings for Biomaterials: A Bibliometric Analysis	203
<i>Diana-Petronela Burduhos-Nergis, Andrei Victor Sandu, Dumitru-Doru Burduhos-Nergis, Carmen Nejneru, Petrica Vizureanu, and Costica Bejinariu</i>	
Author Index	215



State-of-the-Art and Future Trends of Thermoelectric Generation Systems in Automotive Industry

George Achitei^(✉) , Andrei Ionut Dontu , Bogdan Chiriac ,
and Aristotel Popescu 

Faculty of Mechanical Engineering, “Gheorghe Asachi” Technical University of Iasi,
61 Prof. Dimitrie Mangeron Street, 700050 Iasi, Romania
george.achitei@academic.tuiasi.ro

Abstract. Recovery of the energy contained within the waste heat from various processes represents an important concern for the efficiency of energy utilization. This paper aims to present an overview of currently employed methods for waste heat energy recovery in the automotive industry, with an emphasis on processes within thermal combustion engines and recovery methods based on thermoelectric generators (TEG). While TEG technology is capable of direct conversion of heat into electricity, conversion efficiency is quite low. Efforts are made to optimize these systems (number, size, form, positioning, location, etc.) in order to minimize heat loss and maximize energy recovery. The review concluded that the efficiency of TEG conversion might be improved by choosing appropriate characteristics for the recovery system for specific processes analyzed, such as thermoelectric materials, geometry, location, and type of cooling fluid.

Keywords: Thermoelectric generator · Thermal management · Waste energy · Automotive

1 Introduction

Originally identified by Peltier in 1834, this phenomenon generates electrical power for thermoelectric devices (thermoelectric modules). In the past, semiconductor materials were rarely used to generate cooling or heating effects. Through the development of semiconductor materials, a wide range of thermoelectric refrigeration applications have become possible [1].

A semiconductor material’s Seebeck coefficient and its absolute temperature determine the Peltier coefficient, which governs the Peltier effect. In the case of current flowing from an n-type material to a p-type material, there is a cooling effect, and in the case of current flowing from a p-type material to an n-type material, there is a heating effect. As the current direction changes, the temperature at the hot and cold ends of the circuit is reversed [2].

In a perfect world, the ratio of the Peltier coefficient [3] to the current running through the semiconductor material will determine how much heat is absorbed at the cold end

and how much heat is dissipated at the hot end. Two sources, conducted heat and joule heat, effectively limit the net quantity of heat absorbed at the cold end due to the Peltier effect. Heat will conduct through the semiconductor material from the hot to the cold ends as a result of the temperature difference between the cold and hot ends [4].

The Seebeck effect, which was first identified in 1821, is a property of thermoelectric devices that allows them to transform thermal energy from temperature gradients into electric energy. When there is a temperature difference between the hot and cold ends of a semiconductor material, a voltage is produced known as the Seebeck voltage. Thus, the Seebeck effect [5] really has the opposite impact as the Peltier effect. A thermoelectric device may also serve as a power generator as a result of the Seebeck effect. As a result of heating one junction, an electric current flow through the circuit, providing power to the device. As a matter of fact, a “module” is created by connecting a number of these thermocouples in series with each other [6].

A thermoelectric device (module) is typically built using more than one pair of semiconductors. Each semiconductor used in the module is referred to as a thermoelement, and a thermocouple is a pair of thermoelements [7].

2 State-of-the-Art

The thermoelectric generator (TEG), which is used for thermal energy harvesting, can directly convert heat into electricity. The thermopile, which is composed of thermocouples coupled electrically in series and thermally in parallel, is the basic structural component of TEG. Micro TEG (-TEG), which has the advantages of small volume and high output voltage, has attracted attention in the past 20 years as a result of the enormous advancements made in microelectromechanical systems technology.

One of the innovative technologies being used to cut gas emissions and manage the effects of global warming is the thermoelectric generator (TEG) [8]. TEGs use a direct, ecologically friendly conversion of thermal energy into electrical energy to implement the Seebeck effect [9]. TEGs have various benefits in addition to not having an influence on the environment. They are adaptable in terms of size and design and have a long lifespan due to the lack of moving components, circulation fluids, or chemical compounds. TEGs are built of numerous thermopiles, and each thermopile has a number of thermocouples that are coupled electrically and thermally in series and parallel, respectively, as shown in Fig. 1, [10–12].

A semiconductor material’s capacity for refrigeration depends on the interaction of its Seebeck voltage, electrical resistivity, and thermal conductivity throughout its operational temperature range between the cold and hot ends. The figure of merit Z is defined as the Seebeck coefficient squared divided by the electrical resistivity and thermal conductivity products. The figure of merit for each n- and p-type semiconductor material is temperature-dependent since each of their attributes changes with temperature. It can be demonstrated that the “temperature averaged” figure of merit of each semiconductor material is directly related to the largest temperature differential that a single pair of n-type and p-type materials may attain [13, 14].

As a result, the main goal in choosing and perfecting thermoelectric materials is to maximize the figure of merit. The heat pumping capacity of each n- and p-type

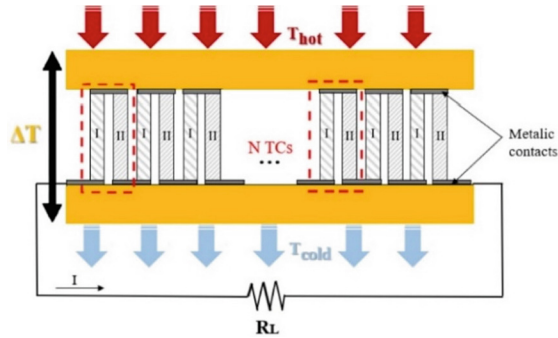


Fig. 1. Thermoelectric Generator (TEG).

semiconductor material is determined by its length-to-area ratio, while the temperature difference is constrained by the semiconductor material's figure of merit. A pseudo-binary alloy known as $(\text{Bi,Sb})_2(\text{Te,Se})_3$ is the most often used thermoelectric material for refrigeration in the temperature range of 120 to 230 °C.

P-type and N-type Bismuth Telluride thermoelements are connected electrically in series and thermally in parallel between the ceramic substrates in a conventional thermoelectric device, which is made up of two ceramic substrates that act as a foundation and electrical insulation. The dimensions range from 3 mm square by 4 mm thick to 60 mm square by 5 mm thick, and the maximal heat-pumping rate ranges from 1 to 125 W for conventional thermoelectric devices. The hot and cold sides can differ in temperature by a maximum of 70 °C. The devices range in thermocouple count from 3 to 127. It is possible to find multistage (cascade) series thermoelectric devices that can handle considerable temperature differences (up to 130 °C). About 100 °C is the lowest practicable temperature that may be reached.

Additionally, according to several studies, the majority of commercially available TEG modules manufactured of bismuth telluride have low operating temperatures (up to 260°C), a maximum figure of merit of 1.2, and low conversion efficiencies (up to 5%). Research on substitutes with superior temperature ranges and figures of merit, such as SiGe alloys, clathrates, skutterudites, and complementary metal-oxide semiconductors, is advised.

The vast majority of TEGs are used in various fields, such as Space Energy - where solar panels [15] are not sufficient, the thermoelectric generator is used to produce electricity in extreme conditions [16], such as in space travel [17–19].

Oil and gas industry - the thermoelectric generator is used to power sensors and other devices in extraction facilities, which are often in extreme conditions [20, 21].

Military technology - the thermoelectric generator [22] is used to power surveillance and communications devices in the field, where conventional power sources are not available. Medical industry - the thermoelectric generator is used in medical devices that need to operate in extreme conditions, such as sterilization rooms or blood cooling and heating devices [23–26].

Last but not least, these can be and are used in the Automotive Industry. The thermoelectric generator is used in hybrid and electric vehicles to charge the batteries, replacing

the traditional alternator, which is less efficient at low temperatures, but much research shows that they have also been tried in vehicles with internal combustion engines. As we all know, some components in internal combustion cars have various areas where waste heat is dissipated without being reused to its full potential. In this respect, based on TEGs, research has been carried out by positioning these devices in the exhaust or engine compartment area, where the level of heat release is very high and high temperatures can be reached.

One of the first tests using a TEG was carried out by Nissan in 1998 [27] when they developed an advanced type of thermoelectric module based on SiGe for application to a gasoline engine. This module consists of 8 pairs of these SiGe elements, which are electrically connected in series and have a maximum electrical power of 1.2 W, with a standing temperature difference of about 300 degrees Celsius. The modules are arranged between an exhaust pipe with a rectangular cross section and a water jacket around the exhaust pipe.

Another study shows that the thermal efficiency of brakes (BTE) can be improved by TEG, as they can recover significant heat losses from old internal combustion engine vehicles. Sok and Kusaka [28] conducted an experimental and modeling analysis of thermal recovery in a 2.2 L diesel engine to maximize its performance by demonstrating that a thermoelectric module (TEM) layout in TEG must be optimized, taking into account a trade-off between increased pump loss and TEG effective power, in order to fully utilize TEG in the engine. First, a high-fidelity 1D TEG model is created, and a fresh approach to model calibration is suggested by leveraging condensed user-defined functions for flow friction and heat transfer. The TEG heat exchanger's measured thermal performances are replicated for a variety of fin pitches, Reynolds numbers, and inlet gas conditions.

To increase its BTE and power, the TEG model is coupled with a precisely calibrated engine. Peak BTE at 2250 RPM, 60% load, and BTE = 48.7% and 52.1 kW braking power are the conditions that yield the highest efficiency. These results are obtained under the base scenario without TEG. The 3-layer TEG type (1.5 A4 paper size, 150 mm height, 36 kg weight) produces 1.1 kW of effective power in an ideal 9×10 TEM configuration. Finally, a next-generation, extremely efficient hybridized diesel engine is developed that achieves a 1.1% BTE improvement without sacrificing output.

This article examines the capabilities of thermoelectric materials, such as their ability to recover lost energy, cool electronic equipment, and use a heat source to regenerate electrical energy by using the thermoelectric effect.

Authors Zhang and Zhao [29] conducted extensive research on the thermoelectric quality factor, figure of merit, and thermoelectric material properties. All these factors are highly significant in determining the ability to transfer heat into electricity as well as the efficiency of thermoelectric materials.

At the same time, the authors examine various thermoelectric material classes, including semiconductors, graphite-based materials, intermetallics, and organic materials. Thermoelectric materials have enormous promise for enhancing energy efficiency and lowering CO₂ emissions.

The influence of metal foam thickness inside an automotive exhaust gas line with external thermoelectric generators (TEGs) is quantitatively examined in this paper by

Buonomo et al. [30]. Considered is a forced convective regime two-dimensional steady state heat transfer problem in a porous medium inside a conduit. The study enables a comparison of metal foam's impact on TEG performance for various foam thicknesses, porosities, pore densities, and mass flow rates of exhaust gas. The findings are displayed as temperature and pressure drop profiles. The major parameters are estimated and used to represent TEG efficiency and electric power. The major conclusions demonstrate that the channel's wall temperatures significantly increase when metal foams are used. As a result, increases in TEG efficiency are seen for a variety of metal foam thickness values.

According to the authors, Fernández-Yañez, P et al. [31], the main goal of this research is to examine the potential of TEGs in light-duty diesel engines, where there is less energy accessible in the exhaust systems and more difficulty in achieving energy recovery. Additionally, the engine was tested far from the full-load curve in the region of the engine map that is most frequently employed for passenger automobiles. This work also fills in the gaps in the development and deployment of thermoelectric generator prototypes by offering a fresh, practical understanding of the flow inside TEGs and the impact of catalysts. A TEG was created using a distinct methodology that focused on both minimizing engine impact (not always taken into account) and increasing electrical power production. Using computational fluid dynamics (CFD), the main design issues for the devices in this scenario are identified, and the implications of size and internal topology are researched. An innovative and detailed module-by-module methodology was used to thoroughly validate the CFD model that calculates electricity production. The engine map's common driving situations region of high load, high engine speed can recover some energy, according to the results [31].

Another piece of research demonstrates the importance of on-board power generation in light of the growing trend of electrification in road vehicles. The performance of a unique temperature-controlled thermoelectric generator (TCTG) concept in a light duty vehicle is evaluated in the current work, as well its effects on fuel efficiency and GHG emissions under actual driving situations. Corrugated pipes integrated in a matrix of cast aluminum make up the new exhaust heat exchanger (HE) idea, and variable conductance heat pipes (VCHPs) serve as spreaders of extra heat along the longitudinal direction. Due to its ability to prevent overheating by dispersing heat rather than squandering it through by-pass devices, this technology appears to have pretty excellent potential for highly variable thermal load applications. In addition, it does not require gravity aid and has a form factor similar to conventional generators, which are differences from the group's earlier designs. With as much as 572 W and 1538 W of average and maximum electric powers during a driving cycle, respectively, and a very promising reduction of 5.4% in fuel consumption and CO₂ emissions, it also seems to be capable of delivering a breakthrough electric output for TEG systems in such light vehicles [32].

In general, this branch of renewable energy is growing, and solutions are being sought to reduce pollution levels in the first place, but in this part of the vehicle sector, the aim is to make maximum use of waste or waste heat, mainly from vehicles equipped with internal combustion engines. It must be recognized that research in this area has been limited in number and that the cost of producing these devices is quite high. For this reason, the search is on for the best way to make a thermoelectric generator that is

productive for a vehicle but at the same time costs as little as possible, but so far good results have been achieved in this direction.

3 Conclusions

This review presents the current status of thermoelectric generators, as well as the Peltier and Seebeck effects used in several fields of activity, with the main emphasis on the field of road vehicles. We note that in this industry, attempts are being made to optimize a device based on a TEG using the Seebeck effect by positioning it in a vehicle with an internal combustion engine in the most suitable places, where heat is wasted in nature and the temperature difference is quite high. In the future, it is hoped to develop such devices to produce auxiliary electrical energy for the vehicle, which can be used in various forms but at the lowest possible production cost.

References







1. Alashkar, A., Alami, A.H.: Overview of Thermoelectric Materials. Elsevier, Encyclopedia of Smart Materials (2022)
2. Olabi, A.G., et al.: Potential applications of thermoelectric generators (TEGs) in various waste heat recovery systems. *Int. J. Thermofluids* **16**, 100249 (2022)
3. Kuz'minskii, Y.V., Gorodyskii, A.V.: Thermal analysis of electrochemical reactions: Part I. Kinetic method of determining Peltier heats. *J. Electroanalytical Chemistry and Interfacial Electrochemistry* **252**(1), 2137 (1988)
4. Wang, J., Cao, P., Li, X., Song, X., Zhao, C., Zhu, L.: Experimental study on the influence of Peltier effect on the output performance of thermoelectric generator and deviation of maximum power point. *Energy Conversion and Management* **200**, 112074 (2019)
5. Nan, B., Xu, G., Yang, Q., Zhang, B., Zhou, X.: Innovative design and optimized performance of thermoelectric transistor driven by the Seebeck effect. *Energy Conversion and Management* **283**, 116880 (2023)
6. Mahan, G.D.: Thermoelectric Effect, Reference Module in Materials Science and Materials Engineering. Elsevier (2016)
7. Cao, T., Shi, X.L., Chen, Z.G.: Advances in the design and assembly of flexible thermoelectric device. *Progress in Materials Sci.* **131**, 101003 (2023)
8. Jaziri, N., Boughamoura, A., Müller, J., Mezghani, B., Tounsi, F., Ismail, M.: A comprehensive review of thermoelectric generators: technologies and common applications. *Energy Reports* **6**(7), 264287 (2020)
9. Yuan, D., Jiang, W., Sha, A., Xiao, J., Wu, W., Wang, T.: Technology method and functional characteristics of road thermoelectric generator system based on Seebeck effect. *Applied Energy* **331**, 120459 (2023)
10. Kwan, T.H., Wu, X., Yao, Q.: Thermoelectric device multi-objective optimization using a simultaneous TEG and TEC characterization. *Energy Conversion and Manage.* **168**, 8597 (2018)
11. Gopinath, M., Marimuthu, R.: PV-TEG output: comparison with heat sink and graphite sheet as heat dissipators. *Case Studies in Thermal Eng.* **45**, 102935 (2023)
12. Newby, S., Mirihanage, W., Fernando, A.: Recent advancements in thermoelectric generators for smart textile application. *Materials Today Commun.* **33**, 104585 (2022)
13. Sun, P., Kumar, K.R., Lyu, M., Wang, Z., Xiang, J., Zhang, W.: Generic Seebeck effect from spin entropy. *The Innovation* **2**(2) (2021)

14. Chelly, A., Belhassen, J., Karsenty, A.: Spatial-dependence cross-examination method of the Seebeck effect applied to Ge surface. *Applied Surface Sci.* **585**, 152587 (2022)
15. Liu, Z., Cheng, K., Wang, Z., Wang, Y., Ha, C., Qin, J.: Performance analysis of the heat pipe-based thermoelectric generator (HP-TEG) energy system using in-situ resource for heat storage applied to the early-period lunar base. *Applied Thermal Engineering* **218**, 119303 (2023)
16. Jaworski, M., Bednarczyk, M., Czachor, M.: Experimental investigation of thermoelectric generator (TEG) with PCM module. *Applied Thermal Eng.* **96**, 527533 (2016)
17. Ochieng, A.O., Megahed, T.F., Ookawara, S., Hassan, H.: Comprehensive review in waste heat recovery in different thermal energy-consuming processes using thermoelectric generators for electrical power generation. *Process Safety and Environmental Protection* **162**, 134154 (2022)
18. Chen, L., Lorenzini, G.: Heating load, COP and exergetic efficiency optimizations for TEG-TEH combined thermoelectric device with Thomson effect and external heat transfer. *Energy* **270**, 126824 (2023)
19. Komori, T., Norimasa, O., Yamamoto, H., Hoshino, K., Takada, Y., Takashiri, M.: Effect of Seebeck coefficient distribution across pn-junction in carbon nanotube films for photothermoelectric power generation by localized sunlight irradiation. *Diamond and Related Materials* **136**, 109929 (2023)
20. Chen, W.H., Lin, Y.X., Chiou, Y.B., Lin, Y.L., Wang, X.D.: A computational fluid dynamics (CFD) approach of thermoelectric generator (TEG) for power generation. *Applied Thermal Eng.* **173**, 115203 (2020)
21. Dalane, K., Josefsen, N.T., Ansaloni, L., Hillestad, M., Deng, L.: Thermopervaporation for regeneration of triethylene glycol (TEG): Experimental and model development. *J. Membrane Science* **588**, 117205 (2019)
22. Sharma, A., Masoumi, S., Gedefaw, D., O'Shaughnessy, S., Baran, D., Pakdel, A.: Flexible solar and thermal energy conversion devices: Organic photovoltaics (OPVs), organic thermoelectric generators (OTEGs) and hybrid PV-TEG systems. *Applied Materials Today* **29**, 101614 (2022)
23. Jamali, E., Nobakhti, M.H., Ziapour, B.M., Khayat, M.: Performance analysis of a novel model of photovoltaic PV-TEGs system enhanced with flat plate mirror reflectors. *Energy Conversion and Manage.* **279**, 116766 (2023)
24. Wang, J., Choi, C.U., Shin, S.: Rapid microfluidic-thromboelastography (μ -TEG) for evaluating whole blood coagulation and fibrinolysis at elevated shear rates. *Sensors and Actuators B: Chemical* **390**, 133873 (2023)
25. Sánchez, J., Cortés-Hernández, D.A., Rodríguez-Reyes, M.: Synthesis of TEG-coated cobalt-gallium ferrites: Characterization and evaluation of their magnetic properties for biomedical devices. *J. Alloys and Compounds* **781**, 10401047 (2019)
26. Morizane, K., et al.: A novel thermoelectric cooling device using Peltier modules for inducing local hypothermia of the spinal cord: the effect of local electrically controlled cooling for the treatment of spinal cord injuries in conscious rats. *Neuroscience Res.* **72**(3), 279282 (2012)
27. Ikoma, K., Munekiyo, M., Furuya, K., Kobayashi, M., Izumi, T., Shinohara, K.: Thermoelectric module and generator for gasoline engine vehicles, Seventeenth International Conference on Thermoelectrics. *Proceedings ICT98 (Cat. No.98TH8365)*, Nagoya, Japan (1998)
28. Sok, R., Kusaka, J.: Experimental and modeling analysis on thermoelectric heat recovery to maximize the performance of next-generation diesel engines dedicated for future electrified powertrains. *Applied Thermal Eng.* **219**, 119530 (2023)
29. Zhang, X., Zhao L.D.: Thermoelectric materials: Energy conversion between heat and electricity. *J. Materiomics* **1**(2), 92105 (2015)
30. Buonomo, B., Cascetta, F., di Pasqua, A., Manca, O.: Performance parameters enhancement of a thermoelectric generator by metal foam in exhaust automotive lines. *Thermal Science and Engineering Progress* **38**, 101684 (2023)

31. Fernández-Yañez, P., Armas, O., Capetillo, A., Martínez-Martínez, S.: Thermal analysis of a thermoelectric generator for light-duty diesel engines. *Applied Energy* **226**, 690702 (2018)
32. Pacheco, N., Brito, F.P., Vieira, R., Martins, J., Barbosa, H., Goncalves, L.M.: Compact automotive thermoelectric generator with embedded heat pipes for thermal control. *Energy* **197**, 117154 (2020)



Tribological Characterization of Phosphate Coatings Deposited on Ti6Al4V

Diana-Petronela Burduhos-Nergis , Andrei Victor Sandu ,
Dumitru-Doru Burduhos-Nergis, Nicanor Cimpoesu , Marcelin Benchea ,
Mihai Popa , and Costica Bejinariu 

“Gheorghe Asachi” Technical University of Iasi, 41 “D. Mangeron” Street, 700050 Iasi, Romania
sav@tuiasi.ro, costica.bejinariu@yahoo.com

Abstract. In recent years, improving the surface of titanium implants is increasingly being studied, in order to reduce their rejection rate. Thus, there are several methods by which the properties of the base material, in this case, the titanium alloy, can be improved, such as anodizing, micro-arc oxidation, plasma spraying, physical vapour deposition, biomimetic deposition, chemical conversion deposition etc. Regarding the deposition process by chemical conversion, the phosphating process presents a multitude of advantages, including good adhesion to the substrate and the capacity of improving cellular adhesion due to the porosity of the layer. Therefore, the paper aims to study the tribological characteristics by evaluating the adhesion and coefficient of friction of three types of phosphate layers deposited on the surface of the titanium alloy, Ti6Al4V, using a UMTR 2M-CTR Micro-tribometer and SEM. The results of the scratch tests revealed that the phosphate layers have good adhesion to the substrate and the values of the coefficient of friction were increased due to the roughness of the surface.

Keywords: Tribological characterization · Titanium · Phosphate layers

1 Introduction

Researchers' interest in bioengineering has expanded as a result of the accelerated expansion in demand for orthopaedic implants. Metallic materials, such as titanium alloys, stainless steel, and Co-Cr alloys, have long been employed in medical applications. Among these, titanium and its alloys, particularly Ti6Al4V, are the most often utilized biomaterials for the production of orthopaedic implants. The latter offers a variety of benefits, including good biocompatibility, low density, adequate corrosion and wear resistance, etc. The biggest drawback of Ti6Al4V titanium alloy, according to Pesode and Barve [1], is that it cannot interact with human bone because of its bio-inert surface, which can result in implant failure. Multiple studies [2–4] mentioned the likelihood of aluminium or vanadium being absorbed by the human body. This will have negative effects on the human body [5].

To find a solution to these identified problems, several researchers have tried to modify the surface characteristics of titanium and its alloys by depositing layers on the

metal surface [6–9]. Thus, one of the most studied types of coatings is the deposition of hydroxyapatite, by different processes such as electrochemical deposition [10], physical vapor deposition (PVD), sol-gel method [11] etc. Regarding the tribological characteristics, it was observed that the deposited layer has good resistance to the pressure of the blade, but its adhesion to the substrate is lower compared to those deposited by the chemical conversion process [5, 12].

Sovak [13] studied the osseointegration of Ti6Al4V after its coating with TiN coating, observing as a disadvantage a low adhesion of the layer to the substrate. Also, Qin [14] analyzed the improvements in the antibacterial and wear characteristics of Ti6Al4V after the deposition of a composite layer on the metal surface. The authors observed that the coefficient of friction decreased significantly and the antibacterial and cytocompatibility are good.

Recently, much attention has been paid to coatings on biometals surfaces deposited by a chemical conversion process called phosphating [15, 16]. The advantages of this method are highlighted in many studies, the most significant being: the promotion of osseointegration, the low cost of the deposition process, the enhancement of corrosion and wear resistance etc. [17, 18]. In addition, the deposited layers show high adhesion to the substrate due to the chemical conversion reactions between the metal and the phosphating solution [19].

Regarding the deposition of phosphate layers on titanium or its alloys, three types of coatings based on zinc, strontium, zinc-strontium, and zinc-calcium are known [17, 20, 21], depending on the nature of the metal ion in the phosphating solution. So, one of the novelties of this work is the use of three types of phosphate solutions. Two are completely original, based on zinc-magnesium and zinc-zirconium. The third one is based on zinc-calcium but with different activators and inhibitors. Over time, it has been observed that the bonding strength between the base material and the phosphate layer is influenced by the surface roughness, the activation process, the morphology of the coating, etc. [16].

Solanke [22] tested from the point of view of wear resistance several metal biomaterials, including Ti6Al4V, thus concluding that of all those tested, the titanium alloy is one of the most suitable for medical implants, however, considering that it is essential to use a surface coating. Even if the mechanical properties of the Ti6Al4V alloy have been analyzed, it is also necessary to analyze the tribological characteristics of the layers formed on its surface. Thus, this work studies the possibility of promoting cell adhesion and enhancing the surface properties of the titanium alloy. This is done by depositing new phosphate layers deposited by the chemical conversion process (phosphating). In this case, adhesion, coefficient of friction and surface scratch behaviour are studied for three different phosphate layers based on Mg-Zn, Zr-Zn, and Ca-Zn and also for the Ti6Al4V uncoated sample.

2 Materials and Methods

2.1 Material

The material used as the substrate for the deposition is Ti6Al4V, which was purchased from AEMMetal (Hunan, China). Its chemical composition according to the supplier is shown in Table 1.

Table 1. The chemical composition of Ti6Al4V.

Element	Titanium	Aluminium	Vanadium	Iron	Oxygen	Carbon
wt, %	balance	6.14	4.22	0.12	0.11	0.03

2.2 Phosphating Process

Before the phosphating process, the bars were cut into 10x10x55 mm square samples. After this, the samples were sanded up to 1200 grit to obtain a homogeneous surface.

The steps involved in the phosphating process are shown in Fig. 1. The process starts with the degreasing of the samples by washing them, for 10 min, in an ultrasonic cleaner, by immersing them subsequently in three different media: technical acetone, ethanol, and distilled water. The second stage of the process is the removal of oxides and the activation of the surface. This is done by immersing for 15 s in a 2% HF solution and for 30 s in a titanium colloidal solution, at room temperature. During the third stage, the layer is obtained by immersing the samples in the phosphating solution for 60 min at 90 °C. In this paper, three different phosphating solutions based on zinc-magnesium, zinc-zirconium, and zinc-calcium were used. The phosphating solutions are a mixture of nitric acid, orthophosphoric acid, iron powder, sodium tripolyphosphate,

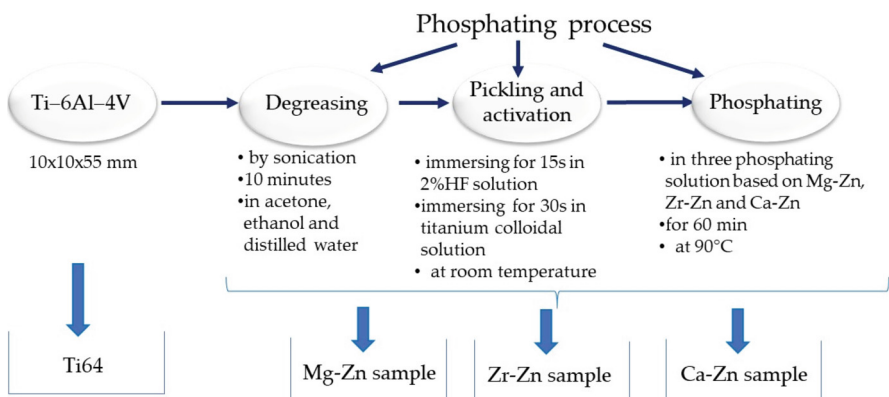


Fig. 1. The flow of the phosphating process and the types of samples obtained.

sodium hydroxide, sodium nitrite, sodium fluoride, zinc, and, depending on the type of solution, magnesium carbonate, zirconium oxide, or calcium nitride.

In order to be easier to understand, was used the following abbreviations:

Ti64 – for Ti6Al4V uncoated;

Mg-Zn – for the samples coated with a magnesium-zinc phosphate layer;

Zr-Zn – for the samples coated with a zirconium-zinc phosphate layer;

Ca-Zn – for the samples coated with a calcium-zinc phosphate layer.

2.3 Characterization Methods

A scanning electron microscope (Vega Tescan LMH II), equipped with Energy-dispersive X-ray spectroscopy (EDX) analysis equipment was used to examine the morphology and scratch traces of the samples.

Scratch tests were performed using a UMTR 2M-CTR Micro-tribometer. The scratch test settings are as follows: the distance covered by the blade is 10 mm, the blade speed is 167 $\mu\text{m}/\text{second}$, and the normal force grows with time from 0 to 10N. Using this test, the layer was gradually removed from the Ti6Al4V surface. This test examines the parameters described further: F_x , which is the response force value, F_z , which is the normal load force, F_f which is the friction force, COF, which is the coefficient of friction and AE which is acoustic emission.

3 Results and Discussions

The Ti6Al4V uncoated sample. The Ti64 sample presents an approximately constant value with small variations of the coefficient of friction due to its homogeneous surface, as can be observed in Fig. 2.

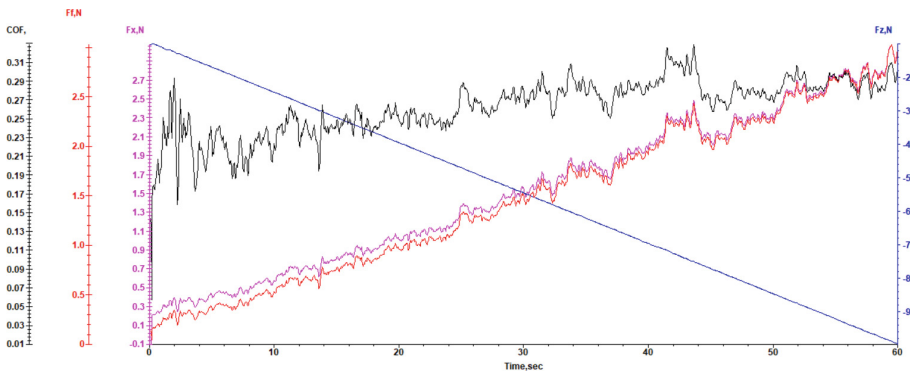


Fig. 2. Time variation of F_x , F_z , F_f and COF during the scratch test for the Ti64 sample.

In this case the average value of the coefficient of friction was close to 0.26 value, with a standard deviation (std) of 0.03. Between 40–45 s can be observed that it is a significant increase in the values of COF close to the 3 N, followed by a decrease of

the F_x value. This can be explained by the material that was blocked in the front of the blade. Also, the average value of F_f is close to 2.21, with a std of 0.09. Furthermore, as can be seen from Fig. 3, the acoustic emission is decreasing after the COF has stabilized, its average value being close to 0.07 with a std of 0.003. These values are influenced by the mechanical preparation of the surface, this one being grinding at 800 grids.

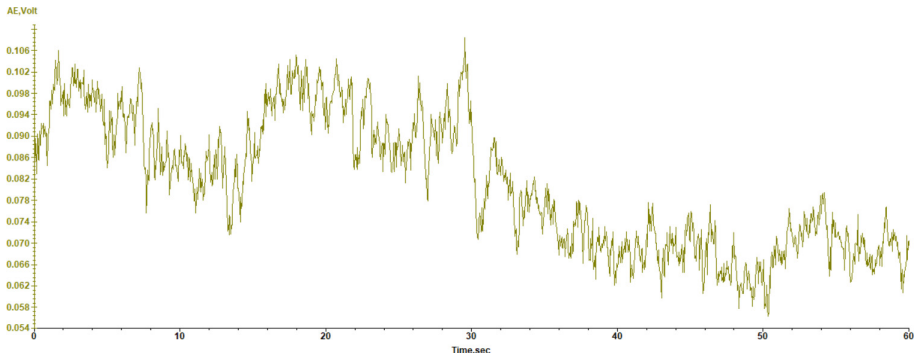


Fig. 3. Time variation of AE during the scratch test for the Ti64 sample.

The microstructural analysis of the scratch and the trace profile are presented in Figs. 4a and 4c. Also, in Fig. 4b and the 3D profile (Fig. 4d) can be observed close to the end of the scratch, the material parts stuck.

The Mg-Zn sample. After deposition of the magnesium-zinc phosphate layer on the Ti6Al4V alloy surface, the average value of the coefficient of friction almost doubles to 0.48, with a std of 0.09. Close to 25 s, the slope of the COF and F_f is changing, probably due to the cracking of the phosphate crystals (Fig. 5), close to a load value of 3 N. The fluctuation of the COF values is related to the roughness of the phosphate layer, which has a value of 2.21 μm . The AE presented in Fig. 6 shows a constant profile, with small variations which are probably appearing due to the crystal's cracks. The AE average value is 0.002 with a std of 0.002.

The SEM analysis of the Mg-Zn phosphate layer deposited on the Ti6Al4V surface shows crystals specific to the phosphate layer based on Zn, which were partially removed from the titanium alloy surface, close to the final part of the scratch (Fig. 7a). This aspect can be observed, also, in Fig. 7b, where can be seen parts of the crystals on the scratch track. The roughness of the surface is visible in Figs. 7c and 7d. The elemental mapping shows the end of the scratch track. As can be seen from Fig. 8, due to the fact that the layer was obtained by a chemical conversion process, the presence of the principal elements of the layer (Zn, Mg, Fe, P and O) can be observed, but in small quantities compared with the edges. Also, at this moment, a big part of the layer was removed and the quantity of Ti in that zone was increased.

The Zr-Zn sample. The scratching behaviour of the Zr-Zn sample is different from that of the Mg-Zn solution phosphate sample (Fig. 9). Thus, a sudden increase in the coefficient of friction can be observed, which corresponds to a load force of 4.7 N, close to 22 s. The mean value of COF is 0.34, with a std of 0.12, while the mean value of F_f is

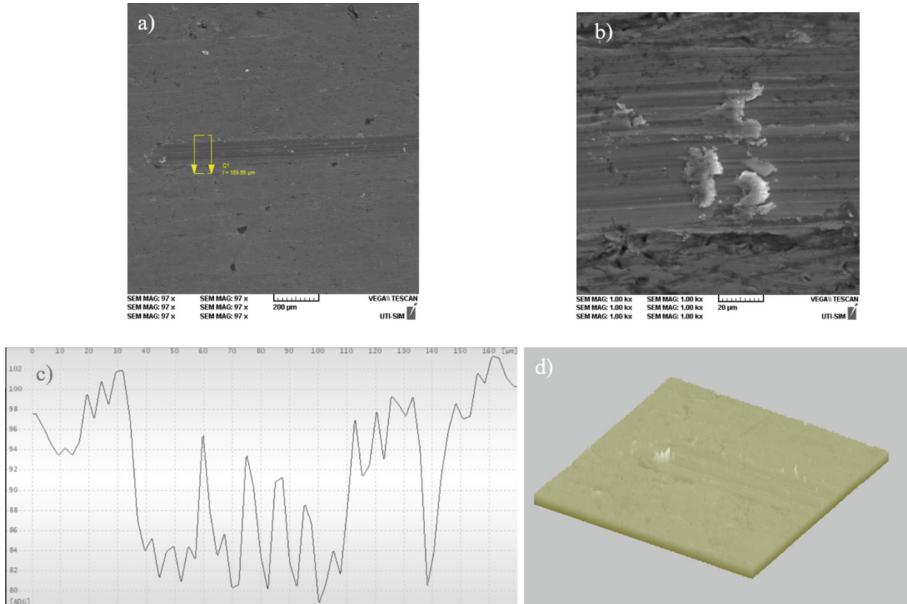


Fig. 4. Ti64 microstructure after scratch test a) SEM morphology of the trace 250x; b) SEM image of stuck material 1kx; c) scratch profile; d) 3D profile.

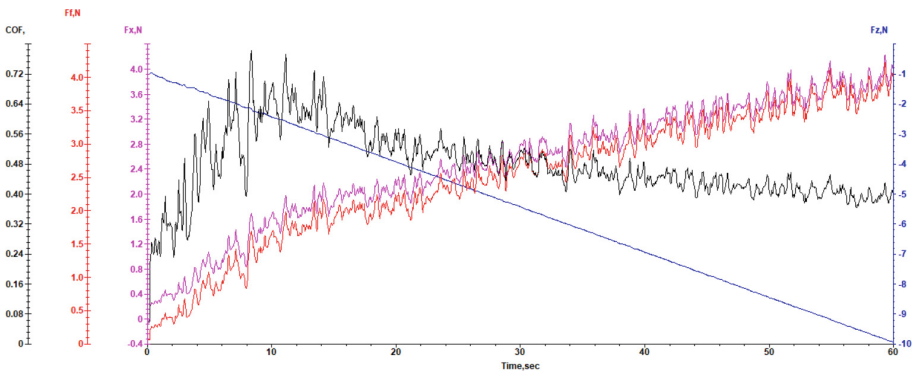


Fig. 5. Time variation of F_x , F_z , F_f and COF during the scratch test for the Mg-Zn sample.

2.07 N, with a std of 1.26. Compared to the Mg-Zn phosphate-coated sample, the Zr-Zn sample has a much lower roughness value, approximately $0.96 \mu\text{m}$, thus explaining the lower values of COF and F_f . The same change close to 22 s can be observed also in Fig. 10, where the AE curve presents variations after this time, probably due to different dimensions and positions of crystals which are cracking at contact with the blade. In this case, the AE average value is 0.003 with a std of 0.003.

The SEM images of the Zr-Zn phosphate layer show crystals specific to compounds formed on the surface of Ti6Al4V, especially of zinc phosphate tetrahydrate (Fig. 11a). In

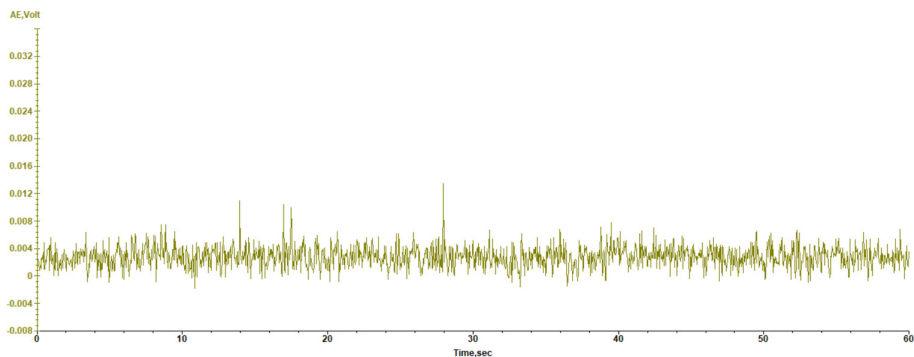


Fig. 6. Time variation of AE during the scratch test for the Mg-Zn sample.

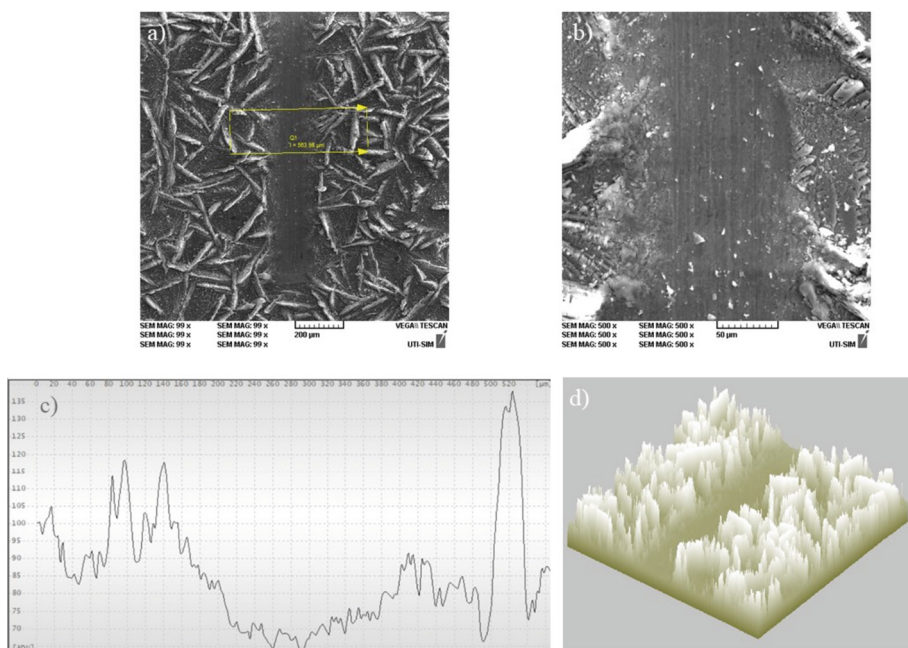


Fig. 7. Mg-Zn sample microstructure after scratch test a) SEM morphology of the trace 100x; b) SEM morphology with crack crystals 500x; c) scratch profile; d) 3D profile.

this case, compared with the Mg-Zn sample, the phosphate crystals are denser, covering the entire surface of the sample (Fig. 11b). Also, can be observed that the intercrystalline zones are smaller compared with the Mg-Zn phosphate layer, which determines a lower roughness value (Figs. 11c and 11d). Moreover, can be observed that the phosphate layer was removed from the surface of Ti6Al4V, with only small parts of the crystals remaining. The EDX analysis determined the elemental mapping of the main elements of the layer at the end of the scratch (Fig. 12). As can be seen, the presents of Ti in

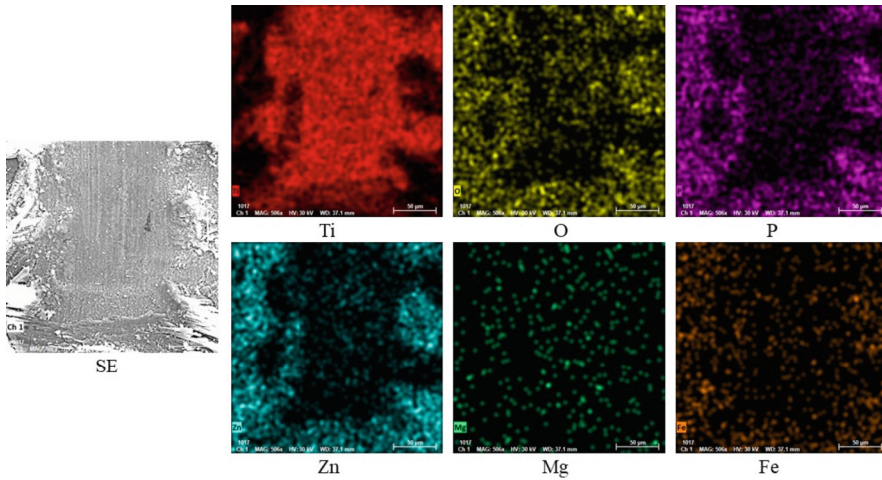


Fig. 8. The elemental mapping of the main elements of the Mg-Zn sample after the scratch test.

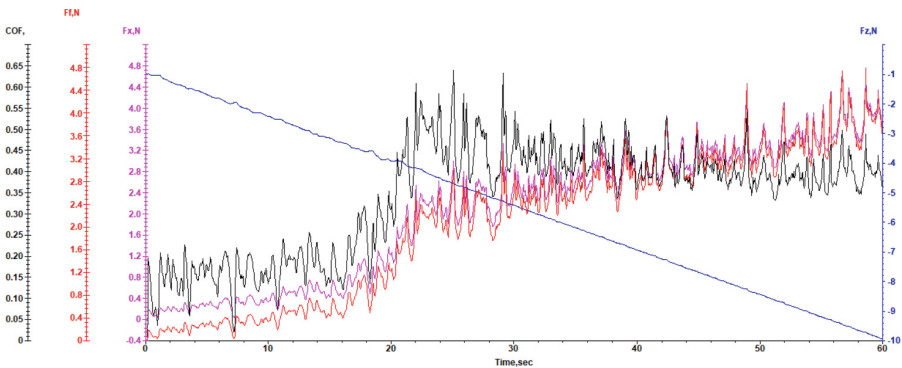


Fig. 9. Time variation of F_x , F_z , F_f and COF during the scratch test for the Zr-Zn sample.

high quantity indicates that the phosphate layer was partially removed, but taken into consideration that the phosphate layer was formed by chemical conversion process and just a small quantity of ZrO_2 was used in the phosphating solution, the Zn, Zr, P, O and Fe can be detected on the track's blade.

The Ca-Zn sample. The sample on which was deposited a Ca-Zn phosphate layer shows similar scratching behaviour to the sample coated with an Mg-Zn layer, as can be seen in Fig. 13. At the same time, the average value of the friction coefficient is 0.47, with a std of 0.1, very close to the value of the Mg-Zn sample (0.48). This behaviour is also due to the specific roughness of the layer, amounting to $1.34 \mu\text{m}$. As can be observed in Fig. 13, close to 19 s the crystals started to yield under the pressure of the blade and the COF becomes almost constant, at a load force of 2.1 N. Also, the AE graphic presents many peaks which can be attributed to the failure of big

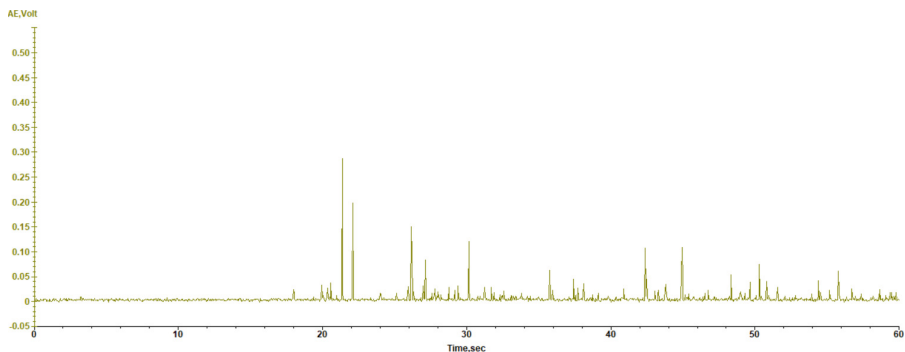


Fig. 10. Time variation of AE during the scratch test for the Zr-Zn sample.

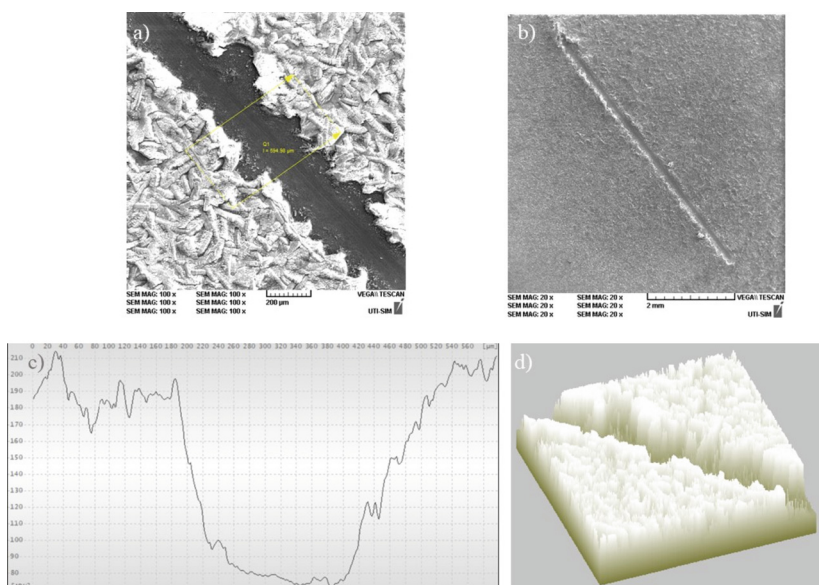


Fig. 11. Zr-Zn sample microstructure after scratch test a) SEM morphology of the trace 100x; b) SEM morphology with the entire scratch track 25x; c) scratch profile; d) 3D profile.

phosphate crystals at contact with the blade, the average AE value being 0.004 with a std of 0.002, Fig. 14.

The difference between the morphology of the Ca-Zn phosphate layer compared with the Zr-Zn and Mg-Zn layer can be observed in Figs. 15a and 15b. The biggest difference in structure is between the Zr-Zn and Ca-Zn layers, especially regarding the dimensions of the crystals, which are smaller for the Zr-Zn sample. The Ca-Zn layer also presents intercrystallite zones which are similar to the Mg-Zn sample structure. The presence of these zones and the dimension of crystals explain the value of roughness, which can be observed also in Figs. 15c and 15d. The elemental mapping of the main elements of the

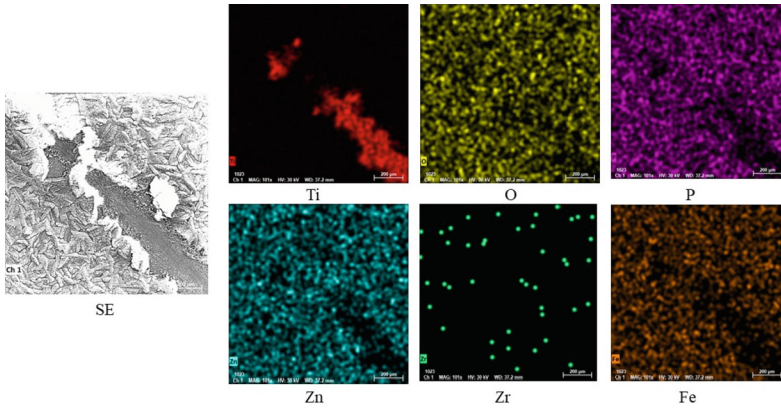


Fig. 12. The elemental mapping of the main elements of the Zr-Zn sample at the end of the scratch track.

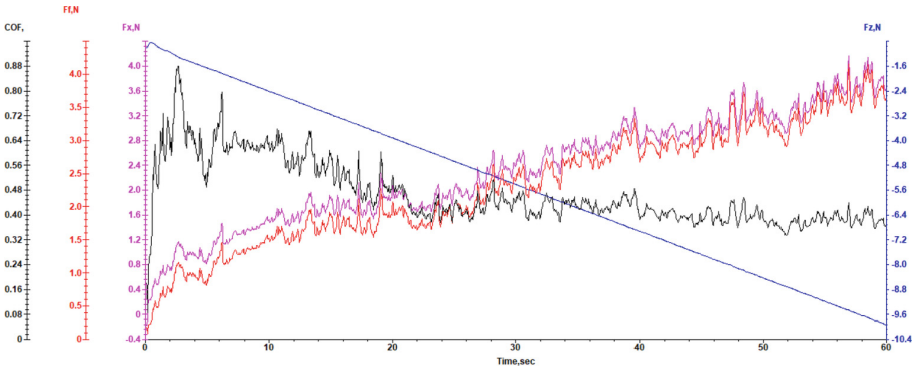


Fig. 13. Time variation of F_x , F_z , F_f and COF during the scratch test for the Ca-Zn sample.

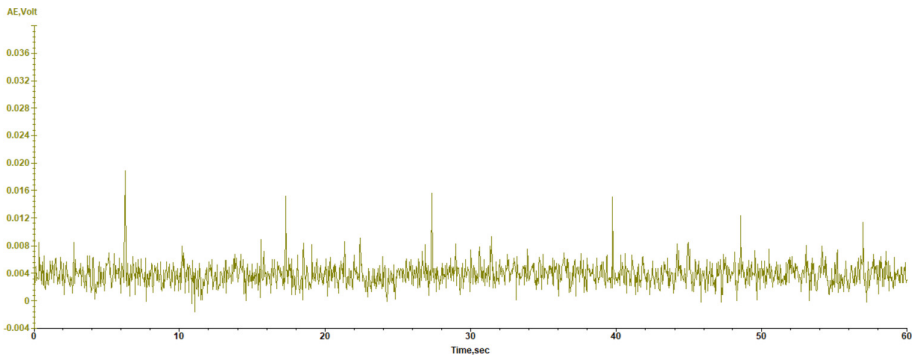


Fig. 14. Time variation of AE during the scratch test for the Ca-Zn sample.

Ca-Zn phosphate layer after the scratch test is presented in Fig. 16. As can be observed, the phosphate layer was removed partially, but as in other cases (Mg-Zn and Zr-Zn) some parts of the crystals remain on the surface of Ti6Al4V. Another important aspect is the big quantity of Ti, which indicates that in the intercrystalline zone, the layer of phosphate is very thin, being easier for the blade to remove the layer in those areas.

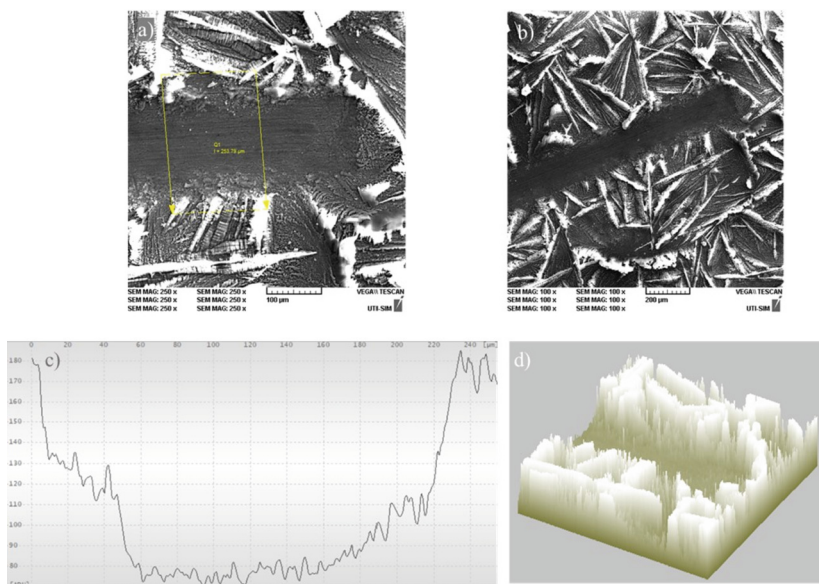


Fig. 15. Ca-Zn sample microstructure after scratch test; SEM morphologies of the trace a) 250x and b) 100x; c) scratch profile; d) 3D profile.

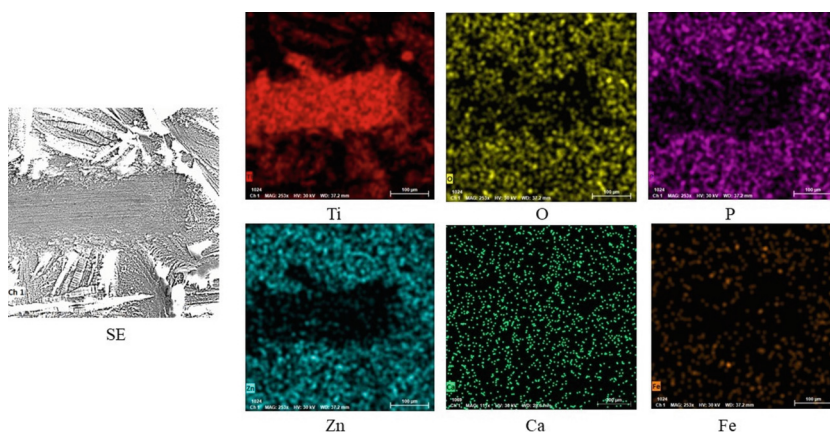


Fig. 16. The elemental mapping of the main elements of the Ca-Zn sample at the end of the scratch track.

4 Conclusions

To promote the surface characteristics of the Ti6Al4V alloy was deposited by chemical conversion process three different phosphate layers based on magnesium-zinc, zirconium-zinc and calcium-zinc. The tribological properties of the layers obtained and the uncoated sample were studied using the scratch method. Also, the scratch track was analyzed by SEM and EDX. After deposition, the roughness value of the surface obtained was increased considerably. Influenced by the roughness of the surface, the value of the coefficient of friction has doubled from 0.24 for the uncoated sample to 0.48 and 0.47 for Mg-Zn and Ca-Zn samples. From the coated samples, the one with the smallest roughness is the Zr-Zn sample, the SEM micrographs show that the layer is more compact. Also, the scratch test and EDX analysis revealed that this sample has the best adhesion to the substrate, even if the layer was not completely removed from the other samples either. Due to the modification of the surface characteristics by enhancing the roughness of the layer, can be concluded that the phosphate layer obtained on the surface of Ti6Al4V can promote cell adhesion.

Acknowledgement. This paper was realized with the support of COMPETE 2.0 project nr.27PFE/2021, financed by the Romanian Government, Minister of Research, Innovation and Digitalization. This paper was also supported by “Gheorghe Asachi” Technical University from Iași (TUIASI), through the Project “Performance and excellence in postdoctoral research 2022”.








References

1. Pesode, P., Barve, S.: A review-metastable β titanium alloy for biomedical applications. *J. Eng. Appl. Sci.* **70**, 1–36 (2023)
2. Barchowsky, A.: Systemic and immune toxicity of implanted materials. *Biomaterials Science. An Introduction to Materials in Medicine*, 791–799 (2020)
3. Manivasagam, G., Dhinasekaran, D., Rajamanickam, A.: Biomedical implants: corrosion and its prevention - a review. *Recent Patents on Corrosion Science* **2**, 40–54 (2010)
4. Kim, K.T., Eo, M.Y., Nguyen, T.T.H., Kim, S.M.: General review of titanium toxicity. *Int. J. Implant Dentistry* **5**(1), 1–12 (2019)
5. Singh, G., Sharma, N., Kumar, D., Hegab, H.: Design, development and tribological characterization of Ti–6Al–4V/hydroxyapatite composite for bio-implant applications. *Mater. Chem. Phys.* **243**, 122662 (2020)
6. Neubauer, J.A.: Invited review: physiological and pathophysiological responses to intermittent hypoxia. *J. Appl. Physiol.* **90**, 1593–1599 (2001)
7. Priyadarshini, B., Rama, M., Chetan, Vijayalakshmi, U.: Bioactive coating as a surface modification technique for biocompatible metallic implants: a review. *J. Asian Ceramic Societies* **7**(1), 397406 (2019)
8. Kurup, A., Dhattrak, P., Khasnis, N.: Surface modification techniques of titanium and titanium alloys for biomedical dental applications: a review. *Mater Today Proc.* **39**, 84–90 (2021)
9. Zhao, L., Chu, P.K., Zhang, Y., Wu, Z.: Antibacterial coatings on titanium implants. *J. Biomed. Mater. Res. B Appl. Biomater.* **91B**, 470–480 (2009)
10. Mehrvarz, A., Khalil-Allafi, J., Khosrowshahi, A.K.: Biocompatibility and antibacterial behavior of electrochemically deposited Hydroxyapatite/ZnO porous nanocomposite on NiTi biomedical alloy. *Ceram. Int.* **48**, 16326–16336 (2022)

11. Choi, G., Choi, A.H., Evans, L.A., Akyol, S., Ben-Nissan, B.: A review: recent advances in sol-gel-derived hydroxyapatite nanocoatings for clinical applications. *J. Am. Ceram. Soc.* **103**, 5442–5453 (2020)
12. Behera, R.R., Das, A., Pamu, D., Pandey, L.M., Sankar, M.R.: Mechano-tribological properties and in vitro bioactivity of biphasic calcium phosphate coating on Ti-6Al-4V. *J. Mech. Behav. Biomed. Mater.* **86**, 143–157 (2018)
13. Sovak, G., Weiss, A., Gotman, I.: Osseointegration of Ti6Al4V alloy implants coated with titanium nitride by a new method. *J. Bone Joint Surg Br.* **82**(2), 290–296 (2000)
14. Qin, W., Ma, J., Liang, Q., Li, J., Tang, B.: Tribological, cytotoxicity and antibacterial properties of graphene oxide/carbon fibers/polyetheretherketone composite coatings on Ti-6Al-4V alloy as orthopedic/dental implants. *J. Mech. Behav. Biomed. Mater.* **122**, 104659 (2021)
15. Phuong, N.V., Lee, K., Chang, D., Kim, M., Lee, S., Moon, S.: Zinc phosphate conversion coatings on magnesium alloys: a review. *Met. Mater. Int.* **19**, 273–281 (2013)
16. Liu, B., Zhang, X., Xiao, G.Y., Lu, Y.P.: Phosphate chemical conversion coatings on metallic substrates for biomedical application: a review. *Mater. Sci. Eng. C* **47**, 97–104 (2015)
17. Liu, B., Shi, X.M., Xiao, G.Y., Lu, Y.P.: In-situ preparation of scholizite conversion coatings on titanium and Ti-6Al-4V for biomedical applications. *Colloids Surf B Biointerfaces* **153**, 291–299 (2017)
18. Zhao, D.W., et al.: Interleukin-4 assisted calcium-strontium-zinc-phosphate coating induces controllable macrophage polarization and promotes osseointegration on titanium implant. *Mater Sci Eng C Mater Biol Appl.* **118**, 111512 (2021)
19. Zuo, K.Q., et al.: Controllable phases evolution and properties of zinc-phosphate/strontium-zinc-phosphate composite conversion coatings on Ti: effect of temperature. *Surf Coat Technol.* **447**, 128885 (2022)
20. Zhao, D.W., et al.: Strontium-zinc phosphate chemical conversion coating improves the osseointegration of titanium implants by regulating macrophage polarization. *Chem. Eng. J.* **408**, 127362 (2021)
21. Liu, B., Xiao, G.Y., Chen, C.Z., Lu, Y.P., Geng, X.W.: Hopeite and scholizite coatings formation on titanium via wet-chemical conversion with controlled temperature. *Surf Coat Technol.* **384**, 125330 (2020)
22. Solanke, S., Gaval, V., Sanghavi, S.: In vitro tribological investigation and osseointegration assessment for metallic orthopedic bioimplant materials. *Mater Today Proc.* **44**, 4173–4178 (2021)



Flow Characteristics in Subsurface Storm Water Perforated Pipe for Drainage System Application

Junaidah Abdullah¹ , Mohd Remy Rozainy Mohd Arif Zainol^{1,2} ,
Mohd Sharizal Abdul Aziz³ , Mohd Fazly Yusof¹ , Nor Ariza Azizan¹ ,
Siti Fairuz Juani¹ , and Khairul Rahmah Ayub¹ 

¹ River Engineering and Urban Drainage Research Centre (REDAC), Universiti Sains Malaysia,
14300 Nibong Tebal, Penang, Malaysia

ceremy@usm.my

² School of Civil Engineering, Universiti Sains Malaysia,
14300 Nibong Tebal, Penang, Malaysia

³ School of Mechanical Engineering, Universiti Sains Malaysia,
14300 Nibong Tebal, Penang, Malaysia

Abstract. This study investigates the performance of a subsurface stormwater perforated pipe as a subsurface conveyance component in a laboratory flume at Physical Laboratory, River Engineering and Urban Drainage Research Centre (REDAC), Universiti Sains Malaysia. The Manning's roughness coefficient (n) was measured at 9 points along the pipe to assess its relationship with the velocity, depth, and Froude number of simulated runoff flows. In this paper, a case study of Gate partially open for slope 1:500 with 10 cm water depth is investigated. The results show that flow in the perforated pipe was mostly turbulent, and the calculated flow discharges and velocities from the outlets were higher under the effects of the calculated Manning coefficients ranged from 0.009 to 0.011, and an inverse linear relationship between Manning's n and flow velocity was observed. Higher values of Manning's n reduced flow velocity in the pipe, indicating the potential for peak flow attenuation and better control of stormwater quantity in subsurface urban drainage.

Keywords: Sustainable Urban Drainage System · Manning coefficient · Perforated Pipe · Storm water runoff

1 Introduction

Flash floods are a recurrent natural calamity in Malaysia that poses substantial risks to the nation. Malaysia, characterized by a tropical climate, witnesses abundant rainfall year-round, especially during the monsoon seasons. Flash floods transpire when an excessive volume of precipitation transpires within a condensed timeframe, surpassing the capacity of drainage systems and leading to rapid water accumulation.

The implementation of subsurface stormwater drains is recognized as an effective measure to reduce the risk of flash floods in Malaysia. Subsurface stormwater drains,

also known as underground or subsurface drainage systems, involve the installation of pipes or channels beneath the ground to collect and convey excess water away from the surface.

The implementation of subsurface stormwater drainage involves the installation of an artificial pathway or conduit beneath the water table, ensuring that the hydraulic head of the conduit is lower than that of the soil being drained. Various types of subsoil drain commonly utilized, including the basic system, geotextile filter, pipe drain, pipe drain with a cap to prevent surface water intrusion, geotextile surrounding the pipe, geocomposite drain in a narrow trench, geocomposite drain in a shallow trench, and soil filter layer to mitigate the risk of geotextile clogging. [1].

The use of perforated pipes reduces subgrade moisture, which is crucial for durable and healthy pavement. These pipes are buried close to the foundation of the pavement construction for efficient water drainage [2]. In aquifer dewatering applications, Stuyt et al. (2005) [3] indicated that the inflow per unit length of a perforated pipe could not be constant. If native soils are permeable, Abida and Sabourin (2006) [4] discovered that a perforated pipe–grass swale design might substantially minimize storm runoff. Several researchers referred to a porous pipe as an orifice [5]. However, experimental findings reported in support of the orifice hypothesis have limitations due to the restricted number and range of variables investigated [6].

The installation of a perforated subsurface drain serves the purpose of intercepting, collecting, and conveying excessive groundwater to a stable outlet. It is commonly employed for drainage applications. Perforated subsurface drains are manufactured using a combination of high-frequency vibration and extrusion techniques, resulting in the production of durable pipes with consistent and exceptional quality. These pipes are extensively utilized for subsoil drainage, catering to various requirements. An interesting characteristic of perforated subsurface drainage pipes is their ability to facilitate water infiltration across the entire surface.

The performance of subsurface drain for different parameters is also investigated by Zakaria et al. [7], Ab. Ghani, A., et al. [8], and Abdullah et al. (2023) [9]. The objective of this study is to analyze the flow characteristics of perforated subsurface stormwater drains by incorporating the backflow effects for drainage system applications.

2 Methodology

2.1 Experimental Setup

In this section, a concise overview of the experimental procedure is provided. The experiment took place in a rectangular straight flume measuring 5.9 m in length at the Physical Laboratory, River Engineering and Urban Drainage Research Centre (REDAC), Universiti Sains Malaysia. The slope of this channel can be adjusted using an adjusting jack, allowing for variability. For the purposes of the experiment, a longitudinal slope of 1/500 with a water depth of 10 cm was employed. This experiment investigates the backflow of water with 2 cm gate partially open at the outlets.

As illustrated in Fig. 1, this laboratory test was set up with a single arrangement of corrugated High-Density Polyethylene (HDPE) with a standard diameter of 300 mm. In this investigation, nine segments were analysed. During the experiment, the depth

and velocity of the flow were measured. Three measurements were averaged for each measurement to determine the average velocity and depth. The velocity is measured at $0.6Y$, which is ($Y = \text{flow depth}$). All measurements were performed with a consistent flow. 10 to 20 min are required for this experiment to steady the flow. Figures 2, 3 represents the measurements of depth and velocity while Fig. 4 represents the Outlet condition of Gate Partially Open with opening 2cm .



Fig. 1. The experiment was set up.



Fig. 2. Depth Measurement.



Fig. 3. Velocity Measurement.



Fig. 4. Outlet condition of Gate Partially Open with opening 2cm.

2.2 Hydraulic Parameters

This study took into account several hydraulic parameters, including the Froude Number (Fr), Reynolds Number (Re), flow depth (y), flow velocity (v), and discharge (Q). The laboratory results were analyzed using the Manning Formula, which was calculated based on the reference [10].

$$n = \frac{1}{v} R^{\frac{2}{3}} S^{\frac{1}{2}} \quad (1)$$

where

n = Mannings,

v = Velocity (m/s),

R = Hydraulic Radius and

S = Slope.

Froude number relates to the state of flow and is described in Table 1 [10].

$$Fr = \frac{V}{\sqrt{gY}} \quad (2)$$

where Fr = Froude number,

V = the velocity of flow in m/s,

g = acceleration of gravity in m^2/s ,

Y = the depth of the flow section in m .

Table 1. State of Flow described by Froude Number.

Froude Number Fr	State of Flow	Description
$Fr = 1$	Critical	Flow celerity equal to flow velocity
$Fr < 1$	Subcritical	Slow flow-tranquil and streaming
$Fr > 1$	Supercritical	High velocity-rapid, shooting and torrential

The performance of the Manning formula was evaluated by determining the coefficient of R^2 determination [10].

$$R^2 = \left[\frac{\sum_{i=1}^n (O_i - \bar{O})(P_i - \bar{P})}{\sqrt{\sum_{i=1}^n (O_i - \bar{O})^2 \sum_{i=1}^n (P_i - \bar{P})^2}} \right]^2 \quad (3)$$

3 Results and Discussion

This section presents the experimental results and discussion. Figure 5 illustrates the relationship between manning and depth. The trend has been observed to be directly proportionate. The calculated range of manning is 0.009–0.011, while the calculated range of depth, y , is 0.08–0.10. The correlation value, r value, is 0.61, which is a positive addition, and the p -value is calculated to be 0.01, which is statistically significant ($p < 0.05$). There is a slight correlation between the highest depth as well as the highest value of manning, n .

Figure 6 shows the relationship of manning, n , with velocity (m/s). It was observed that the trend is inversely proportional. The standard manning's value of Polyethylene PE Corrugated with smooth inner walls the range of 0.009 - 0.015[4]. However, the value of manning for this study was calculated to be 0.009–0.011 which is good agreements with the standard manning, n . The range of velocity is examined to be 0.59–0.66 m/s . From the graph, it can be seen that the correlation value, r value is 0.17, which is these results if fluctuating value. And the p -value is analyses to be 0.001, which is significant ($p < 0.05$). It can be related that the lowest velocity gives the higher value of the manning, n .

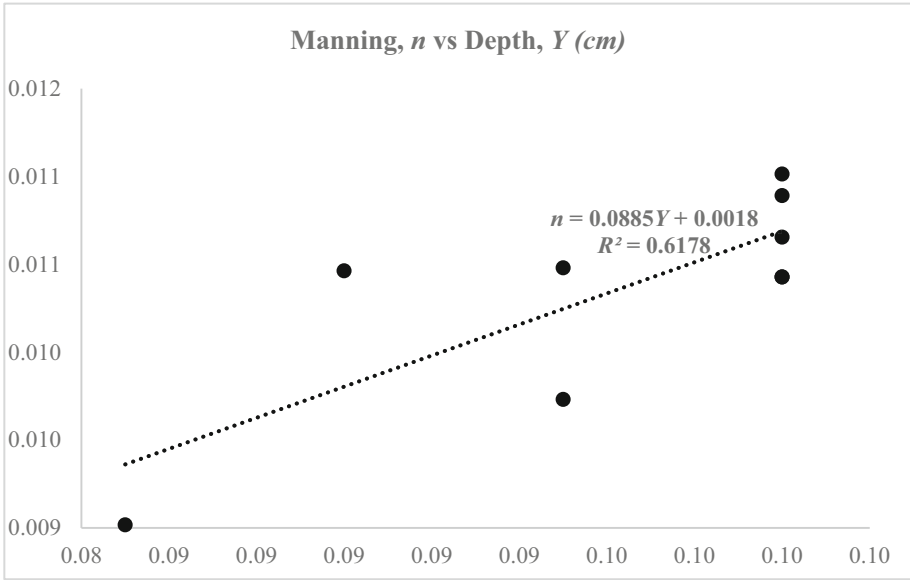


Fig. 5. The relationship between Manning, *n* and depth (m).

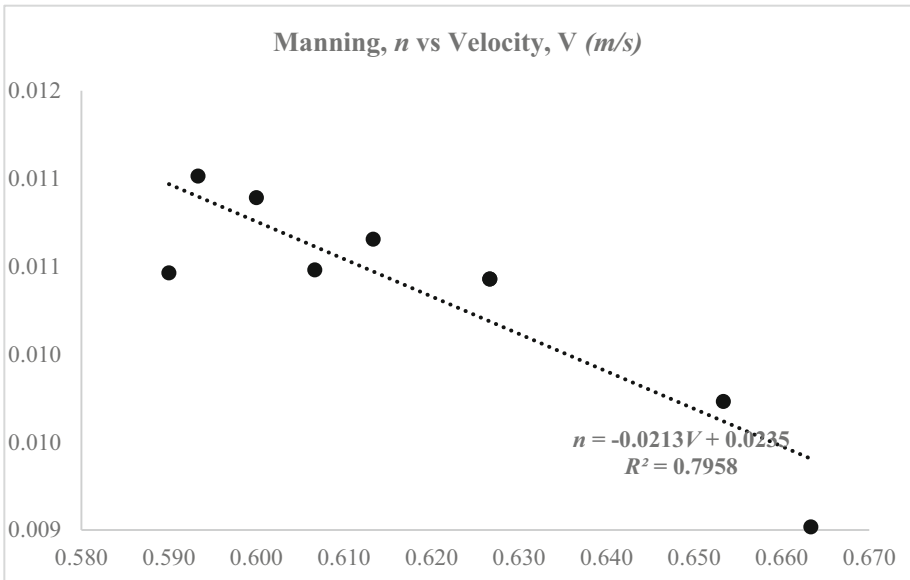


Fig. 6. The relationship between Manning, *n* and velocity (m/s).

Figure 7 illustrates the relationship between the Manning coefficient (*n*) and discharge (m^3/s). The distribution pattern observed is inversely proportional. The calculated *R*-value of 0.14 indicates the fluctuating between the variables. Furthermore, the

relationship between the Manning coefficient (n) and discharge can be expressed as $n = 0.2625Q - 0.0072$.

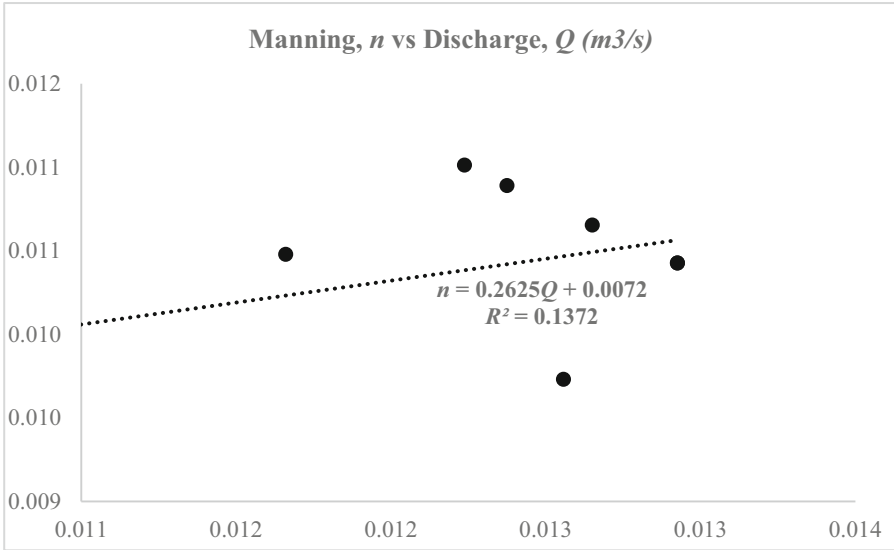


Fig. 7. The relationship between Manning, n and discharge (m^3/s).

A similar pattern was observed between the Manning coefficient (n) and Froude Number (Fr), as depicted in Fig. 8. It is evident that there is an inverse proportionality between Manning coefficient (n) and Froude Number (Fr). The range of Manning coefficient was found to be 0.009–0.011, while the calculated range of Froude Number was 0.59–0.73. Supercritical flow conditions were observed in this study. The observed correlation value (R -value) was 0.997, indicating a slightly strong agreement (close to 1) between the variables.

To validate the experimental findings, a comparison was made with the results of Muhammad et al. (2018) [11] in terms of depth, velocity, discharge, and Manning coefficient. The data collected in the previous study are presented in Table 2. A notable difference was observed in the water level depth, with Muhammad et al. (2018) [11] reporting higher values (0.07–0.18) compared to the present study (0.09–0.120). Similarly, the velocity and discharge values from Muhammad et al. (2018) [11] were consistently higher than those obtained in the present study. Regarding the Manning coefficient, the present study yielded values in the range of 0.009–0.011, which were notably lower than the range reported in the previous study (0.067–0.206) by Muhammad et al. (2018) [11]. At overall, these findings indicate a good agreement between the present study and Muhammad et al. (2018)[11] in terms of water discharge capacity.

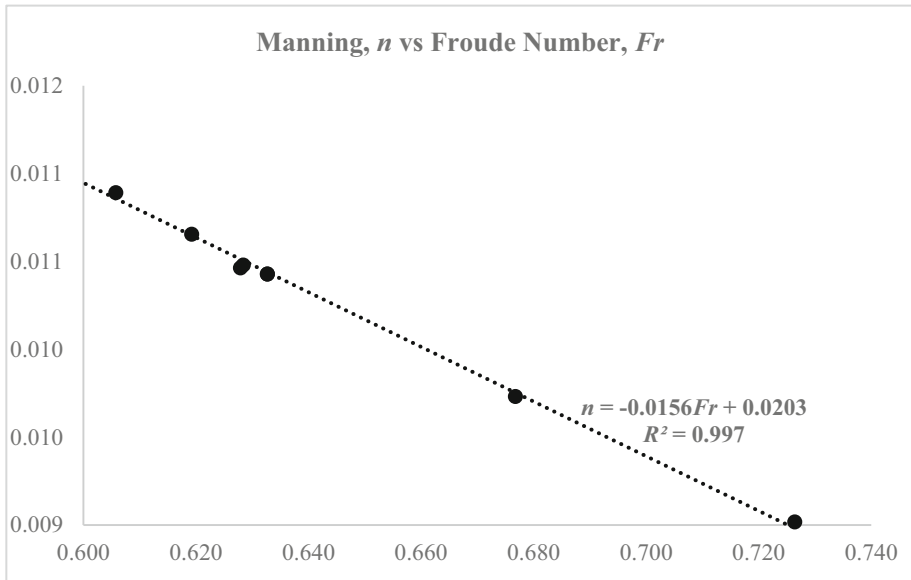


Fig. 8. The relationship between Manning, n and Froude Number.

4 Conclusion

The research was carried out to investigate flow resistance along the perforated subsurface stormwater drain. The outlet condition of a gate partially open with a longitudinal slope of 1/500 and water depth 10cm is considered in this study to analyse the backflow effects of water. The finding shows the relationship between Manning, n and discharge, Q is in strong agreement with an r value close to 1 (0.99). The sub-critical (slow flow-tranquil and streaming) turbulence flow has occurred in this study. In general, this study verifies that the current research aligns well with Muhammad et al. (2018) [13] findings regarding the water discharge capacity by incorporating the backflow effects of water. In order to gain a comprehensive understanding of the impact of flow resistance on the perforated subsurface stormwater drain leading to the flash flood effects, it is recommended to incorporate other forms of subsurface stormwater channels.

Acknowledgements. The authors express their gratitude to Ministry of Higher Education, Malaysia, under the Higher Institution Centre of Excellence (HiCoE) for a research grant of 311. PREDAC.4403901 and Universiti Sains Malaysia for providing the facilities.





References

1. Department of Irrigation Malaysia (DID). Urban Stormwater Management Manual for Malaysia (MSMA). 1st Edition (2020)
2. Afrin, T., Khan, A.A., Kaye, N.B., Testik, F.Y.: Numerical model for the hydraulic performance of perforated pipe underdrains surrounded by loose aggregate. *Journal of Hydraulic Eng.* **142**(8), 04016018 (2016)

3. Stuyt, L.C.P.M., Dierickx, W., Martinez, B.J.: *Materials for Subsurface Land Drainage Systems*. Food and Agriculture Organization of the United Nations, Rome (2005)
4. Abida, H., Sabourin, J.F.: Grass swale-perforated pipe system for stormwater management. *J. Irrigation and Drainage Eng.* **132**(1), 55–63 (2006). [https://doi.org/10.1061/\(ASCE\)0733-9437\(2006\)132:1\(55\)](https://doi.org/10.1061/(ASCE)0733-9437(2006)132:1(55))
5. Schwartz, S.S.: Effective curve number and hydrologic design of pervious concrete stormwater systems. *J. Hydrol. Eng.* **15**(6), 465–474 (2010)
6. Murphy, P., Kaye, N.B., Khan, A.A.: Hydraulic performance of aggregate beds with perforated pipe underdrains running full. *J. Irrigation and Drainage Eng.* **140**(8), 04014023 (2014). [https://doi.org/10.1061/\(ASCE\)IR.1943-4774.0000740](https://doi.org/10.1061/(ASCE)IR.1943-4774.0000740)
7. Zakaria, N.A., Ab Ghani, A., Abdullah, R., Mohd Sidek, L., Ainan, A.: Bio-ecological drainage system (BIOECODS) for water quantity and quality control. *Int. J. River Basin Manag.* **1**, 237–251 (2003)
8. Ab Ghani, A., et al.: Bio-ecological drainage system (BIOECODS): concept, design and construction. In: *Proceedings of the International Conference on HydroScience and Engineering*, Brisbane, Australia (2004)
9. Abdullah, J., et al.: Investigating the relationship between the manning coefficients (n) of a perforated subsurface stormwater drainage pipe and the hydraulic parameters. *Sustainability* **15**, 6929 (2023). <https://doi.org/10.3390/su15086929>
10. Zainalfikry, M.K., Ab Ghani, A., Zakaria, N.A., Chan, N.W.: *Flow Resistance in Ecological Subdrainage Channel* (2020). https://doi.org/10.1007/978-3-030-32816-0_84
11. Muhammad, M.M., Wan Yusof, K., Mustafa, M., Zakaria, N.A., Ab Ghani, A.: *Hydraulic Performance of Subsurface Drainage Module*. 37th IAHR World Congress, 13–18 August, Kuala Lumpur, Malaysia (2018)



XRD and TG-DTA Analysis of Fly Ash Based Geopolymer Composite Reinforced with Recycled Glass Fibers

Dumitru-Doru Burduhos-Nergis¹ , Petrica Vizureanu^{1,2} ,
Andrei Victor Sandu^{1,3} , and Bogdan Istrate^{4,4} 

¹ Faculty of Materials Science and Engineering, “Gheorghe Asachi” Technical University of Iasi-Romania, 67 Prof. D. Mangeron Blvd., 700050 Iasi, Romania
peviz2002@yahoo.com

² Technical Sciences Academy of Romania, 26 Dacia Blvd, 030167 Bucharest, Romania

³ Academy of Romanian Scientists, 54 Splaiul Independentei Street, Sect. 5, 050094 Bucharest, Romania

⁴ Faculty of Mechanical Engineering, “Gheorghe Asachi” Technical University of Iasi-Romania, 67 Prof. D. Mangeron Blvd., 700050 Iasi, Romania

Abstract. Geopolymerization is the most suitable method for the valorization of mineral wastes with high contents of Si and Al oxides. Compared to Ordinary Portland Cement (OPC) materials, the geopolymers exhibit better compressive strength and thermal stability, but their flexural strength is also limited by their brittle matrix. The aim of this study is to evaluate the thermal behavior of ambient-cured fly ash-based geopolymers reinforced with recycled glass fibers in order to estimate the possibility of manufacturing precast concrete products. The thermogravimetric analysis (TGA) showed a low weight loss up to 200 °C, followed by a much lower decrease in the 200 °C–500 °C temperature range. The TA curves follow closely the trend of the Differential Thermodynamic Analysis (DTA) curves, which confirm a highly endothermic reaction in the 20 °C–200 °C temperature range due to the removal of free or physically bound water. Above this temperature, small peaks corresponding to the dihydroxylation of -FeOOH or transformation of Ca(OH)₂ to CaCO₃ can be observed. The thermal behavior of both samples is similar, confirming that the presence of glass fibers doesn't influence the thermal behavior of fly ash-based geopolymers.

Keywords: Recycled glass fibers · Microstructural analysis · Thermal behavior · Eco-friendly · Fly ash · Geopolymer composite

1 Introduction

The demand for construction materials showed a significant increase over the past few years [1]. This trend may be explained by the high tendency to move from urban to rural areas, which consequently resulted in a high need for building new houses and infrastructure. Among the construction materials, ordinary Portland cement (OPC)-based products

are the most common [2]. Therefore, a significant increase in OPC manufacturing and use took place. The increased demand for OPC is explained, especially, by its low price. However, in terms of environmental costs, the effects produced by its manufacturing cannot be removed or substituted by any means. OPC production is considered to be responsible for more than 9% of the total CO₂ emissions worldwide [3].

To overcome these disadvantages, the principles of sustainable development have been formulated and supported by the authorities in most countries. According to these directions, the circular economy concept has been developed [4]. Accordingly, many technologies were designed to incorporate the secondary products from one stage as raw materials in further manufacturing stages or to find innovative solutions to valorize the secondary products of other industries. In the manufacture of OPC, due to the costs associated with virgin raw material consumption and the high temperatures necessary for calcination, the researchers found different methods to incorporate other types of cementitious byproducts or decrease the calcination temperature [5, 6]. Moreover, a totally different method of obtaining products with properties similar to those based on OPC was found in the geopolymerization technology [7].

Geopolymers are inorganic materials based on aluminum and silicon oxides [8]. Compared to OPC-based products, these materials showed tailored properties, high chemical attachment resistance, capacity to incorporate heavy metals, etc. while using only recycled minerals as raw materials. One of the main secondary products used to manufacture geopolymers is fly ash [9]. This powder, rich in aluminum and silicon oxides, is still available in large quantities in most of the countries that use coal as fuel for thermal power plants. The properties of fly ash depend on its characteristics and the type of coal that has been burned. The coal ash's physicochemical properties, particle size distribution, fineness modulus, particle morphology, and other types of specific characteristics will influence the dissolution degree and the behavior of the coal ash during activation [10]. Therefore, its performances as a raw material are varied, which consequently leads to the need for experimental validation for any application.

The influence of the raw materials characteristics on the properties of the final product is usually applicable to most byproducts that can be recycled. Another aspect of these wastes is their large range of quality parameters (homogeneity cannot be strictly assured, while different types of contaminants can also be found in some parts of the dumps) [11]. To reduce the influence of these negative aspects and to remove the intrinsic disadvantages of cementitious products, different types of additives or reinforcing elements may be introduced into the structure. In the case of geopolymers, commonly, the setting time can be reduced by increasing the activator concentration; the water permeability and freeze-thaw resistance can be increased by increasing the amount of sodium silicate; higher compressive strength can be achieved with aggregate addition; and most of the fibers compatible with OPC-based products can also be incorporated into the geopolymer matrix to improve their flexural strength. The addition of fibers is mainly necessary to prevent the sudden failure of concrete products. Due to fiber presence, the product's failure will be slower with enough visible signs (crack appearance, fiber exposure, debris etc.) to assure the necessary time for repair before failure [12]. Zwaiter et al. [13] studied the influence of hybrid glass fiber introduction on the properties of slag-fly ash-based geopolymers. According to their publication, the addition of glass fibers of different

lengths can significantly increase the buildability of geopolymers due to fiber interlocking, while their value can be controlled by mixing short with long fibers. Moreover, fiber addition will result in better performance for all evaluated characteristics: modulus of elasticity, splitting test, water absorption, abrasion resistance, and compressive strength.

Some publications also address the relationship between the behavior of the reinforced structure and the type of fiber. As presented in [14], carbon fibers performed better than E-glass fibers as reinforcements. Carbon fibers remained intact during three-point bending, while glass fibers showed weak interlaminar strength. Steinerova et al. [15] observed that both the amount of fiber and the amount of sand influence the brittleness and chemical resistance of geopolymer composites. In their study, a 5 wt.% replacement of the matrix with 4.5 mm-long glass fibers and an addition of 50–70 wt.% sand aggregates resulted in the optimum mechanical and chemical properties. The amount of glass fiber in the previously described study was significantly high compared to the literature; most of the studies showed that an addition of over 3 wt.% wouldn't lead to better performances but rather challenges in filling the form or removing the air bubbles from the composition. In the case of carbon fiber addition, the maximum amount is even lower; as Gu et al. [16] observed, when the addition exceeds 0.4 wt.% of the matrix weight, the carbon fibers tend to agglomerate. However, considering the high manufacturing costs of carbon fibers, the introduction of this type of reinforcement is justified only when high electrical conductivity is sought.

Despite the type of reinforcement, the mechanical performance of the developed composite will be influenced by different factors specific to the interface and compatibility between the matrix and the fiber, such as chemical adhesion, friction, and mechanical interlocking. All three parameters can be evaluated through mechanical tests such as beam anchorage tests, pull-out tests, flexural strength tests, and spliced beam tests [17]. However, when it comes to the thermal behavior of the developed composites, the exposure temperature along with the phase composition of the matrix can significantly influence the performance of the product. Up to now, the previous studies focused on the fresh, mechanical, or chemical properties of the fiber-reinforced geopolymer composites, but very few studies have examined the thermal behavior of these products, and none of them used recycled glass fibers as reinforcements. In this study, coal ash-based geopolymers reinforced with two types of recycled glass fibers have been obtained, and their thermal behavior and phase composition have been studied through simultaneous thermal analysis and X-ray diffraction.

2 Materials and Methods

Any waste that is available or can be ground to powder form and contains suitable amounts of silicon and aluminum oxides can be used as raw materials to manufacture geopolymer composites. However, the rationale for choosing the type of waste that will be recycled through technology strongly depends on the availability of that byproduct along with the target product for that manufacturing technology. For example, if the raw material is available in small quantities, only a technology that will produce high-value products related to the amount of used waste will be suitable, while if the waste is available in large quantities, the technology can be developed to manufacture any product that can substitute those based on OPC.

2.1 Materials

In this study, two types of coal ashes (fly ash and flue gas desulfurization fly ash - noted as lime fly ash) have been used as an aluminosilicate component in order to obtain a geopolymeric matrix suitable for the incorporation of recycled glass fibers. Both coal ashes are byproducts available in high amounts and deposited in land fields by a local thermal power plant (S.C. Holboca C.E.T. II S.A., Iasi, Romania). The chemical composition of both raw materials has been analyzed by X-ray fluorescence (XRF) using an XRF S8 Tiger (Bruker GmbH, Karlsruhe, Germany) in order to establish a suitable activation method. Also, to assure experiment repeatability, the collected wastes have been dried until a constant weight (as described in [18]) and sifted (according to SR EN 933–1:2012) to remove any impurities larger than 100 μm in diameter.

To reinforce the geopolymeric matrix, two types of glass fibers were collected from the waste resulting from the manufacture of different types of products that consist of glass fibers impregnated with resins. The waste was collected from the dump site of a local factory (Prod Company Romania, which manufactures products from polystyrene reinforced with glass fiber). Moreover, to further improve the mechanical properties of the developed composites, a mixture of fine and coarse aggregates [19] was introduced into the mixture.

As activators, commercially available sodium silicate solution (S.C. KYNITA S.R.L., Valcea, Romania) and sodium hydroxide flakes from the same supplier were chosen. Prior to mixing with the Na_2SiO_3 solution, the NaOH flakes were dissolving in tap water at the desired concentration.

2.2 Sample Design and Preparation

To find the optimum composition from compressive strength point of view, the Taguchi method was used, while the influence factors and their values were selected based on preliminary studies [7, 20]. In accordance with Taguchi's L9 orthogonal matrix method (36), 9 different mixtures were designed to establish the influence of the following involved factors (Table 1).

Table 1. The composition of the solid component.

		Raw material, wt.%		
		FA	FS	A
Mixture code	C1	67.5	7.5	25
	C2	45	5	50
	C3	22.5	2.5	75

The description of the designed samples is as follows: (a) three combinations between the both types of coal ash (fly ash - FA, lime fly ash - FS) and aggregates (A) consisting of C1 = 67.5% FA + 7.5% FS + 25% A, C2 = 45% FA + 5% FS + 50% A and C3 =

22.5% FA + 2.5% FS + 75% A (Table 2), (b) three different Na/Al ratios (0.50, 0.625 and 0.75), (c) three different liquid/solid ratios (0.70, 0.75 and 0.80). The design of the three-factor, three-level experiments are shown in Table 3.

Table 2. Experimental factors and levels.

Experimental factor	Level 1	Level 2	Level 3
A. Mixture code	C1	C2	C3
B. Na/Al ratio	0.5	0.625	0.75
C. Liquid/solid ratio	0.7	0.75	0.8

Table 3. The composition of the geopolymers without reinforcing fibers.

		Sample code								
		S1	S2	S3	S4	S5	S6	S7	S8	S9
Experimental factor	A	C1	C1	C1	C2	C2	C2	C3	C3	C3
	B	0.50	0.625	0.75	0.50	0.625	0.75	0.50	0.625	0.75
	C	0.70	0.75	0.80	0.75	0.80	0.71	0.80	0.70	0.75
Compressive strength, MPa		5.71	5.92	7.25	3.81	4.31	10.58	4.95	6.52	7.25

Further, the geopolymer that exhibited the highest compressive strength was optimized by introducing two types of recycled glass fibers into its composition. According to the compressive strength results, the mixture specific to sample code S6 exhibits the highest mechanical properties. Therefore, its composition was further chosen as the matrix for the glass fiber-reinforced composites.

The glass fibers were prepared at two different lengths (25 and 60 mm, respectively) and incorporated in three different amounts (1, 2, or 3 wt.%) related to the amount of coal ash in the composition of each sample. The composition of the studied samples is presented in Table 4, while the process flow diagram for obtaining these fiber-reinforced geopolymers is shown in Fig. 1.

According to the three-point bending strength test, the addition of glass fibers significantly increases the flexural strength of the geopolymers without affecting their compressive strength. Moreover, of all six mixtures, the composite with a 2 wt.% addition of long fibers (S6-F12) exhibited the optimum mechanical performances.

2.3 Methods

The phase transition of both types of coal ashes during alkali activation has been studied through X-ray diffraction (XRD). Furthermore, the structure stability and the chemical reactions that took place during heating the obtained materials have been evaluated

Table 4. The composition of fiber reinforced geopolymer composite.

Sample code	Solid component				Liquid component		Flexural strength, MPa
	FA, wt. %	FS, wt. %	A, wt. %	Fiber, wt. %	Na ₂ SiO ₃ , wt. %	NaOH 10.8M, wt. %	
S6-NoF	45	5	50	0	84.60	15.40	0.017
S6-Fs1				1			0.049
S6-Fs2				2			0.026
S6-Fs3				3			0.017
S6-FI1				1			0.062
S6-FI2				2			0.063
S6-FI3				3			0.050

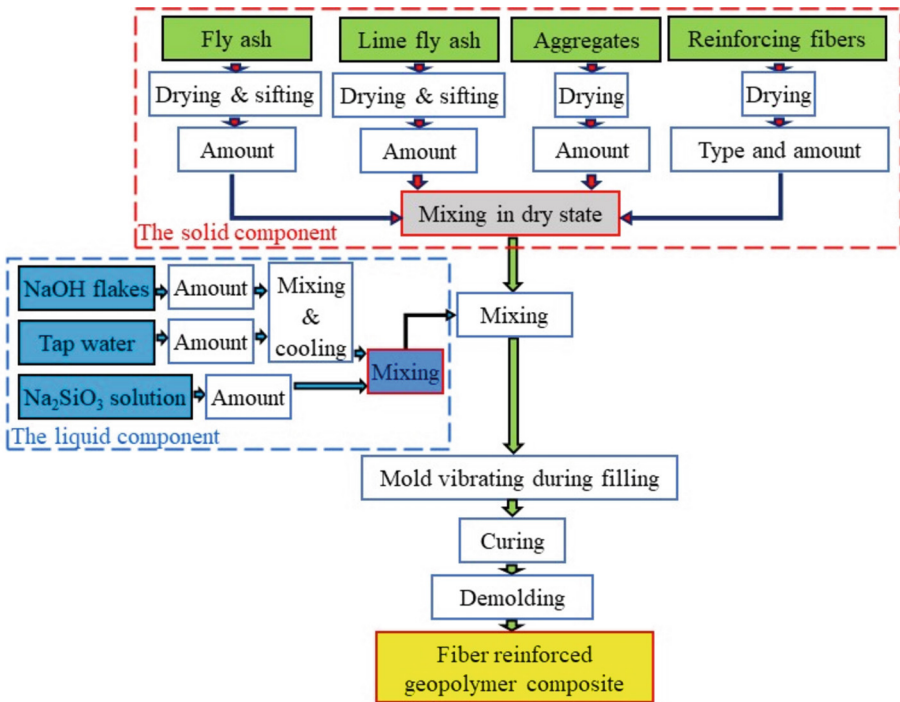


Fig. 1. Process flow diagram of obtaining geopolymer composites reinforced with different types of recycled glass fibers.

by simultaneous thermal analysis (STA), which combines thermogravimetric analysis (TGA) with differential thermal analysis (DTA).

X-ray Diffraction. XRD analysis was carried out on both the raw materials and the obtained geopolymers. A true representative sample of each type of coal ash has been analyzed, while for the evaluation of the geopolymers, some chips resulting from mechanical tests have been ground up to powder form. The diffraction patterns were collected using X'Pert Pro MPD equipment (Malvern Panalytical Ltd., Eindhoven, Netherlands) with a CuK source at 45 kV/40 mA. The radiation was recorded between 5° and 60° 2θ at a step of 0.013° .

Simultaneous Thermal Analysis. The phase transition and weight evolution in the range of 25 – 500°C were analyzed in a static air atmosphere at a heating rate of $10^\circ\text{C}/\text{min}$. Both the thermogravimetric analysis (TGA) and the differential thermal analysis (DTA) were performed at the same time by means of STA PT-1600 equipment (Linseis, Selb, Germany).

3 Results and Discussions

3.1 Microstructural Analysis

The morphology of the fly ash particles influences the dissolution rate as well as the characteristics of the final product. As presented in literature [21], raw materials with finer particles will react faster and result in structures with better mechanical properties than those that contain a high amount of large particles. Higher proportions of spherical particles will result in better fluidity, a slightly lower reaction degree, and higher compressive strength [22]. This behavior is related to the impossibility of the activator to dissolve and activate the surface of some large sphere particles that have been created at high temperatures and have a thicker wall than the others. Therefore, those particles will remain almost intact in the geopolymer and act as large dimension pores which will negatively affect the mechanical properties of the developed product. However, different methods, such as mechanical (grinding) [23], fusion [24] or chemical activation (frontal polymerization) [25] can be involved to improve the reactivity of the raw materials. In this study, only dried and sifted coal ash has been used; any supplementary activation has been avoided in order to keep the manufacturing method simple and as cost-effective as possible. Also, both initial processing steps (drying and sifting) can be eliminated in industrial applications by performing a moisture test on raw materials and adjusting the water content of the activator depending on the amount of water in the coal ash and sand.

The microstructural analysis of the obtained geopolymers and the raw materials was studied by means of scanning electron microscopy (SEM) using an SEM type FEI Quanta FEG 450 (FEI Company, Washington, DC, USA). The morphological analysis of both types of coal ashes shows that the collected fly ash has a homogenous composition with a significantly high amount of spherical particles (Fig. 2). Moreover, the microstructural analysis at high magnifications shows that most of the spherical particles have diameters lower than $30\ \mu\text{m}$, while the larger particles are porous and irregularly shaped. The lime fly ash (Fig. 3) is much finer; most particles from its composition are irregularly shaped and have a diameter lower than $20\ \mu\text{m}$.

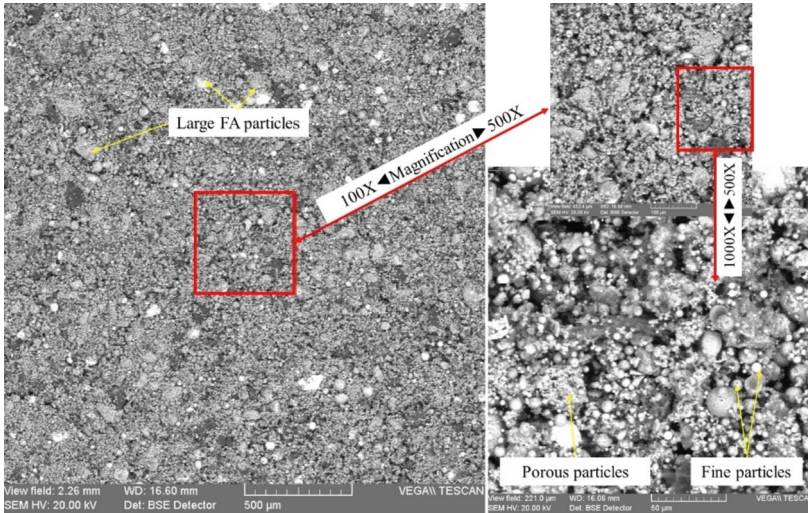


Fig. 2. Morphology of fly ash at different magnification.

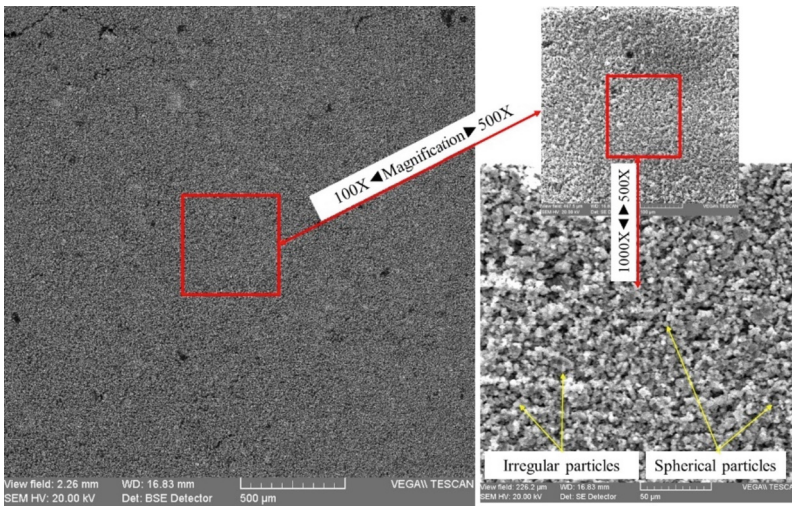


Fig. 3. Morphology of lime fly ash at different magnification.

The oxide chemical composition analyzed by X-ray fluorescence (XRF) using a XRF S8 Tiger equipment (Bruker, Karlsruhe, Germany) shows a class F fly ash (according to ASTM C618) with a high content of SiO₂ (50.16 wt.%), Al₂O₃ (27.02 wt.%), Fe_xO_y (8.40 wt.%) and CaO (6.49 wt.%), while the rest of the oxides from its composition (K₂O, MgO, TiO₂, Na₂O, P₂O₅, SO_x etc.) are available in quantities lower than 2 wt.%. The lime fly ash, instead, has a significantly high CaO concentration (68.22 wt.%), SO_x

(26.87 wt.%) and SiO_2 (4.86 wt.%), while the rest of the elements (Al, Fe, Ti, P etc.) are lower than 0.01 wt.%.

Considering the morphological analysis as well as the chemical composition of both types of ashes, it is expected that FS will exhibit a higher reaction degree than FA due to its fines and high content of Ca [26, 27]. However, considering the fine line that separates geopolymers of alkali-activated materials [28], the FS content was maintained at low addition, so the system will have a higher Al/Si ratio than a Ca/Si ratio.

The microstructure of the obtained geopolymers is presented in Fig. 4. As can be seen, the geopolymer without reinforcing fibers (Fig. 4 a) shows a homogenous structure with large voids and pores and some unreacted particles in areas close to the voids; probably, the particles were captured into the air bubbles and didn't get into contact with the activator. The glass fiber-reinforced composite (Fig. 4 b) shows similar morphology.

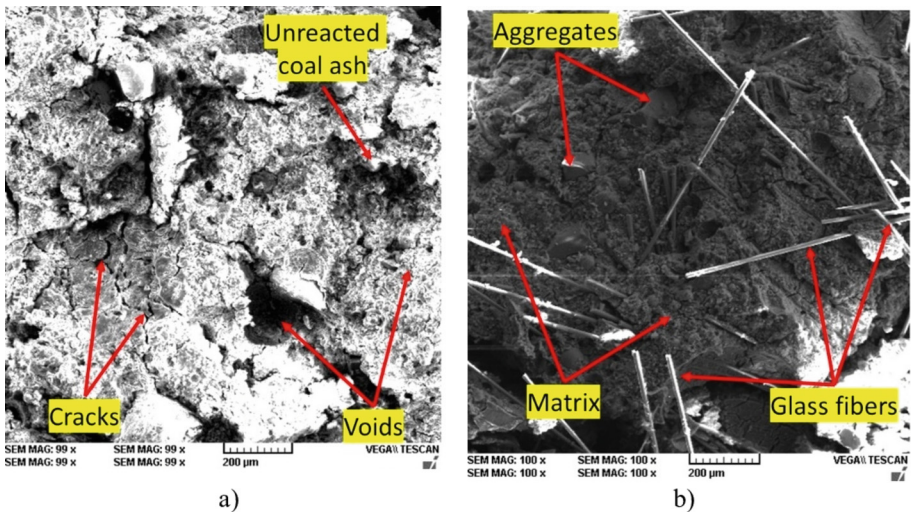


Fig. 4. Microstructure of the obtained samples: a) the geopolymer without reinforcing fibers (S6-NoF); b) the fiber reinforced geopolymer composite (S6-FI2).

The microstructural analysis of the obtained geopolymers was performed on fracture surfaces; therefore, the presence of cracks could also be related to the destruction mechanism that occurred during the compressive strength test.

3.2 Mineralogical Analysis

The XRD analysis of both raw materials confirms the presence of quartz or silicon oxide as well as multiple complex phases that include the main chemical elements detected through the chemical composition analysis, Fig. 5. The XRD pattern of the FA sample also shows the presence of sillimanite, mullite, goethite and anorthite [18, 29]. In the case of the FS sample, different phases with Ca or S content are detected, such as portlandite and hannebachite [30], as well as calcite, pyrite, gypsum and sphalerite, which were also observed in the composition of ashes with high sulphur content [31, 32].

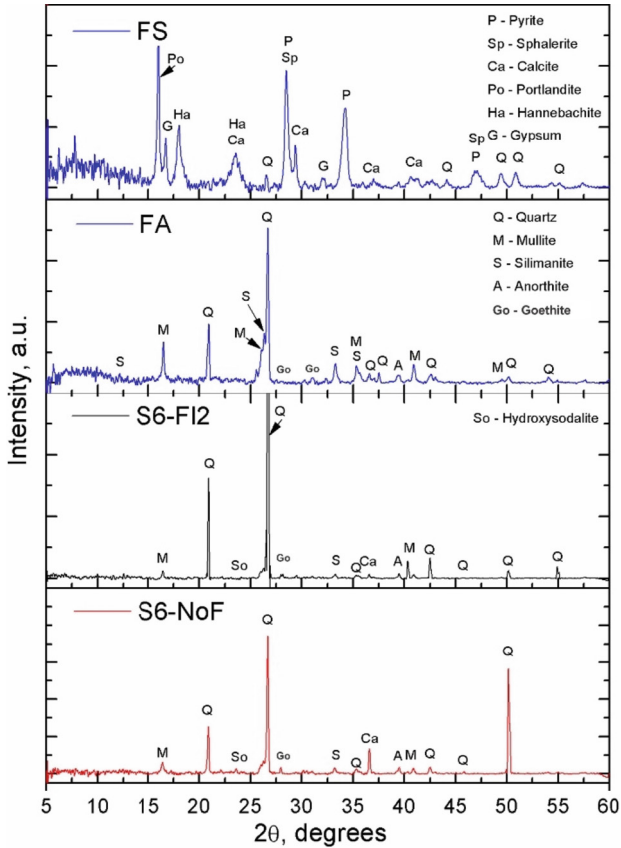


Fig. 5. XRD patterns of the raw materials and the obtained geopolymers.

After activation, the XRD pattern of both raw materials is significantly changed; mostly, the phases corresponding to FS have been converted to amorphous phases specific to geopolymerization, while those from FA have only changed in intensity. The geopolymerization reaction is also confirmed by the formation of a new semi-crystalline phase, hydroxysodalite ($\text{Na}_4\text{Al}_3\text{Si}_3\text{O}_{12}\text{OH}$), which was also observed by [33]. Moreover, it seems that the addition of recycled glass fibers won't influence the phase transition in alkali-activated geopolymers.

3.3 Thermal Behavior Analysis

In order to evaluate the possibility of using recycled glass fibers to develop geopolymers that can be used for the manufacture of different types of products suitable for civil engineering applications, the thermal behavior of the obtained materials has been evaluated through simultaneous thermal analysis. The DTA analysis (Fig. 6 a) of both samples show highly similar behavior. Both curves exhibit multiple fluctuations corresponding to water evaporation or oxidation reactions. The highest endothermic peak

is the one around 130 °C (indicated with “A” on the DTA curves), which corresponds to the evaporation of free and physically bound water [18, 34]. As indicated with “B,” around 230 °C, water evaporation from zeolitic channels occurs, while the transition of $\text{FeO}(\text{OH})$ to Fe_2O_3 is detected around 300 °C (“C”). When the temperature increases to 490 °C, Portlandite decomposition to calcium carbonate takes place (“D”).

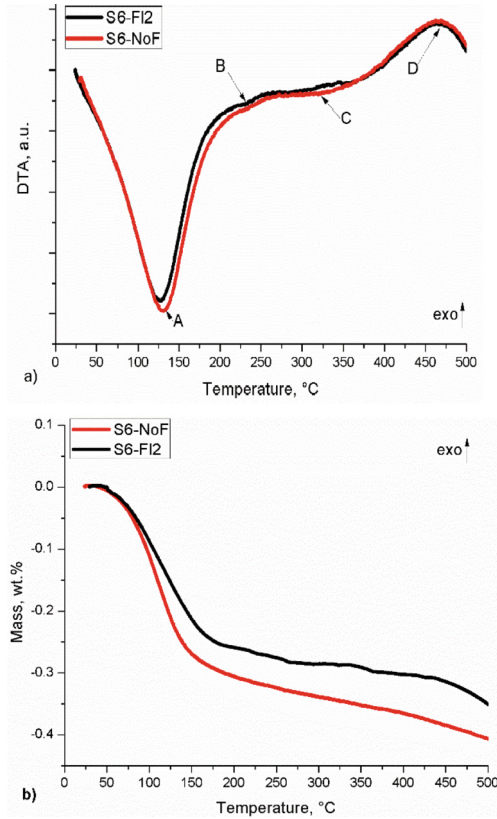


Fig. 6. TG-DTA analysis of fly ash-based geopolymers with and without glass fiber addition: a) DTA curves; b) TGA curves.

The TGA curves (Fig. 6 b) showed a low mass loss, especially in the range of water evaporation. Geopolymers are known for their porous matrix; therefore, the introduction of compact glass fiber explains the difference between the curves. Moreover, all reactions that lead to mass fluctuations are associated with water elimination or oxidation of compounds specific to the phases detected in the matrix, i.e., not in the composition of glass fibers.

4 Conclusions

This study evaluates the influence of recycled glass fiber addition on the structure and thermal behavior of different fly ash-based geopolymers. According to the obtained results, the following conclusions can be drawn:

- flue gas desulfurization Fly ash can be incorporated into geopolymer mixtures without having a negative influence on the mineralogical composition or thermal behavior of these sustainable products.
- the addition of recycled glass fibers into the matrix of coal ash-based geopolymer will improve the mechanical properties, even though a slight increase in mass loss was observed.
- the phase transition during activation won't be influenced by the presence of glass fibers. During alkali activation, some of the phases from the raw materials will be converted to amorphous content, while only one new semi-crystalline phase (hydroxysodalite) will be created.
- the mass loss will be slightly higher for the reinforced composite due to a higher content of water in the composition, while the phase transition will remain the same as for the geopolymer without glass fiber addition.

Acknowledgment. This paper was financially supported by the Project “Network of excellence in applied research and innovation for doctoral and postdoctoral programs”/InoHubDoc, project co-funded by the European Social Fund financing agreement no. POCU/993/6/13/153437. This paper was also supported by “Gheorghe Asachi” Technical University from Iași (TUIASI), through the Project “Performance and excellence in postdoctoral research 2022”.

References



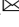


1. Marinova, S., Deetman, S., van der Voet, E., Daioglou, V.: Global construction materials database and stock analysis of residential buildings between 1970–2050. *J. Clean. Prod.* **247**, 119146 (2020)
2. Singh, N.B., Kumar, M., Rai, S.: Geopolymer cement and concrete: properties. *Mater Today Proc.* **29**, 743–748 (2020)
3. Shan, Y., Liu, Z., Guan, D.: CO₂ emissions from China's lime industry. *Appl. Energy* **166**, 245–252 (2016)
4. Damtoft, J.S., Lukasik, J., Herfort, D., Sorrentino, D., Gartner, E.M.: Sustainable development and climate change initiatives. *Cem. Concr. Res.* **38**, 115–127 (2008)
5. Schneider, M., Romer, M., Tschudin, M., Bolio, H.: Sustainable cement production-present and future. *Cem. Concr. Res.* **41**, 642–650 (2011)
6. Ortiz, O., Castells, F., Sonnemann, G.: Sustainability in the construction industry: a review of recent developments based on LCA. *Constr. Build. Mater.* **23**, 28–39 (2009)
7. Vizureanu, P., Burduhos Nergis, D.D.: Green materials obtained by geopolymerization for a sustainable future. *Materials Research Foundations*, 105 Springdale Lane, Millersville, PA 17551 U.S.A. (2020)
8. Cong, P., Cheng, Y.: Advances in geopolymer materials: a comprehensive review. *Journal of Traffic and Transportation Engineering (English Edition)* **8**, 283–314 (2021)

9. Dindi, A., Quang, D.V., Vega, L.F., Nashef, E., Abu-Zahra, M.R.M.: Applications of fly ash for CO₂ capture, utilization, and storage. *Journal of CO₂ Utilization* **29**, 82–102 (2019)
10. Das, D., Rout, P.K.: A review of coal fly ash utilization to save the environment. *Water Air Soil Pollut.* **234**, 128 (2023)
11. Shehata, N., Sayed, E.T., Abdelkareem, M.A.: Recent progress in environmentally friendly geopolymers: a review. *Science of the Total Environment* **762**, 143166 (2021)
12. Jat, D., Motiani, R., Dalal, S., Thakar, I.: Mechanical properties of geopolymer concrete reinforced with various fibers: a review. *Lecture Notes in Civil Engineering*, 139–156 (2023)
13. Zuaiteer, M., El-Hassan, H., El-Maaddawy, T., El-Ariss, B.: Properties of slag-fly ash blended geopolymer concrete reinforced with hybrid glass fibers. *Buildings* **12**, 1114 (2022)
14. Samal, S.: Interface failure and delamination resistance of fiber-reinforced geopolymer composite by simulation and experimental method. *Cem. Concr. Compos.* **128**, 104420 (2022)
15. Steinerova, M., Matulova, L., Vermach, P., Kotas, J.: The brittleness and chemical stability of optimized geopolymer composites. *Materials* **10**, 396 (2017)
16. Gu, G., Pei, Y., Ma, T., Chen, F., Zhang, J., Xu, F.: Role of carbon fiber in the electrothermal behavior and geopolymerization process of carbon fiber-reinforced FA-GBFS geopolymer composite. *Constr. Build. Mater.* **369**, 130597 (2023)
17. Vembu, P.R.S., Ammasi, A.K.: A comprehensive review on the factors affecting bond strength in concrete. *Buildings* **13**, 577 (2023)
18. Burduhos-Nergis, D.D., Vizureanu, P., Sandu, A.V., Burduhos-Nergis, D.P., Bejinariu, C.: XRD and TG-DTA study of new phosphate-based geopolymers with coal ash or metakaolin as aluminosilicate source and mine tailings addition. *Materials* **15**, 202 (2022)
19. Burduhos Nergis, D.D., Vizureanu, P., Corbu, O.: Synthesis and characteristics of local fly ash based geopolymers mixed with natural aggregates. *Rev. Chim.* **70**, 1262–1267 (2019)
20. Burduhos Nergis, D.D., Vizureanu, P., Lupescu, S., Burduhos Nergis, D.P., Perju, M.C., Sandu, A.V.: Microstructural analysis of ambient cured phosphate based-geopolymers with coal-ash as precursor. *Arch. Metall. Mater.* **67**, 595–600 (2022)
21. Assi, L.N., Eddie Deaver, E., Ziehl, P.: Effect of source and particle size distribution on the mechanical and microstructural properties of fly Ash-Based geopolymer concrete. *Constr. Build. Mater.* **167**, 372–380 (2018)
22. Ma, J., Wang, D., Zhao, S., Duan, P., Yang, S.: Influence of particle morphology of ground fly ash on the fluidity and strength of cement paste. *Materials* **14**, 1–18 (2021)
23. Kumar, S., Kumar, R.: Mechanical activation of fly ash: effect on reaction, structure and properties of resulting geopolymer. *Ceram. Int.* **37**, 533–541 (2011)
24. Demir, F., Moroydor Derun, E.: Response surface methodology application to fly ash based geopolymer synthesized by alkali fusion method. *J. Non Cryst Solids* **524**, 119649 (2019)
25. Alam, S., et al.: Rapid curing prospects of geopolymer cementitious composite using frontal polymerization of methyl methacrylate monomer. *Constr. Build. Mater.* **309**, 125198 (2021)
26. Chen, X., Kim, E., Suraneni, P., Struble, L.: Quantitative correlation between the degree of reaction and compressive strength of metakaolin-based geopolymers. *Materials* **13**, 1–13 (2020)
27. Sevinç, A.H., Durgun, M.Y.: Properties of high-calcium fly ash-based geopolymer concretes improved with high-silica sources. *Constr. Build. Mater.* **261**, 120014 (2020)
28. Rakhimova, N.R., Rakhimov, R.Z.: Reaction products, structure and properties of alkali-activated metakaolin cements incorporated with supplementary materials - a review. *J. Market. Res.* **8**, 1522–1531 (2019)
29. Srikant, S., Singh, S., Mukherjee, P., Rao, R.: Value addition to red sediment placer sillimanite using microwave energy and in depth structural and morphological characterization of mullite. *J. Minerals and Materials Characterization and Eng.* **11**, 1055–1062 (2012)

30. Navarrete, I., Vargas, F., Martinez, P., Paul, A., Lopez, M.: Flue gas desulfurization (FGD) fly ash as a sustainable, safe alternative for cement-based materials. *J. Clean. Prod.* **283**, 124646 (2021)
31. Ibrahim, S., El Anadouli, B., Farahat, M., Selim, A., Elmenshawy, A.: Desulphurization of Pyritic Sulphur from Egyptian Coal Using Falcon Concentrator **32**(6), 588-594 (2013)
32. Saikia, B.K., Mahanta, B., Gupta, U., Sahu, O., Saikia, P., Baruah, B.: Prasad: mineralogical composition and ash geochemistry of raw and beneficiated high sulfur coals. *J. Geol. Soc. India* **88**, 339–349 (2016)
33. Sivasakthi, M., Jeyalakshmi, R., Rajamane, N.P., Jose, R.: Thermal and structural micro analysis of micro silica blended fly ash based geopolymer composites. *J. Non Cryst. Solids* **499**, 117–130 (2018)
34. Burduhos Nergis, D.D., Abdullah, M.M.A.B., Sandu, A.V., Vizureanu, P.: XRD and TG-DTA study of new alkali activated materials based on fly ash with sand and glass powder. *Materials* **13**, 343 (2020)



The Potential of Hybrid Polymer in Treating Textile Wastewater: Optimization of pH and Dosage Using Response Surface Methodology

Siti Aisyah Ishak¹ , Mohamad Fared Murshed¹  ,
Mohd Remy Rozainy Mohd Arif Zainol¹ ,
and Mohd Mustafa Al Bakri Abdullah^{2,3} 

¹ School of Civil Engineering, Engineering Campus, Universiti Sains Malaysia, 14300 Nibong Tebal, Pulau Pinang, Malaysia

cefaredmurshed@usm.my

² Geopolymer and Green Technology, Centre of Excellence (CEGeoGTech), Universiti Malaysia Perlis (UniMAP), Perlis, Malaysia

³ Faculty of Chemical Engineering Technology, Universiti Malaysia Perlis (UniMAP), Perlis, Malaysia

Abstract. The study aimed to evaluate the effectiveness of hybrid polymer ZOPAT compared to single polymers in treating textile wastewater. The research analyzed reduction of color, chemical oxygen demand (COD), turbidity, and suspended solids using jar testing. Response Surface Methodology (RSM) was employed to optimize the treatment, analyze variance, and create perturbation and desirability plots for multiple responses. The storage conditions of the hybrid polymer were also investigated. The results showed that ZOPAT was highly effective in reducing color, with a 93% reduction compared to other treatments. Additionally, turbidity and suspended solids were reduced by 100%, and COD was reduced by up to 80%. The RSM multi-response outcome showed a desirability plot of 0.592. The hybrid polymer required only 17.5 min for coagulation treatment, while the other treatments required more than 40 min to achieve maximum effectiveness. The validation test showed that the optimization model's error rate was less than 1%. The study recommended that hybrid polymer solutions be stored in a cold room for up to 20 days to maintain consistency. The findings suggest that hybrid polymer is a highly effective coagulant for treating textile wastewater, with significant reductions in color, turbidity, and suspended solids. The use of RSM allowed for the optimization of the treatment, and the storage conditions were determined to ensure consistent results over time. Overall, the study's results have significant implications for the water treatment industry, with potential applications in treating wastewater in other industries.

Keywords: Hybrid polymer · Response Surface Methodology · Perturbation plot · Desirability plot · Storage conditions

1 Introduction

Malaysia's textile and apparel industry is ranked eleventh in the country's manufacturing sector, with 84.1 million meters of cotton cloth exported in 2020 [1]. However, after the textile treatment process, the discharge is typically released into nearby rivers. This issue has been reported extensively in China and India, with textile contamination causing significant problems in rivers [2]. The concentration of textile effluent ranges from 10 to 250 mg/L [3], depending on the dye types, with the highest concentration reaching up to 7,000 mg/L in the reactive dye industry [4]. It is estimated that the production of 1 kg of textile material requires 200 L of water [5], and studies indicate that approximately half of the dyes used in the textile industry end up as discharge wastewater containing organic and inorganic chemicals, dyestuffs, bleaching agents, finishing chemicals, starch, thickening agents, surface-active chemicals, wetting and dispersing agents, as well as metal salts [6]. This discharge contributes to high levels of pH, COD, BOD, color, suspended solids, turbidity, heavy metals, and other contaminants. As a result, it is crucial for wastewater treatment plants in every industry to be effective and systematic in their approach.

Currently, coagulation and flocculation are employed in primary treatment to separate gritty materials and suspended solids, and pH is an important factor that influences the effectiveness of coagulation. Typically, metal salts are used for coagulation, along with coagulant aids, which create larger flocs during slow mixing. The destabilization of charged particles allows flocs to form and settle during sedimentation. Inorganic, organic, and modified coagulants are commonly used today, but the effectiveness of inorganic coagulants is limited to a small pH range, typically between 5.5 and 7.5. To address this limitation, a hybrid coagulant has been developed that is effective over a wider pH range. In a study conducted by [7], a hybrid coagulant made of polyacrylamide and polymeric aluminum ferric chloride was found to be effective for the removal of Congo Red over a pH range of 6 to 9, and for the removal of Fast Turquoise Blue GL over a pH range of 4 to 7, with more than 90% removal achieved. The hybrid coagulant showed a high capability for adsorption bridging. Since pH is a critical factor in the coagulation process [8], it is important to determine the optimum conditions for coagulation, and the Response Surface Methodology is a useful analytical tool for achieving this.

Hybrid or modified coagulants have gained popularity in recent times due to their ability to enhance the efficiency of the coagulation and flocculation process. This is achieved by generating a high capacity of hydroxyl ions for charge neutralisation, as reported in literature [7]. The effectiveness of modified coagulants has been demonstrated in studies where they were able to reduce almost 90% of dye color [9] and more than 70% of organic compounds [8]. These coagulants can be composed of various combinations such as inorganic-inorganic, inorganic-organic, inorganic-natural, organic-organic, organic-natural and natural-natural polymers. Previous studies have explored the use of hybrid coagulants with zinc and various inorganic or organic polymers in the coagulation process [10–12].

The use of Zinc Oxide as a coagulant for pharmaceutical wastewater has been proven effective in reducing COD from 19,850 mg/L to 500 mg/L [13]. By modifying ZnO with an organic polymer such as polyacrylamide, longer chains can be produced, resulting in an abundance of binding sites. This modified ZnO has a broad pH range and

high adsorption bridging capabilities [7]. Zhu et al. [11] discovered that blending polyacrylamide with iron and zinc as a coagulant base resulted in a higher floc growth rate (119.82 $\mu\text{m}/\text{min}$) and recovery factor (26.96) than non-hybrid versions. This hybrid also had a more significant effect on turbidity and dissolved organic nitrogen removal compared to non-hybrid versions such as polymeric Al-Zn-Fe and Polyaluminium chloride [9].

In this study, the various impacts of color, COD, turbidity, and suspended solids were examined using single polymers (zinc oxide, zinc oxide + acrylamide, acrylamide, tannin, and polyaluminium chloride (PACl)), as well as a hybrid polymer composed of zinc oxide, acrylamide, and tannin. The Response Surface Methodology - Central Hybrid Design (RSM-CCD) was employed to analyze the perturbation plot at the optimized pH and ZOPAT dose, as well as the impact of multiple responses on the desirability plot. Additionally, the effects of storage conditions at both cold room temperature (4–6°C) and room temperature (30°C) were studied, with a duration of up to 60 days.

2 Experiments

The method involved using zinc chloride (ZnCl_2), acetic acid (CH_3COOH), sulfuric acid (H_2SO_4), sodium hydroxide (NaOH), glycerol ($\text{C}_3\text{H}_8\text{O}_3$), and ethanol ($\text{C}_2\text{H}_5\text{OH}$) obtained from Qrec without any purification to synthesize zinc oxide. Tannin with a molecular weight of 1701.18 g/mol was procured from Shaanxi Kanglai Ecology Agriculture Co., Ltd. Cationic polyacrylamide with a molecular weight of 1 million g/mol was purchased from R&M chemicals. The raw textile wastewater was collected six times from textile industries in 2018, with an average pH of 11.25, turbidity of 150.58 NTU, COD of 2250 mg/L, color of 1724 Pt/Co, and suspended solids of 172.58 mg/L.

A homogeneous solution was created by blending zinc oxide, polyacrylamide, and tannin in different weight ratios (1:1:1) using 2% w/w. Glycerol was used as a stabilizer, and its effectiveness was confirmed in a previous study [14]. To reduce turbidity, color, COD, and suspended solids, one-factor-at-a-time experimentation was conducted. To achieve the highest removal efficiency, various ratios of ZnO, polyacrylamide, and tannin were tested to determine a suitable proportion of these ingredients. The best pH and ZOPAT dosage were also investigated.

In this study, a standard jar-test apparatus (Velp Scientifica JLT 6) equipped with six stainless steel paddles and a stirrer was used as the experimental setup. The reactor was a 1000 mL glass beaker with a sample volume of 500 mL. The maximum allowable addition of ZOPAT was 10 mL from a stock solution of 20,000 mg/L. The pH adjustment was made using NaOH or H_2SO_4 , with a maximum addition of 30 mL for each beaker, which was less than 10% of the total 500 mL of textile wastewater. The preliminary test was used to determine the optimal range for pH, dosage, speed of rapid mixing, duration of rapid mixing, speed of slow mixing, duration of slow mixing, and sedimentation time.

Following the previous method [15], the impact of storage conditions was evaluated for a 60-day period. ZOPAT samples were subjected to two different conditions: room temperature (30 °C) and cold storage (4–6 °C). The percentage reduction of color and COD was monitored and graphed over the course of the experiment to observe any differences between the two storage conditions.

3 Results and Discussion

3.1 A Comparative Analysis of Coagulation Studies Utilizing Different Polymers

Various polymers, including ZnO, ZnO + PAM, PAM, ZOPAT, and Tannin, were employed to treat wastewater to reduce turbidity, color, COD, and SS. Table 1 presents the parameters used for each polymer in the coagulation treatment based on the results obtained in the preliminary study. The residual values, measured in mg/L (except for turbidity and color, which were measured in NTU and Pt/Co, respectively), were used to report the results. As shown in Fig. 1, the hybrid polymer ZOPAT demonstrated strong performance in reducing turbidity, color, and suspended solids in textile wastewater. The study also showed that the hybrid polymer is effective over a wide range of pH [7]. Previous studies have reported that hybrid polymers can lengthen polymer chains and provide additional binding sites with various functional groups, which may contribute to their effectiveness [8].

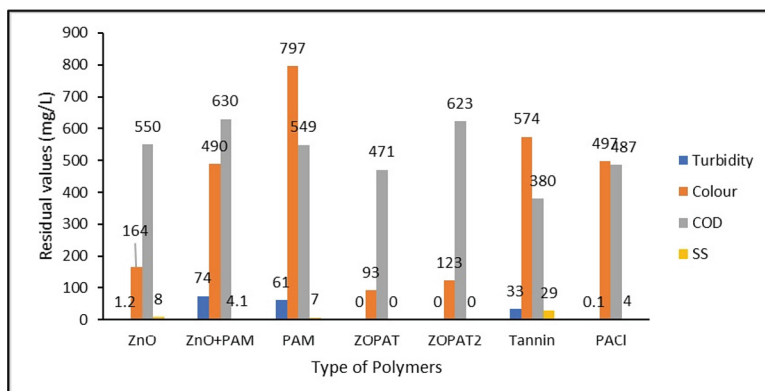


Fig. 1. The residual value of turbidity, colour, COD and SS for different type polymer.

ZOPAT demonstrated excellent performance in decolorizing wastewater, with residual color of less than 100 Pt/Co observed across a wide pH range (from pH 4 to pH 10). The broad pH range treatment provides significant benefits for treating various types of wastewater, and the low cost of pH adjustment prior to treatment is advantageous [16]. The reduction of color was consistently higher than the reduction of COD due to the formation of complex coagulants. Even if the wastewater is colorless after treatment, the combined complex with the surface of the dye molecule may reduce the color point but not the COD. Previous studies have reported that the reduction of color is faster than the oxidation of organic compounds (COD) [17]. At pH 8 and 800 mg/L of ZOPAT, the reduction rate of color was 94%, while the oxidation of COD was only 79%. Thus, it can be concluded that the rate of COD reduction is lower than that of color, even under the same treatment conditions.

In contrast, tannin at a dose of 400 mg/L resulted in the best residual COD concentration, achieving a value of 380 mg/L, although it did not show the best performance in

reducing turbidity, colour, and suspended solids. However, a previous study [18] reported achieving a water quality of less than 10 NTU using 3000 mg/L tannin obtained from *Acacia catechu*. In this study, the reduction of colour was observed up to 574 Pt/Co at a minimal concentration of less than 400 mg/L. However, exceeding the limit of tannin concentration can lead to re-stabilisation, resulting in high colour content in the wastewater. It is generally observed that increasing the amount of coagulant improves efficiency before reaching a point of overdosing [19]. Furthermore, the bridging site must not be limited by the adsorbed amount.

A complete removal of suspended solids was achieved at a concentration of 200 mg/L and 800 mg/L of PAM and ZOPAT, respectively, while ZnO required a concentration of 1200 mg/L to achieve a concentration of 1 mg/L of suspended solids. However, ZnO showed better removal of colour, achieving a reduction of up to 90%, but requiring a dosage of more than 1000 mg/L. When PAM was added alone, a worse reduction of colour was observed. However, when added in combination with ZnO as the primary coagulant, the colour degradation showed better performance. This indicates that PAM requires a metal coagulant to achieve an efficient coagulation-flocculation process. Regarding turbidity reduction, ZOPAT, PACl, and ZnO achieved almost 100% efficiency, while PAM, ZnO + PAM, and Tannin showed the worst reduction. Tannin required pH 2 to perform at its best. Generally, natural organic polymers have optimum pH conditions in the acidic range [20]. If strong alkaline is applied, it may cause another problem such as high colour content in the water, which is not favourable for textile wastewater, as it usually releases raw effluent at alkaline pH [5].

The effectiveness of PACl in reducing colour in textile wastewater was found to be less favourable compared to COD reduction. Even with the application of 200 mg/L PACl, the residual colour in the wastewater was still high at 900 Pt/Co, and up to 4000 mg/L PACl was required to achieve a reduction to 300 Pt/Co. However, a study involving the use of 300 mg/L of PACl under the influence of temperature reported positive results [21]. This indicates that PACl alone may not be suitable for treating textile wastewater due to the high colour residue. In contrast, the COD reduction achieved with 200 mg/L of PACl was near 500 mg/L. Nonetheless, a previous study reported that 100 mg/L of PACl as a flocculant could reduce COD to 700 mg/L [22]. Therefore,

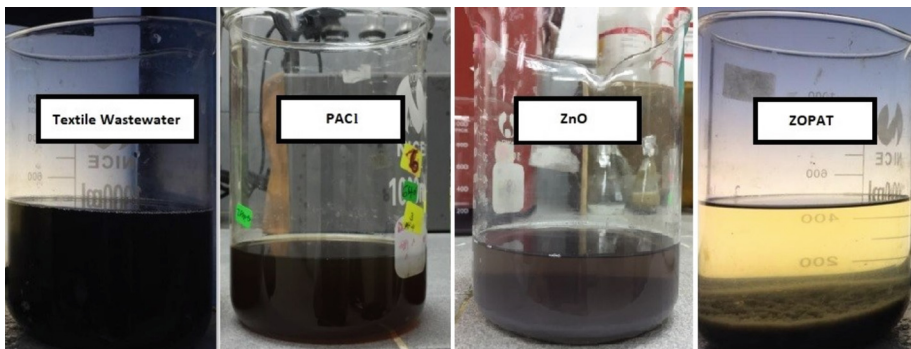


Fig. 2. The coagulation process after the treatment using ZOPAT, PACl and ZnO at optimum condition.

PACl needs to be used in combination with other polymers to achieve better coagulation results. Figure 2 provides a comparison of the sedimentation phase between ZOPAT, PACl, ZnO, and raw textile wastewater.

3.2 Optimization of Using RSM-CCD

In this section, a study on optimization using RSM-CCD was conducted with a rotatable design to reduce prediction errors and provide constant prediction variance at all points. The pH and dose ranges were selected based on the highest reduction observed in the preliminary jar test condition. The pH range was narrowed down to pH 8 for the lower limit and pH 10 for the upper limit, while the ZOPAT dosage range was set at 600 mg/L for the lower limit and 1000 mg/L for the upper limit. The speed and duration of rapid mixing, slow mixing, and sedimentation time were kept constant at the best reduction as observed in Table 1. The results showed almost 100% removal of turbidity and suspended solids, but only 93% and 78% reduction in colour and COD, respectively. ANOVA was then used to calculate the results obtained from the CCD experimental design, which are tabulated in Table 2. Further analysis, such as ANOVA, 3D plot surface, and validation for optimization, will be discussed in detail.

Table 1. Set of optimum parameters for each polymer applied in the jar testing.

Parameters	ZnO	ZnO + PAM	PAM	Tannin	PACl	ZOPAT
pH	12.0	12.0	2.0	12.0	8.0	7.2
Dose (mg/L)	1000	1000	400	400	800	800
Speed of rapid mixing	280	280	200	200	200	280
Time of rapid mixing	2.5	2.5	2	2	3	2.5
Speed of slow mixing	50	50	75	75	50	50
Time of slow mixing	5	5	15	15	15	5
Sedimentation time	30	30	30	30	30	10

3.3 Analysis of Variance (ANOVA)

The results in Table 2 present the P-values for four different responses, namely (a) turbidity, (b) colour, (c) COD, and (d) suspended solids, with two variables, pH and ZOPAT dose. The quadratic model was found to be statistically significant based on the P-value of less than 0.05 and the coefficient of determination (r^2) of 0.95. The significance of the model equation was confirmed by the 95% confidence interval ($P < 0.05$), indicating the effects of quadratic and interaction terms on the predicted responses. The r^2 value represents the proportion of variability in the response data that is explained by the fitted regression line, with values close to 1 indicating a good fit. The r^2 values for the reduction percentages of turbidity, colour, COD, and suspended solids using

Table 2. The P-value of factors and responses included in RSM-CCD. *A: pH, B: ZOPAT dose.

	Source	Sum of Squares	Mean Square	F Value	Prob > F	R- squared
Colour	Model	258.73	51.75	26.68	0.00	0.95
	A	10.12	10.12	5.22	0.05	
	B	41.92	41.92	21.62	0.00	
	A2	11.98	11.98	6.18	0.04	
	B2	161.11	161.11	83.07	0.00	
	AB	42.25	42.25	21.78	0.00	
COD	Model	66.25	13.25	22.88	0.00	0.94
	A	4.25	4.25	7.33	0.03	
	B	1.12	1.12	1.94	0.21	
	A2	23.49	23.49	40.56	0.00	
	B2	38.01	38.01	65.64	0.00	
	AB	6.25	6.25	10.79	0.13	
Turbidity	Model	211.70	42.34	22.42	0.00	0.94
	A	8.00	8.00	4.24	0.08	
	B	115.40	115.40	61.10	0.00	
	A2	0.03	0.03	0.01	0.91	
	B2	70.68	70.68	37.42	0.00	
	AB	16.00	16.00	8.47	0.02	
SS	Model	230.40	46.08	13.49	0.00	0.96
	A	21.92	21.92	6.42	0.04	
	B	134.47	134.47	39.37	0.00	
	A2	0.35	0.35	0.10	0.76	
	B2	61.57	61.57	18.03	0.00	
	AB	12.25	12.25	3.59	0.10	

ZOPAT were 0.94, 0.95, 0.94, and 0.91, respectively, suggesting that more than 90% of the total variation was explained by the empirical models, with less than 10% remaining unexplained. Overall, the coefficient of determination values was satisfactory, as r^2 values close to 1 were obtained.

The significance of the factors on the response was determined by P-values, where lower values indicated a greater impact of the factors [23]. In this study, all responses showed a fitted model with $P < 0.05$, except for the ZOPAT dose, which was insignificant only in relation to COD, indicating that COD was not affected by varying amounts of ZOPAT. Similarly, the effects of pH on turbidity and colour were not significant with P-values greater than 0.05, indicating that these responses were not influenced by changes

in pH. However, the interaction between pH and ZOPAT dose was found to be significant for all responses except suspended solids, with $P < 0.05$.

The purpose of plotting Fig. 3 was to examine the impact of different conditions on the percentage reduction. It was observed that sets 4 and 9 performed poorly due to a higher dosage of ZOPAT, which caused an overdose reaction resulting in re-dispersion of particles and a positive charge. This is supported by a significant P value of coagulant dose in Table 2. On the other hand, set 2 with a pH of 9 and 800 mg/L of ZOPAT showed excellent performance, achieving the highest reduction for all associated responses. Although COD had the lowest removal rate of approximately 80%, turbidity and suspended solids were effectively removed from the wastewater.

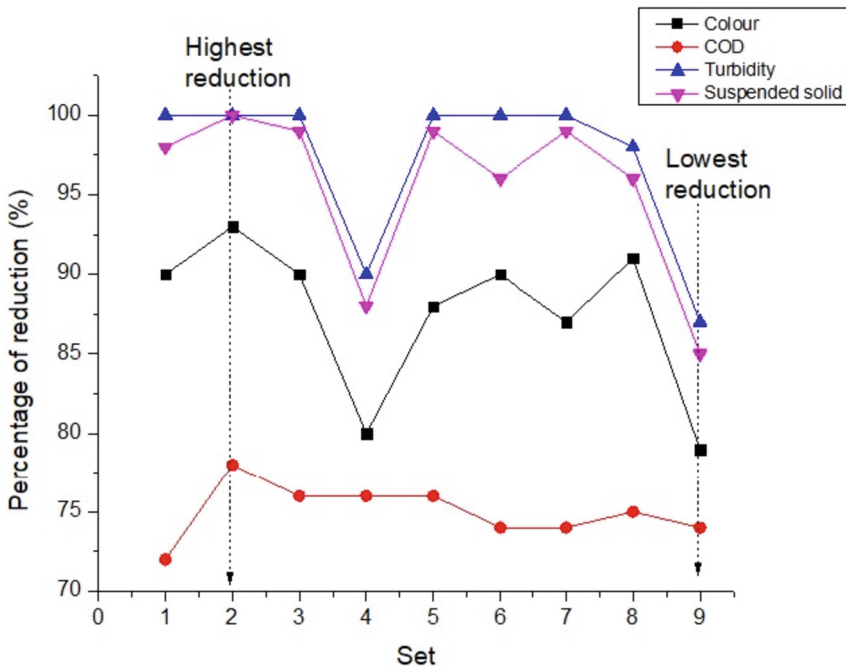


Fig. 3. Nine sets of different pH and polymer dose of ZOPAT were plotted to see the percentage of reduction for turbidity, colour, COD and suspended solids.

Previous research has demonstrated that the removal of suspended solids is influenced by gravity. The addition of chemicals can attract charges on the surface of colloidal particles, causing them to clump together and settle due to the effects of gravity [24]. Set 2 managed to achieve a color reduction of up to 94%. This is because the blended ZnO, PAM, and tannin generated reactive functional groups such as carboxyl, hydroxyl, and amide groups that can attack dye compounds. For instance, the reaction between the hydroxyl group (OH⁻) and sodium (Na⁺) forms sodium hydroxide compound. When a negatively charged ion forms a bond with a positively charged ion, and one atom transfers electrons to another, an ionic bond is formed. This destabilizes the colloidal particles,

neutralizes the electrostatic charges on the dye particles, facilitates agglomeration, and results in separation from the aqueous phase.

The best result obtained was an 80% reduction in COD, which could be due to the strong oxidizing behavior of the process, which causes a reduction in pH, resulting in a more transparent solution and compact sludge. On the other hand, the worst conditions were observed in sets 4 and 9, where a higher dose of ZOPAT (>1000 mg/L) resulted in lower efficiency for all responses. The increase in COD is mainly attributed to the redispersion of solids containing inorganic material [25]. This can occur because the amount of metal ions used can destabilize negatively charged colloids, leading to their adsorption onto the solid. Additionally, the use of Ethylenediaminetetraacetic acid (EDTA) or Diethylenetriamine pentaacetic acid (DTPA) in the bleaching process can also disrupt the metallic ions, resulting in lower COD reduction [26]. Moreover, the presence of substantial chemicals and auxiliaries in textile wastewater can make it challenging to remove [27].

3.4 Perturbation Plot of pH and Dose of ZOPAT

Figure 4, which is a perturbation plot, shows the effect of A (pH₂) and B (the dose of ZOPAT₂) on the reduction percentage of turbidity, color, COD, and SS. The sharp curvature observed in the plot indicates that the pH and the dose of ZOPAT are highly sensitive towards the reduction of color and COD. It can be observed from the plot that increasing the dose of coagulant leads to an increase in the percentage reduction for all parameters. However, overdosing with more than 1000 mg/L causes a certain degree of charge reversal of the particles, which reduces the effectiveness of the treatment [8]. The effect of overdosing results in the re-stabilization of dye particles and increased sludge formation due to the high amount of added chemicals [28].

In addition, Fig. 4 shows a straight line for A, which represents pH₂, in relation to (c) turbidity and (d) suspended solid. This suggests that both lines are less sensitive when compared to the others. The perturbation plot also reveals that the p-value for pH₂ for turbidity and suspended solid was 0.91 and 0.76, respectively. These values indicate that both variables have insignificant p-values > 0.05. The flat surface of pH on the plot indicates less sensitivity towards the pH environment between pH 8 and pH 10. This finding is consistent with a previous study that rejected the correlation between pH and turbidity of wastewater samples in India, as the correlation coefficient was only 0.11 [29]. This supports the idea that both studies involved real wastewater from the textile industry, which can influence the correlation between pH and turbidity.

The purpose of Fig. 5 is desirability ramp is to optimize multiple responses concurrently. The desirability range for a given response ranges from zero to one, indicating how close the response is to its ideal value.

As shown in Fig. 6, the desirability ramp resulted in a desirability value of 0.592. A value of one indicates a significant P-value for all parameters, whereas a value near zero indicates that one or more responses fall outside the desirability range. The low desirability value suggests that suspended solids were responsible for the reduced performance. According to the p-value, suspended solids were not significant for the interaction between pH and ZOPAT dose. Therefore, higher suspended solid removal can be

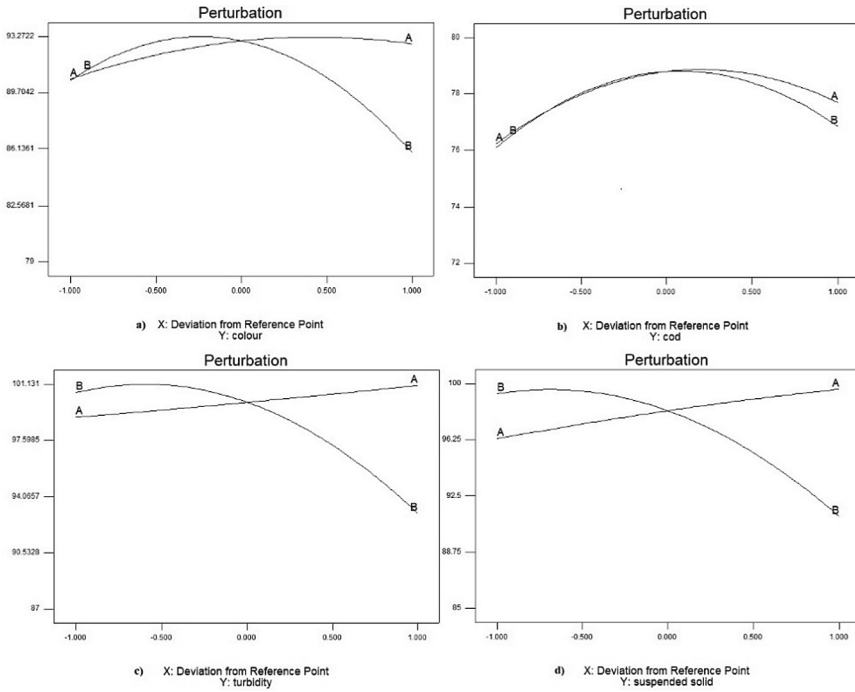


Fig. 4. Perturbation plot for each reduction such as a) colour, b) COD, c) turbidity and d) suspended solid at different pH2(A) and dose2(B).

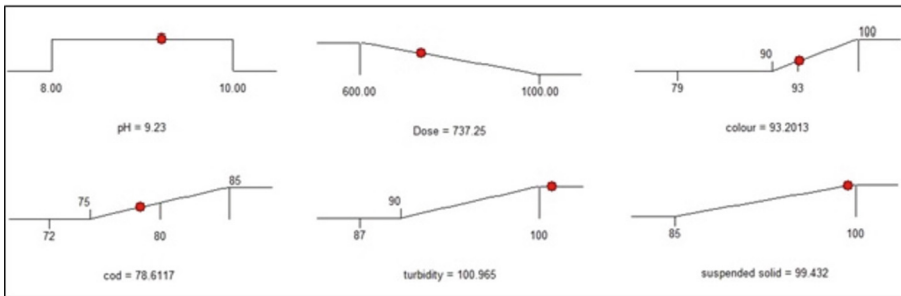


Fig. 5. The desirability ramp based on the outcome solution.

achieved with any pH and dose within the specified range. The gravitational effect and floc size make it easier to remove suspended solids during the sedimentation phase [30].

The optimization process was validated three times, as outlined in Table 3, using the outcome solution obtained from the desirability ramp.

The results of the chosen pH and ZOPAT dosage were evaluated based on their percentage reduction of turbidity, colour, COD, and suspended solids. The desirability ramp suggested the conditions that achieved the highest percentage reduction. The validation

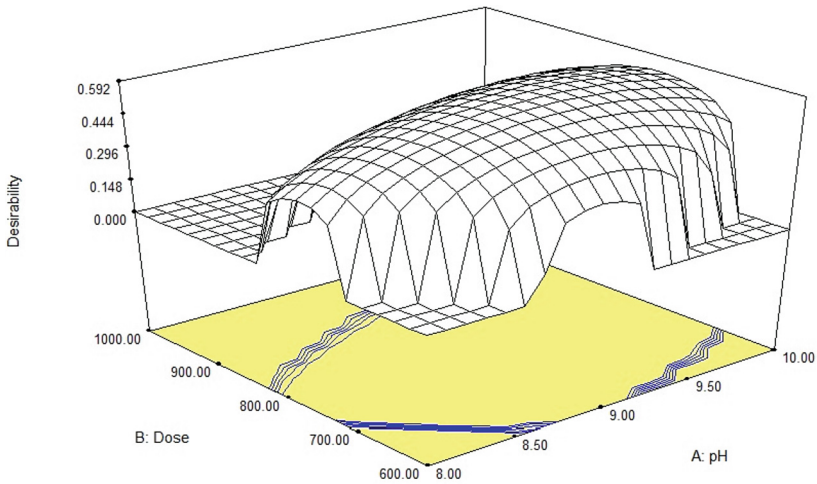


Fig. 6. The desirability plot at varied pH and doze ZOPAT.

Table 3. Validation of experimental results based on desirable ramp.

Experimental of percentage reduction (%)						
Set of Exp	pH	ZOPAT dosage (mg/L)	Turbidity (%)	Colour (%)	COD (%)	Suspended Solid (%)
1	9.22	737	100	93	79	99
2	9.20	737	100	92	78	99
3	9.22	737	100	93	80	100

* The initial concentration of the raw textile wastewater: Turbidity: 151 NTU, Colour: 1724 Pt/Co, COD: 2250 mg/L, Suspended Solid: 173 mg/L.

tests demonstrated that the reduction of colour, COD, turbidity, and suspended solids differed by less than 1%. The model's accuracy in estimating the reduction percentage for all parameters was acceptable. Therefore, the final optimal condition, which involved applying 737 mg/L of ZOPAT at pH 9.22, successfully achieved a high reduction of colour, COD, turbidity, and suspended solids.

3.5 Influence on pH After the Treatment with ZOPAT

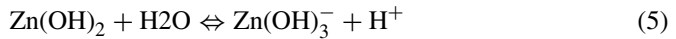
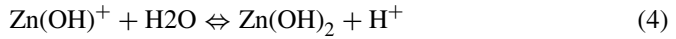
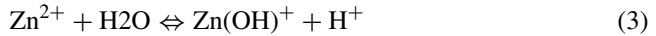
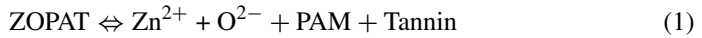
Table 4 shows that there was a slight pH difference before and after the coagulation treatment, which was attributed to the addition of ZOPAT to the suspension. The data in Table 4 reveals that the initial pH values for pH 4, pH 6, pH 8, and pH 12 were lowered as a result of the influence of ZOPAT.

When metal coagulants are added during the treatment of wastewater, the pH value of the wastewater decreases [31]. Additionally, some hydrolytic reactions take place during

Table 4. Result of pH before and after treatment with ZOPAT.

pH before treatment	pH after treatment with ZOPAT
2	2.0
4	3.9
6	5.4
8	6.5
10	8.0
12	10.2

the coagulation process, producing numerous positively charged hydrolysis products that interact chemically with negatively charged dye colloids. This generates multivalent charged hydroxyl species [32], as shown in Eqs. 1, 2, 3, 4, 5, and 6. The formation of metal hydrolysis also contributes to the solubility constant in Eq. 6.



The ANOVA test indicated that both the pH and the dose of ZOPAT had a significant effect, as indicated by their P-values. This suggests that there is a strong correlation between the pH and the coagulant dose.

3.6 Zeta Potential at Optimum Condition

Table 5 presents the evaluation of the zeta potential of ZOPAT, as well as the zeta potential of the agglomerated dye particles during jar testing. Prior to treatment, the wastewater sample exhibited a zeta potential of -28 mV. However, with the introduction of ZOPAT into the textile wastewater, destabilization occurred among the particles.

The negatively charged particles on the colloids were neutralized by cations in the polymer. In this case, the cations may include Zn^{2+} and $\text{Zn}(\text{OH})^+$, which attract negative dye compounds such as Cl^- , SO_3^{2-} , OH^- , and O_2^- , causing agglomeration among the flocs. This indicates that bond breakage occurs in the dye structure. During the rapid

Table 5. Different sample wsamplesken for wastewater (WW), during rapid mixing (RM), slow mixing (SM) and after sedimentation (AS) for zeta potential analysis.

Coagulation phase	Zeta Potential (mV)
Initial wastewater	-28
Rapid mixing (RM)	3.0
Slow mixing (SM)	2.4
After sedimentation (AS)	0.9

mixing phase, the zeta potential was close to 5 mV, which is consistent with a previous study that reported agglomeration occurring between -5 mV to $+5$ mV [33]. Charge neutralization and sweep flocculation occurred due to the reaction between the positively charged polymers and the sulfonic group of dye molecules [34]. The zeta potential of the flocs during the slow mixing time remained positive, and their size gradually increased through adsorption-bridging ability. As the flocs became larger, they settled and reduced the color in the wastewater. Surface adsorption was also activated, which removed the balance of free colloids by enmeshing them in the flocs [35]. After sedimentation, the treated wastewater had a zeta potential closer to $+1$ mV. The maximum agglomeration can be between 0 charges and 3 mV [33].

Effect of Temperature on Storage Conditions. A previous study [15] conducted a storage test on ZOPAT, analyzing the effect of storage temperature in a cold room ($4-6$ °C) and at room temperature (30 °C) for a duration ranging from 0 to 60 days. The results were presented for color reduction and COD reduction in Fig. 7. Figure 7 illustrates that the reduction of color was notably affected after 28 days, but it deteriorated considerably after 60 days at room temperature. This suggests that storing ZOPAT in a cold environment can help stabilize it.

Additionally, Fig. 8 shows that the physical appearance of ZOPAT became foamy and darker after 60 days. Similar observations were made in another study involving the use of natural coagulant (*M. oleifera*) in the hybrid coagulant, which resulted in changes after 30 days [15].

This indicates that natural coagulants can also affect the storage stability of hybrid coagulants. The reduction of COD followed a similar pattern to that of color reduction, with no significant difference in the efficiency of the hybrid coagulant within a week. The COD percentage reduction began to decline significantly after 28 days, from 70% to 60%, and then decreased slowly until 60 days. According to [8], the aging of the hybrid coagulant may trigger some chemical reactions, such as an increase in temperature and duration of time. Based on these findings, it is recommended to store ZOPAT in a cold room for not more than 20 days to maintain its quality.

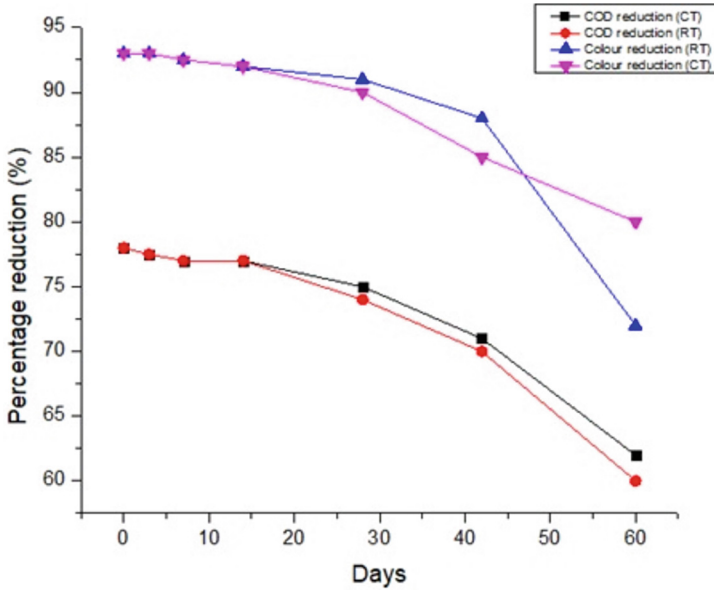


Fig. 7. The storage stability of ZOPAT in colour and COD reduction for 60 days *CT: Cold temperature and RT: Room temperature.

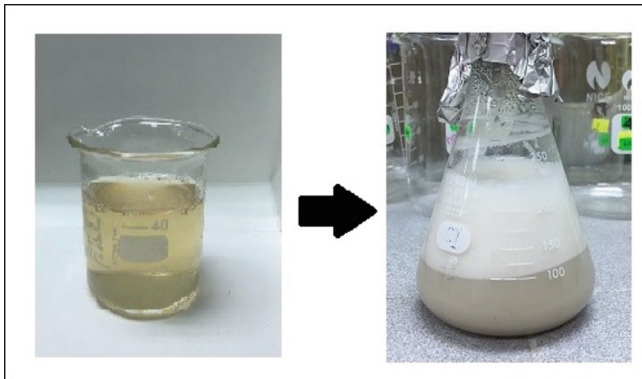


Fig. 8. ZOPAT appearance after 60 days in room temperature.

4 Conclusions

The study evaluated the effectiveness of different polymers in treating textile wastewater, including a hybrid polymer ZOPAT composed of zinc oxide, acrylamide, and tannin. ZOPAT demonstrated strong performance in reducing turbidity, color, and suspended solids in a wide range of pH levels. It was also more effective in reducing color than COD and consistent at low doses. Tannin showed the best residual COD concentration, but its performance in reducing other pollutants was not as good as ZOPAT. ZnO showed better

removal of color but required a high dosage. PACl alone was found to be less effective in reducing color but could be used in combination with other polymers. According to the RSM-CCD, the model showed a strong relationship between the independent (pH and ZOPAT dose) and dependent variables, and the hybrid polymer had the highest efficiency in removing pollutants from wastewater. The plot indicated that the pH and the dose of ZOPAT had a significant effect on the reduction of color and COD. Increasing the dose of coagulant led to an increase in the percentage reduction for all parameters but overdosing with more than 1000 mg/L reduced the effectiveness of the treatment. The study recommended storing ZOPAT in a cold room for not more than 20 days to maintain its quality. Overall, the study provides valuable insights into the use of hybrid polymer ZOPAT in treating wastewater and sheds light on the optimal storage conditions for the hybrid polymer. It highlights the importance of using multiple polymers in treating wastewater to achieve better coagulation results. The study's findings can aid in developing efficient and cost-effective wastewater treatment methods.

Acknowledgments. This research has been funded by Research University grant 203.PAWAM.6071298.

References










1. Department of Statistics Malaysia Official Portal. Malaysia External Trade Statistics Bulletin (2021). https://www.dosm.gov.my/v1/index.php?r=column/cthemByCat&cat=139&bul_id=YUh5aTBOazIxdEwzb1QwaG1TdnlzZz09&menu_id=azJjRWpYLOVBjYU90TVhpc1ByWjdMQT09
2. Manogaran, M., Manogaran, B., Othman, A.R., Gunasekaran, B., Abd Shukor, M.Y.: Decolourisation of reactive red 120 by a heavy metal-tolerant bacterium Isolated from Juru River. Malaysia. Bioremediation Science and Technol. Res. **8**(1), 23–26 (2020)
3. Ghaly, A.E., Ananthashankar, R., Alhattab, M.V.V.R., Ramakrishnan, V.V.: Production, characterisation and treatment of textile effluents: a critical review. J. Chem. Eng. Process Technol. **5**(1), 1000182 (2014)
4. Mishra, S., Mohanty, P., Maiti, A.: Bacterial mediated bio-decolourization of wastewater containing mixed reactive dyes using jack-fruit seed as co-substrate: process optimization. J. Clean. Prod. **235**, 21–33 (2019)
5. Yaseen, D.A., Scholz, M.: Textile dye wastewater characteristics and constituents of synthetic effluents: a critical review. Int. J. Environ. Sci. Technol. **16**(2), 1193–1226 (2019)
6. Markies, P.R., Moonen, J.P., Colin, P.O., Evers, R.W., Van Den Beucken, F.J. Peng, K.U.S.: Aqueous Inkjet Priming Composition Providing Both Pinning and Ink Spreading Functionality. Patent Application 15/938,893, 28 (2018)
7. Wang, X., Jiang, S., Tan, S., Wang, X., Wang, H.: Preparation and coagulation performance of hybrid coagulant polyacrylamide–polymeric aluminium ferric chloride. J. Appl. Polym. Sci. **135**(23), 46355 (2018)
8. Zhou, L., Zhou, H., Yang, X.: Preparation and performance of a novel starch-based inorganic/organic composite coagulant for textile wastewater treatment. Sep. Purif. Technol. **210**, 93–99 (2019)
9. Huang, X., Wan, Y., Shi, B., Shi, J., Chen, H., Liang, H.: Characterisation and application of poly-ferric-titanium-silicate-sulfate in disperse and reactive dye wastewaters treatment. Chemosphere, 126129 (2020)

10. Zhu, G., et al.: Toward a better understanding of coagulation for dissolved organic nitrogen using polymeric zinc-iron-phosphate coagulant. *Water Res.* **100**, 201–210 (2016)
11. Zhu, G., Liu, J., Bian, Y.: Evaluation of cationic polyacrylamide-based hybrid coagulation for the removal of dissolved organic nitrogen. *Environ. Sci. Pollut. Res.* **25**(15), 14447–14459 (2018)
12. Fu, Y., Wang, Y.Z.: An organic-inorganic hybrid coagulant containing Al, Zn and Fe (HOAZF): preparation, efficiency and mechanism of removing organic phosphorus. *J. Water Reuse and Desalination* **8**(2), 202–213 (2018)
13. Hassan, S.S., Abdel-Shafy, H.I., Mansour, M.S.: Removal of pharmaceutical compounds from urine via chemical coagulation by green synthesized ZnO-nanoparticles followed by microfiltration for safe reuse. *Arab. J. Chem.* **12**(8), 4074–4083 (2019)
14. Wang, Z., Li, H., Tang, F., Ma, J., Zhou, X.: A facile approach for the preparation of nano-size zinc oxide in water/glycerol with extremely concentrated zinc sources. *Nanoscale Res. Lett.* **13**(1), 202 (2018)
15. Dalvand, A., et al.: Comparison of *Moringa stenopetala* seed extract as a clean coagulant with Alum and *Moringa stenopetala*-Alum hybrid coagulant to remove direct dye from textile wastewater. *Environ. Sci. Pollut. Res.* **23**(16), 16396–16405 (2016)
16. Yoo, S.S.: Operating cost reduction of in-line coagulation/ultrafiltration membrane process attributed to coagulation condition optimisation for irreversible fouling control. *Water* **10**(8), 1076 (2018)
17. Wong, P.W., Teng, T.T., Norulaini, N.A.R.N.: Efficiency of the coagulation-flocculation method for the treatment of dye mixtures containing disperse and reactive dye. *Water Quality Research J.* **42**(1), 54–62 (2007)
18. Thakur, S.S., Choubey, S.: Use of tannin based natural coagulants for water treatment: an alternative to inorganic chemicals. *Int. J. ChemTech Res.* **6**(7), 3628–3634 (2014)
19. Irfan, M., Butt, T., Imtiaz, N., Abbas, N., Khan, R.A., Shafique, A.: The removal of COD, TSS and colour of black liquor by coagulation–flocculation process at optimized pH, settling and dosing rate. *Arab. J. Chem.* **10**, S2307–S2318 (2017)
20. Dotto, J., Fagundes-Klen, M.R., Veit, M.T., Palácio, S.M., Bergamasco, R.: Performance of different coagulants in the coagulation/flocculation process of textile wastewater. *J. Clean. Prod.* **208**, 656–665 (2019)
21. Islam, M.R., Mostafa, M.G.: Characterisation of textile dyeing effluent and its treatment using polyaluminium chloride. *Appl Water Sci* **10**(5), 1–10 (2020)
22. Ngadi, N., Yahya, N.Y., Muhamad, N.: Treatment of industrial textile wastewater using polyacrylamide (Pam) and polyaluminium chloride (Pac). *Journal Teknologi* **60**, 41–44 (2013)
23. Myers, R.H., Montgomery, D.C., Anderson-Cook, C.M.: Process and product optimisation using designed experiments. *Response Surface Methodol.* **2**, 328–335 (2002)
24. Uhlmann, M., Doychev, T.: Sedimentation of a dilute suspension of rigid spheres at intermediate Galileo numbers: the effect of clustering upon the particle motion. *J. Fluid Mech.* **752**, 310–348 (2014)
25. López-Maldonado, E.A., Oropeza-Guzman, M.T., Jurado-Baizaval, J.L., Ochoa-Terán, A.: Coagulation–flocculation mechanisms in wastewater treatment plants through zeta potential measurements. *J. Hazard. Mater.* **279**, 1–10 (2014)
26. Sillanpää, M.: Environmental fate of EDTA and DTPA. *Reviews of Environmental Contamination and Toxicology*, 85–111 (1997)
27. Lee, K.E., Goh, T.L., Simon, N.: Textile industrial wastewater treatment by polyacrylamide aided magnesium chloride hybrid coagulant. *Nature Environment & Pollution Technology* **16**(2) (2017)

28. Khader, E.H., Mohammed, T.H.J., Mirghaffari, N.: Use of natural coagulants for removal of COD, oil and turbidity from produced waters in the petroleum industry. *J. Pet. Environ. Biotechnol.* **9**(374), 2 (2018)
29. Mandal, H.K.: Influence of wastewater pH on turbidity. *Int. J. Environ. Res. Dev* **4**(2), 105–114 (2014)
30. Zhang, J., Shen, X., Zhang, Q., Maa, J.P.Y., Lin, M.: Role of gravity in coagulation of colloidal particles under low-shear environments. *Mar. Geol.* **449**, 106822 (2022)
31. Birjandi, N., Younesi, H., Bahramifar, N.: Treatment of wastewater effluents from paper-recycling plants by coagulation process and optimization of treatment conditions with response surface methodology. *Appl Water Sci* **6**, 339–348 (2016)
32. Tetteh, E.K., Rathilal, S.: Evaluation of different polymeric coagulants for the treatment of oil refinery wastewater. *Cogent Engineering* **7**(1), 1785756 (2020)
33. Salopek, B., Krasic, D., Filipovic, S.: Measurement and application of zeta-potential. *Rudarsko-geolosko-naftni zbornik* **4**(1), 147 (1992)
34. Cruz, D., Pimentel, M., Russo, A., Cabral, W.: Charge neutralization mechanism efficiency in water with high color turbidity ratio using aluminium sulfate and flocculation index. *Water* **12**(2), 572 (2020)
35. Ghernaout, D., Ghernaout, B.: Sweep flocculation as a second form of charge neutralisation—a review. *Desalin. Water Treat.* **44**(1–3), 15–28 (2012)



A Study of Flow Pattern and Sedimentation in Hydraulic Physical Model

Muhammad Nasri Nasehir Khan¹ , Mohd Remy Rozainy Mohd Arif Zainol^{1,2} ,
Mohd Azmier Ahmad³ , Nazirul Mubin Zahari⁴ , Mohd Hafiz Zawawi⁴ ,
Mohd Rashid Mohd Radzi⁵ , Nurhanani Abd Aziz⁴ ,
Farah Nurhikmah Che Ghazali⁴ , and Mohamad Aizat Abas⁶ 

¹ School of Civil Engineering, Universiti Sains Malaysia, Nibong Tebal, Malaysia
ceremy@usm.my

² River Engineering and Urban Drainage Research Institute (REDAC), Nibong Tebal, Malaysia

³ School of Chemical Engineering, Universiti Sains Malaysia, Nibong Tebal, Malaysia

⁴ Department of Civil Engineering, Universiti Tenaga Nasional (UNITEN), Kajang, Malaysia

⁵ Business Development (Asset) Unit, TNB Power Generation Division, Kuala Lumpur, Malaysia

⁶ School of Mechanical Engineering, Universiti Sains Malaysia, Nibong Tebal, Malaysia

Abstract. Sustainability of hydroelectric dams has been questioned due to the sedimentation, erosion and vortex formation at the dams. This study had assessed the potential of sedimentation, erosion and vortex formation based on the flow pattern formed via hydraulic physical model (Scale of 1:100). Four cases have been tested which are Case 1 (the position of water inlet at the middle with stage of 0.38 m), Case 2 (the position of water inlet at the middle with stage 0.34 m), Case 3 (the position of water inlet at the side with stage of 0.38 m) and Case 4 (the position of water inlet at side with stage 0.34 m). Based on Case 3, the range of flow velocities obtained was 0.3–2.1 m/s at 20% from water surface, leading to erosion at the dam bank and sedimentation which focused on the side of the dam that threatened the stability of the dam due to the concentrated load of sediment. Vortex type 5–6 had been identified for a period of 15–30 s. Overall, the flow pattern at the dam up-stream was influenced by the position of water inlet from dam's upstream, flowrate of the dam and the depth from the water level.

Keywords: Flow Pattern · Hydraulic Physical Model · Dam

1 Introduction

A dam is a massive impounding construction or barrier which is built on a watercourse to contain vast amount of water and regulate the water flow. Typically, a reservoir and a dam are existed together [1]. For the hydroelectric generation, water level has been raised to create sufficient head which may rotate the turbines in an electricity generating power plant that usually located at the dam's toe [2]. To ensure high efficiency and safe hydroelectric dams, factors such as flow pattern of the dam and its impacts towards sedimentation, erosion and vortex formation should be acknowledged. In order to assess these factors, physical hydraulic model should be made.

Physical model can be referred as a scaled representation of hydraulic flow scenario in which the flow field and geometry conditions must be scaled accordingly [3]. For this study, the flow pattern will be assessed via dam physical model approach. In order to assess the flow pattern, a hydraulic physical dam model with a scale of 1:100 (model to prototype ratio) has been made and its flow pattern along the model has been analysed. Flow pattern can be significantly influenced by the flow rate of the system, pressure, surface tension, density, geometry and distance from the inlet [4]. According to [5], flow pattern formed will assist in determining the sediment deposition and erosion based on the flow velocity. Deposition of sediment occurs at dam due to the low flow velocity due to the increased of flow depth in which reduces the transport of sediment capacity and accelerates the sedimentation process [6]. Many studies indicated that sedimentation has reduced the dam storage capacity [9–11]. Reduction of reservoir storage capacity may lead to high-cost maintenance due to more frequent and high cost of dredging and removal [10]. According [11], the depleted dam storage does not only reduce the hydropower generation, but also can lead to the impairment of dam's mechanical components. Besides, according to [12], erosion consists of removal and transportation of solid material due to the action of water, wind or ice which also includes the abrasion of the sediments they transport. Erosion may lead to deposition of sediment in dams as stated by [13] where soil erosion has led to the serious accumulation of sedimentation. Therefore, a study of the flow pattern based on the hydraulic physical dam model can provide overall view of the exact condition of the dam.

2 Methodology

For this study, the first stage is focusing on the collection of data. It should start after the calibration of velocity meter and the efficiency of the hydraulic physical model have been validated and certified, Fig. 1 and Fig. 2. The velocity of flow with different depths (20%, 60% and 80%) at every measurement point had been recorded with the aid of Nixon Streamflo Velocity Meter and 403 Standard Low Speed Velocity Probe which had been calibrated. It is important to ensure that the velocity meter had been calibrated in order to ensure that all the data obtained were valid. Besides, the formation of vortex throughout the laboratory test had been observed and its duration and type were recorded.

For the collection of data, there were two positions of the inlet – middle and side positions which can be observed from Fig. 3. For every inlet position, it will have two sets of tests will be conducted for the maximum (0.38 m) and minimum (0.34 m) water level respectively as depicted in Fig. 4. The influence of the inlet position and water level in the model towards the flow pattern and formation of vortex will be studied. Overall, there will be four cases for the data collection based on the position of water inlet and stage as illustrated in Table 1.

The second stage of the study is to analyse the collected data for all the sets of tests by using a modelling software, known as Surfer version 13.0. Surfer is a 2D and 3D visualization, contouring and surface modelling software which able to display the data and maintain the accuracy via interpolation feature [14]. As mentioned, the collected data were based on velocity, hence by using the software, contours of flow pattern for all the sets of measurement along the upstream of the dam can be realised. Contouring

of flow pattern will assist in verifying the areas which were prone to sedimentation and erosion in a better representation.

For contouring purpose via the Surfer version 13.0, Kriging Method had been implemented for the gridding method as it is more flexible which able to provide a better and accurate contouring map for unevenly spaced with minimum variance. In this method, all the data obtained will be weighted in their importance based on their spatial location and degree of correlation so that the estimation error is minimized [15]. Thus, by using this Surfer via Kriging Method, all the data can be presented clearly and visually which aids in better understanding of the flow pattern along the hydraulic physical dam model.

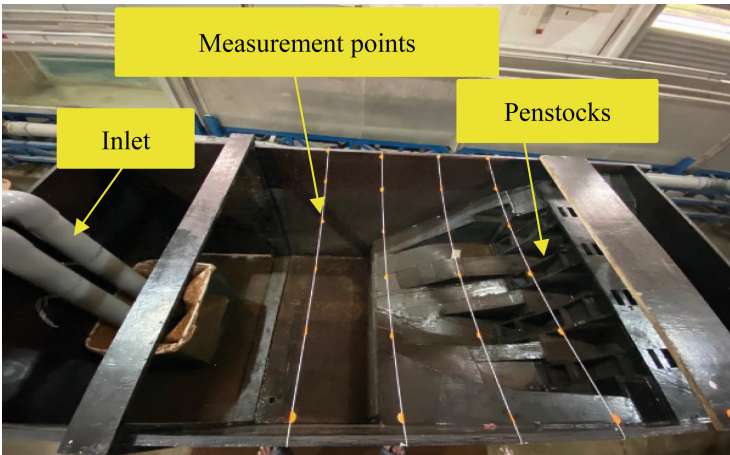


Fig. 1. Hydraulic physical dam model.



Fig. 2. Outlets of the physical model.



Fig. 3. Inlet Position (a) Side Position; (b) Middle Position.

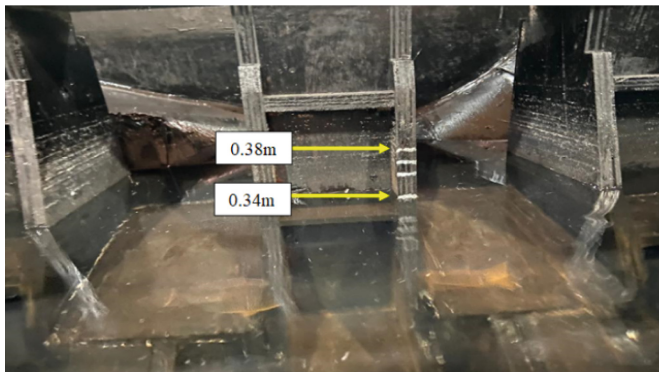


Fig. 4. Water level.

Table 1. Cases for Data Collection.

Case	Water Inlet	Stage (m)
1	Middle	0.38
2	Middle	0.34
3	Side	0.38
4	Side	0.34

3 Results and Discussions

3.1 Flow Pattern Contours

The flow velocity collected from the hydraulic physical model had been illustrated in the form of contours via Surfer 13.0 software. The flow pattern from the upstream of the dam until the flow reached the penstocks have been illustrated. For interpolation method,

Kriging Method was implemented into the modelling. The results for every case have been depicted in Fig. 5, Fig. 6, Fig. 7 and Fig. 8.

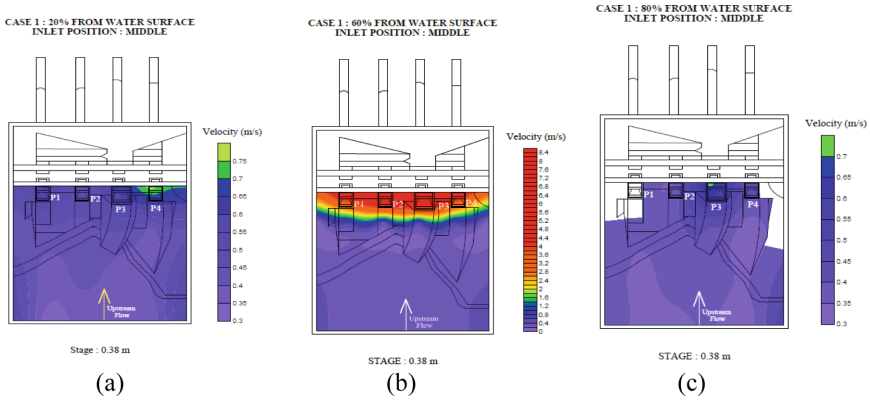


Fig. 5. Flow Pattern of Case 1 (a) 20% from water surface; (b) 60% from water surface; (c) 80% from water surface.

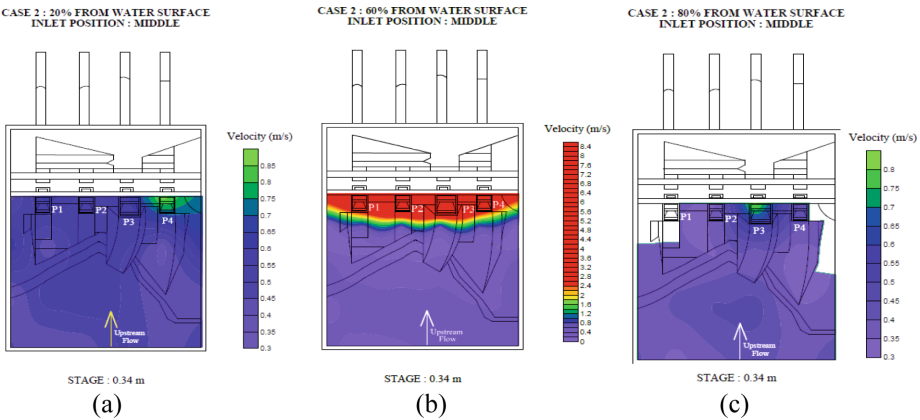


Fig. 6. Flow Pattern of Case 2 (a) 20% from water surface; (b) 60% from water surface; (c) 80% from water surface.

Based on the figures above, it can be observed that the elevation of water at the dam or also known as stage influenced the flow pattern at the upstream of the dam significantly. Based on Case 1 – Fig. 5(a) and Case 2 – Fig. 6(a), it can be compared that at higher stage, the flow velocity is greater due to higher flow rate. The same condition occurred for Case 3 and Case 4 which can be observed from Fig. 7(a) and Fig. 8(a) respectively. Based on the Continuity Equation, flow rate is directly proportional to velocity of flow if the cross-sectional area is constant, but from the data collection, it can be depicted that even though the stage (cross-sectional area of flow) had increased but the change in velocity can still be identified with different stages of water at the upstream of the dam.

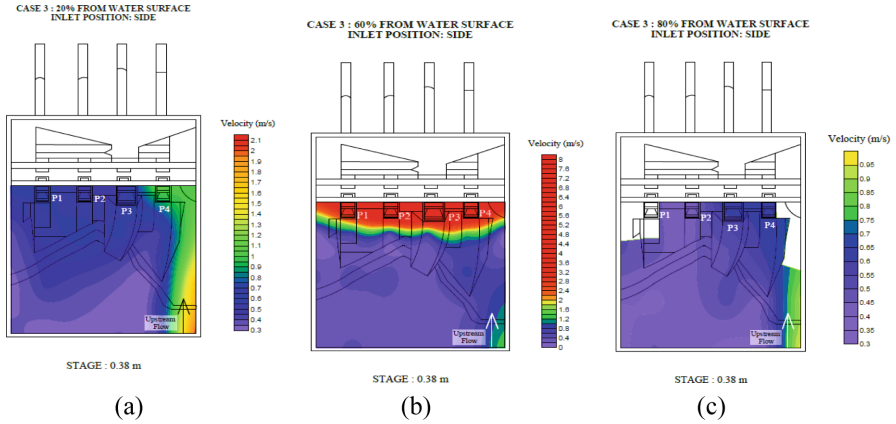


Fig. 7. Flow Pattern of Case 3 (a) 20% from water surface; (b) 60% from water surface; (c) 80% from water surface.

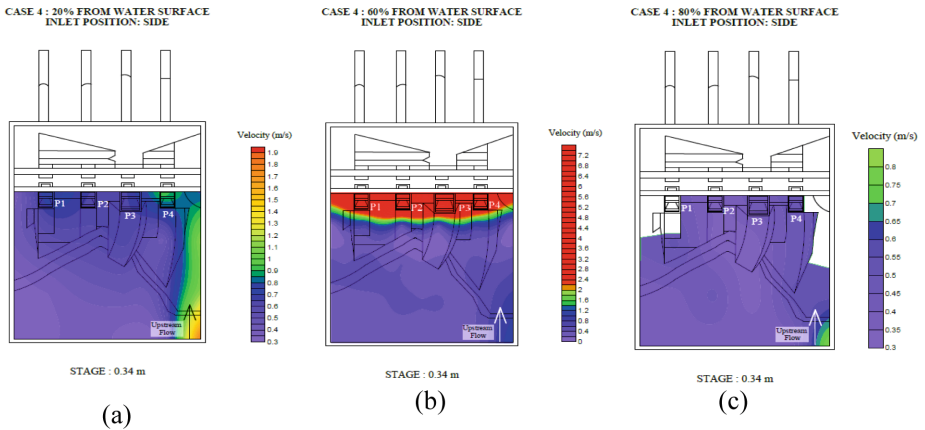


Fig. 8. Flow Pattern of Case 4 (a) 20% from water surface; (b) 60% from water surface; (c) 80% from water surface.

Besides, it can also be observed that the flow pattern can be greatly influenced by the water depth. For example, in Case 1, it can be illustrated that the velocity of flow reduced with depth as shown in Fig. 5 (a–c). At greater depth from the water surface, the velocity of flow decreased. The velocity of flow near the bed low due to the presence of friction at the bed surface. However, at the depth of 60% from the water surface (Fig. 5(b), Fig. 6(b), Fig. 7(b) and Fig. 8(b)) the velocity of flow was higher due to the existence of penstocks which allowed the water to flow from the upstream of the dam to the power generation center.

However, in this research, it can be noticed that distribution of flow pattern along the dam can be influenced significantly by the position of water inlet from the upstream of the dam. This condition can be observed when Case 1 and Case 3 were being compared. From Fig. 5(a) and Fig. 6(a), the flow pattern for inlet at the middle was more uniform

and stable flow pattern compared to the inlet at the side. From Case 3, water flows from inlet at the side produced greater velocity with the range of 0.3–2.1 m/s especially, alongside the bank of the dam and its maximum velocity was greater compared to water flows from inlet at the middle. Unstable distribution of velocity flow or flow pattern may lead to adverse effects towards the dam safety.

3.2 Erosion

From the flow contours, areas which prone to erosion along the model had been determined for every case. The determination is based on the minimum velocity required for erosion to occur. According to [18, 19], the minimum velocity for erosion to occur for natural ground equal to 1.5 m/s. The determination of the value has been made after considering the type and size pf particles. The locations which exposed to erosion had been depicted in Fig. 9, Fig. 10, Fig. 11 and Fig. 12.

Based on Case 1 and Case 2, for 20% and 80% from the water surface, it can be observed that the erosion affect may not be so significant due to the well-distributed flow velocity along the dam because of the position of water inlet (upstream) at the middle. At this level from water surface, the velocity of water below than 1.5 m/s, resulting low potential for erosion to occur along the dam. Besides, at the greater depth, for example, at 80% from water surface, due to higher surface roughness at the bed, has slowed down the velocity of flow, lowering the risk for erosion to occur at the bed of the dam. The same condition has occurred for Case 3 and Case 4 at 80% from water surface. This phenomenon has proven the relationship between the water depth and the risk for erosion to occur.

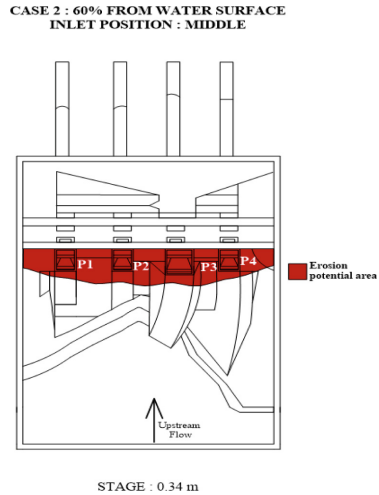
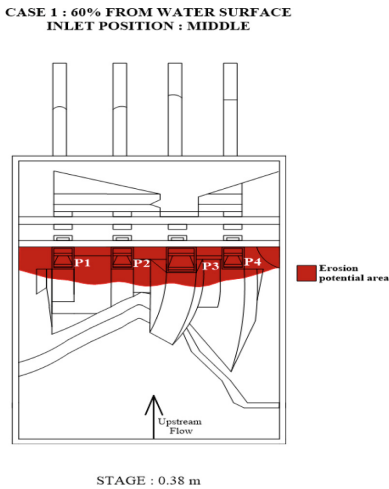


Fig. 9. Erosion potential area for Case 1 (60% from water surface).

Fig. 10. Erosion potential area for Case 2 (60% from water surface).

For Case 3 and Case 4, for 20% from the water surface, it can be observed from Fig. 11(a) and Fig. 12(a) respectively, high velocity of more than 1.5 m/s occurred along the side of the dam which may resulted in bank erosion. High flow velocity at the side can be due to the position of water inlet from the upstream. Hence, this condition signifies the importance of ensuring the stable distribution of flow velocity along the dam so that the erosion at the concentrated point can be reduced as flow velocity had been distributed uniformly. Besides, it can be compared from both figures that at higher stage, the potential for erosion to occur is greater, resulting wider area for erosion to occur. For instance, Case 3 with greater stage (0.38 m) had resulted wider area which potential for erosion to occur at the dam's bank compared to Case 4 with lower stage (0.34 m). Higher stage can be resulted from higher discharge from upstream which flow into the dam. Hence, indicating the relationship of upstream discharge towards the risk of erosion at the dam. Besides, from the contours and analysis which had been made, it can be observed that by identifying location with high risk of erosion, erosion protections can be installed at these identified areas to ensure there will be no occurrence of landslides or bank slumping at the dam.

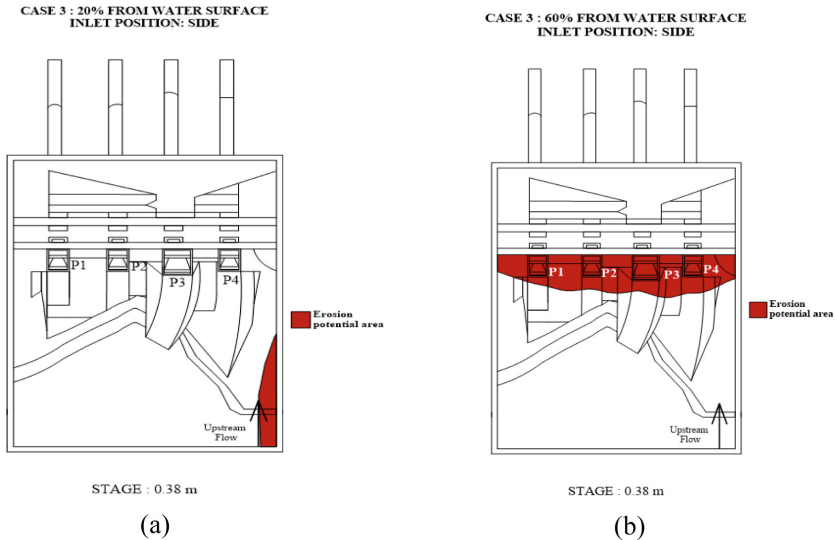


Fig. 11. Erosion potential area for Case 3 (a) 20% from water surface; (b) 60% from water surface.

However, for velocity flow at 60% from water surface for all cases (Fig. 9, Fig. 10, Fig. 11(b) and Fig. 12(b)) indicated high velocity at the penstock which exceeded 1.5 m/s and up to 8.4 m/s, leading to high risk for erosion to occur at the area. The high flow velocity at the penstocks is due to the high kinetic energy. This high energy has been produced by the accumulated water at the upstream of the dam which stores high amount of gravitational potential energy.

As the water flows through the penstocks which are located at the lower part of the dam, the gravitational potential energy will be converted into high kinetic energy, resulting high velocity at the penstocks. This phenomenon also fulfilled the Principle of

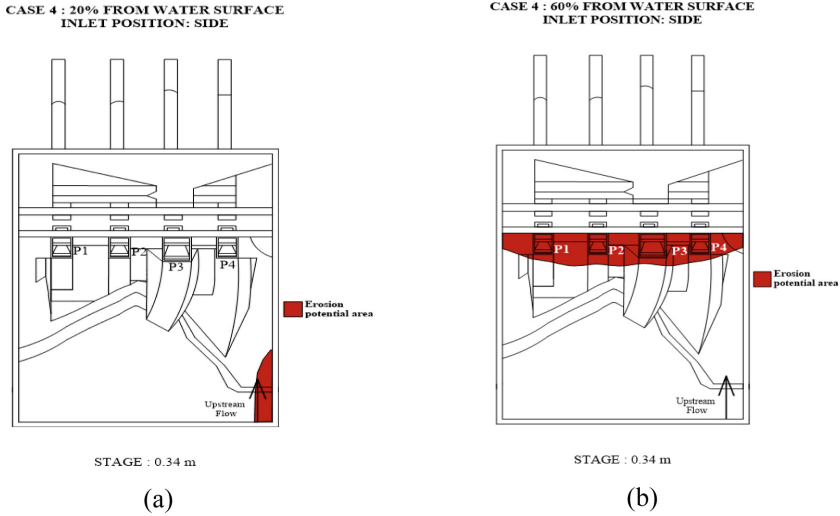


Fig. 12. Erosion potential area for Case 4 (a) 20% from water surface; (b) 60% from water surface.

Conservation of Energy [18]. Hence, erosion protections are essential in order to ensure the safety of the dam especially at the area near to the penstocks by selecting the right material for the dam and penstocks (outlets) accordingly.

3.3 Sedimentation

From the flow contours, areas which prone to sedimentation along the model can be determined when the velocity of flow had reduced to 0.6 m/s [18, 19]. The areas which prone to the sedimentation can be observed from Fig. 13, Fig. 14, Fig. 15 and Fig. 16.

For Case 1 and Case 2 at 20% from water surface as indicated in Fig. 13(a) and Fig. 14 (a) respectively, due to the position of upstream flow at the middle, velocity of flow had been distributed almost uniformly, leading to low value of flow velocity at both sides of the dam which may promote sedimentation at both sides of the dam. Since Case 1 had higher stage compared to Case 2, it can be observed that wider areas will be exposed to sedimentation for Case 2 compared to Case 1. This phenomenon can also be proven from Case 3 and Case 4 based on the Fig. 15(a) and Fig. 16(a). Thus, higher stage may result in greater velocity of flow, lowering the risk for the sedimentation to occur by reducing the area for sedimentation to occur. Hence, signifying the relationship between the stage of water and the risk for sedimentation to occur at dam.

Besides, for every case, it can be observed that at the greater depth, wider area will be exposed to the deposition of sediment. For example, Case 1, the area which will be prone to sedimentation became wider extent at greater depth from the water surface as shown in Fig. 13 (a–c). At the greater depth, the velocity of flow reduced due to the surface roughness of the bed. As the velocity of flow reduced, deposition of sediments may occur which led to the occurrence of sedimentation, causing reduction of dam storage [19].

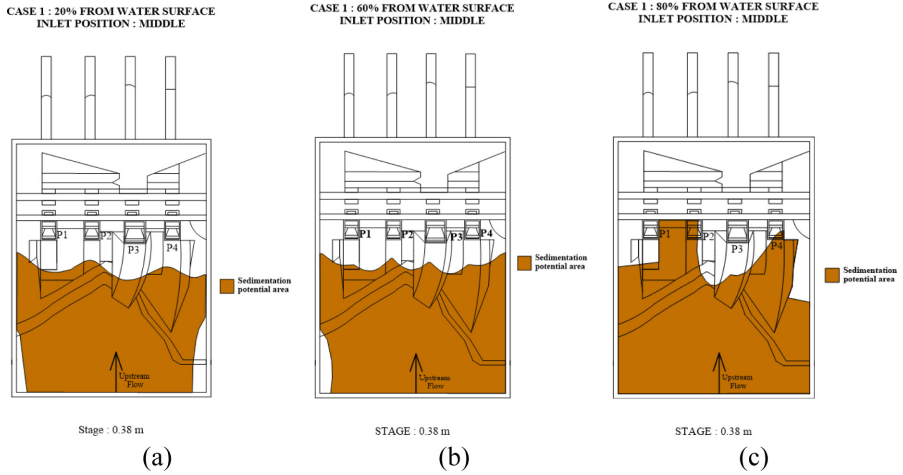


Fig. 13. Sedimentation potential area for Case 1 (a) 20% from water surface; (b) 60% from water surface; (c) 80% from water surface.

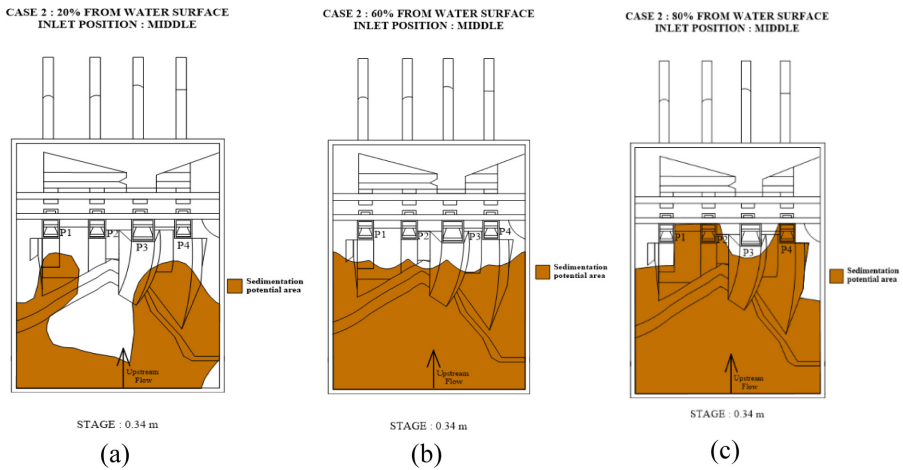


Fig. 14. Sedimentation potential area for Case 2 (a) 20% from water surface; (b) 60% from water surface; (c) 80% from water surface.

For Case 3 and Case 4, it can be depicted that the deposition of the sediment may occur at the left side of the dam due to the low flow velocity within that area as shown in Fig. 15(a) and Fig. 16(a). This condition occurred due to the position of the water inlet at the upstream of the dam. The position of water inlet at the side had created non-uniform flow pattern, leading to unstable distribution of sediment deposition. Besides, it may also result in concentrated load at the one-side of the dam due to the accumulation of sediment, effecting the ground stability. Thus, from the result, it can also be depicted

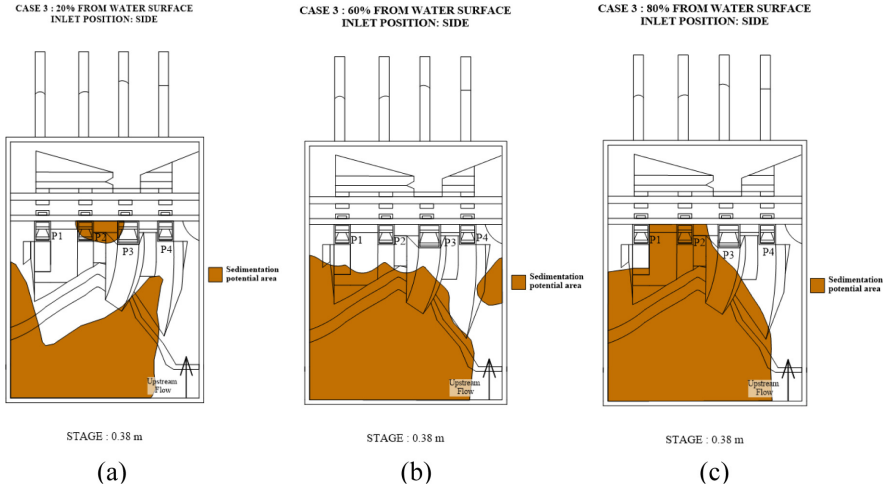


Fig. 15. Sedimentation potential area for Case 3 (a) 20% from water surface; (b) 60% from water surface; (c) 80% from water surface.

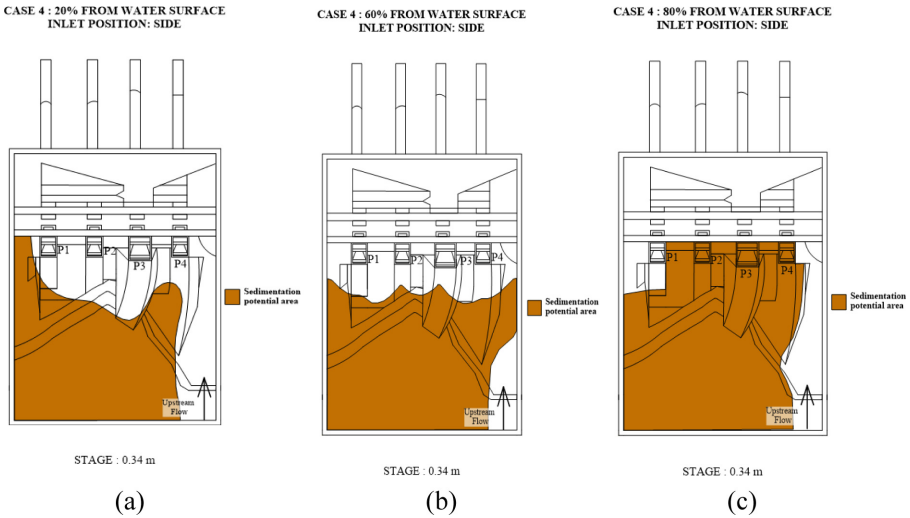


Fig. 16. Sedimentation potential area for Case 4 (a) 20% from water surface; (b) 60% from water surface; (c) 80% from water surface.

the relationship between the position of water inlet at the upstream and the risk for sedimentation to occur at the dam.

3.4 Vortex Formation

The vortices formed along the hydraulic physical dam model were observed for every case. The vortex properties such its types, duration and location of where it was formed was recorded as tabulated in Table 2.

Table 2. Vortex formation and its properties.

Vortex Formation				
Case	Location	Diameter (cm)	Type	Duration (s)
1	P1	0.6	1–2	2–3
	P2	0.7	1–2	2–3
2	P1	0.6	1–2	2–4
	P2	0.7	1–2	2–4
3	P1	1.0	1–2	5–10
	P4	2.0	5–6	15–30
4	P1	1.0	1–2	5–10
	P2	0.6	1–2	2–5
	P4	2.0–2.5	5–6	30–60

To identify the type of vortex, Alden Research Laboratory has been referred [20]. The locations for every vortex had been illustrated in Fig. 17.

From the data obtained, based on Case 1 and Case 2, vortices formed at P1 and P2 which had been classified as Type 1 and Type 2 due to weak rotations of flow or slight surface drop on the water surface. However, due to the lower stage (water level), it can be observed that the vortices formed for Case 2 were more significant compared to Case 1 where the duration of vortices formed were longer (2–4 s) compared to the Case 1 (2–3 s). The condition can be due the water level below critical submergence, therefore the possibility of vortex formation is high and more significant [21]. Besides, vortex formation was observed to be quite consistent at the same location for both cases due to the asymmetric flow conditions and abrupt changes in flow direction.

Moving on to Case 3 and Case 4, it can be observed that vortex formed were more severe compared to Case 1 and Case 2. The main factor is due to the position of upstream flow at the side had caused non-uniformly distributed flow pattern along the dam.

It can also be observed for both cases, the vortices formed at P4 were Type 5 and Type 6 which able to pull constant stream of air into intake and may damage the turbine significantly. The durations of the vortices were quite long in period as stated from Table 2, leading to adverse impact to the hydroelectric turbines such cavitation and vibration [22]. Besides, the existence of air core into the intake due to the formation of Type 5 and Type 6 vortex, amount of discharge and electricity generation will reduce [20].

For vortices formed at P1, their durations for Case 3 and Case 4 were longer compared to Case 1 and Case 2 which can be due to the unstable flow pattern. For Case 4, it can

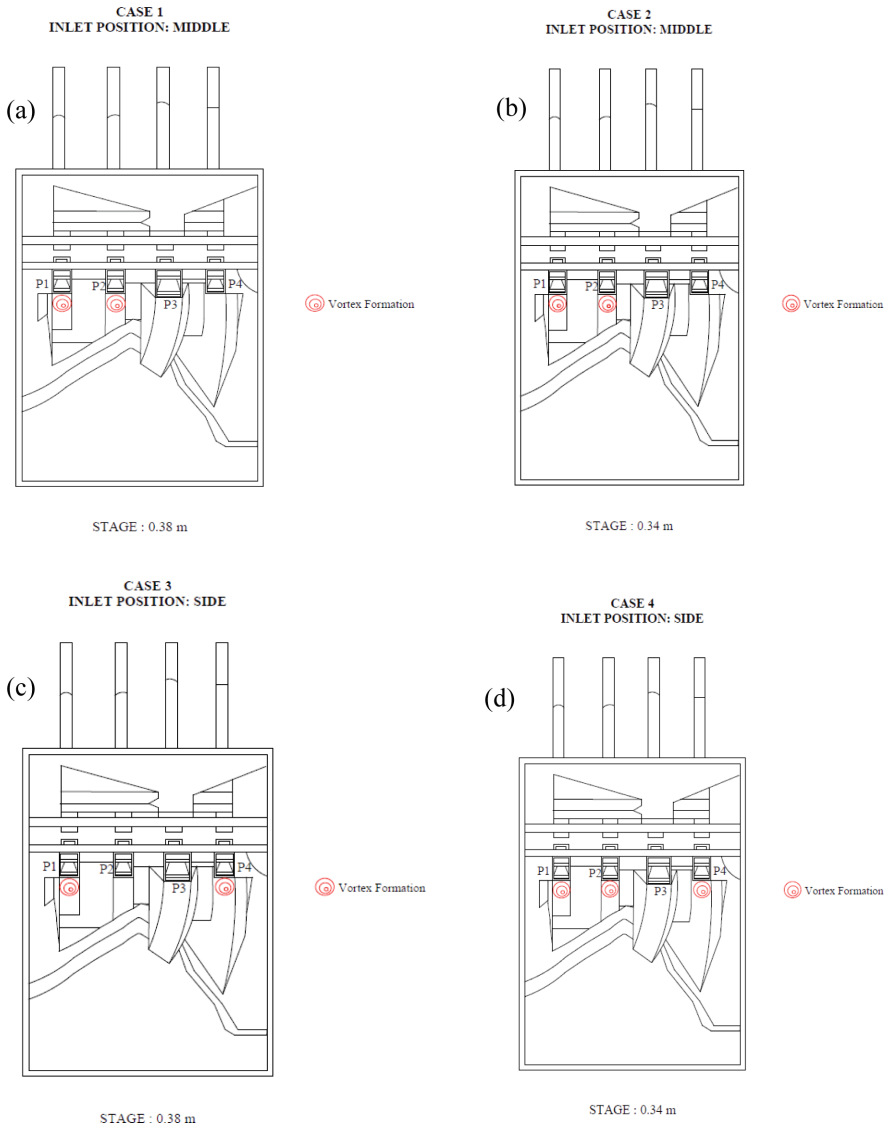


Fig. 17. Location of vortex (a) Case 1; (b) Case 2; (c) Case 3; (d) Case 4.

also be observed that there was another vortex formed at P2 for a period of 2–5 s and this can be due to the condition of lower water level and unstable flow pattern because of the position of upstream inlet.

4 Conclusion

Flow pattern greatly impacts the safety and sustainability of the dam. Based on the contours generated, it had proven that flow pattern is influenced by the position of the upstream inlet, the depth from water level and flowrate of the dam. Position of water inlet from upstream at side had caused non-uniform and unstable flow pattern which adversely impacted the dam. Meanwhile, position of upstream flow at the middle had created more stable flow pattern along the dam. From the flow patterns generated, it can be observed that Case 3 had the maximum velocity of 2.1 m/s at 20% from the water surface. Besides, the range of velocities obtained near the penstocks for all the cases were within 4.1–8.0 m/s. Unstable flow pattern had resulted severe condition of erosion, sedimentation and vortex formation. Upstream flow from side position had caused erosion which occurred alongside the dam as observed in Case 3 and Case 4. Unstable flow pattern due to position of water inlet from side had caused non-uniform distribution of sediment deposition which not only affect the storage but also the stability of the dam. From Case 3 and Case 4, the deposition of sediment which focused on one-side of the dam caused high concentrated load at the region which adversely affect the stability of the dam. Case 3 and Case 4 caused the formation of Type 5 and Type 6 vortices at the dam's penstocks when the upstream flow was from side position. Although vortices (Type 1 and Type 2) were formed in Case 1 and Case 2, the impact due to these vortices were not critical. However, vortices shall be minimized in order to ensure the effectiveness and sustainability of the hydroelectric dam. These vortices which formed shall be reduced by installing anti-vortex inhibitors. Besides, proper mitigation measures have also been proposed in order to improve the efficiency and sustain the dam by minimizing the impacts of sedimentation, erosion and vortex formation at the dam.






References

1. Bharti, M.K., Sharma, M., Islam, N.: Study on the dam & reservoir, and analysis of dam failures: a data base approach. *Int. Res. J. Eng. Technol. (IRJET)* **7**(5), 1661–1669 (2020)
2. Deangeli, C., Giani, G.P., Chiaia, B., Fantilli, A.P.: Dam failures. Dam-break problems, solutions and case studies. *WIT Trans. State Art Sci. Eng.*, 1–50 (2009)
3. Chanson, H.: *The Hydraulics of Open Channel Flow: An Introduction: Basic Principles, Sediment Motion, Hydraulic Modelling, Design of Hydraulic Structures*, 2nd edn. Elsevier Ltd., Australia (2009)
4. Tan, C., Dong, F: Sensor instrumentation for flow measurement. Reference module in biomedical sciences. *Encycl. Sens. Biosens.* **3**, 536–554 (2021)
5. Kantoush, S., Sumi, T.: Influence of stilling Basin geometry on flow pattern and sediment transport at flood mitigation dams. In: *Proceeding of the 9th Federal Interagency Sedimentation Conferences, United States of America*, pp. 115–133 (2010)
6. Hydro Review Homepage: Dealing with sediment: Effects on dams and hydropower generation. <https://www.hydroreview.com/world-regions/dealing-with-sediment-effects-on-dams-and-hydropower-generation/>. Accessed 17 Aug 2022
7. Obialor, C.A., Okeke, O.C., Onunkwo, A.A., Fagorite, V.I., Ehujuo, N.N.: Reservoir sedimentation: causes, effects and mitigation. *Int. J. Adv. Acad. Res.* **5**(10), 92–109 (2019)
8. Zahabi, H., Torabi, M., Alamatian, E., Bahiraei, M., Goodarzi, M.: Effects of geometry and hydraulic characteristics of shallow reservoirs on sediment entrapment. *Water* **10**(12), 1725 (2018)

9. Petkovsek, G., Roca, M.: Impact of reservoir operation on sediment deposition. *Proc. Inst. Civ. Eng. Water Manag.* **167**(10), 577–584 (2014)
10. Akademi Sains Malaysia: ASM Position Paper on Erosion & Sedimentation (2018). <https://www.akademisains.gov.my/asm-publication/asm-position-paper-on-erosion-sedimentation/>
11. Rashid, M.U., Miqdad, H., Hassan, M.S., Haseeb, A.: Evaluation of sediment management strategies for large reservoirs. *Research Square* (2021)
12. International Hydropower Association (IHA): How-to guide: Hydropower erosion and sedimentation. *How-to Guide: Hydropower Erosion and Sedimentation*. <https://www.hydropower.org/publications/hydropower-erosion-and-sedimentation-how-to-guide>. Accessed 17 Aug 2022
13. Mohammad Basri, E., Mohamad Adam, O., Teh, S.Y., Wan Maznah, W.O.: Identification of critical erosion prone areas in Temengor Reservoir Basin using universal soil loss equation (USLE) and geographic information system (GIS). *IOP Conf. Ser. Earth Environ. Sci.* **380**(1), 012011 (2019)
14. Vohat, P., Gupta, V., Bordoloi, T.K., Naswa, H., Singh, G., Singh, M.: Analysis of different interpolation methods for uphole data using surfer software. *Geophysical services, western onshore Basin, ONGC, Vadodara-9*. In: 10th Biennial International Conference & Exposition, Koshi (2013)
15. Kuta, A.A., Ajayi, O.G., Osunde, T.J., Ibrahim, P.O., Dada, D.O., Awaal, A.A.: Investigation of the robustness of different contour interpolation models for the generation of contour map and digital elevation models. In: *School of Environment Technology International Conference, SETIC* (2018)
16. Panchuk, K., Earle, S.: *Physical Geology*, 2nd edn. BCcampus Open Publishing, Canada (2019)
17. DID: *Urban Stormwater Management Manual for Malaysia (MSMA)*, 2nd edn. DID, Kuala Lumpur (2011)
18. Yoosefdoost, A., Lubitz, W.D.: Sluice Gate Design and calibration: simplified models to distinguish flow conditions and estimate discharge coefficient and flow rate. *Water* **14**(8), 1215 (2022)
19. Garg, S.K.: *Hydrology and Water Resources Engineering*. Khanna Publisher, India (2013)
20. Kiviniemi, O., Makusa, G.P.: *A scale model investigation of free surface vortex with particle tracking velocimetry* (2009)
21. Domfeh, M.K., Gyamfi, S.A., Amo-Boateng, M., Andoh, R.Y., Ofosu, E.A., Tabor, G.R.: Free surface vortices at hydropower intakes: – a state-of-the-art review. *Sci. Afr.* **8**, e0035 (2020)
22. Azman, A., et al.: The impact of vortex formation due to the operational dam condition: a review. *IOP Conf. Ser. Mater. Sci. Eng.* **920**(1), 012025 (2020)



Effect of Different Foaming Temperature on Properties of NaHCO₃ – Natural Rubber Latex Foam

Mohammad Syahrin Smail^{1,2} , Zunaida Zakaria^{1,2} , Hakimah Osman¹ ,
Abdulahakim Masa³ , and Anusha Leemsuthep⁴ 

- ¹ Faculty of Chemical Engineering and Technology, Universiti Malaysia Perlis (UniMAP), Arau, Perlis, Malaysia
syahrinsmail@gmail.com
- ² German Geopolymer and Green Technology, Centre of Excellence (CEGeoGTech), Universiti Malaysia Perlis (UniMAP), Arau, Perlis, Malaysia
- ³ Rubber Engineering and Technology Program, International College, Prince of Songkla University, Hat Yai, Songkhla, Thailand
- ⁴ Penchem Technologies Sdn Bhd., Kawasan Perindustrian Bukit Minyak, 14100 Bukit Minyak, Pulau Pinang, Malaysia

Abstract. High volatile fatty acid natural rubber latex foam (H-VFA NRLF) was prepared via the Dunlop process using sodium bicarbonate, NaHCO₃ as the blowing agent. The influence of different foaming temperatures (140 °C, 150 °C, 160 °C, 170 °C, and 180 °C) on relative foam density, average cell size, cell size distribution frequency and compression stress-strain of H-VFA NRLF were studied. The average cell sizes were related to the relative foam density of H-VFA NRLF. As the temperature increased, the relative foam density increased, and eventually the average cell size decreased due to high amount of gas generated by blowing agents simultaneously. Meanwhile, smaller cell sizes were distributed as the temperature increased. It was found that the optimum temperature for H-VFA NRLF was 150 °C due to the lowest relative foam density and significantly larger uniform cell size were produced. Thus, the lowest compression stress up to 60% of strain was found at 150 °C and increased with increasing temperature. The mechanical properties were correlated with the morphology and physical properties of the H-VFA NRLF, respectively.

Keywords: Natural Rubber Latex · Volatile Fatty Acid · Foams · Sodium Bicarbonate · Foaming Temperature · Compressive

1 Introduction

Natural rubber latex foam (NRLF) is typically manufactured directly in liquid form using the Dunlop method since the 1920s [1–4]. It is known that natural rubber latex is a stable colloidal dispersion of latex particles in aqueous medium [5, 6]. The colloidal properties of NRLF depend on a delayed-gelling agent or heat-sensitize gelling agent

to perform colloidal destabilization to set the foam [7–10]. Also, the colloidal system of latex foam consists of an aqueous phase – rubber particles and aqueous phase – air needs to be manipulated to produce the successful latex foam manufacturing [11, 12].

Manufacturing NRLF requires surfactant to maintain its colloidal stability system, which consists of potassium oleate (P.O.) as a foaming agent and diphenyl guanidine (DPG) as a secondary gelling agent, while sodium silicofluoride (SSF) acts as a primary gelling agent that determines the foam's microcellular structure. Long storage natural rubber latex or high-volatile fatty acid (H-VFA) latex is the latex which is typically rejected due to its unsuitability for processing. The pre-gelled high volatile fatty acid natural latex with high viscosity formed due to long preservation and inhibition by microbes. High volatile fatty acids result in the loss of colloidal stability and coagulation of latex where the VFA No. exceeds than 0.06 [13]. Theoretically the colloidal stability system of the H-VFA NRLF can be maintained by using of sodium bicarbonate as blowing agent. This is due to the sodium bicarbonate could breaks down to form sodium and bicarbonate when exposed into the water and thus makes a solution alkaline [14]. Where the mild alkaline properties of this sodium bicarbonate which is like ammonia could stabilize NRL [15]. Over the years, NaHCO_3 has also received increasing attention on rubber foams for applications such as sound absorption, where most open-cell foams are produced using compounds containing sodium bicarbonate as their blowing agent [16]. Furthermore, NaHCO_3 possesses the properties of decomposing endothermically at a wide temperature range between $119\text{ }^\circ\text{C}$ – $188\text{ }^\circ\text{C}$ [17] and is soluble in water making it suitable for use in NRLF [18, 19].

There have been previous studies conducted on the use of sodium bicarbonate as a blowing agent but most of them were used with dry rubber [20–24]. Ariff et al. [25] emphasized that processing parameters including variation of foaming temperatures could yield different foam properties. In their study, higher temperatures caused higher gas decomposition of the blowing agent, thus inducing higher foam cell expansion in natural rubber (NR) foam. Several studies have also reported that different foaming temperatures in EPDM foam with blowing agents increased crosslink density which subsequently produced larger cell size [26]. Accurate determination of foaming temperature is necessary as it can adversely affect the colloidal stability of the lattices to ensure the end properties of the NRLF. However, little effort has been carried out to study the optimum processing temperature of NRLF. Therefore, a study on the decomposition temperature of the blowing agent is essential to understand their effect towards properties of H-VFA NRLF with blowing agent.

In this study, the effects of different foaming temperatures on H-VFA NRLF properties were investigated according to physical properties, including cell morphology, cell size distribution and foam density, as well as mechanical properties such as compression stress-strain of H-VFA NRLF using sodium bicarbonate as the blowing agent.

2 Materials and Methods

2.1 Materials

High volatile fatty acid (H-VFA) latex and other compounding ingredients such as sulphur dioxide (SiO_2), zinc oxide (ZnO), zinc diethyldithiocarbamate (ZDEC), zinc dibutyldithiocarbamate (ZDBC), and antioxidant and diphenyl guanidine (DPG), prepared in dispersion form, were supplied by Zarm Scientific & Supplies Sdn. Bhd. Malaysia. Sodium bicarbonate (NaHCO_3) was used as the blowing agent obtained from AR Alatan Sains (K) Sdn. Bhd., Malaysia. Table 1 shows the alternative formulation of NRLF compound prepared according to 100 parts by weight of rubber (phr).

Table 1. Formulation of NRLF compounds.

Ingredient	Part by Weight	
	Dry Weight	Wet Weight
62% High Volatile Fatty Acid (H-VFA) Latex	100	161.3
50% Sulphur (SiO_2)	2.0	4
50% Zinc Oxide (ZnO)	1.0	2
50% Zinc Diethyldithiocarbamate (ZDEC)	0.5	1
50% Zinc Dibutyldithiocarbamate (ZDBC)	0.5	1
50% Antioxidant	2.0	4
40% Diphenyl Guanidine (DPG)	0.5	1.25
Sodium Bicarbonate (NaHCO_3) added as dry	10	10

2.2 Sample Preparation

High volatile fatty acid natural latex rubber foam (H-VFA NRLF) was prepared using the formulation shown in Table 1. To begin with, the HA latex was measured and poured into the beaker. The natural rubber latex was stirred with a mechanical stirrer at 230 rpm for 30 min. After 30 min, sulphur, ZDEC, ZDBC and antioxidant were poured into the latex, and the stirrer speed was increased to 400–500 rpm for maturation process and left for 2 h. Using a mixer, the latex compounding was thoroughly beaten (about 6 min) and then formed foam up to twice or more than the initial volume. Subsequently, the speed was slowly decreased to obtain finer foam. While stirring and beating continuously for 90 s, ZnO and DPG were added to the NRLF compounding. Sodium bicarbonate was then added to the foam for 45 s with continuous stirring and immediately poured into the mold, followed by simultaneous curing and foaming in an air circulating oven at different temperatures of 140 °C, 150 °C, 160 °C, 170 °C and 180 °C for 45 min. The cured foam was stripped from the mold and washed thoroughly. After washing, the cured NRLF was dried in an air circulating oven at 60 °C for 2 h.

2.3 Morphology

The morphology of H-VFA NRLF was observed using scanning electron microscope (SEM) model TM 3000. ImageJ was used to analyze and measure the average cell size of the H-VFA NRLF. The foam surface was razor cut perpendicular to the direction of foaming and covered with soot. The average cell size of the foam cell was evaluated from 300 measurements and the cell distribution frequency was calculated.

2.4 Relative Foam Density

The relative foam density was measured according to ASTM D3575 using Eq. (1).

$$\rho^* = \frac{\rho_f}{\rho_s} \quad (1)$$

where ρ^* is the relative density of the foam, ρ_f is NRLF foam density, and ρ_s is NRLF solid density.

2.5 Compression Stress-Strain

A crosshead speed of 25 mm/min was used in accordance with ASTM D575-91. Five samples of latex foam were prepared with dimensions of 30 mm × 30 mm × 30 mm from different batches were deflected to a maximum strain to produce compression strains up to 80% between two parallel flat plates.

3 Results and Discussion

3.1 Relative Foam Density

Variations of relative foam density with different foaming temperatures are shown in Fig. 1. It can be perceived that the relative foam density of the NRLF increased as the foaming temperature increased. It was assured that the decrease in the relative density could involve the cell wall thickness and the presence of excess matrix in the H-VFA NRLF. As cells continue to grow in the continuous aqueous phase due to higher colloidal destabilization/cure rate at higher temperatures, the cells are restricted to growth and form certain smaller open-cells interconnected with each other. Besides, sodium bicarbonate used releases carbon dioxide gas during its decomposition, and this will produce an open cell structure [18, 26]. Smaller open-cells interconnected are formed due to the inability of the foam to hold the gas and thus rupture or coalesce with each other to form cell opening [28, 29]. Furthermore, this also due to the high curing rate was occur at high temperature thus restricted the free expansion of foam [30]. Thus, more open-cells in smaller size accumulate in the continuous phase at higher temperatures which suppresses foam formation and then leaves an excess of the matrix. Meanwhile, the lowest relative foam density was observed at 150 °C. This indicated that the cell foams expanded and combined to form larger cell size which relatively contributed to lower relative density of the NRL foam. This was consistent with results of morphology and cell distribution of H-VFA NRLF.

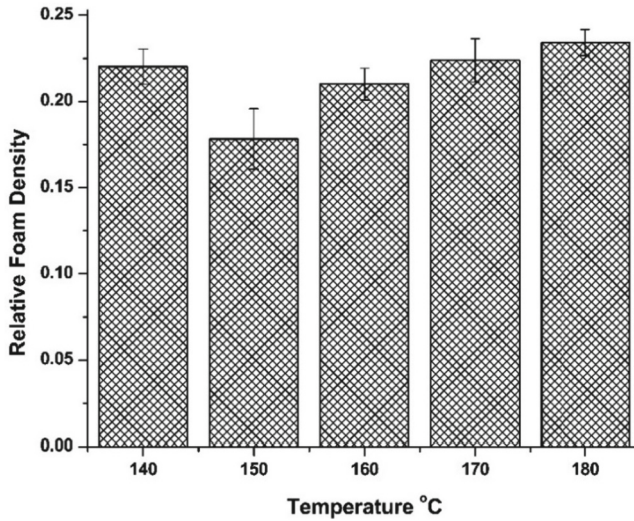


Fig. 1. Relative foam density of H-VFA NRLF at different foaming temperatures.

3.2 Average Cell Size

Figure 2 shows the plot of average cell size of H-VFA NRLF with SEM images and supported by cell distribution frequency of each sample as shown in Fig. 3 (a)–(e) at different foaming temperatures.

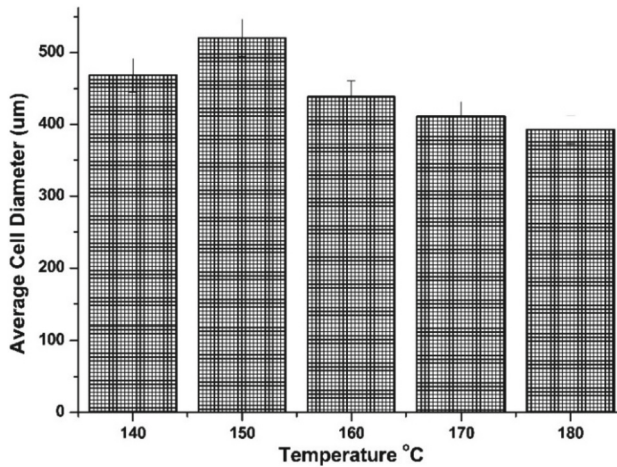


Fig. 2. Average cell diameter of the H-VFA NRLF at different foaming temperatures.

Clearly, the average cell size of NRL foam increased up to 150 °C and then decreased for further foaming temperature increases. It was found that larger cell size of H-VFA NRLF was produced at foaming temperature of 150 °C (Fig. 3 (a)). Moreover, the cell

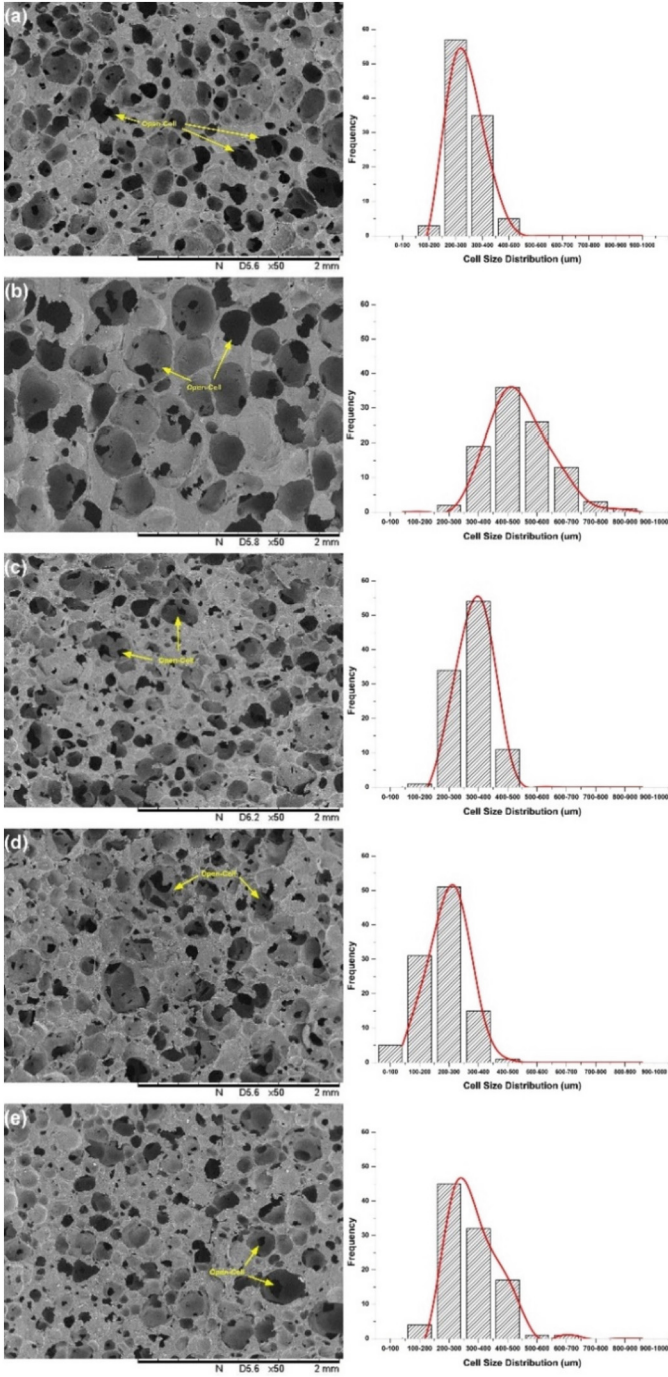


Fig. 3. SEM micrograph images of cell size distribution of H-VFA NRLF at different forming temperatures; (a) 140 °C, (b) 150 °C, (c) 160 °C, (d) 170 °C and (e) 180 °C.

size distribution at 150 °C resulted in a wider range to the right indicating mainly uniform large cell size as shown in Fig. 3 (b). This may be due to the relatively low colloidal destabilization/cure rate during heating on the colloid latex which allowed cell formation to contact and combine. As the temperature increases, the cell formation was restricted due to fast curing rate. Besides, Zhang et al. [31] and Kajon et al. [32] explained that at high foaming temperature, the cells are smaller because of the limited gas solubility in the polymer. According to Fasihi and Targhi [33], temperature rise will adversely affect the viscosity and curing rate of natural rubber foam.

In Fig. 3 (c)–(e), it can be clearly observed that the foam structure produced was an open cell at all temperatures. The distribution of the cell size formerly became narrowed and shifted towards left as the temperature increased, indicating that each cell size decreased. This was likely due to the decomposition of blowing agent occurring simultaneously at higher foaming temperatures and leading to a smaller cell size distribution above 150 °C. From Kim et al. [20] rubber foams result in larger cell size as the temperature increases. This situation contrasted with H-VFA NRLF which was influenced by rapid destabilization or high cure rate of NRLF colloidal system associated with more gases generated from blowing agent decomposition at higher temperatures. Furthermore, when the polymer viscosity decreases via a temperature increase, the rate of cell growth increases because of the decrease in resistance against it [34]. Consequently, the cells were restrained from further expansion forming smaller open-cell sizes in the continuous aqueous phase of the colloidal system. Overall, the data obtained for the effects of different foaming temperatures on the morphology of NRLF supported the qualitative findings depicted in Fig. 1.

3.3 Compressive Stress

Figure 4 summarizes the effects of different foaming temperatures on the compressive stress–strain of H-VFA NRLF. It can be seen that the compressive stress increased as the foaming temperature increased. NRL foam at 150 °C exhibited the lowest stress among other foaming temperatures with compressive modulus 0.642 MPa. This was due to larger and uniform distribution of cell size at 150 °C as previously discussed, which subsequently provided less resistance to buckling and collapse, thus decreasing the modulus. Meanwhile, the increase in stress for foaming temperatures above 150 °C was influenced by the smaller open–cells formation packed together, which offered stiffness to the NRL foam. This is further supported by the observation of morphology in Fig. 3, the sample produced at 150 °C dominants with gas phase, meanwhile the sample at 180 °C is solid phase dominant.

This can be seen from Table 2 at temperature 180 °C presents high compressive stress at all strains. On the contrary, temperatures below 150 °C demonstrated predominantly smaller cell distribution present in the H-VFA NRLF that increased stress. Furthermore, it can be observed in Fig. 5 (a) that the linear elasticity region for NRL foam cells at each temperature started to bend in 20% strain.

Moreover, the cell walls then collapsed as the elastic buckling stage was above 20% strain. Significant changes of NRL foam at 150 °C can be seen during the progressive cell collapse due to larger cell size and almost similar to the others with increasing foaming temperature below 150 °C as shown in Table 2, respectively.

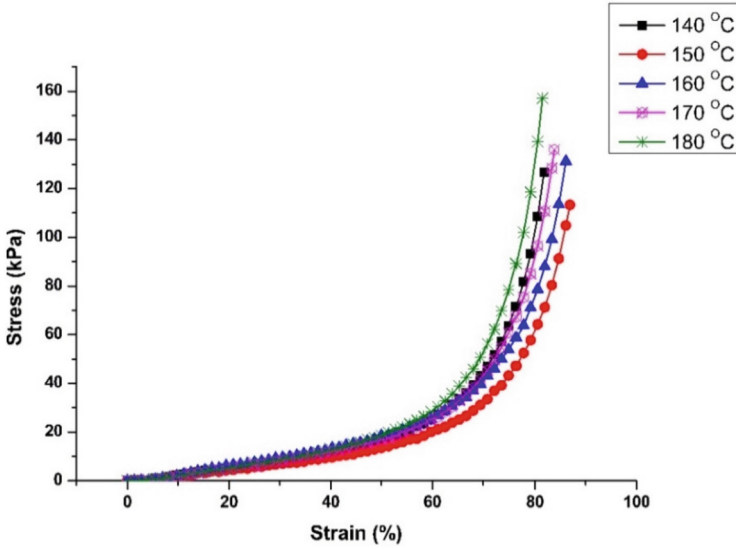


Fig. 4. Compressive stress of H-VFA NRLF at different foaming temperatures.

Table 2. Data for compression stress – strain of the H-VFA NRLF at different foaming temperatures.

H-VFA NRLF Compressive Stress	Temperature (°C)				
	140	150	160	170	180
Compression Strength (MPa)	0.188 ± 0.023	0.116 ± 0.004	0.136 ± 0.050	0.138 ± 0.018	0.168 ± 0.010
Compression Modulus (MPa)	1.109 ± 0.164	0.642 ± 0.012	0.764 ± 0.038	0.779 ± 0.013	0.919 ± 0.038
At 20% strain rate (kPa)	6.177 ± 1.202	4.345 ± 0.353	5.086 ± 1.742	4.557 ± 0.320	6.260 ± 0.878
At 60% strain rate (kPa)	28.436 ± 3.605	21.755 ± 1.476	23.733 ± 4.432	23.689 ± 2.016	32.047 ± 3.696

This may be contributed by the smaller cells size produced at temperatures above 150 °C by increasing the stress from the bend and extending or contracting the cell membranes until ruptured.

According to Prasopdee & Smitthipong [35], the pore sizes structure significantly influenced the properties of their elasticity. The decrease in cell sizes (smaller cell sizes) to some extent could increase the stiffness of the foam. Moreover, the interconnected foam matrix also affects the mechanical properties of H-VFA NRLF not only depending on the morphological properties [34].

In addition, it was postulated that densification region occurred when the opposing cell walls collapsed in contact with each other and further strain compressed the solid

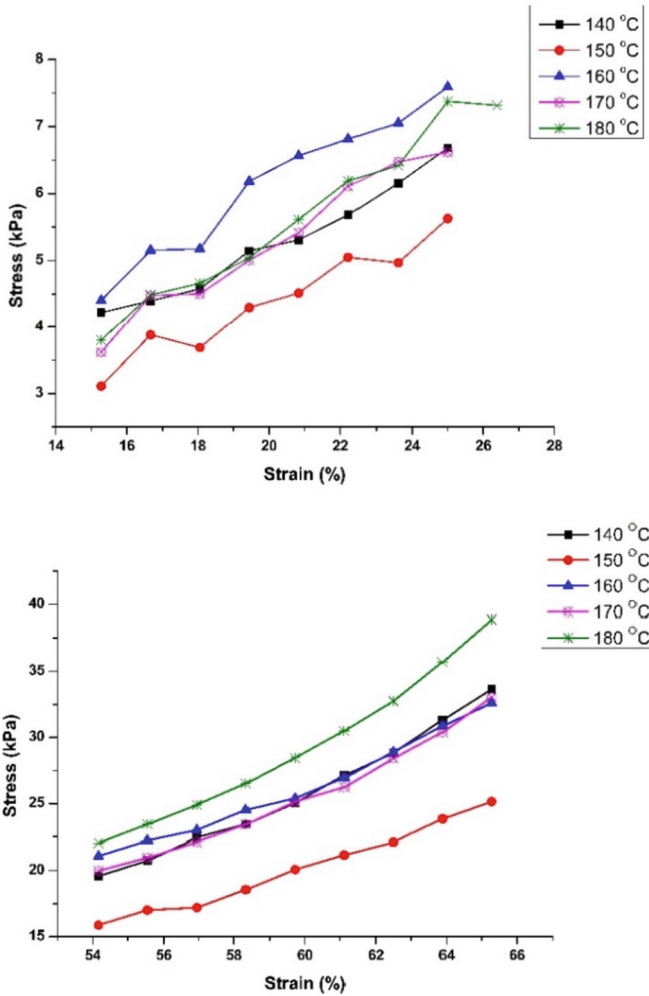


Fig. 5. Compression stress – strain at: (a) 20% strain (kPa); (b) 60% strain (kPa) of the H-VFA NRLF.

NRL foam, obtaining a rapidly increasing stress [37]. This is the strain at which all the interconnected open porous cells space has been collapsed and known as the densification regime [38]. This occurred at strain above 60% as depicted in the compression stress-strain (Fig. 5 (b)). Therefore, the changes in the compression stress-strain properties of H-VFA NRLF can be appreciated in the densification region trend which further supported the morphological and density properties.

4 Conclusion

The effects of different foaming temperatures on the properties of NaHCO₃-H-VFA NRLF were examined. It was found that the relative density of H-VFA NRLF increased with increasing foaming temperature. As the temperature increased, more excess matrixes were formed in relation to the average cell size. From the results obtained, the cell size decreased as the uniformly distributed cell size was smaller. It was evidenced from the compression stress-strain results, that progressive increase of stress occurred as the temperature increased. However, the foaming temperature at 150 °C had the greatest influence on the foam density, followed by cell size morphology and compression stress-strain. It is suggested that future work will seek to involve viscosity and crosslink density which could improve the foundation in the future.

Acknowledgments. The authors would like to thank the Department of Higher Education, Ministry of Higher Education (MOHE) for funding this research through the RAGS with the grant number 9018-00065. The authors also would like to acknowledge all the team members in Faculty of Chemical Engineering & Technology, University Malaysia Perlis (UniMAP) for their guidance and help.

References

1. Blackley, D.C.: Latex foam rubber. In: Blackley, D.C. (ed.) *Polymer Latices: Science and Technology Volume 3: Applications of Latices*, 2nd edn., pp. 229–326. Springer, Dordrecht (1997). https://doi.org/10.1007/978-94-011-5848-0_4
2. Ramasamy, S., Ismail, H., Munusamy, Y.: Aqueous dispersion of rice husk powder as a compatible filler for natural rubber latex foam. *Adv. Mater. Res.* **626**, 530–536 (2013)
3. Karim, A.F.A., Ismail, H., Ariff, Z.M.: Properties and characterization of kenaf-filled natural rubber latex foam. *BioResources* **11**(1), 1080–1091 (2016)
4. Suethao, S., Phongphanphanee, S., Wong-Ekkabut, J., Smitthipong, W.: The relationship between the morphology and elasticity of natural rubber foam based on the concentration of the chemical blowing agent. *Polymers* **13**(7) (2021)
5. Ramasamy, S., Ismail, H., Munusamy, Y.: Effect of rice husk powder on compression behavior and thermal stability of natural rubber latex foam. *BioResources* **8**(2), 4258–4269 (2013)
6. Ramasamy, S., Ismail, H., Munusamy, Y.: Tensile and morphological properties of rice husk powder filled natural rubber latex foam. *Polym. Plast. Technol. Eng.* **51**(15), 1524–1529 (2012)
7. Phomrak, S., Nimpaiboon, A., Newby, B.M.Z., Phisalaphong, M.: Natural rubber latex foam reinforced with micro- and nanofibrillated cellulose via Dunlop method. *Polymers* **12**(9), 1–16 (2020)
8. Norhazariah, S., Azura, A.R., Azahari, B., Sivakumar, R.: Preliminary study of semi-refined carrageenan (SRC) as secondary gelling agent in natural rubber (NR) latex foam. In: *AIP Conference Proceedings*, vol. 1901 (2017)
9. Roslim, R., Hashim, M.Y.A., Augurio, P.T.: Natural latex foam. *J. Eng. Sci.* **8**, 15–27 (2012)
10. Roslim, R., Mok, K.L., Fatimah Rubaizah, M.R., Shamsul, K., Tan, K.S., Amir Hashim, M.Y.: Novel deproteinised natural rubber latex slow-recovery foam for health care and therapeutic foam product applications. *J. Rubber Res.* **21**(4), 277–292 (2018)
11. Rostami-Tapeh-esmaeil, E., Vahidifar, A., Esmizadeh, E., Rodrigue, D.: Chemistry, processing, properties, and applications of rubber foams. *Polymers* **13**(10), 1–53 (2021)

12. Sirikulchaikij, S., Kokoo, R., Khangkhamano, M.: Natural rubber latex foam production using air microbubbles: microstructure and physical properties. *Mater. Lett.* **260** (2020)
13. Narongwongwattana, S., Rittiron, R., Lim, C.H.: The rapid determination of volatile fatty acid number in para rubber latex using fourier transform-near infrared spectroscopy based on quantification and discrimination model. *J. Innov. Opt. Health Sci.* **8**(05), 1550042 (2015)
14. Medical New Today. <https://www.medicalnewstoday.com/articles/314932>. Accessed 12 May 2023
15. Chaiya, P., Phaechamud, T.: Theophylline extended-release monolithic matrix comprising natural rubber latex as binder. *IOP Conf. Ser. Mater. Sci. Eng.* **1234**(1), 012001 (2022)
16. Harnnarongchai, W., Chaochanchaikul, K.: Effect of blowing agent on cell morphology and acoustic absorption of natural rubber foam. *Appl. Mech. Mater.* **804**(1), 25–29 (2015)
17. Luo, D., et al.: Modification of sodium bicarbonate and its effect on foaming behavior of polypropylene. *E-Polymers* **21**(1), 366–376 (2021)
18. Hussein, M.S., Leng, T.P., Rahmat, A.R., Zainuddin, F., Keat, Y.C.: The influence of sodium bicarbonate loading as blowing agent on the properties of epoxy foam. *Solid State Phenom. SSP* **280**, 270–276 (2018)
19. Tangboriboon, N., Pannangetch, W., Aranyik, K., Petcharoen, K., Sirivat, A.: Embedded eggshells as a bio-filler in natural rubber for thermal insulation composite foams. *Prog. Rubber Plast. Recycl. Technol.* **31**(3), 189–206 (2015)
20. Phiri, M.M., Sibeko, M.A., Phiri, M.J., Hlangothi, S.P.: Effect of free foaming and pre-curing on the thermal, morphological and physical properties of reclaimed tyre rubber foam composites. *J. Clean. Prod.* **218**, 665–672 (2019)
21. Nasruddin, Bondan, A.T., Agustini, S.: The effect of sodium bicarbonate ratio for the mechanical properties of underarm pads rubber for crutches. *IOP Conf. Ser. Mater. Sci. Eng.* **980**(1) (2020)
22. Kim, J.H., Choi, K.C., Yoon, J.M.: The foaming characteristics and physical properties of natural rubber foams: effects of carbon black content and foaming pressure. *J. Ind. Eng. Chem.* **12**(5), 795–801 (2006)
23. Ariff, Z.M., Rahim, N.A.A., Low, L.C.: Effect of compound formulation on the production and properties of epoxidised natural rubber (ENR-25) foams. In: *Polymer Processing Society 24th Annual Meeting*, M. (2008)
24. Tangboriboon, N., Rortchanakarn, S., Petcharoen, K., Sirivat, A.: Effects of foaming agents and calcium carbonate on thermo-mechanical properties of natural rubber foams. *Polimeri* **35**(1), 10–17 (2015)
25. Ariff, Z.M., Zakaria, Z., Tay, L.H., Lee, S.Y.: Effect of foaming temperature and rubber grades on properties of natural rubber foams. *J. Appl. Polym. Sci.* **107**(4), 2531–2538 (2008)
26. Zakaria, Z., Mohamad Ariff, Z., Lee Hwa, T., Stephen Sipaut, C.: Effect of foaming temperature on morphology and compressive properties of ethylene propylene diene monomer rubber (EPDM) foam. *Malays. Polym. J. (MPJ)* **2**(2), 22–30 (2007)
27. Najib, N.N., Ariff, Z.M., Bakar, A.A., Sipaut, C.S.: Correlation between the acoustic and dynamic mechanical properties of natural rubber foam: effect of foaming temperature. *Mater. Des.* **32**(2), 505–511 (2011)
28. Yamsaengsung, W., Sombatsompop, N.: Effect of chemical blowing agent on cell structure and mechanical properties of EPDM foam, and peel strength and thermal conductivity of wood/NR composite-EPDM foam laminates. *Compos. B Eng.* **40**(7), 594–600 (2009)
29. Timpano, C., Abdoli, H., Leung, S.N., Melenka, G.W.: Characterization of open-cellular polymeric foams using micro-computed tomography. *Polymer* **202**, 122628 (2020)
30. Bayat, H., Fasihi, M.: Curing characteristics and cellular morphology of natural rubber/silica composite foams. *Polym. Bull.* **77**(6), 3171–3184 (2020)
31. Zhang, Y., Rodrigue, D., Ait-Kadi, A.: High-density polyethylene foams. I. Polymer and foam characterization. *J. Appl. Polym. Sci.* **90**(8), 2111–2119 (2003)

32. Kajon, S., Somsongkul, V., Suwanna, P.: Development of natural rubber latex foam for hand exercising application. *Key Eng. Mater. KEM* **861**, 154–158 (2020)
33. Fasihi, M., Targhi, A.A.: Investigation of material characteristics and processing conditions effects on bubble growth behavior in a physical foaming process. *E-Polymers* **16**(5), 387–394 (2016)
34. Ariff, Z.M., Afolabi, L.O., Salmazo, L.O., Rodriguez-Perez, M.A.: Effectiveness of microwave processing approach and green blowing agents usage in foaming natural rubber. *J. Mater. Res. Technol.* **9**(5), 9929–9940 (2020)
35. Prasopdee, T., Smitthipong, W.: Effect of fillers on the recovery of rubber foam: from theory to applications. *Polymers* **12**(11), 1–17 (2020)
36. Notario, B., Pinto, J., Rodríguez-Pérez, M.A.: Towards a new generation of polymeric foams: PMMA nanocellular foams with enhanced physical properties. *Polymer* **63**, 116–126 (2015)
37. Suethao, S., Ponloa, W., Phongphanphanee, S., Wong-Ekkabut, J., Smitthipong, W.: Current challenges in thermodynamic aspects of rubber foam. *Sci. Rep.* **11**(1), 1–12 (2021)
38. Messinger, R.J., Marks, T.G., Gleiman, S.S., Milstein, F., Chmelka, B.F.: Molecular origins of macroscopic mechanical properties of elastomeric organosiloxane foams. *Macromolecules* **48**(14), 4835–4849 (2015)



Mapping of Geological Structures: Potential Geohazards in Tropical Highlands

Nurfirdaus Sapawie¹ , Afikah Rahim¹ , Nazri Ali¹ , Hamzah Hussin² ,
Nor Shahidah Mohd Nazer³ , Agus Winarno⁴ , Deddy Tenggara⁵ ,
and Asmawi Hisham¹ 

¹ Faculty of Civil Engineering, Universiti Teknologi Malaysia, 81310 Johor Bahru, Malaysia
m.nurfirdaus98@gmail.com

² Department of Geoscience, Faculty of Earth Science, Universiti Malaysia Kelantan,
17600 Jeli, Kelantan, Malaysia

³ Department of Earth Sciences and Environment, Universiti Kebangsaan Malaysia,
43600 Bangi, Malaysia

⁴ Department of Mining Engineering, Faculty of Engineering, Mulawarman University,
Samarinda 75119, Indonesia

⁵ Kampus Tunjung Nyaho, Yos Sudarso Street, Palangka Raya City, Kalimantan Tengah
73112, Indonesia

Abstract. Landslides in tropical hilly terrain have become a threat to the community. The difficulty of predicting future landslides can be overcome by detecting signs of past landslides especially in tropical hilly terrain like Cameron Highland, Pahang Darul Makmur. Basic skills in geomorphology and remote sensing are needed in detecting and mapping past landslides due to its geomorphological features that have been modified because of erosion, weathering, and development. However, an approach by using remote sensing and Geographic Information System techniques, the detection of geomorphological features can be done. Among the features that can be seen is hummocky topography, existence of articulating head scarps, crowns, main scarp, side scarps and convex hillslopes followed by concave hillslopes. The activation of inactive landslides is usually caused by natural factors and human factors. Natural factors consist of high rainfall distribution which weakens the soil structure and causes physical and chemical weathering process or rate to increase. About 40% of slopes in the study area with the steepness of 25° which is identified as the main natural factor to slope failures. Human factors comprise of the construction of permanent and large-scale infrastructure which exerts load hence weakening the slope strength. This causes a growth of tension cracks which are perpendicular to the slope face and is expanding up to this day.

Keywords: Landslide · Geohazard · Slope failure

1 Introduction

Research related to landslide in Gunung Pass, Cameron Highlands have actively been studied [1–6]. Various parties had proposed multiple methods in predicting and mitigating the potential dangers of such landslides.

The study area covers the Cameron Highland district in Pahang Darul Makmur. Gunung Pass is located at the border between Pahang and Perak. The location is approximately 31 km from Tanah Rata and 46 km from Ringlet. This study focuses on Gunung Pass which is commonly known as FT185 Simpang Pulai-Cameron Highland Road. This road was built as an alternative to access Cameron Highland from Perak. The construction of paved road by the cut slope of Gunung Pass had caused reactivation of past landslides which disturbs the stability of the slope. This location was chosen due to past histories of previous landslides which can be seen clearly using Google Maps. This study is important to obtain the latest information regarding geological aspects based on remote sensing observations and identifying early signs of geohazards to alert the public.

Highlands with tropical climate are prone to geohazards such as landslides and flooding. This causes destruction of public properties, disruption of daily activities, and a danger to the public. In this research, the word geohazard refers to an occurrence that is hazardous and could potentially be a geo-disaster. Geo-disasters on the other hand refers to an event of a geologically related disaster.

2 General Geology

Peninsular Malaysia is divided into three longitudinal belts, Western, Central and Eastern based on the geology and rock distribution. Cameron Highland is at the eastern side of the Main Range Granite of Peninsular Malaysia, or commonly known as the Titiwangsa Mountains. According to the geological map of Peninsular Malaysia, Cameron Highland and Gunung Pass comprise of two main lithologies which are: igneous and metamorphic rocks. These metamorphic rocks originated from sedimentary rocks which were intruded by granitic body during Upper Triassic [7].

Jamaluddin and Hassan [8] described the igneous rocks in Ringlet, Cameron Highland as granite biotite with hypidiomorphic coarse grain. This granite biotite contains quartz, feldspar, and black spots which is believed to be biotite and/or tourmaline. Krähenbuhl [9] described the granitoid to be brittle to ductile rocks due to fault zone deformation. The feldspar is disturbed and filled with quartz and albite. K-feldspars are mostly perthite, cross mixture with chlorite/muscovite shows growth of pseudomorphic (amphibole?); zoned plagioclase with saussurite core, muscovite absent, tourmaline growth present.

Metasedimentary rocks in the study area have obvious and perfect schistosity. Zaid et al. [10] states that there are three types of schists in Gunung Pass namely Quartz-Mica Schist, Quartz Schist and Garnet-Mica Schist. (a) Quartz-Mica Schist which has the lowest metamorphic grade where muscovite and biotite forms foliation, quartz mineral has strain and wavy distinction, and oxidized iron exist as accessory mineral. (b) Quartz Schist has the same structure as quartz-mica schist where the only difference is the quartz mineral percentage is over 80% in the quartz schist. Biotite and muscovite exist in plates and forms foliation. However, some muscovite plates are second generation minerals. (c) Garnet-Mica Schist is described by the presence of porphyroblastic garnets, and this disrupts the schistosity of the rock which is formed by plates of biotite and muscovite.

3 Geohazardous Natural Terrain

Hussin et al. [11] defines geohazards as geologically related events which are threatening to the public, properties, and the environment. Article [12] defines geohazard as a geological process or phenomenon that can cause loss of lives, injuries and health complications, damage to public properties, loss of livelihood and services, social and economic disruption, and destruction of the environment. The processes and phenomena include internal earth processes such as earthquakes, volcanic activities, and related geophysical processes – mass movement, landslides, rock slips, and debris/mud flows. Landslides are disastrous events that affect to the people, public properties, and social activities even though no accurate statistics obtained, the frequency of slope failures and landslides are related closely to the growth of infrastructure in hilly terrains [13]. Slope failures are the aftermath of geomorphological, hydrological, and geological conditions that is caused by geodynamic processes, plants and human activities, rainfall distribution and seismicity [14] due to various shapes of slope failures, [15] defines slope failure as a complex phenomenon and has many causing factors. Cruden and Varnes [16] defines landslides as downwards movement of rock body, earth, or debris where gravity and water are the main cause of this geomorphological process [17]. Záruba, and Mencl [18] also defined landslides as rapid sliding movements of a layer of rock separated from the base a stationary slope. Landslides are often associated with unstable slope structure, uncontrolled human activity in hazard prone area and chemical watering which weakens the body. Komoo and Lim [19] refers landslides in natural tropical terrain such as in Malaysia can be found in units, systems, or complexes.

4 Methodology

Assessing landslide hazards is a complex method that requires a combination of different techniques and methodology. A flow chart of the methodology of this study is shown in Fig. 1.

4.1 Geomorphology of Landslides

Old landslides are landslides that might have happened tens to hundreds of years ago and can be reactivated by main factor or other factors. To understand previous landslides, the basic principle of geology “uniformitarianism” [20] must be applied which is the past and present is the key to the future. This principle clearly shows that slope failure, either happening in the past or future will show the same features as present landslides. However, these features will not last forever due to the tropical climate and will disappear due to erosion, weathering, and vegetation growth.

Usually, a landslide will produce some notable features and most of them can be identified, class and mapped on field or through aerial photograph [16]. Most features left behind are morphological features such as changes in the shape, position, or appearance of topography [21].

Though these features are difficult to find on field, main features can be identified through the landscape of the landslide itself in natural terrain. These main features include

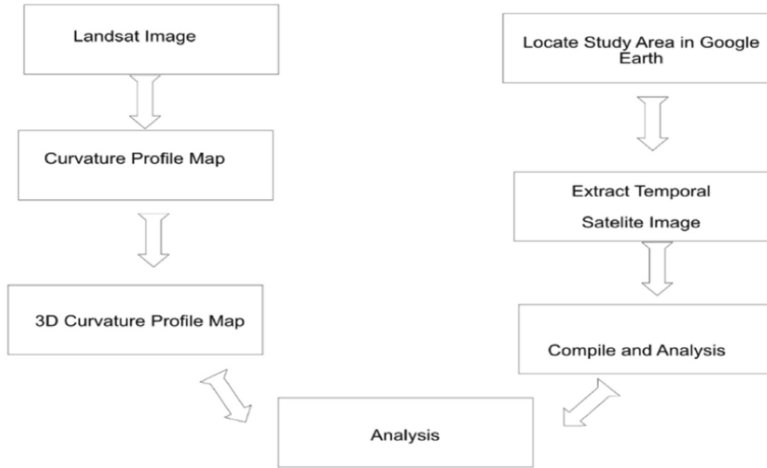


Fig. 1. Methodology of the study.

crown, main scarp, longitudinal cracks, zone of depletion and zone of accumulation. According to [21], the features that will be the main clues to detect old landslides are the crown, curved scarps on the head or foot, side scarps, convex slopes followed by a concave topography and hummocky at the slope foot. Other features include presence of colluvium accumulation on the slope foot, Y-shaped drainage at the head of the slope, step like morphology and vegetation density can be used as clues to assist in identifying old landslides. Other geomorphological features are present as well such as cracks, grabens, ponds, vegetation displacements and other changes in morphology can be used as additional information to estimate a landslide activity. Remote sensing by satellite image is used in this study to identify old landslides.

Evaluation is made according to guidelines prepared by [21] which focuses on certain factors; (1) topography and geomorphology, (2) streams and drainage, and (3) vegetation growth.

5 Geohazards in Tropical Highlands – Gunung Pass, Cameron Highland

Landslides are a natural phenomenon that constantly becomes a threat to the public. Obviously, a new landslide can easily be mapped by observing the “wound” itself. However, time heals only the pain but never the scars. In this study, Gunung Pass and Cameron Highland were chosen due to their history with landslides and still show significant movements until today. Image satellites from Google Earth were used to conduct the observations and analysis was done through Geographic Information System (GIS) software.

5.1 Topographic Features

Gunung Pass has a hilly topography and receives high volumes of downpour annually hence promotes mechanical and chemical weathering. Figure 2 shows the curvature profile of Gunung Pass generated by ArcMap 10.5. The map portrays the geometry of Gunung Pass by showing the positively curved area marked in green and negatively curved area marked in red. Areas marked in yellow are considered neutral or planar. The map shows that both sides of Gunung Pass have similar and repetitive curvature patterns which are negative-neutral-positive -neutral. This pattern can be used as evidence of mass movement happening periodically.

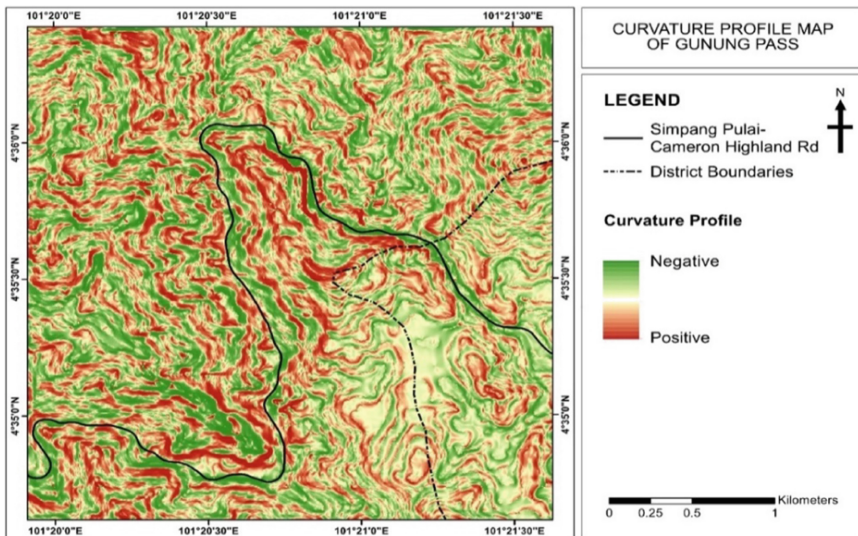


Fig. 2. Curvature Profile Map of Gunung Pass.

According to [22], a slope with convex topography has the highest stability followed by planar slopes and concaved slopes are the least stable. These convex-concave slopes are often associated with the presence of depletion and accumulation zones of a landslide. Figure 3 shows a three-dimensional view of the western side of Gunung Pass. Concaved slopes can be seen more often by the cut slope compared to convexed slopes. These poor stability slopes might be caused by the construction of the highway (black). A similar pattern can be seen at the eastern side where concaved slopes are more dominant by the roadside compared to convex slopes. The presence of both these features can be related to depletion zone and accumulation zone of a landslide. The convex slope might be caused by past landslide activity which results in mass movement on the foot slope thus creates a concaved slope. The eastern side (Fig. 4) shows a very similar pattern to the western side. These patterns may have been caused by the construction of Simpang Pulai-Cameron Highland Road which might have affected the stability of the slope itself.

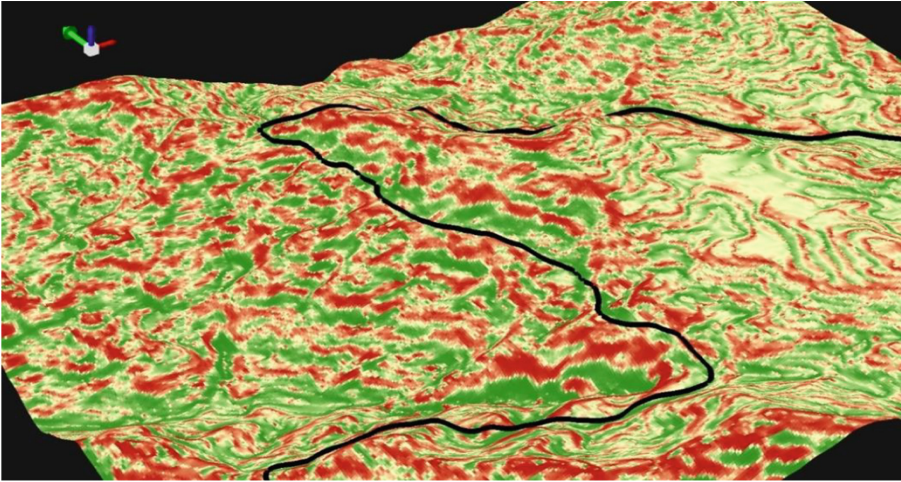


Fig. 3. Three-Dimensional view of Gunung Pass (west) overlain by the Curvature Profile Map.

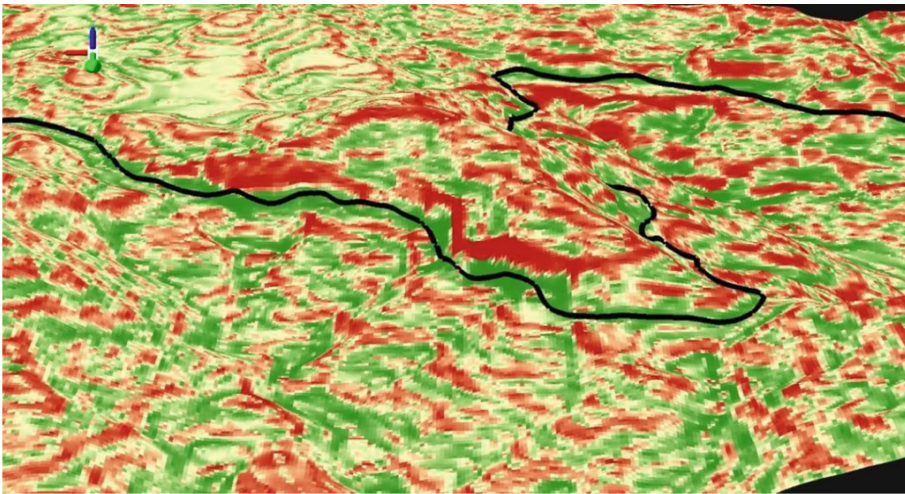


Fig. 4. Three-dimensional view of Gunung Pass (east) overlain by Curvature Profile.

5.2 Secondary Vegetation

Vegetation growth can be a key indicator to identifying geohazards in natural hilly terrains such as Cameron Highland. Secondary vegetation growth is often younger and more sparse compared to other plants surrounding them. This vegetation coverage can be seen clearly through satellite images.

The trend in vegetation coverage can be observed by analyzing the boundaries of secondary vegetations through past satellite images. Figure 5 shows the trend of vegetation growth on past landslides using satellite images from the year 2001 to 2019.



Fig. 5. Trend in vegetation coverage of Gunung Pass from 2001 to 2019.

A landslide event in 2001 had caused a bald spot in the incident area. Restoration has been done in 2008 by building terraces to reduce the risk of future landslides. In 2015, secondary vegetation starts to partially cover the scars left by the 2001 landslide and covers entirely in 2019. A small slope failure occurred in 2015 caused a few sparse spots in the area. These spots begin to be covered up by second generation of secondary vegetation in 2019.

5.3 Factors Causing Landslide Geohazard

A slope is considered a failure when the build material detaches away from the surface of the slope. A slope failure can happen due to various factors such as its build material, rate of movement, failure mechanism, shape, and geometry of the failure [23]. A landslide can occur either naturally or caused by human interference.

Natural Factors. A naturally induced landslide can be broken down into a few aspects which includes the climate, geology, and natural disasters. Cameron Highland has a

hilly topography and receives high volumes of downpour annually. The mean monthly downpour in Cameron Highland can be up to 2500 mm to 3000 mm. Rainfall, which is a weathering agent, speeds up the oxidation and degeneration rates of a rock body thus turns hard solid rocks into loose soil units. These promote erosion hence weakens the stability of the slope. Naturally steep slopes in Cameron Highlands can also be a factor. The steeper the slope is, the less stable it becomes. An analysis of the slope steepness map shows about 40% of slopes in Gunung Pass have a steepness of more than 25%. These areas of very steep slopes are dominant on the western side of Gunung Pass and worryingly very close to the roadside.

Man-Made Factors. Slope failure caused by human interference can neither be detected by laboratory nor field test. These factors can only be observed through field investigations [23]. However, these factors can also be observed on a large scale by using satellite images. Large scale constructions can cause a disturbance to the stability of a certain slope.

Figure 6 shows the evolution of tension cracks on the eastern side of Gunung Pass.



Fig. 6. Trend in tension cracks of Gunung Pass from year 2001 to 2019.

This disturbance weakens the natural structure of the slope thus causing growth of tension cracks. The crack will grow larger due to overburden and erosion and eventually cause slope failure.

These thin cracks can be seen rapidly growing perpendicularly to the face of the slope and eventually cause a potentially massive failure to the slope in the future.

6 Discussion

Landslides are a type of natural terrain geohazard in tropical highlands. Either small or large, this geohazard is very hazardous and disastrous if reactivated. Landslides may exist in forms of units, system and complexes and can be classified based on its geomorphic cycle, which is new landslides, adolescence, mature and old. These classifications are based on geometry, geomorphic features, physical characteristics, stream pattern and vegetation coverage. By using remote sensing techniques and GIS, making early assessments, and observing the trend of physical changes of the slope is possible. Cardinali et al. [24] proposed a similar method by studying geomorphology of landslides. The study was done by observing the changes in the distribution and pattern of landslides in a period of 60 years. The collected data was then compiled into a multi-temporal map which shows the evolution of slopes and distribution and pattern of existing and past landslides. The proposed method was proven to be reliable and cost effective, allowing for a detailed definition of landslide hazard and risk in urban and rural areas. However, like this research, the method requires extensive geomorphological judgement which should be done by skilled geomorphologist.

To study the temporal behaviour of a certain landslide requires years of observation and evaluation. A longer observation period will produce an even better evaluation thus an even better multi-temporal inventory map can be produced. If a study is done in a shorter period, the reliability of the hazard forecast is reduced [24]. Failure to recognize a landslide event may lead to negative consequences. To create better judgement and prediction, multiple sets of aerial photographs and satellite images from different periods of time are required. Though this information is sometimes very difficult to obtain even with the help of the world wide web.

7 Conclusion

Geohazards features on Gunung Pass can be seen clearly through different aspects, The random topographic pattern of Gunung Pass plus its hummocky terrain affects the stability of the slopes. The concave-convex profile of the slope topography is clear evidence of depletion zone and accumulation zones. Other features such as curved head scarps, crowns, main scarps, and side scarps can also be seen though satellite images. Other evidence such as secondary vegetation and stream patterns are also crucial as they can be visual clues to identify past landslides. With the help pf satellite images, comparison can be made between newer images and old ones. These comparisons are done to observe the trend in secondary vegetation growth and presence of tensions cracks which weakens a certain slope.

Cause of landslides can be divided into two main factors, natural cause, or man-made factors. Gunung Pass has a high altitude which receives frequent rainfall hence rapids the erosion process thus promoting slope failures. High weathering activity weakens the physical structure and eventually will fail when heavy rain comes. Very steep cut slopes also increase the risk of reactivation of past landslides. Man-made factors are also heavily related which can be seen its effects by observing the rapid growth of tension cracks. All these factors certainly play a role in reducing the slope stability of

Gunung Pass. However, we must not blame certain parties whenever a slope failure happens. Countermeasures must be taken by everyone to reduce the risk of this tragedy happening again.

Acknowledgments. This work was supported by the Fundamental Research Grant Scheme (FRGS) awarded by the Ministry of Education of Malaysia, titled 'Enhanced Coalbed Methane Recovery Processes by Coupling Fluid Flow of Mukah-Balingian Coal Deposits' with the referral no. R.J130000.7851.5F371. This work was supported by the Universiti Teknologi Malaysia Encouragement Research Grant (UTMER) awarded by Universiti Teknologi Malaysia, titled 'Diagnosis of Alkali-Aggregate Reaction – Polarizing Microscopy and SEMEDS Analysis' with the referral no. Q.J130000.3851.19J79.









References

1. Jebur, M.N., Pradhan, B., Tehrany, M.S.: Using ALOS PALSAR derived high-resolution DInSAR to detect slow-moving landslides in tropical forest: Cameron Highlands, Malaysia. *Geomat. Nat. Haz. Risk* **6**(8), 741–759 (2015)
2. Khan, Y.A., Lateha, H., Jerfriza, A.W.M., Muhiyuddin, B.: Monitoring of hill-slope movement due to rainfall at Gunung pass of Cameron Highland district of Peninsular Malaysia. *Int. J. Earth Sci. Eng.* **3**, 6–12 (2010)
3. Umor, M.R., Rafek A.G.: The Influence of natural slope geomorphology on active cut slope failures near Gunung Pass, Simpang Pulai-Lojing highway. In: National Geoscience Conference, pp. 2–3 (2012)
4. Md Yusoff, Z., Azmi, N.A., Nahazanan, H., Nik Daud, N.N., Abd Aziz, A.: Engineering geological of an active slope in KM46 Simpang Pulai, Perak. *Malays. J. Civ. Eng.* **28**(1), 35–41 (2016)
5. Zakaria, M.T., et al.: Slope instability evaluation using geophysical methods of Gua Musang-Cameron Highland highway. *Lowl. Technol. Int.* **22**(1), 172–179 (2020)
6. Malone, A, Hansen, A., Hencher, S., Fletcher C.: Post-failure movements of a large slow rockslide in schist near Pos Selim, Malaysia. In: *Landslides and Engineered Slopes. From the Past to the Future*, pp. 457–61. CRC Press (2008)
7. Scrivenor, J.B.: The geology of Malaya. *Geograph. J.* (1931)
8. Jamaluddin T.A., Hassan, A.N.: Engineering geology of slopes for the preparation of EIA reports: a case study from the proposed site for a national secondary school at Ringlet, Pahang Darul Makmur. In: *Proceedings - Annual Geological Conference*, vol. 15, pp. 247–253 (2001)
9. Krähenbuhl, R.: Magmatism, tin mineralization and tectonics of the Main Range, Malaysian Peninsula: consequences for the plate tectonic model of southeast Asia based on Rb-Sr, K-Ar and fission track data. *Bull. Geol. Soc. Malay.* **29**, 1–100 (1991)
10. Zaid, S.N.M., Abd Kadir, A., Rahamat Noor, N.F.: Geochemistry and petrogenesis of metamorphic rock along Simpang Pulai, Perak - Cameron Highland, Pahang Road. In: *National Geoscience Conference*, pp. 146–48 (2011)
11. Hussin, H., Ghani, S.A.A., Jamaluddin, T.A., Razab, M.K.A.A.: Tanah Runtuh Di Malaysia: 'Geobencana' Atau 'Geobahaya'. *Jurnal Teknologi* **1**, 229–35 (2015)
12. UNISDR: 2009 UNISDR Terminology on Disaster Risk Reduction. *International Strategy for Disaster Reduction (ISDR)* (2009)
13. Jamaluddin, T.A.: Faktor Manusia Dan Kegagalan Cerun Di Malaysia. *Geol. Soc. Malays. Bull.* **52**, 75–84 (2006)

14. Soeters, R., Van Westen C.J.: Slope instability recognition, analysis, and zonation. Special Report - National Research Council, Transportation Research Board (1996)
15. Komoo, I.: Masalah Kestabilan Cerun Di Malaysia (1989)
16. Cruden, D.M., Varnes D.J.: Landslide types and processes. Special Report - National Research Council, Transportation Research Board (1996)
17. Lu, N., and Godt J.W.: Hillslope Hydrology and Stability (2011)
18. Záruba, Q., Mencl, V.: Landslides and Their Control: Developments in Geotechnical Engineering. Elsevier Science, Amsterdam (2014)
19. Komoo, I., Lim, C.S.: The Kundasang landslides complex: a detailed mapping of the Kundasang national secondary school area (Kompleks Gelinciran Tanah Kundasang: Pemetaan Terperinci Di Kawasan Sekolah Menengah Kebangsaan Kundasang). Bull. Geol. Soc. Malays. **46**, 387–392 (2003)
20. Lyell, C.: Principles of Geology, vol. 3. Murray, London (1830)
21. Jamaluddin, T.A., Sulaiman, N., Shahidah, N., Nazer, M.: Penilaian Geomorfologi Tanah Runtuh Lama Di Tanah Tinggi Tropika – Kajian Kes Cameron Highlands Dan Kundasang, Malaysia. Bull. Geol. Soc. Malays. **69**, 111–124 (2020)
22. Regmi, N.R., Giardino, J.R., McDonald, E.V., Vitek, John D.: A review of mass movement processes and risk in the critical zone of earth. In: Developments in Earth Surface Processes (2015)
23. Jamaluddin, T.A.: Reactivated ancient slides at the Sungai Kelalong Dam site, Bintulu Sarawak, East Malaysia. Bull. Geol. Soc. Malays. **49**, 5–12 (2006)
24. Cardinali, M., et al.: A geomorphological approach to the estimation of landslide hazards and risks in Umbria, Central Italy. Natl. Hazards Earth Syst. Sci. **2**(1/2), 57–72 (2002)



A Review on Concrete Performance Towards Incorporation of Recycled Material - Coal

Syuhaidah Azam¹ , Afikah Rahim¹ , Nazri Ali¹ , Hamzah Hussin² ,
Nor Shahidah Mohd Nazer³ , Agus Winarno⁴ , Deddy Tanggara⁵ ,
and Asmawi Hisham¹ 

- ¹ Faculty of Civil Engineering, Universiti Teknologi Malaysia, 81300 Johor Bahru, Malaysia
aidafiza96@gmail.com
- ² Department of Geoscience, Faculty of Earth Science, Universiti Malaysia Kelantan,
17600 Jeli, Kelantan, Malaysia
- ³ Department of Earth Sciences and Environment, Universiti Kebangsaan Malaysia,
43600 Bangi, Malaysia
- ⁴ Department of Mining Engineering, Faculty of Engineering, Mulawarman University,
Samarinda 75119, Indonesia
- ⁵ Kampus Tunjung Nyaho, Yos Sudarso Street, Palangka Raya City, Kalimantan Tengah
73112, Indonesia

Abstract. The use of coal additives in concrete has acquired popularity in recent years due to their potential performance-enhancing benefits. The ability to mitigate aggressive ion penetration, a chemical reaction that can cause concrete to degrade and potentially fail, is one of their most significant advantages. This literature review concentrates on the effect of coal additives, specifically coal fly ash and bottom ash, on the performance of concrete, with an emphasis on its strength and resistance to chemical attack. The review investigates several studies that investigate the properties of coal additive concrete, including its compressive strength, durability, and chemical penetration resistance. The findings indicate that the addition of coal to concrete can improve its properties, resulting in enhanced performance and durability. However, certain limitations must be considered, such as variations in the properties of coal residue based on the source and combustion process, for which geochemical analysis can provide insight into the causes. To fully comprehend the potential of coal additives in concrete and to address any limitations associated with their use, additional research is required.

Keywords: Coal · Bottom Ash · Coal additive concrete

1 Introduction

Coal is a fossil fuel that has been used for many years as a source of energy. Coal accounts for 27% of global energy consumption and 38% of electricity generation, with projections indicating 47% of global electricity supply will come from coal-fed thermal plants by 2030. Global coal consumption rose by 0.9% in 2019, mainly driven by Asia. This has resulted in a divide between countries transitioning to renewable

energy and those heavily reliant on coal power generation like China and India, making it challenging to build agreements on coal emissions and reductions. The surge in demand to provide electricity in those developing countries, especially for industrial purposes, has left dreadful carbon footprints to the environment with coal untreated coal wastage and the pollutants that it caused. However, in recent times, there has been a shift towards sustainable practices and the use of waste materials in construction. Coal waste, such as fly ash and bottom ash, is produced during the combustion of coal in power plants. This waste material has been found to have potential benefits when used as an additive in concrete. On the other hand, cities are struck with major developments, exploration of untouched lands for the erections of buildings for commercial and industrial purposes had increased the demand for building materials such as sand and cement. Cement production is a significant contributor to greenhouse gas emissions and has a negative impact on the environment. The demand for cement has been steadily increasing, particularly in developing countries, which has further exacerbated the issue.

According to a research paper published in the *Journal of Cleaner Production* in 2018, the cement industry is responsible for approximately 8% of global CO₂ emissions, with this percentage expected to increase due to the growing demand for cement [1]. Another study published in the same journal in 2019 found that cement production is also a significant contributor to air pollution, with particulate matter, nitrogen oxides, and sulfur oxides emitted during the production process [2].

Furthermore, cement production also has a significant impact on land use and biodiversity. Cement production requires the extraction of raw materials, which can lead to habitat destruction and soil erosion. A study published in the journal *Nature* in 2018 found that global demand for sand and gravel, which are used as aggregates in cement production, has resulted in significant impacts on rivers and ecosystems, including loss of habitats and biodiversity. The use of coal additives in concrete has been found to improve several properties of the material. For example, the use of coal fly ash in concrete can reduce the amount of cement required in the mixture, resulting in a lower carbon footprint. Coal fly ash has also been found to improve the workability and pumpability of concrete, making it easier to handle and place. Additionally, the use of coal additives has been found to improve the durability of concrete, making it more resistant to water and chemicals.

2 Significance of Research

The review contains information on the production, use, and disposal of ashes from thermal power facilities that burn coal. It emphasizes the importance of using the ashes in a meaningful way rather than to simply disposing of the waste. Concrete made with coal ashes has the potential to be more affordable and environmentally friendly. The review discusses the impact of various coal ash types on the qualities of conventional and self-compacting concrete made with natural and recycled aggregates in terms of freshness, strength, and resistance to aggressive ions. The well-burned ashes can be used in the concrete industry as fine aggregate or a cement substitute since they have high pozzolanic qualities. Utilizing ashes in the concrete-making process preserves natural resources and yields concrete that is affordable, long-lasting, resilient, and energy-efficient.

2.1 Concrete

Concrete's heterogeneous microstructure comprises three components which are cement paste, pore structure, and an interfacial transition zone (ITZ) between the cement paste and aggregates. Increasing the quality of these three elements improves the mechanical strength and durability of concrete. The primary source of concrete's strength is the interfacial bonding between the solid constituents of hydrated cement paste. This bonding can be ascribed to the van der Waals laws, with the degree of adhesiveness depending on the size and composition of the solid surfaces involved. Particularly, certain hydrated products, such as C-S-H crystals, calcium sulfoaluminate hydrates, and hexagonal calcium aluminate hydrates, possess large surface areas coupled with strong adhesion properties, facilitating their adhesion to each other particles, including as lime, aggregate as well as anhydrous cement particles. To cater for practicality and its usage, additives can be introduced in the raw material mixes to meet desirable properties of the concrete [3], Fig. 1.

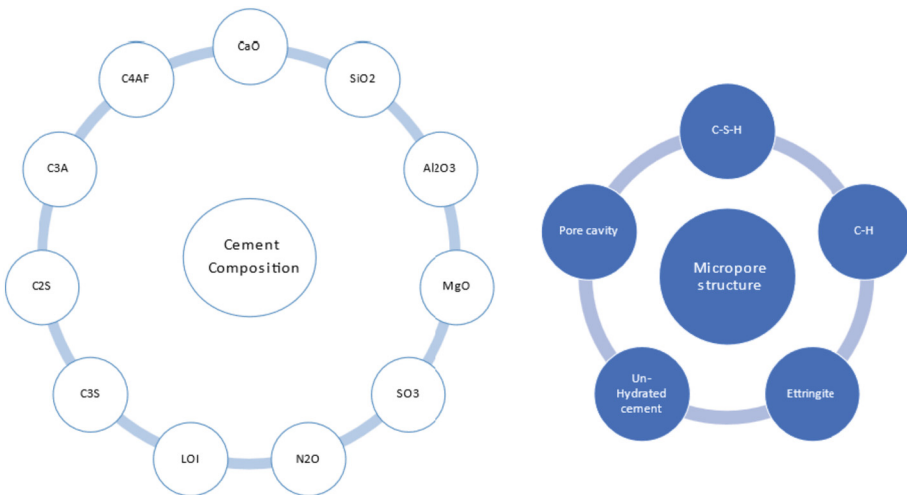


Fig. 1. Consisting of the chemical elements of cement and consisting elements of concrete pore structure.

To increase the durability as well the strength requirement, the impact would not be significant if the effort only focuses on reducing the capillary porosity as it is vital to reduce the gel porosity as it plays a role to the C-S-H structure from porous to needle-like crystalline phase, i.e., change in concrete microstructure. About one quarter of the overall volume of CSH-gel is comprised of the gel's pores, which take up roughly one quarter of the total volume. The definition of these holes is anything smaller than 20 nm. Capillary pores are defined as pores with a size greater than 20 nm.

As per SEM imaging above, Fig. 2, the needle-like structure of C-S-H gel phase was from a reaction of alite and belite in cement that resulting into calcium silicate hydrate and calcium hydroxide phases [4].

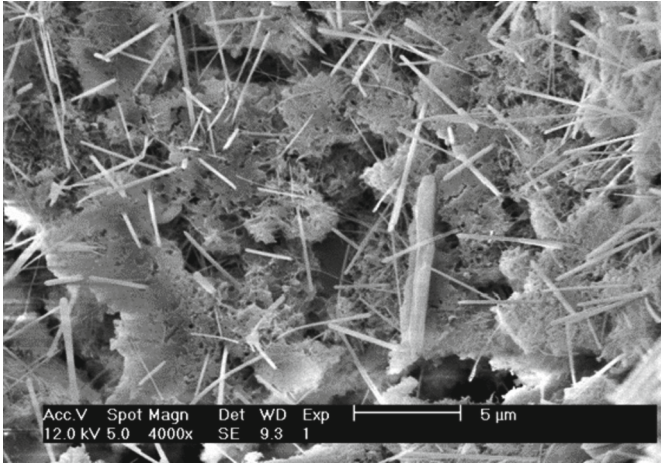


Fig. 2. Illustrate a needle-like C-S-H structure erected under SEM imaging.

2.2 Coal

Coal, one of the most abundant fossil fuels and has been an important energy source for generations, Table 1. It is primarily used to generate electricity and heat in industrial and residential settings. Coal's energy is released during combustion, which generates heat, vapor, and other byproducts such as fly ash.

Table 1. Table represent the classification of coal based on the value % if chemical composition.

Chemical component	Values in (%)		
	Anthracite or Bituminous	Sub-bituminous coal	Lignite
SiO ₃	20–60	40–60	15–45
Al ₂ O ₃	5–35	20–30	20–25
Fe ₂ O ₃	10–40	4–10	4–15
CaO	1–2	5–30	5–40
LOI	0–15	0–3	0–5

Depending on its carbon content and energy density, coal can be classified based and graded accordingly based on its chemical composition.

- Anthracite is the highest grade of coal and is distinguished by its high carbon content, low moisture content, and high energy density. When incinerated, anthracite coal produces a pristine and intense heat.
- Bituminous coal is the most common form of coal and contains a moderate amount of carbon. It is widely employed in the production of electricity and industrial applications.

- Sub-bituminous coal has a lower carbon content and a higher moisture content than bituminous coal. Subbituminous coal is frequently used for energy production.
- Lignite is the lowest rank of coal, containing the least carbon and the most moisture. Lignite is primarily used to generate electricity and is less energy-dense than other forms of coal.

Fly ash, spherical shape with sub amorphous and sub crystalline structure, commonly form in fine size averaging in 10 μm , and further classification as below:

- Class F fly ash is produced by the combustion of anthracite or bituminous coal. It is distinguished by a high concentration of silica, alumina, and iron oxide. Class F fly ash has weaker reactive qualities than Class C fly ash, which means it takes longer to build strength in concrete. It is often used in concrete as a pozzolanic material, which improves workability, reduces water consumption, and improves long-term strength and durability.
- On the other hand, the combustion of sub-bituminous or lignite coal forms Class C fly ash. It includes more calcium, silica, alumina, and iron oxide than Class F fly ash, making it more chemically reactive. Class C fly ash has self-cementing capabilities, which means it hardens and gains strength faster in the presence of water. It is frequently used in concrete as a cementitious ingredient, partially replacing Portland cement. Class C fly ash benefits the concrete in terms of increased early strength development and lower heat of hydration, Fig. 3.

While for coal bottom ash (CBA), spherical shape particles and it is obtained from the bottom part of the boiler making it much coarser in size and usually act as replacement to coarse aggregate. Even though the chemical composition can be said to be derived from FA, the carbon content tends to be higher for CBA.

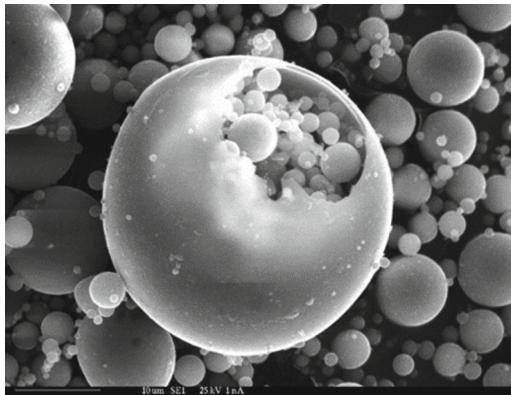


Fig. 3. Showing the shape of fly ash, a glassy pherospheres surface can be seen under scanning electron microscope.

3 Effect of FA on Fresh Properties

The addition of ash in concrete is believed to retain water-cement ratio in the system, leading to an increase in workability of fresh cement mix. During fresh concrete state, the concrete is formed as plastic state where no strength loss or gained that contributes to the final reading and additives like superplasticizer can be added to aid the curing process. In contrast to cement, FA has a lower specific gravity, and this results in greater paste volume per unit volume. Hence, when FA is substituted with cement while maintaining the same water-to-cement ratio, the outcome is an increase in concrete cohesiveness and plasticity. Additionally, past research pointed that spherical nature of FA particles had better transportability which benefits in reducing the water requirements [5–7]. On the other hand, the characteristics of FA with low levels of loss of ignition (LOI) also exhibits in low water requirements as well as having increased compressive strength, decreased water permeability, slowed chloride diffusion, and lowered carbonation rate. An experimental study has confirmed the findings where samples with 11% LOI had showed better strength and resistance as compared to other lower percentage samples. This peculiar finding seems debatable to others as high value of unburnt cellular carbon represents low quality of ash with high level of carbonation and water entrapment, hence, the water demand would increase simultaneously. The samples however consist of silica fumes as an aid to prevent delayed in pozzolanic activity, as higher surface areas of silica fume particles increase the water requirement. These effects of fly ash and silica fume possess an impact on slump properties making it increase in workability and performed better than OPC [8].

While in terms of setting time, Nochaiya claimed that when compared to regular Portland cement paste, the addition of fly ash lengthens the initial and final setting durations. Fly ashes with a high carbon content (denoted by a high LOI) are said to slow the setting time of mortars given their chemical composition. Research, where FA and CBA were being used as replacement for cement, a similar trend of longer setting time being observed such that low cement content causing low heat development as limited availability of Tricalcium aluminate (C3A) [9–12]. However, with additional of admixtures, the excessive water can be curb that ultimately improves setting time. In conclusion, regardless of the theory of reaction, chemical combination of elements would definitely produce several possibilities of reaction. Hence, in-depth knowledge in the material as well as to determine the crucial element such as water ratio important during design phase.

4 Effect of Coal on Hardened Concrete - Mechanical Properties

4.1 Compressive Strength

It is common practice in today's application of adding coal as partial replacement for fine aggregate or the cement itself. Various positive experimental results to conclude the compressive test findings on addition as well as substitution of coal in concrete design mix [13, 14] have been recorded. A trend has been observed where consistent positive performance has been seen in lower amount of fine aggregate substitution whereas higher amount substitution only resulting to decreased in workability as well as compressive

strength results. This scenario occurs as performance of cement mix does not reply entirely to percentage of additives added, however, several variable factors that may influence the reaction such as water/cement ratio that aided in hydration process which leads to strength performance of a concrete.

Subsequently, Singh and Siddique conducted a study involving various levels of CBA as fine aggregates replacement, ranging from 0% to 100% as compared to differing cement content in concrete mixes. The results revealed similar trends which support the statement of higher replacement of FA tend to decrease the quality of concrete. The recommended amount of up to 40% CBA replacement has been found to be the most practicable composition for producing concrete with satisfactory strength compared to conventional concrete [15]. By implementing SEM scanning, the decline of strength in concrete comprising CBA as fine aggregate replacement was examined, and it was discovered that CBA-containing concrete is far more porous than concrete comprised of natural sand, Fig. 4.

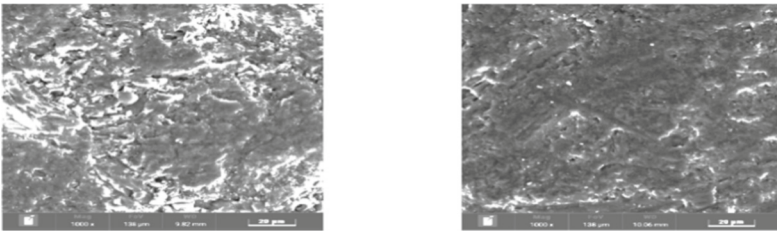


Fig. 4. Showing SEM imaging of coal gangue being used as coarse aggregate as compared to natural gravel. The formation in (b) showing compact and denser surfaces as of (a).

On the other hand, a study conducted by Kang et al. [16], proved that volume of fly ash replacement by itself has null impact to the performance while it also influenced fairly from the chemical composition of each type of particle as well as period of curing. He found that samples with categories contain reactive components with high concentrations of Al_2O_3 , CaO , and SiO_2 ; the increasing alumina content significantly affects the reaction rate. The compressive strength of composite cement mortars containing synthesised $\text{CaO-Al}_2\text{O}_3\text{-SiO}_2$ glasses is an outcome of two variables: the degree of glass reaction and the real stage of composition. Apart from that, these categories also highlighted a relatively high percentage of P_2O_5 as well as MgO . The reaction leads to the formation of magnesium phosphate, which could shorten setting time, enhance early strength AFm and AFt, and exhibit exceptional durability, including resistance to chemical attack and penetration. As a result, the findings associated with strength performance for both 20% and 40% high reactivity fly ash replacement [16, 17].

Another experimental study has been performed by substituting coal bottom ash as coarse aggregate to be utilized as concrete road paving block had published unclear correlation between the concrete's performance with the percentage of coal added in concrete. It was found that even with 20%–40% replacement of coarse aggregate to coal, the strength of concrete is heavily dependent on the correct w/c ratio of the design mix. Two mixtures without CBA and six with CBA were utilized with two water-to-cement

ratios (0.63 and 0.73). These two values were selected based on research conducted by Silva et al. [18], using the same materials for dried concrete. The most suitable water-to-cement ratios for concrete with cement-coal production were found to be 0.63 and 0.73. The testing results showed sample consisting of CBA (w/c ratio of 0.73) exhibited a better reading f_c (25.05 MPa) at 28 days in relation to the alternative mix with a w/c ratio of 0.63 (11.38 MPa).

Due to its brittle state, the utilization of CBA as coarse aggregate has not been a popular option. However, CBA as coarse aggregate shows good prospect for low-cost concrete application with satisfactory strength as to control concrete with slight effect in compressional test while decrease in flexural strength due to CBA's filler condition. Flexural load cracks propagated through bottom ash particles but were hard to penetrate by typical aggregates, changing the crack propagation direction. As for w/c ratio, the research does not emphasize on the impact to the concrete but rather showing a high absorption rate in CBA followed by FA (Shanmugan et al. [19]; Kim and Lee [20]). This finding validates the fact that that coal requires more water as compared to mortar containing only Ordinary Portland Cement (OPC) which closely related to the availability of unburnt carbon. Consequently, a higher w/c ratio facilitates hydration, resulting in the release of the silicate component, which interacts with the additional free lime supplied by the dissolution of limestone. Therefore, more calcium silicate hydrate (CSH) is released, which is responsible for the strength (Olubajo et al. [21]).

As proven in previous research, factors such as low specific gravity, porous microstructure, low crushing value, and w/c ratio regulate the decrease in strength, Fig. 5. The high absorbance capability of CBA resulting in losses of amount of free water available for reaction, resulting in a lower w/c ratio for concrete. In general, a lower w/c ratio results in enhanced strength. However, with CBA in place for substitution to sand, the contribution of CBA's low crushing value is unscathed to the concrete's performance.

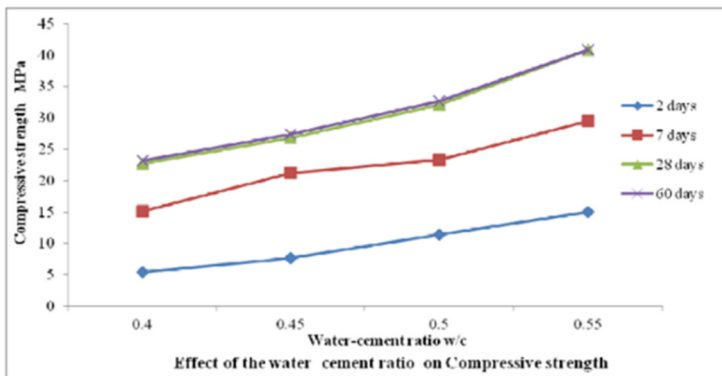


Fig. 5. Showing the results of compressive tests of samples with varying w/c ratio from 0.4 to 0.55 of OPC blended with 10wt% coal bottom ash.

Alternately, interesting observation has been recorded where fly ash is being used as cement replacement and tested in three different categories of LVFA, MVFA as well

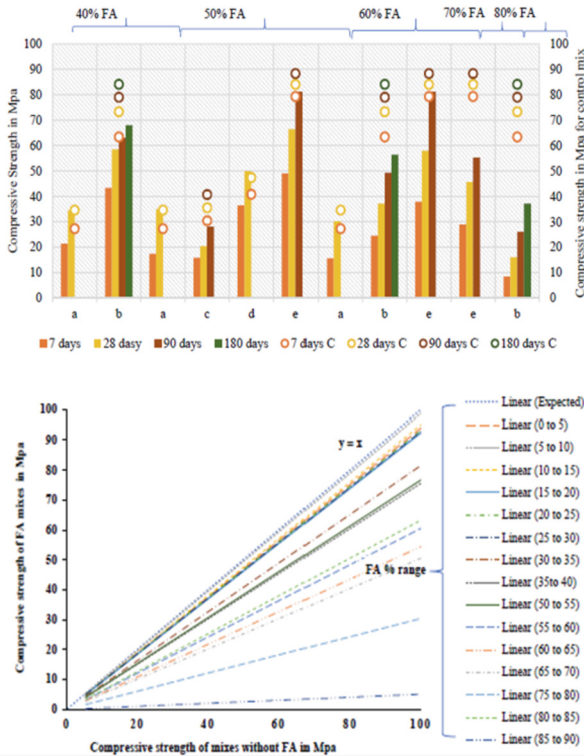


Fig. 6. Showing the compressive strength with various percentage FA added in relation to mixes without FA.

as HVFA. The strength gain potential of LVFA is up to 30% FA in concrete, whereas MVFA (FA between 30% and 50%) and HVFA (50% to 60%) have a slower strength gain in early stages but increases at later stages of curing. The insufficient heat of hydration demonstrated by fly ash (FA) within the concrete matrix prevents sufficient hydration for attaining strength when fly ash (FA) is used in excess of 60% of the concrete mix. This phenomenon results from the differences between low-volume fly ash (LVFA) and high-volume fly ash (HVFA) in terms of their influence on strength development. Particularly, LVFA contributes to the enhancement of strength by promoting the formation of calcium silicates and calcium aluminate hydrates, thereby enhancing the interfacial bond strength. On the contrary, HVFA tends to reduce strength due to its reduced hydration rates and limited pozzolanic activity. As for 70% of FA, the strength was not even on par with cement concrete due to excessive FA being added as illustrated in Fig. 6. The analysis depicted in Fig. 6 demonstrates conclusively that incorporating up to 10% fly ash (FA) in concrete has a negligible effect on strength, making it a promising material for practical applications. Due to the complete reaction of calcium hydroxide (CH) via pozzolanic activity and concomitant pore-filling, the potential for strength gain in concrete containing up to 30% low-volume fly ash (LVFA) can be accurately predicted. In LVFA concrete, the rate of early strength development deviates from that of FA-free

concrete, increasing during later curing phases due to the pozzolanic effect and secondary reaction of FA, consequently leading to the development of calcium-silicate-hydrate (C-S-H) gel.

In moderate-volume fly ash (MVFA) concrete, with a fly ash content between 30% and 50%, the early strength increase is not as pronounced as in FA-free concrete. However, similar to LVFA concrete, the strength increases during later curing phases due to the synergistic effect of the pozzolanic outcome and the subsequent reaction of FA, which results in the formation of a C-S-H gel. In high-volume fly ash (HVFA) concrete with fly ash (FA) content between 50 and 60%, the early strength development is negligible. In the later phases, however, the strength begins to increase, primarily due to the low heat of hydration exhibited by FA in the concrete matrix. Additionally, exceeding the 60% FA threshold does not result in a significant strength increase in the investigated concrete system. Hence, it can be concluded that strength gain of concrete does not entirely depend on the type nor level of replacement, the increase in strength of concrete comprising coal varies depending on several factors, including the type and grade of coal used, the amount of coal replaced by other materials, such as cement or fine aggregates, and the curing conditions. If optimal conditions are fulfilled, using coal as a partial replacement for cement in concrete can increase the compressive strength of the concrete. The chemical and mineralogical properties of coal ash, such as its calcium oxide (CaO), silicon dioxide (SiO₂), and aluminium oxide (Al₂O₃) content, can play a significant role in determining the strength gain, coupled with the rate and duration of curing also influence the increase in strength of concrete containing anthracite. Concrete can take several weeks or even months to attain its maximum strength potential after proper curing.

4.2 Chemical Attack

The basis of having a durable concrete structure is emphasized by having to incorporate the raw materials effectively to kick start a chemical reaction and coupled with adequate curing time. As mentioned above, the critical criterion that should be tested and confirmed prior to starting a project, is the w/c ration, type of aggregate, grade, and percentage of additives as well as during curing stage. Chloride and sulfate attack is one of the common chemical attacks that usually occur with the availability of water within the vicinity, Fig. 7. The active minerals in the concrete structure were exposed to chloride and sulphate, and not limiting to submersions condition or under freeze and thaw situation would have the risk of attack. With prolong exposure to extreme weathering, such attack would penetrate the available pore cervices of the structure and assisted by difference in capillary pressure, the harmful particles could advance further and attacking the reinforcement structure which then led to corrosion and ultimately affecting the overall durability of the structure.

It is believed that with the help of additives, it would act as a shield or form of resistance to cancerous chemical attack. Once the penetration succeeded, prolonged attack will cause a greater impact such as ASR formation that causing gel-like structure to form and expand. A study has been performed by Maliki et al., to analyze the physical properties of OPC concrete with CBA as a partial sand replacement under influence of chloride and sulfate solution. Concrete samples were left for curing until desired strength



Fig. 7. The condition of deteriorated structure after sulphate and chloride attack.

is obtained which then continued to be kept under water and of 5% Na_2SO_4 and in 5% NaCl solution for a period of 90 days and the weight of samples being recorded on intervals of 28, 45 and 90 days of submersion.

The weight of concrete samples was recorded under pre- and post-exposure conditions under sodium sulphate and sodium chloride (ASTMC39/ C39M-18). The weight changes of the control mix (M1) and the concrete mix containing 10% pulverized CBA (M2) were scrupulously recorded over the 28-day, 56-day, and 90-day curing periods to assess the level of damage incurred during this time. Under normal water curing conditions, the weight stability of both varieties of concrete was unaltered. However, when exposed to 5% Na_2SO_4 and 5% NaCl solutions, all combinations exhibited substantial weight variations. In particular, M1 (control mix) exposed to Na_2SO_4 for 56 days gained the most weight, whereas M2 (concrete containing pulverized CBA) gained significantly less weight under the same conditions. Upon compressional test, 60% of CBA added as sand replacement depicted as the effective amount to produce maximum target strength while 30% CBA replacement as an optimal to achieve the target value [22] as in Fig. 8. This finding suggests that incorporating pulverized CBA into concrete effectively prevents the penetration of ions, resulting in less weight change than the control mix.

A similar method was being adopted with longer curing time till 270 days to assess the depth of attack in corresponding to duration of curing in the 5% Na_2SO_4 solution. The fly ash for this study was taken from Tongshan Electricity Plant, a Class F Grade II as per ASTM C618 classification and aided with Superplasticizer to produce high-performance concrete HPC samples.

Though the results obtained were in-line as Malik's, however, they found that there were two stages involved in the process. Initially, the weight recorded was decreased

Specimen detail	Curing Period (days)	Immersed under		
		Water	5% Na ₂ SO ₄	5% NaCl
Control Mix (M1)	28	3	3	3
	56	3	3	3
	90	3	3	3
Concrete containing 10% CBA (M2)	28	3	3	3
	56	3	3	3
	90	3	3	3
Sub total		18	18	18
Total number of specimens		54		

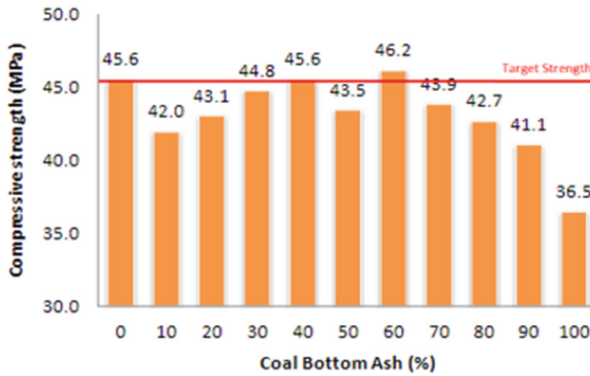


Fig. 8. Represent specimens curing conditions (above) as well as the performance after the exposure (below).

before the specimen mass increased again at a later stage. The reason for this scenario is explained as COH dissolution rate had surpassed the sulphate diffusion rate at early stage and resulting in weight loss during the immersion days. As the reaction is stable, the sulphate ions penetrate to the pores, advance through the capillary line causing a reaction with hydration products and resurrect an expansive gel formation. The gel had the ability to expand and fill the capillary pores making the structure to be denser which contributes to mass gain. Compressional tests were done and as predicted; it was found that it improves HPC resistance towards sulphate attack due to better microstructural condition followed by the higher the water-to-cement ratio, the faster sulphate ions might infiltrate the concrete [23].

Apart from that, two different solutions, MgSO₄ and Na₂SO₄ have been used to immerse the concrete with FA incorporated as partial cement replacement had found a chain of reaction that explains the strength loss but gain in sulphate resistance while the ability to curb gel expansion. After the samples were immersed for 400 days, the Self-compacting concrete (SCC) samples being tested for sulphate attack were subjected to a comprehensive visual inspection to assess the apparent softening, cracking, and spalling indications. Typical examples of SCC specimens damaged by sulphate attack after 400 days of immersion in both sulphate solutions are displayed in Fig. 9. Although a

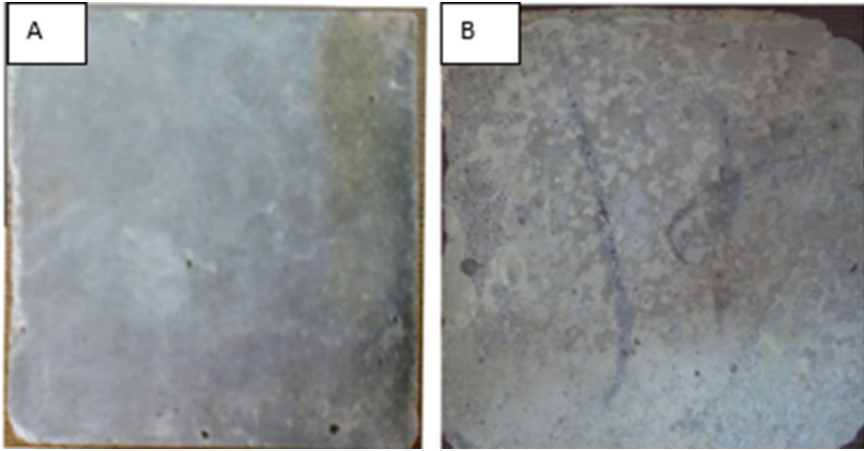


Fig. 9. Showing a comparison of concrete condition after immersion with Na_2SO_4 for 400 days. (A) SCC with FA (B) SCC FA-free.

small amount of spalling was observed at the edges and corners of the highest-performing specimen, GBFS40, the model showed no visible deterioration and no detectable weight loss upon visual inspection after 400 days of immersion in a sodium sulphate solution. On the control specimen, visual examination yielded distinct results while no visual indication for FA samples being discussed in the paper. Upon the compressional testing, FA series performed very well resistance to sodium sulphate attack and showed lower strength loss than other specimens though GBFS40 has null effect to the sulfate attack [24].

The usage of fly ash may improve the microstructural condition, by restricting the porosity and permeability of the concrete, limiting the ingress of active ions. As aforementioned, the curing period has great impact to the durability of the concrete as well as higher water-cement ratio brought benefits of resistance towards chemical attack [23, 25]. Interestingly, the fineness of the FA also plays an important role in determining the microstructural condition of the concrete as it was found that grounded or blended FA incorporated to the cement mix will have a denser and refined pore system. Hence, it will ultimately cease the ability of active ions like sulphate and chloride to ingress in the pore structure due to high interfacial tension between aggregates interfaces [26].

On the other hand, the absorption rate is claimed to be closely dependent on the percentage of FA content in the concrete due to large pore size observed during early time which delays the hydration products to form and fill the micropores, making the concrete to be porous and permeable. When FA, a low alkali and low lime content is replaced with cement, it reduces the amount of alkali and hydroxyl ions in the pore solution, which in turn reduces the amount of chloride penetration. The exact amount of this reduction is determined by the proportion of cement that is replaced by the FA in the concrete. As the interconnectedness of pores is connecting with absorption rate, the water-cement ratio can be appointed as one of the crucial factors to be consider during design process as higher w-c ratio also influences absorption on the rising side, as larger

w-c ratios generate greater open porosity [26, 27]. Both the pore-filling and pozzolanic activities of FA have a key influence in the concrete's ability to resist chloride ion penetration. Pore filling is particularly critical. Thus, it can be concluded that absorption is a function of curing regime and curing period.

5 Conclusion

It is apparent that the usage of coal ash in concrete would benefit the structure as well as the environmental health. Based on the research, several conclusions can be drawn:

- A general strength gain for concrete with additional of FA and CBA as per discussed in this paper proves that percentage of additive/replacement added will not depicted the end results as there are several factors to consider.
- The FA/CBA application in concrete improves workability and bleeding given its spherical form with a large surface area but increases the setting time which related to low hydration heat as well as unburnt carbon (LOI).
- Low hydration in concrete containing FA/CBA causing delayed strength gain which will improves after subjected to curing period due to pozzolanic activities and pore filling.
- CBA/FA utilization has better impact as fine and grounded form, it improves microstructural condition in terms of compaction which inhibit later penetration of aggressive ions as compared to being utilized as coarse aggregate alone but promising in standard.

Acknowledgments. This work was supported by the Fundamental Research Grant Scheme (FRGS) awarded by the Ministry of Education of Malaysia, titled 'Enhanced Coalbed Methane Recovery Processes by Coupling Fluid Flow of Mukah-Balingian Coal Deposits' with the referral no. R.J130000.7851.5F371.

This work was supported by the Universiti Teknologi Malaysia Encouragement Research Grant (UTMER) awarded by Universiti Teknologi Malaysia, titled 'Diagnosis of Alkali-Aggregate Reaction – Polarizing Microscopy and SEMEDS Analysis' with the referral no. Q.J130000.3851.19J79.

References






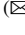

1. Costa, F.N., Ribeiro, D.V.: Reduction in CO₂ emissions during production of cement, with partial replacement of traditional raw materials by civil construction waste (CCW). *J. Clean. Prod.* **276**, 123302 (2020)
2. Zheng, C., et al.: Characteristics of CO₂ and atmospheric pollutant emissions from China's cement industry: a life-cycle perspective. *J. Clean. Prod.* **282**, 124533 (2021)
3. Awang, H., Hafiz Ahmad, M., Zuhair Al-mulali, M., Awang, H., Ahmad, M.H., Al-Mulali M.Z.: Influence of kenaf and polypropylene fibres on mechanical and durability properties of fibre reinforced lightweight foamed concrete (2015)
4. Singh, M.: Coal Bottom Ash. Waste and Supplementary Cementitious Materials in Concrete: Characterisation, Properties and Applications, pp. 3–50 (2018)

5. Kapoor, K., Singh, S.P., Singh, B.: Effect of high-volume fly ash and microsteel fiber on flexural toughness and durability properties in self-compacting lightweight mortar (SCLM). *Constr. Build. Mater.* **128**, 67–76 (2016)
6. Ma, J., Wang, D., Zhao, S., Duan, P., Yang, S.: Influence of particle morphology of ground fly ash on the fluidity and strength of cement paste. *Materials* **14**, 1–18 (2021)
7. Ravina, D., Mehta, P.K.: Properties of fresh concrete containing large amounts of fly ash. *Cem. Concr. Res.* **16**, 227–238 (1986)
8. Nochaiya, T., Wangkeo, W., Chaipanich, A.: Utilization of fly ash with silica fume and properties of Portland cement–fly ash–silica fume concrete. *Fuel* **89**(3), 768–774 (2009)
9. Demirbas, A.: Optimizing the physical and technological properties of cement additives in concrete mixtures. *Cem. Concr. Res.*, 1737–1744 (1996)
10. Singh, M., Siddique, R.: Effect of coal bottom ash as partial replacement of sand on properties of concrete. *Resour. Conserv. Recycl.* **72**, 20–32 (2013)
11. Sadat, S., et al.: Safe disposal of coal bottom ash by solidification and stabilization techniques. *Constr. Build. Mater.* **197**, 705–715 (2019)
12. Boscaro, F., Palacios, M., Flatt, R.J.: Formulation of low clinker blended cements and concrete with enhanced fresh and hardened properties. *Cem. Concr. Res.* **150** (2021)
13. İsa, Y., Turhan, B., Ömer, Ö.: Durability of concrete incorporating non-ground blast furnace slag and bottom ash as fine aggregate. *Build. Environ.* **42**(7), 2651–2659 (2007)
14. Andrade, L.B., Rocha, J.C., Cheriaf, M.: Influence of coal bottom ash as fine aggregate on fresh properties of concrete. *Constr. Build. Mater.* **23**(2), 609–614 (2009)
15. Singh, M., Siddique, R.: Strength properties and micro-structural properties of concrete containing coal bottom ash as partial replacement of fine aggregate. *Constr. Build. Mater.* **50**, 246–256 (2014)
16. Kang, S., Lloyd, Z., Kim, T., Ley, M.T.: Predicting the compressive strength of fly ash concrete with the particle model. *Cem. Concr. Res.* **137** (2020)
17. Durdziński, P.T., Dunant, C.F., Ben Haha, M., Scrivener, K.L.: A new quantification method based on SEM-EDS to assess fly ash composition and study the reaction of its individual components in hydrating cement paste. *Cem. Concr. Res.* **73**, 111–122 (2015)
18. Silva, R.V., de Brito, J., Dhir, R.: Properties and composition of recycled aggregates from construction and demolition waste suitable for concrete production. *Constr. Build. Mater.* **65**, 201–217 (2014)
19. Shanmugan, S., Deepak, V., Nagaraj, J., Jangir, D., Viyagula Jegan, S., Palani, S.: Enhancing the use of coal-fly ash in coarse aggregates concrete. *Mater. Today Proc.*, 174–182 (2020)
20. Kim, H.K., Lee, H.K.: Use of power plant bottom ash as fine and coarse aggregates in high-strength concrete. *Constr. Build. Mater.* **25**(2), 1115–1122 (2011)
21. Olubajo, O.O., Osha, A.O., El- Nafaty, U.A., Adamu, H.A.: Effect of water-cement ratio on the mechanical properties of blended cement containing bottom ash and limestone. *Civ. Environ. Res.* **6**(12) (2014)
22. Ahmad Maliki, A.I.F., et al.: Compressive and tensile strength for concrete containing coal bottom ash. *IOP Conf. Ser. Mater. Sci. Eng.* **271** (2017)
23. Xu, H., Zhao, Y.X., Cui, L., Xu, B.: Sulphate attack resistance of high-performance concrete under compressive loading. *J. Zhejiang Univ. Sci. A* **14**(7), 459–468 (2013)
24. Uysal, M., Sumer, M.: Performance of self-compacting concrete containing different mineral admixtures. *Constr. Build. Mater.* **25**(11), 4112–4120 (2011)
25. Ortega, J.M., Esteban, M.D., Sánchez, I., Climent, M.A.: Performance of sustainable fly ash and slag cement mortars exposed to simulated and real in situ Mediterranean conditions along 90 warm season days. *Materials* **10**(11) (2017)

26. Bouzoubaâ, N., Zhang, M.H., Malhotra, V.M.: Laboratory-produced high-volume fly ash blended cements: compressive strength and resistance to the chloride-ion penetration of concrete. *Cem. Concr. Res.* **30**(7), 1037–1046 (2000)
27. Dinakar, P., Kartik Reddy, M., Sharma, M.: Behaviour of self-compacting concrete using Portland pozzolana cement with different levels of fly ash. *Mater. Des.* **46**, 609–616 (2013)



Assessment of Hydrogen-Rich Syngas From Biogas Using Aspen HYSYS

Adlina Alia Nofal Firhat¹ , Muhammad Zulfaiz Hilmi Riduan¹ ,
Hanafiah Zainal Abidin¹ , Normadyzah Ahmad¹ , Norhasyimi Rahmat¹  ,
and Mohd Mustafa Al Bakri Abdullah² 

¹ School of Chemical Engineering, College of Engineering, Universiti Teknologi MARA,
40150 Shah Alam, Malaysia

norhasyimi@uitm.edu.my

² Centre of Excellence Geopolymer and Green Technology (CEGeoGTech), Universiti Malaysia
Perlis (UniMAP), Arau, Perlis, Malaysia

Abstract. This study aims to compare and assess the quality of two biogas reforming processes: steam reforming of biogas (SRB) and tri-reforming of biogas (TRB). SRB is the conventional method of producing hydrogen efficiently. TRB, on the other hand, is a relatively new innovative way to achieve higher hydrogen yield at less energy expense and lower carbon dioxide (CO₂) production. Both processes still have room for improvement, so optimizations should be considered to attain higher hydrogen yields and assess the effectiveness of both processes. The process simulation and sensitivity analysis were carried out using chemical process simulator (CPS), Aspen HYSYS, and its built-in sensitivity analysis tool. Direct comparisons of the results and evaluations of specific parameters targeted in the sensitivity analysis were then conducted, where the effects of changing molar ratio, temperature, and pressure were analyzed. The conversion of methane, conversion of CO₂, ratio of hydrogen to carbon monoxide (CO) produced, and hydrogen yield were also calculated. Since this study was only simulated on Aspen HYSYS, the results should be taken as an estimation of the processes under ideal conditions. The results lack chemical analysis and are limited to the software's mathematical and computational abilities. However, the sensitivity analysis obtained decent correlation with literature and recorded trends that showed the feasibility of SRB and TRB in industrial conditions.

Keywords: Biogas · Steam Reforming · Tri-reforming · Sensitivity Analysis · Aspen HYSYS

1 Introduction

1.1 Hydrogen as Renewable Energy

Renewable hydrogen industry is seeing a surge as the world turns towards sustainability efforts and greener approach to mitigate climate change. Hydrogen as an Attractive New Energy Source/Carrier, 2021; Grand View Research, Inc., 2020; expect that the global

market for green hydrogen produced from renewable sources that supposedly yields zero carbon footprints will meet 24% of the world's energy demand by 2050 with a CAGR of about 14.24% from 2020 to 2027. Despite the encouraging market, only 4% percentage of hydrogen is produced via electrolysis of water, an eco-friendly method, due to its costliness [1, 2].

Nevertheless, valorization of biowastes is a growing trend among green alternative for hydrogen production, albeit controversially due to effective carbon neutrality and expectation of methane (CH_4) leakage along the process, respectively. One of the biowaste sources commonly utilized for this method is biogas which could be acquired from biomass, landfill gases and gases emitted from anaerobic digester.

In Malaysia, biogas industry has been identified as one of the National Key Economic Area since 2015. The southeast Asian country, second only to the major player in the palm oil industry dominated by Indonesia, led a sizeable production of crude palm oil (CPO) worth 19 900 metric tons in 2021 [3]. The palm oil industry generates enormous quantities of wastewater known as palm oil mill effluent (POME) which is an oily brownish colloidal mixture. Raw and partially treated POME are still released irresponsibly into waterways because of its costly treatment causing prominent levels of water pollution and severe damage to the aquatic ecosystem.

USDA forecasted 20 million metric tons of CPO production for Malaysia in the year 2021/2022 [4]. For every ton of CPO produced, around 2.5 to 3 tons of POME is generated [5]. Therefore, Malaysia's annual POME production sits around 50 to 60 million metric tons. In recent years, POME has been utilized to generate biogas via anaerobic fermentation. POME-based biogas amount to an average of 65% methane, 35% CO_2 and 1–2% water and traces of impurities including hydrogen sulphide (H_2S) [6–9]. As methane is eighty times more effective than CO_2 in warming up the Earth, irresponsible waste management of POME could lead to serious environmental consequences (EDF, 2021). This also aligns with UN's SDG 7 (United Nations, 2021). Hence, it is an absolute necessity to channel this resource towards an eco-friendly business venture.

Currently, green hydrogen costs around 3 to 6.5 \$/kg as it is considerably complicated to produce [10]. However, there are many alternatives to hydrogen production from biogas including biogas steam reforming (SBR), and combined reforming process such as tri-reforming of methane (TRM). This research is done to compare two methods of hydrogen-rich syngas generation from biogas via SBR and TRM method for feasible and profitable hydrogen production. The former is the conventional method of producing hydrogen efficiently. In contrast, the latter stands as a reasonably new innovative way to achieve higher hydrogen yield at less energy expense and lower CO_2 production [11].

Despite its cost-effectiveness and maturity, SBR is still plagued by a myriad of issues including coke deposition on catalyst and thermodynamic complications. In contrast, TRM is an energy-efficient method allowing simultaneous reaction of CO_2 reforming, SBR, and POX without additional equipment. Notably, this method allows methane conversion of up to 97% alongside decent CO_2 conversion of about 80% without issues of coke deposition on catalyst used [12]. However, as it is relatively new, further research is needed to confirm its reliability in industrial setting.

Both processes still have rooms for improvement, thus, optimizations should be considered in attaining higher yield of hydrogen and assessing the effectiveness of both

processes. To date, there has not been thorough research and comparison between these processes in terms of POME-based biogas. Thus, the area of research is necessary for Malaysia's renewable energy scene. Simulation software such as Aspen HYSYS enables studies to be conducted without incurring actual production cost and time while reducing or preventing human errors in calculations for chemical process design [13].

2 Literature Review

2.1 Background

About half of the global hydrogen production is currently produced from natural gas via steam methane reforming (SMR) method. Reforming of methane tend to yield high percentage of hydrogen, hence, ensuring its dominance in the production of hydrogen industry.

Low-cost production of hydrogen from natural gas which comprises of predominantly methane at a fraction of the cost of other renewable resource, is achieved after years of maturity in the process industry as shown in Table 1.

Table 1. Cost of conventional hydrogen production via SMR.

Aspect	Percentage (%)	Approximate cost	Unit
Overall	100.0	1.8–2.0	\$/kg
Overall	100.0	0.96	\$/kg
Reformer	22.0	21.1	\$/kg
Pressure swing adsorption (PSA)	20.8	20.0	\$/kg
Heat exchanger network	18.1	17.4	\$/kg
Compressor	13.4	12.9	\$/kg
Pre-reformer	10.0	9.6	\$/kg
Expanders	7.7	7.4	\$/kg
Water gas shift (WGS)	7.5	7.2	\$/kg

Apart from the convenience of a mainly methane source, the process is optimized by implementation of performance-enhancing catalyst, sorption-enhancer and microreactors [5]. Unfortunately, despite its efficiency, rising cost of electricity and energy is projected to push the overall cost up [6].

Reforming processes of biogas has been studied over the years by many researchers through experiments and simulations, albeit less extensively than methane reforming processes. Significant parameters of biogas reforming include temperature, pressure, feed gas composition, space velocity and catalysis. Temperature and space velocity of reforming process varies depending on the process. However, low pressure is generally favoured for reforming processes. High percentage of CH₄ in feed stream is also

favoured [7]. Nickel-based catalyst are commonly utilized due to effectiveness, cost-efficiency, and availability as compared to noble metal catalysts despite falling short to coke deposition at high temperatures [8, 9].

It is generally known that SBR and SMR are slightly different due to the difference in composition of CH₄ and CO₂ in biogas and natural gas. Biogas is largely made up of CH₄ (50–70%) and CO₂ (20–40%) whilst natural gas consists of primarily CH₄ ($\leq 70\%$) and around 20% of other hydrocarbons such as ethane, propane, and butane [10]. However, biomethane with more than 94% v/v purity like compressed natural gas (CNG) may be generated from biogas at a cost through upgrading processes such as pressure swing adsorption (PSA) and chemical scrubbing as shown in Table 2.

Table 2. Performance and cost of upgrading POME biogas.

Upgrading Technology	Maximum CH ₄ yield (%)	CH ₄ purity (% v/v)	Operating cost (RM/m ³)
Water scrubbing	94	98	2.00
Physical scrubbing	90	98	4.150
Chemical scrubbing	90	99	12.60
PSA	91	98	2.00
Membrane separation	99.5	99	2.00

These processes are essentially targeting CO₂ removal, hence, cost of pre-treatment of biogas to remove toxic H₂S prior to SBR is also incurred unless included in the upgrading process as with the case of water scrubbing [11]. It is necessary to remove CO₂ and all H₂S for corrosion prevention and simultaneously qualifying it as natural gas [12, 13]. H₂S removal is mandatory due to its hazardous implication on human and the environment [14].

Hong et al. [11] found that off-site water scrubbing, and lorry transportation may be feasible for upgrading process off-site. Thus, on-site usage of upgraded biogas should be more feasible but considerations for cost of transportation still needs further validation depending on the plant design.

Disregarding the economic aspect of biogas pre-treatment, it is assumed that H₂S removal has been done as most literatures found do not include H₂S into their respective biogas composition.

2.2 Steam Reforming of Methane (SRM)

The most mature of the methods available, SMR remains the most widely implemented method for hydrogen production [15]. As shown in Table 3, a total of eight reactions could take place during SMR, although the initial three, Eq. (1) to (3), are the most significant [16, 17].

A life-cycle assessment (LCA) done on a hydrogen plant based on steam reforming of biogas simulation using Aspen Plus found the process very lucrative [18]. Optimal

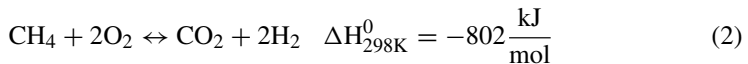
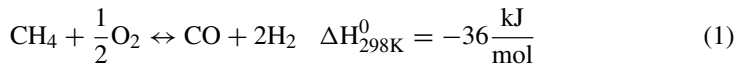
conditions of $P = 1$ bar, $T = 1008\text{--}1063$ K, $O_2/CH_4 = 0\text{--}0.1$, $H_2O/CH_4 = 2.4\text{--}3$ was cited for the optimization of process conditions of mixed reforming of biogas for hydrogen production [19].

Table 3. List of possible reactions occurring during SMR.

Name	Equation	ΔH_{298K}^0 ($\frac{\text{kJ}}{\text{mol}}$)
Steam methane reforming (SMR)	ΔH_{298K}^0 ($\frac{\text{kJ}}{\text{mol}}$)	206
Reverse methanation (RM)	ΔH_{298K}^0 ($\frac{\text{kJ}}{\text{mol}}$)	165
Water gas shift (WGS)	ΔH_{298K}^0 ($\frac{\text{kJ}}{\text{mol}}$)	-41
Dry reforming of methane (DRM)	$CH_4 + CO_2 \leftrightarrow 2CO + 2H_2$	247
Carbon monoxide reduction	$CO + H_2O \leftrightarrow CO_2 + H_2$	-131
Decomposition of methane	$CH_4 \leftrightarrow C + 2H_2$	75
Boudouard reaction	$2CO \leftrightarrow C + CO_2$	-172
Carbon dioxide reduction	$CO_2 + 2H_2 \leftrightarrow C + 2H_2O$	-90

2.3 Autothermal Reforming of Methane (ATR)

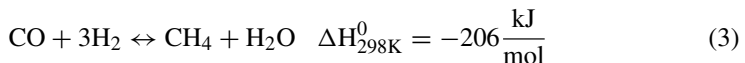
Autothermal reforming (ATR) of biogas is a combination of SMR, and catalytic partial oxidation of methane (POX), [20–22]. Other possible reactions that could occur alongside ATR include WGS, Eq. (3); DRM; and methane oxidation, Eq. (2).



Currently, ATR is less feasible for hydrogen production in terms of cost and efficiency when compared to SMR. Several studies have illustrated that SMR is better than ATR in terms of both energy and exergy comparison [20–23]. The lower performance is attributed to ATR's high energy consumption resulting from lower quality of syngas produced and hydrogen compression requirements [20, 22].

2.4 Dry-Reforming of Methane (DRM)

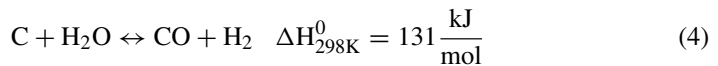
Dry reforming of biogas, not to be mistaken with DRM reaction, otherwise known as CO_2 reforming, is a process still investigated. It involves the Boudouard reaction, 54; two reverse methanation processes, Eq. (1) and Eq. (2); and CO reduction, Eq. (3).



Performance of DRM is not on par with SMR and TRM due to the irregularity of its performance. Apart from being more energy intensive than both processes, it is marred by rapid coke deposition on its catalyst surface due to CH₄ dehydrogenation. Despite presumptions that reaction temperature is the most important factor in this process, inconsistent results that cannot be replicated by other researchers can be found in the literature, suggesting that the kinetics and mechanism of this process are not well understood or that a catalyst may also play a significant role. For example, a study found that good performance is expected at temperature above 850 °C reaching more than 98% CH₄ conversion at 900 °C [24]. Meanwhile, another literature cited low performance overall and loss of performance after 500 °C, citing catalyst optimization, usage of H₂ membrane and operation condition at play [25].

2.5 Tri-Reforming of Methane (TRM)

Tri-reforming of methane is a synergistic process involving three methane reforming processes which are DRM; SMR; and POX, with other expected occurring reactions such as WGS; and reverse CO reduction [7].



It is a reasonably new innovative way to achieve higher hydrogen yield at less energy expense and lower CO₂ production [26–34]. The process is advantageous due to its energy, cost, and environmental friendliness [7]. The process involves major player playing several roles to increase its success. CO₂ is used in the DRM reaction, thus, eliminating extra cost in pre-removal of CO₂, encouraging carbon neutrality and cost-effectiveness. Steam is used in prevention of coke deposition on catalyst surface and SMR which is less energy intensive than DRM. POX is energy efficient as compared to the rest of the processes mentioned, allowing for high energy efficiency [7]. Apart from reduction of cost due to less energy-intensive process, TRM is space-efficient as a specialized reactor is employed to enable simultaneous reactions shown above to occur in one equipment. Theoretically, it should be free of all the setbacks experienced by DRB and SBR [26, 35–42]. TRM also has high performance of up to 99% CH₄ conversion and 80% CO₂ conversion due to the use of SMR, a mature and well-understood process [43–50].

3 Methodology

3.1 Material

The process simulation and sensitivity analysis are done using a chemical process simulator (CPS), Aspen HYSYS and its sensitivity analysis tool.

3.2 Methods

Experimental Set-Up. Aspen HYSYS is used to simulate two methods of hydrogen production via biogas reforming. Then, direct comparison of the results and evaluation

of specific parameters targeted in the sensitivity analysis are conducted where the effect of changing molar ratio, temperature and pressure are analyzed. Data synthesized from the study will be considered regarding optimization of both conventional and innovative method of reforming biogas into hydrogen-rich syngas. There are two methods considered, SBR and TRM, respectively. The biogas is modelled based on palm oil mill effluent (POME) with average composition of 65% methane, 35% carbon dioxide (CO₂).

Software Set-Up. Aspen HYSYS must be set up appropriately before conducting the process simulation. Usage of chemical process simulation software (CPSS) such as Aspen HYSYS, generally follow a similar set of steps. The steps below are taken prior to performing the simulation as shown in Fig. 1.

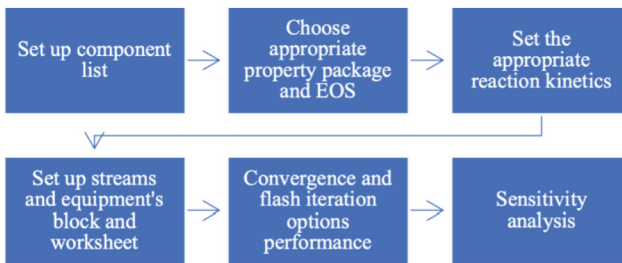


Fig. 1. Steps prior to simulation in Aspen HYSYS.

Firstly, set up a component list including all significant chemical components after starting the software and opening a new case. For both processes, methane, carbon dioxide, water, carbon monoxide, hydrogen, and steam, are chosen from HYSYS's component database. Secondly, choose the appropriate property package and equation of state (EOS) for the process. The options include Peng-Robinson (PR) and Predictive Soave-Redlich-Kwong (PSRK) for these processes. Well-chosen thermodynamic package will determine the reliability of the process simulation. Thirdly, set the heterogenous catalytic reaction constants according to suitable operation parameters for the reactor based on widely used kinetics model [27, 28]. Fourthly, set up the streams and blocks for equipment and their respective worksheets or flow sheeting. Specify units used in the process simulation. Once done, drag individual unit operation onto the process flow area and connect them using streams consecutively. Each unit operation requires three unknown specifications, usually temperature, pressure, and vapor fraction, to complete its degree of freedom to zero, enabling HYSYS to approximate or determine the rest of the parameters. This step includes keying in important parameters such as volume or flow rate of biogas feed and main thermodynamic properties including flow, temperature, or pressure. Repeat this step until the simulation is completely set up. Finally, the simulation set up can be checked for convergence to ensure correct set up. HYSYS indicates convergence with a green bar underneath the process simulation block. Non-convergence could indicate several faults including over-specifying stream conditions or unit operation parameters, using the wrong property package and causing iteration issues due to intricate recycle systems [29].

Process Considered. In this study, steam reforming of methane, steam reforming of biogas, tri-reforming of methane and tri-reforming of biogas will be considered for simulation study.

Process Simulation Set-Up. After setting up component list, appropriate fluid package was chosen. Soave-Redlich-Kwong (SRK) equation of state is used as PSRK is unavailable in the Aspen HYSYS built-in set. The initial simulation in model validation is tested with SRK, PR and a combination of non-random two-liquid model and Redlich-Kwong equation of state, known as NRTL-RK. As SBR is highly endothermic, simulation is done at an initial ideal condition of 700 °C at 1 atm (1.013 bar) and H₂O/CH₄ ratio of 2, well above the range of possibility for carbon formation or coke deposition [24]. Then, sensitivity analysis is done within the temperature range of 700 °C to 1000 °C, at pressure range of 1 to 60 bar and H₂O/CH₄ ratio of 2 to 5 [30]. Finally, for each trial, CH₄ conversion, CO₂ conversion, H₂/CO ratio, H₂/CH₄ ratio and H₂ yield are calculated as follows.

$$\text{CH}_4 \text{ conversion} = \frac{\text{CH}_4 \text{ in} - \text{CH}_4 \text{ out}}{\text{CH}_4 \text{ in}} \quad (5)$$

$$\text{CO}_2 \text{ conversion} = \frac{\text{CO}_2 \text{ in} - \text{CO}_2 \text{ out}}{\text{CO}_2 \text{ in}} \quad (6)$$

$$\frac{H_2}{CO} \text{ ratio of product} = \frac{H_2 \text{ out}}{CO \text{ out}} \quad (7)$$

$$H_2 \text{ yield} = \frac{H_2 \text{ out} - H_2 \text{ in}}{CH_4 \text{ in}} \quad (8)$$

3.3 Kinetic Models

SMR and SBR. Several model validations were done for industrial processes using the widely used kinetics model [28, 31]. In consideration of membrane reactors, model validation is also done for macro-scale membrane reactor [27]. Then, the validated models of SMR processes are fed with biogas, modelled of POME with average composition of 65% methane, 35% carbon dioxide (CO₂).

TRM and TRB. According to some researchers [51–55] just a few of the lab-scale processes for which model validation has been carried out. Then, the validated models of TRM processes are fed with biogas, modelled of POME with average composition of 65% methane, 35% carbon dioxide (CO₂).

4 Results and Discussion

4.1 Set-Up

Several set-ups were tested prior to the simulation phase. Finally, the set-up shown in Fig. 2 was chosen and maintained throughout the research process. The data controlled are tabulated in Table 4. Pressure drop in the pipelines was not considered as it is insignificant towards the research goals. For each sensitivity analysis, the conditions manipulated are tabulated in Table 5.

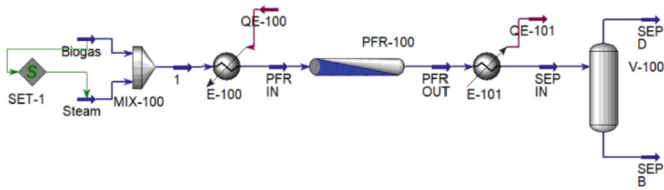


Fig. 2. Block set-up in Aspen HYSYS.

Table 4. Control data for Fig. 2.

Block	Temperature (°C)	Pressure (bar)	Composition	Molar flowrate (kmol/h)
Biogas	25	1.013	Methane	3600
Steam	400	1.013	Steam	7200
PFR IN	700	1.013	0.3333 Methane, 0.6667 Steam	10800
SEP IN	25	1.013	–	10800
SEP D	25	1.013	–	10800
SEP B	25	1.013	–	10800

Table 5. Conditions for sensitivity analysis.

Block	Current value	Units	Start	End	Step size	No. of steps
SET-1	2.0	–	2.0	5.0	0.5	7
PFR IN	700	°C	400	1000	50.0	13
PFR IN	1.013	bar	1.0	60	500.0	12

4.2 Model Validation

Three fluid packages were considered for each design, namely, Peng-Robinson (PR), Soave-Redlich-Kwong (SRK), and non-random two-liquid model and Redlich-Kwong equation of state (NRTL-RK). PSRK was not used due to its unavailability in the Aspen HYSYS built-in set. Finally, SRK was chosen due to its accuracy in modelling the specific systems. Due to limited data, model validation was not done specifically for on biogas reforming systems.

4.3 Sensitivity Analysis

Ratio of S/C. When S/C ratio in feed was increased from 2 to 5, upward trends were found in SMR, SBR and TRM processes as shown in Fig. 3. SMR and SBR have very similar trend of 21% and 28% rising to 38% and 53%, respectively. TRM was found to

have a conversion of 83%, 99% and 100% throughout S/C ratio of 2, 2.5, 3 and above. TRB was recorded to achieve 100% conversion at S/C of 2 until 4, before dropping to 0% at S/C of 4.5 and 5, Chouhan et al. [32]. The endothermic reactions involved in biogas reforming should result in a decrease in methane conversion at constant temperature while increasing S/C ratios as RM reaction is reduced.

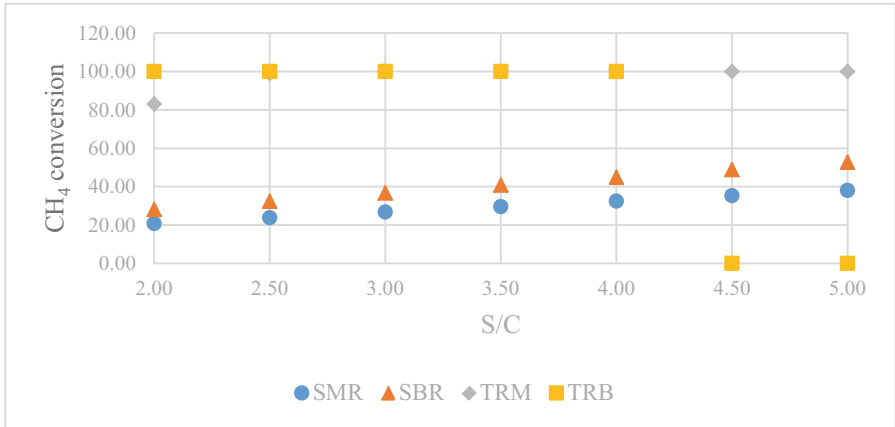


Fig. 3. Methane conversion for different steam to carbon (S/C) ratio for sensitivity.

CO₂ conversion for SBR showed a downward trend whilst TRB dipped down to a minimum of -1.8 at S/C of 4 before rising steeply to 0 at S/C of 4.5 in Fig. 4. Thus, the trend of TRB matches literature trends [24]. Negative values may be attributed to elevated presence of CO₂ resulting from reverse WGS reaction [32].

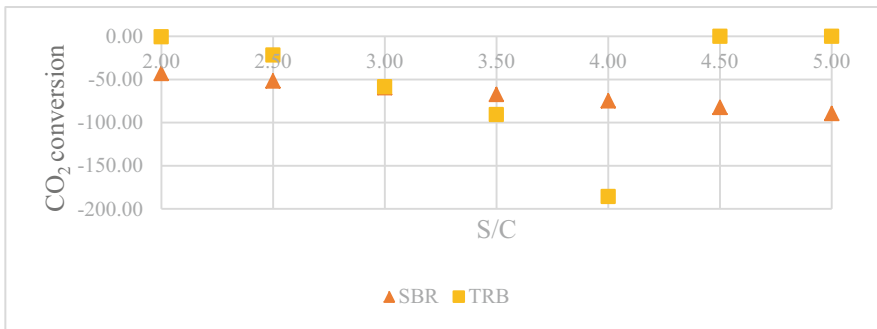


Fig. 4. Carbon dioxide conversion for different steam to carbon (S/C) ratio for sensitivity analysis.

H₂/CO ratio is a significant parameter in characterising syngas. SMR and SBR showed a rising trend from 64.68 and 22.58 to 92.71 and 44.58, respectively in Fig. 5. On the other hand, TRM and TRB rose and dropped slightly at S/C of 3.5 and above in the same figure.

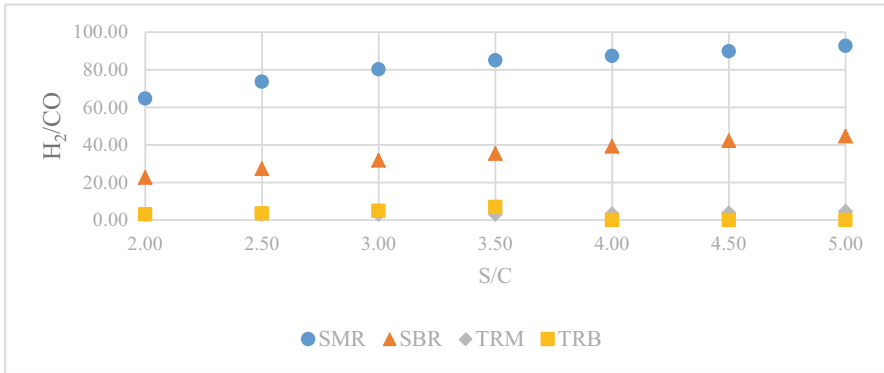


Fig. 5. Ratio of hydrogen to carbon monoxide in different processes for sensitivity analysis.

Hydrogen yield recorded similar trends in Fig. 6 to methane conversion in Fig. 3 due to its dependence on the SMR reaction. When S/C ratio in feed was increased from 2 to 5, upward trends were found in SMR, SBR and TRM processes as shown in Fig. 6. SMR and SBR have very similar trend of 0.82 and 1.07 rising to 1.50 and 2.06, respectively. TRM was found to have a yield of 2.49, 2.97 and 3.00 at S/C ratio of 2, 2.5 and 3 before gradually rising to 3.29 at S/C of 5. TRB was recorded rising from 3.00 to 4.00 throughout S/C of 2 until 4, before dropping to 0 at S/C of 4.5 and 5.

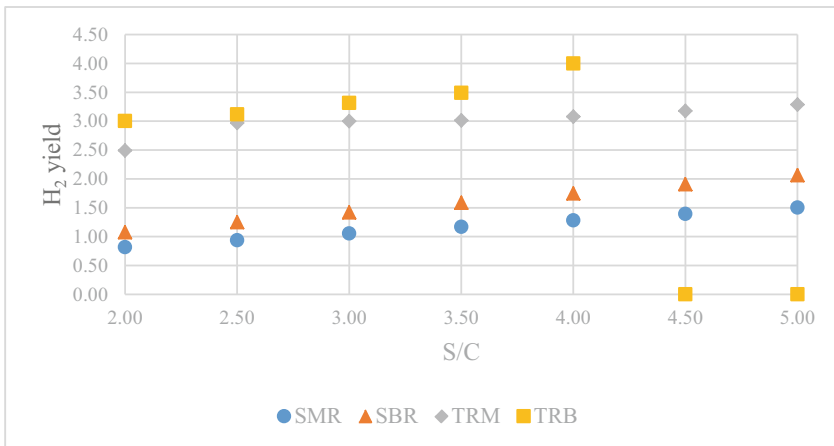


Fig. 6. Hydrogen yield in different processes for sensitivity analysis.

Despite S/C ratio increase enabling CH₄ conversion increase, when it reaches over half, the large amount of excess water burdens the system's energy balance [24]. Apart from that, there is a possibility that the kinetics model of TRM used is not suitable for high S/C conversion as it was not validated at industrial scale or not suitable for TRB due to its CO₂-rich composition.

Temperature. When temperature was increased from 400 °C to 1000 °C, upward trends were found in all four processes as shown in Fig. 7 as cited in literature [24]. SMR, SBR and TRM have very similar trend of 6%, 7% and 66% rising to 39%, 54% and 100%, respectively. TRB was recorded at a constant conversion of 100% throughout the trial.

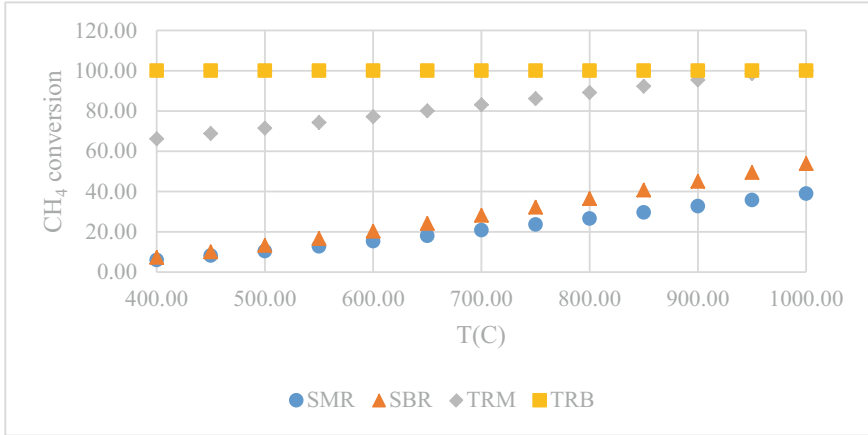


Fig. 7. Methane conversion at different temperature in different processes at different temperatures.

CO₂ conversion for both SBR and TRB show downward trends at increasing temperature in Fig. 8 as CO₂ is constantly present in temperatures above 400 °C [24]. SBR dropped from -13% to -61%. Meanwhile, TRB recorded 0% conversion before 700 °C where conversion was at -1% dipped down to a minimum of -39%.

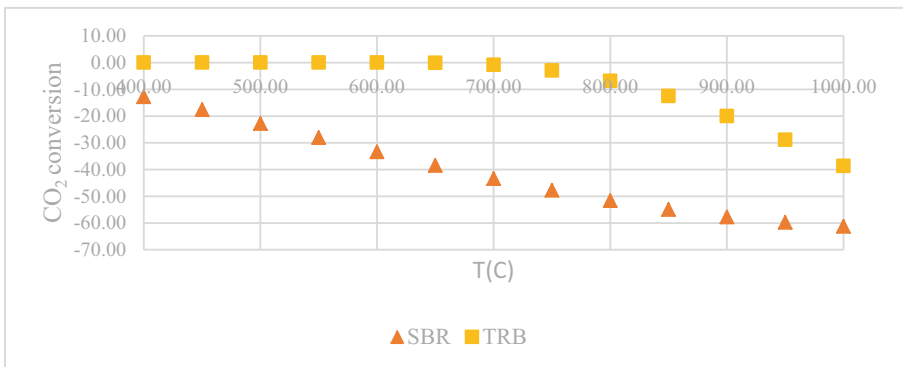


Fig. 8. Carbon dioxide conversion in SBR and TBR at different temperatures.

Both SMR and SBR showed a downward trend from 764.00 and 119.20 to 17.49 and 9.34, respectively in Fig. 9. TRM recorded a constant H₂/CO ratio of 3 throughout

the trial. Meanwhile, TRB remained constant until 700 °C where a ratio of 3.02 was recorded. Then, its values rose gradually to 4.06 at 1000 °C.

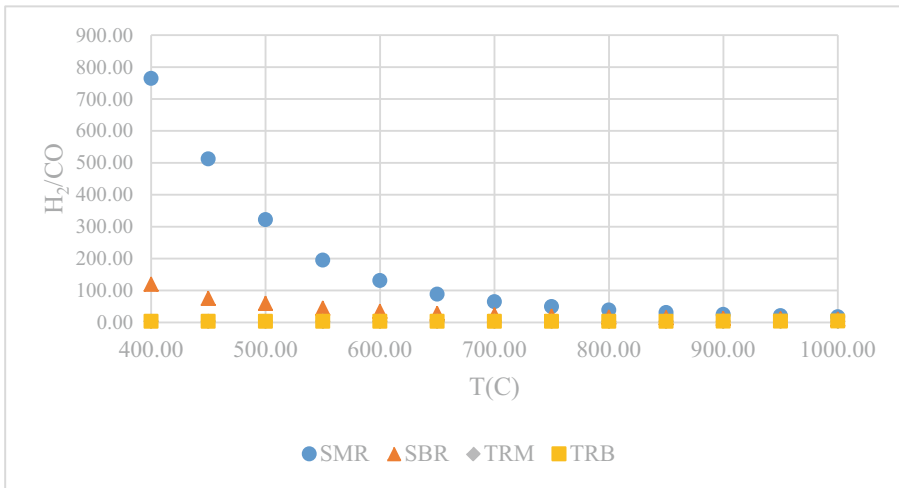


Fig. 9. Ratio of hydrogen to carbon monoxide in different processes at different temperature ranges.

Hydrogen yield recorded similar trends in Fig. 10 to methane conversion in Fig. 7 due to its correlation. It is positively impacted by rising temperature as SMR and DRM reactions are endothermic [33]. When temperature was increased from 400 °C to 1000 °C, upward trends were found in all processes as shown in Fig. 10. SMR, SBR and TRM have very similar trend in yield of 0.24, 0.28, and 1.98 rising to 1.47, 1.94 and 3.00, respectively. TRB has a constant yield of 3.00 until 750 °C where yield of 3.02 was recorded. Then, its values rose gradually to 3.21 at 1000 °C.

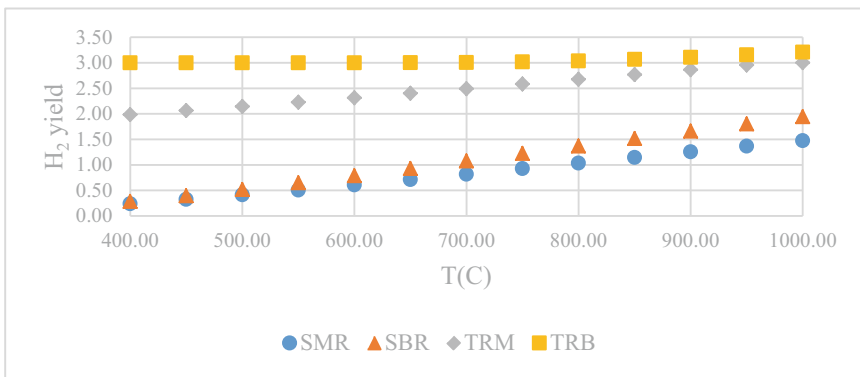


Fig. 10. Hydrogen yield in different processes for different temperatures.

Pressure. Sensitivity analysis was also done for pressure range of 1 to 60 bar. Downward trends were obtained for all processes. SMR, SRB, have methane conversion of 2%, and 28% which dropped to 1% and 16% throughout the trial. TRM maintained 61% at 1 bar to 6 bar before dropping to 60% throughout the rest of the trial. TRB maintained a constant 100% methane conversion throughout the trials, Fig. 11.

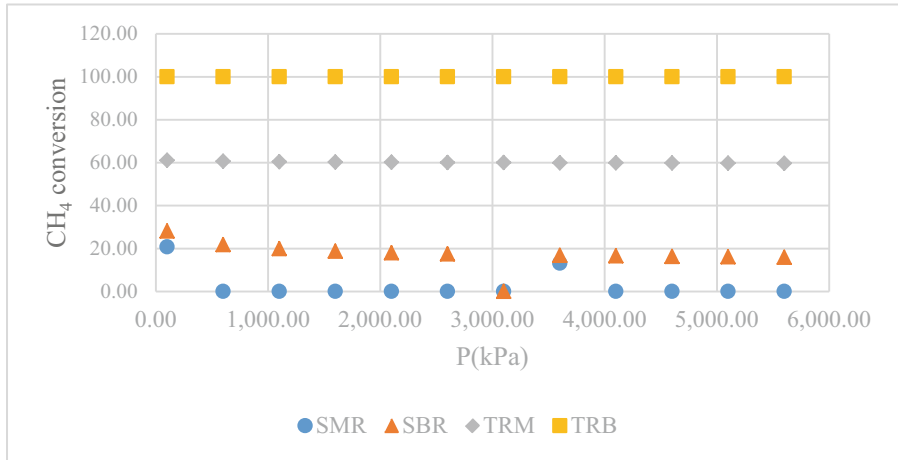


Fig. 11. Methane conversion in different processes at different pressures.

SBR has -43% CO₂ conversion at 1 bar which rose to -22% by 60 bar. TRB has -1% conversion initially before decreasing to -50% at 46 bar onwards, Fig. 12.

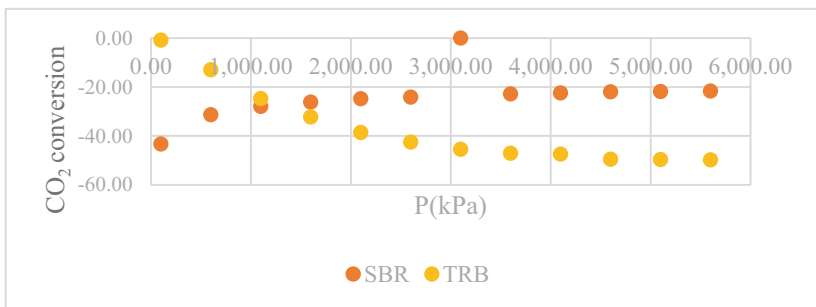


Fig. 12. Carbon dioxide conversion in SRB and TRB at different pressures.

The H₂/CO ratio for SBR dropped from 22.61 to 13.32 throughout the trial. Meanwhile, TRM recorded constant value of 3 throughout the trial. TRB has an initial value of 3.02 at 1 bar which rose gradually to 4.47 at 60 bar, Fig. 13.

Hydrogen yield, Fig. 14, recorded similar trends to methane conversion due to its correlation.

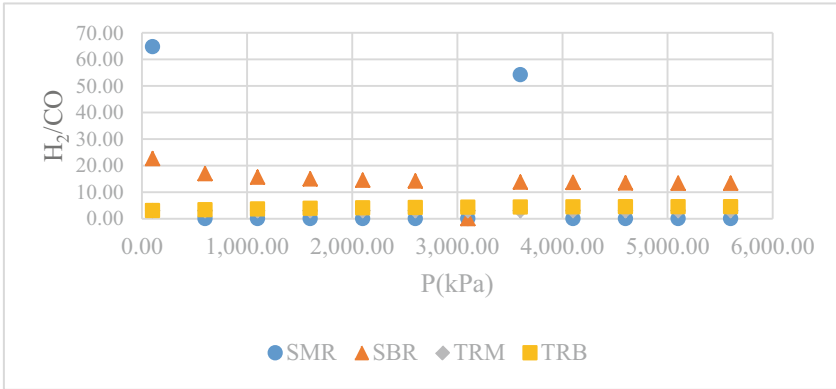


Fig. 13. Ratio of hydrogen to carbon monoxide in different processes at different pressures.

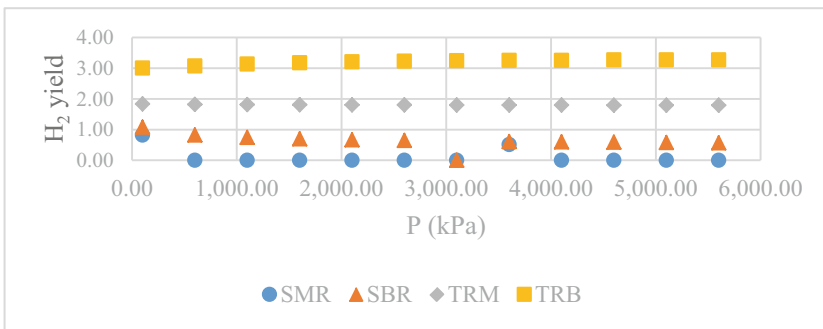


Fig. 14. Hydrogen yield in different processes at different pressures.

It is negatively impacted by rising pressure as cited in many literatures [7, 24, 32]. When pressure was increased from 1 bar to 60 bar, downward trends were found for SMR, SBR and TRM where yield of 0.10, 1.08, and 1.83 decreased to 0.02, 0.57 and 1.79, respectively. TRB has an upward trend where its hydrogen yield increased from 3.00 to 3.27 throughout the trial.

4.4 Limitations

The results for biogas reforming systems are based on retrofitting average POME biogas feed into conventional reforming system, thus, further studies need to be conducted to create specific biogas reforming kinetic models to allow for accurate results. This is due to the characteristically different reaction kinetics and equilibrium involved in the reforming of biogas which has substantial amount of CO₂ naturally.

5 Conclusion

This study achieved its objective to compare and assess the quality of biogas reforming processes via steam reforming of biogas and tri-reforming of biogas with conventional steam reforming (SMR), and tri-reforming (TRM). Sensitivity analysis on S/C ratio, temperature and pressure obtained decent correlation with literature and recorded trends that showed feasibility of SBR and TRB in industrial conditions. Further studies should be done to create and model better biogas reforming kinetics and thermodynamics. Lastly, SRK fluid package was set for the whole experiment due to its accuracy in modelling the specific system. However, within more time, a better prediction might be possible with the usage of PSRK for streams above 10 bar.

References

1. Cavaliere, P.D., Perrone, A., Silvello, A.: Water electrolysis for the production of hydrogen to be. *Metals* **11**(11), 1816 (2021)
2. Kumar, S.S., Himabindu, V.: Hydrogen production by PEM water electrolysis – a review. *Mater. Sci. Energy Technol.* **2**(3), 442–454 (2019)
3. Abad, A.V., Dodds, P.E.: Production of hydrogen. In: *Encyclopedia of Sustainable Technologies*, pp. 293–304 (2017)
4. Katebah, M., Al-Rawashdeh, M., Linke, P.: Analysis of hydrogen production costs in steam-methane reforming considering integration with electrolysis and CO₂ capture. *Clean. Eng. Technol.* **10**, 100552 (2022)
5. Hydrogène, Hydrogen production: Steam Methane Reforming (SMR), 22 June 2022
6. Vanderveen, K., Lutz, A., Klebanoff, L., Drennen, T., Kamery, W., Keller, J.: Projected hydrogen cost from methane reforming for North America 2015–2050. In: *WHEC 16* (2006)
7. Zhao, X., Joseph, B., Kuhn, J., Ozcan, S.: Biogas reforming to syngas: a review. *iScience* **23**(5) (2020)
8. Barroso-Quiroga, M.M., Castro-Luna, A.E.: Catalytic activity and effect of modifiers on Ni-based catalysts for the dry reforming of methane. *Int. J. Hydrog. Energy* **35**(11), 6052–6056 (2010)
9. Rostrup-Nielsen, J.R., Hansen, J.H.B.: CO₂ - reforming of methane over transition metals. *J. Catal.* **144**(1), 38–49 (1993)
10. Wan Abu Bakar, W., Ali, R.: *Natural Gas*. IntechOpen Ltd. (2010)
11. Hong, J.Y., Foong, S.Z.Y., Ng, D.K.S.: Techno-economic evaluation and feasibility study for biogas upgrading projects in a palm oil mill. *J. Oil Palm Environ. Health (JOPEH)* **12**, 96–108 (2021)
12. Maia, D.C.S., et al.: Removal of H₂S and CO₂ from biogas in bench scale and the pilot scale using a regenerable Fe-EDTA solution. *Renew. Energy*, 188–194 (2017)
13. Tira, H.S., Padang, Y.A.: Removal of CO₂ and H₂S from raw biogas using activated natural zeolite. *AIP Conf. Proc.* **1778**, 030006 (2016)
14. Sun, Q., Li, H., Yan, J., Liu, L., Yu, Z., Yu, X.: Selection of appropriate biogas upgrading technology—a review of biogas cleaning, upgrading and utilization. *Renew. Sustain. Energy Rev.* **51**, 521–532 (2015)
15. Persistence Market Research, *Global Market Study on Hydrogen: Emission Reduction Requirements to Create Increased Demand for Hydrogen*, Persistence Market Research, New York City (2020)

16. Navarro, M.V., López, J.P., Grasa, G., Murillo, R.: Effect of oxidation-reduction cycles on steam-methane reforming kinetics over a nickel-based catalyst. *Int. J. Hydrog. Energy* **44**(25), 12617–12627 (2019)
17. Marcobertardino, G.D., Sosia, F., Manzolini, G., Campanari, S.: Fixed bed membrane reactor for hydrogen production from steam methane reforming: experimental and modeling approach. *Int. J. Hydrog. Energy* **40**(24), 7559–7567 (2015)
18. Hajjajji, N., Martinez, S., Trably, E., Steyer, J.P., Helias, A.: Life cycle assessment of hydrogen production from biogas reforming. *Int. J. Hydrog. Energy* **41**(14), 6064–6075 (2016)
19. Rosa, F.D., Smyth, B.M., McCullough, G., Goguet, A.: Using multi-criteria and thermodynamic analysis to optimize process parameters for mixed reforming of biogas. *Int. J. Hydrog. Energy* **43**(41), 18801–18813 (2018)
20. Minutillo, M., Perna, A., Sorce, A.: Green hydrogen production plants via biogas steam and autothermal reforming processes: energy and exergy analyses. *Appl. Energy* **277**, 115452 (2020)
21. Rau, F., Herrman, A., Krause, H., Fino, D., Trimis, D.: Efficiency of a pilot-plant for the autothermal reforming of biogas. *Int. J. Hydrog. Energy* **44**(35), 19135–19140 (2019)
22. Camacho, Y.S.M., Bensaid, S., Piras, G., Antonini, M., Fino, D.: Techno-economic analysis of green hydrogen production from biogas autothermal reforming. *Clean Technol. Environ. Policy* **19**(5), 1437–1447 (2017)
23. Marcobertardino, G.D., Vitali, D., Spinelli, F., Binotti, M., Manzolini, G.: Green hydrogen production from raw biogas: a techno-economic investigation of conventional processes using pressure swing adsorption unit. *Processes* **6**(3), 19 (2018)
24. Minh, D.P., Siang, T.J., Vo, D.V.N., Phan, T.S., Ridart, C., Nzihou, A., Grouset, D.: Hydrogen production from biogas reforming: an overview of steam reforming, dry reforming, dual reforming, and tri-reforming of methane. In: Azzaro-Pantel, C. (eds.) *Hydrogen Supply Chains: Design, Deployment and Operation*, pp. 111–166. Elsevier (2018)
25. Nishimura, A., Takada, T., Ohata, S., Kolhe, M.L.: Biogas dry reforming for hydrogen through membrane reactor utilizing negative pressure. *Fuels* **2**(2), 194–209 (2021)
26. Izquierdo, U., Barrio, V., Requies, J., Cambra, J., Güemez, M., Arias, P.: Tri-reforming: a new biogas process for synthesis. *Int. J. Hydrog. Energy* **38**(18), 7623–7631 (2013)
27. Singh, A.P., Singh, S., Ganguly, S., Patwardhan, A.V.: Steam reforming of methane and methanol in simulated macro & micro-scale membrane reactors: selective separation of hydrogen for optimum conversion. *J. Nat. Gas Sci. Eng.* **18**, 286–295 (2014)
28. Xu, J., Froment, G.F.: Methane steam reforming, methanation and water-gas shift: I. Intrinsic kinetics. *AIChE J.* **35**(1), 88–96 (1989)
29. Ghasem, N.M., Abdullah, E.C.: *Simulation of Unit Operations with Hysys*. Universiti of Malaya Press, Kuala Lumpur (2006)
30. Hydrogen and Fuel Cell Technologies Office: *Hydrogen Production: Natural Gas Reforming*. Hydrogen and Fuel Cell Technologies Office. <https://www.energy.gov/eere/fuelcells/hydrogen-production-natural-gas-reforming>. Accessed 25 Nov 2021
31. Soliman, M., El-Nashaie, S., Al-Ubaid, A., Adris, A.: Simulation of steam reformers for methane. *Chem. Eng. Sci.* **43**(8), 1801–1806 (1988)
32. Chouhan, K., Sinha, S., Kumar, S., Kumar, S.: Utilization of biogas from different substrates for SOFC feed via steam reforming: thermodynamic and exergy analyses. *J. Environ. Chem. Eng.* **7**(2), 103018 (2019)
33. Chouhan, K., Sinha, S., Kumar, S., Kumar, S.: Simulation of steam reforming of biogas in an industrial reformer for hydrogen production. *Int. J. Hydrog. Energy* **46**(53), 26809–26824 (2021)
34. Hydrogen as an Attractive New Energy Source/Carrier, MIDA, July 2021. <https://www.mida.gov.my/hydrogen-as-an-attractive-new-energy-source-carrier/>. Accessed 20 Oct 2021

35. Grand View Research, Inc., Specialty Chemicals Market Worth \$824.1 Billion By 2028 | CAGR: 4.3%, July 2020. <https://www.grandviewresearch.com/press-release/global-specialty-chemicals-market>. Accessed 20 Oct 2021
36. Statista, Leading producers of palm oil worldwide from 2020/2021, 27 January 2021. <https://www.statista.com/statistics/856231/palm-oil-top-global-producers/>. Accessed 20 Oct 2021
37. Wahab, A.G.: Oilseeds and Products Annual. United States Department of Agriculture (2021)
38. Hosseini, S.E., Wahid, M.A.: Pollutant in palm oil production process. *J. Air Waste Manag. Assoc.* **65**(7), 773–781 (2015)
39. Angelidaki, I., et al.: Biogas upgrading: current and emerging technologies. In: *Biofuels: Alternative Feedstocks and Conversion Processes for the Production of Liquid and Gaseous Biofuels: Biomass, Biofuels, Biochemicals*, vol. 2, pp. 817–843 (2019)
40. Shahidul, I., Malcolm, M.L., Eugene, J.: Methane production potential of pome: a review on waste-to-energy [WTE] model. *Environ. Sci.* (2018)
41. Othman, M.N., Lim, J.S., Theo, W.L., Hashim, H., Ho, W.S.: Optimisation and targeting of supply-demand of biogas system through gas system cascade analysis (GASCA) framework. *J. Clean. Prod.* **146**, 101–115 (2017)
42. Madaki, Y.S., Seng, L.: Palm oil mill effluent (pome) from Malaysia palm oil. *Int. J. Sci. Environ. Technol.* **2**(6), 1138–1155 (2013)
43. EDF: Methane: A crucial opportunity in the climate fight. EDF (2021). <https://www.edf.org/climate/methane-crucial-opportunity-climate-fight>. Accessed 20 Oct 2021
44. United Nations: Ensure access to affordable, reliable, sustainable and modern energy, 22 Dec 2021. <https://www.un.org/sustainabledevelopment/energy/>
45. DiChristopher, T.: Experts explain why green hydrogen costs have fallen and will keep falling. S&P Global, 5 March 2021. <https://www.spglobal.com/marketintelligence/en/news-insights/latest-news-headlines/experts-explain-why-green-hydrogen-costs-have-fallen-and-will-keep-falling-63037203>. Accessed 20 Oct 2021
46. Song, C., Pan, W.: Tri-reforming of methane: a novel concept for catalytic. *Catal. Today* **98**(4), 463–484 (2004)
47. Cai, Z., Wang, J., Chen, Y., Xia, L., Xiang, S.: The development of chemical process simulation software. *Chem. Eng. Trans.* **61**, 1819–1824 (2017)
48. Zhao, X., et al.: Correction: conversion of landfill gas to liquid fuels through a TriFTS (tri-reforming and Fischer-Tropsch synthesis) process: a feasibility study. *Sustain. Energy Fuels* **8**, 539–549 (2019)
49. Aboosadi, Z.A., Yadecoury, M.F.: Thermally intensification of steam reforming process by use of methane tri-reforming: a review. *Int. J. Chem. React. Eng.* **17**(12) (2019)
50. Basile, A., Paola, L.D., Hai, F.I., Piemonte, V.: *Membrane Reactors for Energy Applications and Basic Chemical Production*. Woodhead Publishing (2015)
51. Rostrup-Nielsen, J., Christiansen, L.J.: *Routes to Syngas. Concepts in Syngas Manufacture* 10, pp. 1–71. Imperial College Press, London (2011)
52. Schiaroli, N., et al.: Biogas to syngas through the combined steam/dry reforming process: an environmental impact assessment. *Energy Fuels* **35**(5), 4224–4236 (2021)
53. Alipour-Dehkordi, A., Khademim, M.H.: O₂, H₂O or CO₂ side-feeding policy in methane tri-reforming reactor: the role of influencing parameters. *Int. J. Hydrog. Energy* **45**(30), 15239–15253 (2020)
54. Alli, R.D., de Souza, P.A., Mohamedali, M., Virla, L.D., Mahinpey, N.: Tri-reforming of methane for syngas production using Ni catalysts: current status and future outlook. *Catal. Today* (2022)
55. Aboosadi, Z.A., Jahanmiri, A., Rahimpour, M.: Optimization of tri-reformer reactor to produce synthesis gas for methanol production using differential evolution (DE) method. *Appl. Energy* **88**(8), 2691–2701 (2011)



Physical Properties Characterization of Ceramic Waste Particles Used as Filler in Boat Hull Production: A Proposed Study

Fakhrurrazi Rahman¹ (✉) , Che Mohd Ruzaidi Ghazali¹ , Mat Jusoh Suriani¹ , Ahmad Fitriadhy¹ , Nor Aieni Mokhtar² , and Aminnudin³

¹ Faculty of Ocean Engineering Technology and Informatics, Universiti Malaysia Terengganu, 21300 Kuala Terengganu, Terengganu, Malaysia

wanfakhrurrazi41@gmail.com

² Institute of Oceanography and Environment, Universiti Malaysia Terengganu, 21300 Kuala Terengganu, Terengganu, Malaysia

³ Department Teknik Mesin dan Industri, Universitas Negeri Malang, Jawa Timur, Kota Malang 65145, Indonesia

Abstract. Various types of composite materials were being used in boat manufacturing especially for hull production as a main part. Natural composite materials such as teak sawdust, wood ash and silica particles have been utilized in boat hull making from previous researchers. This paper revised mechanical properties impact on several composite materials mixed with epoxy resin matrix by using hand lay-up method. Other than that, the main focused in this study is on the application of ceramic particles waste as a composite material. In-stead of being used as land-filling, ceramic particles waste can be reused in becoming value-added composite materials in specific area which brings benefits to environment and enhance the properties for other materials in terms of physical and mechanical. This study also presents an assembled and up-to-date review of physical, mechanical, durability and other durable potential abilities of ceramic fine aggregate which have huge ability usage in concrete production, soil stabilization, bricks block and road pavement structure. The percentage of particles usage from previous studies were from 2% up to 20% and the findings indicate that usage of ceramic waste particles improves flexural, durability, compressive, geotechnical and mechanical strength properties compare to standard materials usage. Thus, a new application area will be explored from this study on the usage of ceramic particles waste to the resin on the interface between the composite materials and core materials used in production of boat hull.

Keywords: Ceramic Waste Aggregate · Boat Manufacturing · Composite · Mechanical Strength · Boat Hull

1 Introduction

A composite material is a combination of two or more materials that exhibits superior qualities than those of the component parts utilized separately. A reinforcement and a matrix are the two constituents [1].

We can find a matrix-based classification such as the classification through the many composite material classification schemes, where the important types of advanced composites can be depicted in the pie chart below Fig. 1, which describes the five principal types of advanced composite material in wide use. Polymer Matrix Composites (PMC), Metal Matrix Composites (MMC), Ceramic Matrix Composites (CMC), Carbon-Carbon (CC), and Hybrids comprised of a combination of the aforementioned matrices are among the composite varieties [2].

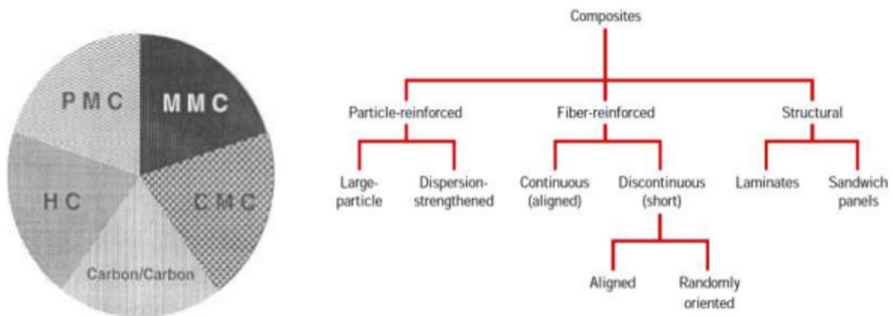


Fig. 1. Composite reinforcement flow [2].

The field of composite materials science is rich and full of design varieties and potentials. In depth study is needed in order to understand the relevant design aspects, methodology and tools of composites; because they differ greatly from those for standard building materials such as steel and aluminum.

The aim of this study is the assessment of the filler properties used within PVC foam for boat hull production using waste ceramic waste particles as natural fine aggregate partial substitute for structural adhesive bond. In order to achieve this, waste ceramic particles were mix in several percentage ratio to test the mechanical properties from the mixing samples.

2 Composite for Boat Hull Production

Composites will play a growing role in boat building due to their lightness, strength, durability, and ease of production. Nonetheless, composites are just recently becoming a key material of choice in some industries. The use of composites in the construction industry is steadily expanding. Fiber reinforced polymer (FRP) composites are widely used for fortifying boat hull because they have many advantages over conventional strengthening methods [3]. Carbon, glass, and aramid fibres are commonly employed in the manufacture of FRP composites for construction. All of these fibres are commercially accessible as continuous filaments. To bind the fibres together, the polymer resin surrounds and encapsulates them, safeguard them from adverse effects, sustain their proper position, and facilitate the division of load between them.

2.1 Natural Composite for Boat Hull Production

Historically, the vast bulk of the maritime sector has relied on various recreational or pleasure boats of various sizes, generally made of conventional composites. Furthermore, the shipbuilding industry has been seeking for many years to include more composite materials in major merchant and passenger ships via hybrid hull designs [4]. Some uses include a composite bow and stern structure, a composite outer layer that is supported by a steel truss, straightforward integration of composite load-carrying decks within a traditional steel ship structure, and even a complete ship hull composed of composite material.

The economics of bio-composites, mechanical properties of different types of bio-composites in standard and marine environments, fouling resistance, and the effects of hygroscopicity, biodegradability, and eutrophication on structural integrity and the marine environment are all addressed in research and development of bio-composites. Study presented by [5] for the usage of epoxy resin mix together for ship hull components studied on tensile and flexural durability with 28 m% bio-based carbon content supplemented with flax and hemp (dry and wet). The results of tensile were 68.6 MPa and 73.8 MPa for dry and wet flax, 73.8 MPa and 39.1 MPa results for flexural test for dry and wet flax. Meanwhile, for tensile test of dry and wet hemp were 45.7 MPa and 31.3 MPa, flexural test resulted in 81.2 MPa and 60.4 MPa for dry and wet hemp. It shows that flax and hemp have different strength in tensile and flexural test. Dry flax has the highest tensile strength for overall results and wet hemp has higher flexural strength compare with dry hemp.

Usage of Ceramic Waste for Improvement in Various Areas. It is believed that around 30% of the daily manufacturing of ceramic tiles goes into waste, which waste will not be recycled in any way at this time [6]. However, Ceramic waste was long-lasting, robust, and resistant to biological, chemical, and physical degrading processes [7]. As the ceramic tiles piled up every day, the ceramic industries were under pressure to find a solution for this form of disposal. Meanwhile, conventional stone crushed aggregate reserves are rapidly dwindling; however, the effective use of inorganic industrial leftover products will result in a more sustainable and environmentally friendly environment [8].

Recyclables ceramic tiles are far too impure to be re-used in tile production and are typically disposed of as junk in landfills. The elimination of ceramic tiles in the surroundings causes problems due to the vast amount of waste produced every single day, which may increase the cost of management. If this waste becomes a burden on the ceramic industries to adopt a feasible solution for this type of disposal, it would have a negative influence on the environment. Unfortunately, the removal of waste ceramic tiles will add an additional maintenance cost to the total production costs [9]. Using this waste for other purposes is one solution to this challenge [10]. Thus, waste ceramic tiles can be recycled in order to save money and introduced as new materials from waste to wealth [11].

Several research have been conducted on the application of ceramic waste as coarse particles, powder, and filler in cement mortar preparation [12–14], concrete [15–17] and self-compacting concretes [18–20], high strength concrete [21] and ultra-high performance concrete [22]. Researchers have also researched and analyzed the mechanical

properties of mortar and concrete containing ceramic waste. The majority of data demonstrated that the mechanical strength of concrete is comparable or even better than those containing natural aggregates for up to optimal percentage substitution of natural sand by ceramic waste. The influence of ceramic waste as aggregate (CW), dust (FTDA), and their combinations on the production of concrete was investigated. They discovered an increase in compressive and flexural strength of around 13.53, 16.70, 2.91% and 23.21, 0.10, 19.47% at 2, 7, and 28 days [7].

Aside from that, ceramic tile waste is used for road slope embankment. Study was done by [23], evaluated the utility of ceramic tile waste (CTW) as an admixture for fine sand, with a focus on increasing the engineering qualities of fine sand to make it capable of reducing cross section of embankment for roadway construction. Results shows that when CTW were used up to 12%, may also increase the height of embankment and at the same time reduce the cost of working materials which varies from 16% to 20% cost of reduction. It shows that the properties of the CTW which is high durability and strength can be used for another replacement in various field of area.

Study done by [24] related with percentage of ceramic particles used in boat hulls production to accelerate aging test and also mechanical test using 2% of nano-silica which is from the ceramic waste particles. Results from this study shows that the addition of 2 wt% nano-silica permitted to increase the material flexural strength in 5.8%. The study also reported for 1000h aged configuration and sample with additional of 2% nano-silica resulted in increased flexural strength up to 8.7%. Silicon painting was applied in order to protect the hull from corrosive environment.

Study done by [25] related with the utilization of ceramic tile demolition waste (CTDW) as a paste were used up to 30% of CTDW comparing with limestone as a reference filler in Portland cement. The results show better increment up to 5% for CTDW comparing with limestone. Throughout this study, the material preparation of CTDW were being follow up as a reference. CTDW powder was processed for 1 h at 300 rpm in a planetary ball mill, yielding a diameter of 76.5 μm .

3 Material and Methodology

Multiple processes are required, beginning with the processing of the ceramic particles from raw sizing into smaller particle sizes via milling. Then, the particles will undergo meshing process using mechanical sieve shaker to segregate the size of ceramic particles before being compared with existing composite industrial filler, which are KONASIL K200 and Q-Cell 5020. The finest ceramic particles from sieving process will be test through the Particle Size Analyzer (PSA) to analyze the peak size of the particles and also undergo morphology to investigate quantified information physical relationship of the size of ceramic particles and existing composite industrial filler. Table 1 shows the properties and application of industrial filler used for production of hull.

Table 1. Properties of industrial filler used for hull production.

	KONASIL K200	Q-CEL 5020
PROPERTIES	<ul style="list-style-type: none"> • Fluffy, white powder of nano-sized amorphous structure • Extremely small particle size and spherical, morphology, high surface area, unique surface chemistry and high purity 	<ul style="list-style-type: none"> • Single cell hollow microspheres appear as a white free flowing powder • As filler to reduce density but can enhance other properties as well
CHEMICAL COMPOSITION	<ul style="list-style-type: none"> • SiO₂ > 99.8% min • Al₂O₃ < 0.05% max • Fe₂O₃ < 0.003% max • TiO₂ < 0.003% max 	<ul style="list-style-type: none"> • SiO₂ + B₂O₃ > 99.5% min • Siloxane < 0.5% max • Methyl Hydrogen < 0.5% max
PARTICLE SIZE	7 μm to 40 μm	30 μm -125μm

3.1 Milling Process

Preparation of the ceramic particles by undergo laboratory mill using Retsch Planetary Ball Mill PM-100 by using several milling speeds in Table 2. The purpose of having milling process is to verify the particles distribution and obtained specific sizes of ceramic particles up to micrometer sizing.

Table 2. Milling Parameter Ball Mill PM-100.

Milling speed (RPM)	Milling time per cycle (min)	Jar sizes	Milling ball types	Milling ball charge (piece)
300	30	250ml	Stainless Steel Grinding Balls	7
350	30			
380	30			

Particle Size. The cone and quartering technique were applied to get the necessary sample for the analysis of ceramic particles following crush, then optimum sieving time, 30 min per cycle to get particle size distributions, it was determined for all samples. For dry sieving testing, a Ro-Tap shaker (Retsch GmbH, Haan, Germany) was utilised (with an amplitude of 50 on a 0–100 scale and a constant vibration frequency of continuous). Apertures on laboratory wire mesh sieves were 425 m, 250 m, 150 m, 63 m, and 32 m. Related with sieving rate, the after milling particles where weight for 50g to be sieved for 30 min. This is because the water absorption for ceramic particles were 4% to 6% when exposed to the surrounding making the particles agglomerate and clumped when the quantity is overload.

Particle Size Analyzer (PSA) Anton Paar 1190 multi-laser system with measurement range liquid of 0.04 m to 2500 m and dry range of 0.1 μm to 2500 μm was used to analyse the distribution of ceramic particles after sieving procedure. In order

to obtain the average distribution pattern for each powder, all sieving samples powder with milling ranges of 300 RPM, 350 RPM, 380 RPM, and existing industrial filler were examined. The particle size distribution and zeta potential of the samples were determined. Dynamic light scattering (DLS) studies with the Litesizer 500 in were used to accomplish laser diffraction measurements. Surfactant must be applied before running to avoid powder agglomeration when the samples are inserted into the PSA medium. Surfactants are amphiphilic molecules that support particle dispersion by reducing surface tension between particles and the surrounding medium. Thus, for ceramic particles 4% of Calgon solution (sodium metaphosphate) were applied to the PSA medium shown in Table 3.

Table 3. PSA setting parameter.

Surfactant media	Ultrasound	Stirrer speed	Pump speed	Measuring time
4% Calgon Solution	During measurement	Medium	Medium	30 s

The morphology of each filler was examined using a JEOL JSM SEM-6360 Scanning Electron Microscope (SEM). Fillers were placed in a graphite die with an external and internal diameter of 30 mm and 15.5 mm, respectively, as well as a graphite punch with a diameter of 15 mm and a height of 20 mm. Subsequently, the powders coated using Aurum (Au) by Auto-Fine coater model JEOL JFC-1600 (Fig. 3.6b) for 5 to 10 min for each sample under an applied pressure of 5 Pa and carried out in a vacuum.

4 Results

4.1 Particle Size Distribution

The screening of ceramic waste particles after milling reveals that a speed of 380 RPM produces the closest mean size to industrial filler, which is in the range of 15 μm to 16 μm as shown in Fig. 2. It shows that ceramic waste particles able to achieve nearest particles size towards the industrial filler (KONASIL K200 and Q-CEL 5020) whereas the highest percentage of materials content in the ceramic waste particles were silica (SiO_2) content which is in the range of 70% to 75%. Thus, this material is suitable to be formulated as filler content in PVC foam for the hull production.

Apparent Density. Perceived density is affected by moisture content, solid type, and air volume percentage. The apparent density of ceramic waste particles was in the range of 0.542 to 0.55 g/cm^3 which is higher than industrial filler as shown in Table 4. Results shows that ceramic waste apparent density higher than industrial filler. Thus, it will slightly affect the weight volume applied on the PVC core in hull production.

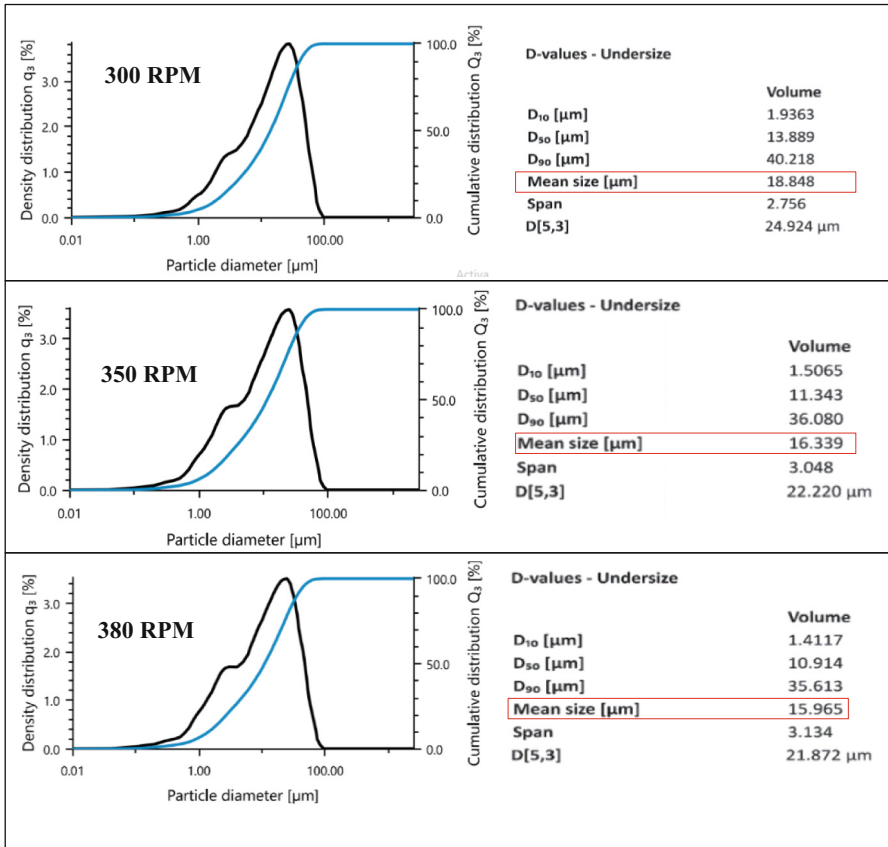


Fig. 2. Mean size after milling for ceramic waste particles.

Table 4. Apparent density of industrial filler and ceramic waste particles.

Fillers Type	KONASIL K200	Q-CEL 5020	CERAMIC WASTE PARICLES
Apparent Density (g/cm ³)	0.212 – 0.2	0.14 – 0.2	0.542 – 0.55

Through this comparison, the mixing formulation for the filler must be considered by this apparent density as it will affect the overall volume and density of the hull production. By the properties presented by industrial filler, it shows that industrial filler has lower Elastic Modulus (E), Hardness (HR) and Tensile Strength (σ) comparing to ceramic waste particles. These properties are related with the apparent density of the materials.

Apparent Density. Specimen Morphology. Zoom magnifications of 150x and 400x, the microstructures of KONASIL K200, Q-CEL 5020, and ceramic waste particles are shown in Fig. 3.

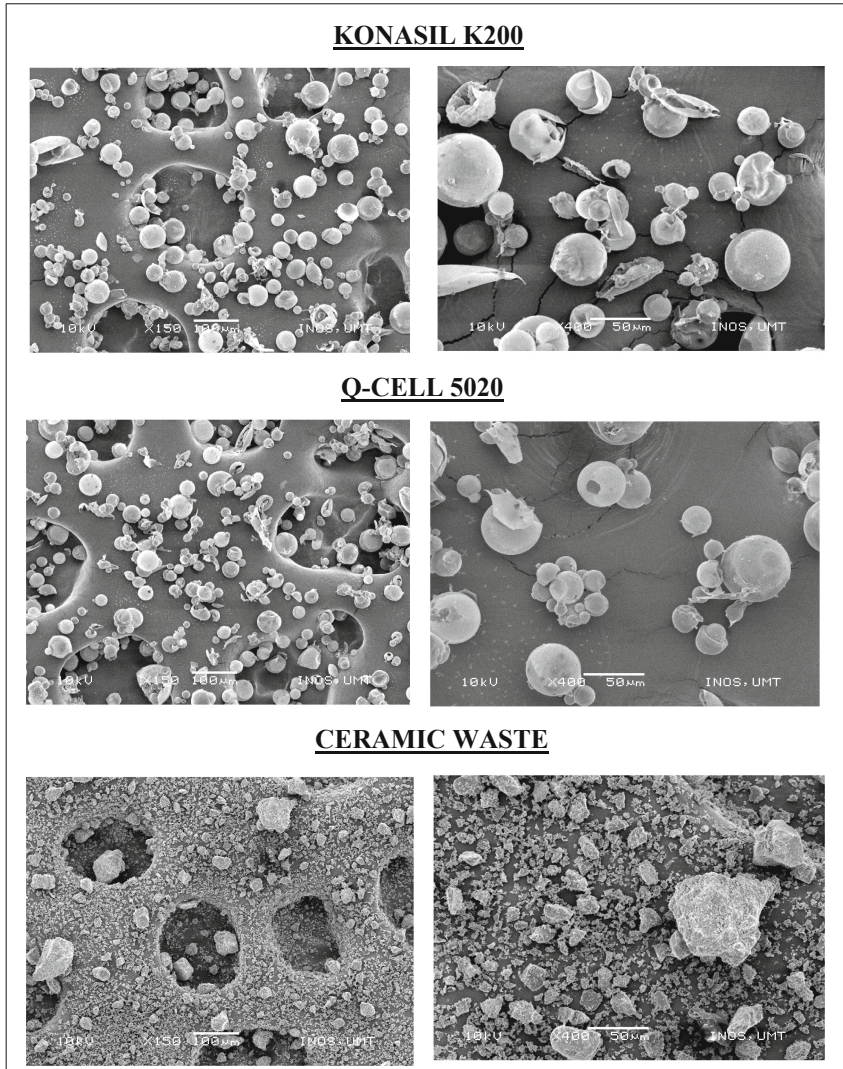


Fig. 3. Microstructure of KONASIL K200, Q-Cel 5020 and ceramic waste particles in 150x and 400x magnification through SEM.

KONASIL K200 has spherical and pure forms. The same occurs for Q-Cell 5020, which contains hollow microsphere forms. Through the properties of these two types materials used for hull production, The microstructure features balloon-type qualities with a density around one-fifth that of ordinary thermoset resins. On an equal weight

basis, Q-Cel hollow micro-spheres take up five times the volume of an equivalent weight resin. They have the ability to displace heavy fillers, reducing the weight of composite materials. Because spheres have the smallest surface area, they require the least amount of resin. Lower viscosities are prevalent, allowing less resin to be utilized while increasing production volume, leading in cost reductions in many applications.

When compared to industrial filler, ceramic waste particles have uneven forms and fill voids. In terms of characteristics, this material is composed of crystalline solids with polyhedral individual particles. This is significant because the underlying dynamics of polyhedral particles differ greatly from those of spherical particles, resulting in tighter packing fractions, distinct flow patterns, and percolation.

5 Conclusion

In this paper, the focused on proposed using ceramic waste particles as filler in boat hull production. The properties of this material were being compared with industrial filler in terms of particle size distribution, apparent density and morphology of the particles. It shows that ceramic waste particles have similar properties and suitable to be mix with the industrial filler in several suitable range. For the achievement of the above work, an experimental work was being prepared where all the necessary inputs will be made. Results from mechanical milling (300 rpm, 350 rpm & 380 rpm), mechanical sieving and particle size characterization were related with achievement in characterize physical properties of ceramic waste particles to be used as filler materials in boat hull production (from waste to wealth). Packing arrangement of the specimens show different characteristics for each specimen which will be closely related to the mechanical behavior of the fillers.

In the future, the mechanical and physical properties of ceramic waste particles will be evaluated using the influence of the mixing ratio of ceramic waste particles mixed with industrial fillers and varied ranges of epoxy resin attached to PVC core.

Acknowledgements. Authors would like to thank all the members under project of “Transforming Coastal Fisheries Through Model Prototype Design and Development” UMT, technicians and staffs from UMT Maritime Technology Lab for their contribution and helps.

Funding. This research study is funded by the Ministry of Science and Technology (MOSTI) under the project “Transforming Coastal Fisheries Through Model Prototype Design and Development” (SRF02211037 MOSTI).

References





1. Campbell, F.C.: Structural Composite Materials. ASM International, Materials Park, Ohio, 1st Edition, pp.1–29 (2010)
2. Vinson, J.R., Sierakowski, R.L.: The Behaviour of Structures Composed of Composite Materials, Kluwer Academic Publishers, ISBN: 1–4020–0904–6 (2004)

3. Gargano, A., Pingkarawat, K., Blacklock, M., Pickerd, V., Mouritz, A.P.: Comparative assessment of the explosive blast performance of carbon and glass fibre-polymer composites used in naval ship structures. *Composite Structure* **171**, 306–316 (2017)
4. Rubino, F., Nisticò, A., Tucci, F., Carlone, P.: Marine application of fiber reinforced composites: a review. *J. Marine Sci. Eng.* **8**(1), 26 (2020)
5. Haramina, T., Hadži'c, N., Keran, Z.: Epoxy Resin Biocomposites Reinforced with flax and hemp fibers for marine applications. *J. Marine Sci. Eng.* **11**, 382 (2023)
6. Binici, H.: Effect of crushed ceramic and basaltic pumice as fine aggregates on concrete mortars properties. *Constr. Build. Mater.* **21**(26), 1191–1197 (2007)
7. Tabak, Y., Kara, M., Günay, E., Yildirim, S.T., Yilmaz, Ş.: Ceramic tile waste as a waste management solution for concrete. In: 3rd International Conference on Industrial and Hazardous Waste Management (2012)
8. Senthamarai, R.M., Manoharan, P.D.: Concrete with ceramic waste aggregate. *Cement Concrete Composite* **27**(9–10), 910–913 (2005)
9. Sourav, R., Mohaiminul, H., Nazmus Sakib, Md., Ayesha Ferdous Mita, Masnun Rahman, M.D., Bibha B.T.: Use of ceramic wastes as aggregates in concrete production: a review. *J. Building Eng.* **43** (2021)
10. Wattanasiriwech, D., Saiton, A., Wattanasiriwech, S.: Paving blocks from ceramic tiles production waste. *J. Clean. Prod.* **17**(18), 1663–1668 (2009)
11. Topçu, İ.B., Canbaz, M.: Utilization of crushed tile as aggregate in concrete. *Iranian J. Sci. Technol. Trans. B, Eng.* **31**(B5), 561–565 (2007)
12. Beata, K., Jacek, S., Paweł, O.: The effect of replacing sand with aggregate from sanitary ceramic waste on the durability of stucco mortars. *Clean Technol. Environ. Policy* **22**, 1929–1941 (2020)
13. Abadou, Y., Kettab, R., Ghrie, A.: Durability of a repaired dune sand mortar modified by ceramic waste. *Eng. Struct. Technol.* **10**(1) (2018)
14. Farinha, C.B., de Brito, J., Veiga, R.: Incorporation of fine sanitary ware aggregates in coating mortars. *Constr. Build. Mater.* **83**, 194–206 (2015)
15. Ogawa, Y., Bui, P.T., Kawai, K., Sato, R.: Effects of porous ceramic roof tile waste aggregate on strength development and carbonation resistance of steam-cured fly ash concrete. *Constr. Build. Mater.* **236**, 117462 (2020)
16. Keshavarz, Z., Mostofinejad, D.: Steel chip and porcelain ceramic wastes used as replacements for coarse aggregates in concrete. *J. Clean. Prod.* **230**, 339–351 (2019)
17. Elci, H.: Utilisation of crushed floor and wall tile wastes as aggregate in concrete production. *J. Clean. Prod.* **112**(1), 742–752 (2016)
18. Subaşı, S., Öztürk, H., Emiroğlu, M.: Utilizing of waste ceramic powders as filler material in self-consolidating concrete. *Constr. Build. Mater.* **149**, 567–574 (2017)
19. Viramgama, P.D., Vaniya, S.R., Parikh, K.B.: Effect of ceramic waste powder in self compacting concrete properties: a critical review. *IOSR J. Mech. Civil Eng.* **13**(1), 8–13 (2016)
20. Huseien, G.F., Mirza, F., Ismail, M.: Effects of high-volume ceramic binders on flexural strength of self-compacting geopolymer concrete. *J. Comput. Theoretical Nanosci.* **24**(6) (2018)
21. Zareei, S.A., Ameri, F., Bahrami, N., Shoaei, P., Musaei, H.R., Nurian F.: Green high strength concrete containing recycled waste ceramic aggregates and waste carpet fibers: mechanical, durability, and microstructural properties. *J. Build. Eng.* 100914 (2019)
22. Soleimani, S.M., Alaaqad, A.R., Jumaah, A., Majeed, A.: Examining the effects of introducing and combining electric-arc furnace slag and ceramic waste in a single self-consolidating. *High-Strength Concrete Mix. Appl. Sci.* **10**(14), 4844 (2020)

23. Parihar, H.S., Verma M.: Reduction in cross section of embankment of road slope with support of software intended at fine sand with ceramic tile waste material. *Mater. Today; Proc.* **45**(2), 3259—3263 (2021)
24. Savva, G.: Accelerated Aging Test on Composite Boat Hulls Produced by Infusion Process. Universidade Nova, online: https://run.unl.pt/bit-stream/10362/92309/1/Savva_2019.pdf (2019)
25. de Matos, P.R., et al.: Utilization of ceramic tile demolition waste as supplementary cementitious material: an early-age investigation. *J. Build. Eng.* **38**, 102187 (2021)



Yield of Biochar from Shrimp Shell Torrefaction and its Characterization: Proximate, Ultimate, and FTIR Spectroscopy Analyses

Nurul Iffah Farhah Mohd Yusof¹ , Alia Syafiqah Abdul Hamed¹ , Aminnudin² ,
Che Mohd Ruzaidi Ghazali¹, and Nur Farizan Munajat³ 

¹ Faculty of Ocean Engineering Technology and Informatics, Universiti Malaysia Terengganu, 21030 Kuala Nerus, Terengganu, Malaysia

² Departemen Teknik Mesin dan Industri, Universitas Negeri Malang, Malang, Indonesia

³ Renewable Energy and Power Research Interest Group (REPRIG), Eastern Corridor Renewable Energy SIG, Faculty of Ocean Engineering Technology and Informatics, Universiti Malaysia Terengganu, 21030 Kuala Nerus, Terengganu, Malaysia
nurfarizan@umt.edu.my

Abstract. This study explores the potential of shrimp shells (SS), a widely available waste material, for biofuel production through torrefaction, offering an alternative approach to address environmental and energy scarcity issues. The torrefaction was conducted at 200, 250, and 300 °C in a fixed bed reactor, resulting in varying yields of biochar, bio-oils, and biogas. As the temperature increased, the biochar yield declined from 64% to 34%, while the bio-oils and biogas yields rose to 28% and 38% respectively. Compositional changes were investigated using proximate and ultimate analyses, revealing significant reductions in moisture (from 22.97% to 4.55%) and volatile matter (from 71.67% to 20.19%), while the fixed carbon content increased from 3.48% to 68.91%. FTIR spectroscopy confirmed structural alterations in the SS, including dehydration and transformations of specific compounds. The results suggest the feasibility of SS torrefaction for biochar production, which has potential applications in carbon sequestration and energy generation.

Keywords: Shrimp shell · Torrefaction · Biochar · Ultimate and proximate analysis · FTIR spectroscopy

1 Introduction

The shrimp industry is a rapidly growing sector globally, with countries like Malaysia significantly contributing to worldwide shrimp production. However, this expansion comes with an increase in waste generation. It is estimated that 50–60% of the total shrimp mass results in solid waste by-products, including the head, viscera, and shell [1]. Shrimp shells, primarily composed of chitin, protein, and mineral salts, offer considerable potential in a range of applications. Additionally, they contain bioactive compounds, including lipids and carotenoids, which are invaluable in food, feed, and functional food

preparation. These bioactive compounds have also shown promise in energy conversion, bioremediation, and bioplastic sectors [1]. Biochar production through thermochemical conversion processes, like pyrolysis, has been identified as an innovative approach for shrimp shell waste utilization. Recent studies, such as those by Elango et al. [2] and Yang et al. [3], have highlighted the innovative uses of SS biochar in the synthesis of carbon quantum dots (CQDs) and the recovery of valuable compounds, respectively. Huang [4] also demonstrated the viability of biochar from mantis shrimp shells as active electrode materials for supercapacitors. Similarly, Yang et al. [3] and Wu et al. [5] provided evidence for using SS-derived biochar to efficiently remove environmental pollutants. Vandecasteele's work [6] further revealed the potential of chemically and thermally processed shrimp shells as sources of chitin, nutrients, salts, and microbial stimulants in soilless strawberry cultivation. Torrefaction, a milder form of pyrolysis, not only yields biochar but also serves as a beneficial preparatory step, potentially enhancing the efficiency of subsequent pyrolysis and thereby improving biochar properties. Despite the considerable amount of research on shrimp shell pyrolysis, studies focusing specifically on shrimp shell torrefaction are relatively scarce. This study, therefore, aims to address this research gap by evaluating the torrefaction process of shrimp shells at varying temperatures, focusing on its impact on biochar yield. In addition, this research delves into the compositional changes in torrefied shrimp shells using proximate, ultimate, and Fourier-transform infrared (FTIR) analyses. Doing so provides insights into the structural and chemical transformations that occur during torrefaction.

2 Materials and Methodology

This study employed white leg shrimp shell (*Litopenaeus vannamei*) as the feedstock, obtained from the local fish market. The SS underwent a drying process under ambient conditions of 25–28 °C for 24 h, followed by grinding and sieving to achieve a particle size of less than 150 µm. The prepared SS was then subjected to torrefaction in a fixed bed reactor, similar to the one used in a previous study [7], at temperatures of 200, 250, and 300 °C. Nitrogen flow was maintained at 50 ml/min for 30 min. Following the torrefaction process, the reactor and samples were cooled down to room temperature, with the volatile byproducts collected and weighed. This procedure was replicated three times to calculate the yield of the solid char, condensable liquid, and gas product with a recorded uncertainty of less than ±1.5%. The raw and torrefied SS solid char were then analyzed for their carbon (C), hydrogen (H), and nitrogen (N) content using a Vario MICRO Cube elemental analyzer, while the oxygen (O) content was calculated by subtracting the sum of the C, H, and N percentages from 100. The moisture content (MC), volatile matter (VM), and ash content (AC) were identified according to the JIS M8812 standards, and the fixed carbon (FC) content was calculated by subtracting the MC, VM, and AC percentages from 100. The functional groups present on the biochar's surface were analyzed using a SHIMADZU IRTracer-100 Fourier-transform infrared (FTIR) spectrometer, scanning the IR spectral region between 4000 to 400 cm⁻¹.

3 Results and Discussions

3.1 Mass Product Yields

The torrefaction of SS at varying temperatures (200 °C, 250 °C, and 300 °C) resulted in different proportions of biochar, bio-oils, and biogas as presented in Fig. 1. An observed trend shows a decrease in biochar yield and an increase in bio-oils and biogas production as the torrefaction temperature rises.

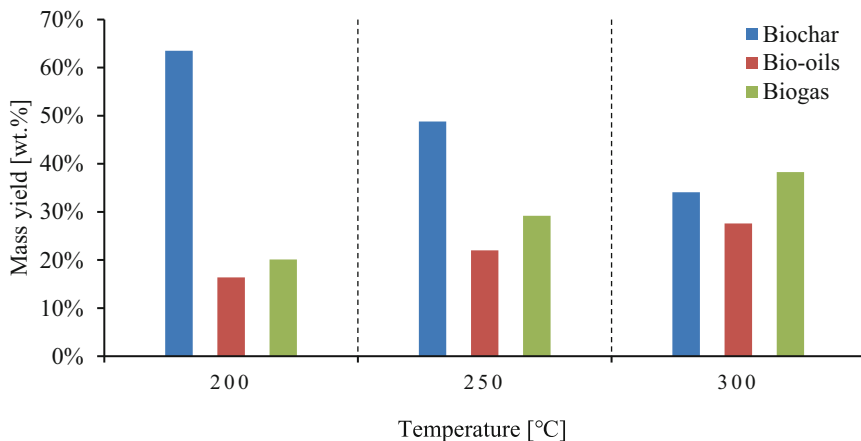


Fig. 1. Mass recovery from the torrefaction process of 30 min.

At the torrefaction temperature of 200 °C, biochar constituted the majority of the product, amounting to 64% of the total yield. The remaining yield was composed of bio-oils and biogas, which accounted for 16% and 20% respectively. Raising the torrefaction temperature to 250 °C led to a reduction in biochar yield to 49%, while the yields of bio-oils and biogas experienced an increase to 22% and 29% respectively. This shift in product distribution favours the production of bio-oils and biogas over biochar with an increase in temperature. At the highest torrefaction temperature of 300 °C, the trend continued, with biochar yield-reducing further to 34%. Meanwhile, the yield of bio-oils and biogas increased to 28% and 38% respectively, indicating a significant enhancement in bio-oils and biogas production at this temperature. These results suggest that the torrefaction temperature plays a significant role in determining the yield and type of bio-products from SS. The higher the torrefaction temperature, the lower the biochar yield, while the bio-oils and biogas yield increases. This trend can be attributed to the increased thermal cracking of the organic compounds present in the SS at elevated temperatures, leading to a higher production of volatile compounds, which in turn form the bio-oils and biogas.

3.2 Ultimate and Proximate Analysis

The proximate and ultimate compositions of the raw SS and the biochar obtained at different torrefaction temperatures (200 °C, 250 °C, and 300 °C) were depicted in Fig. 2.

Initially, the raw SS showed a moisture content (MC) of 22.97% and a volatile matter (VM) of 71.67%. The fixed carbon (FC) and ash content (AC) was relatively low at 3.48% and 1.88% respectively. Torrefaction at 200 °C led to a significant reduction in MC and VM to 7.73% and 44.01% respectively.

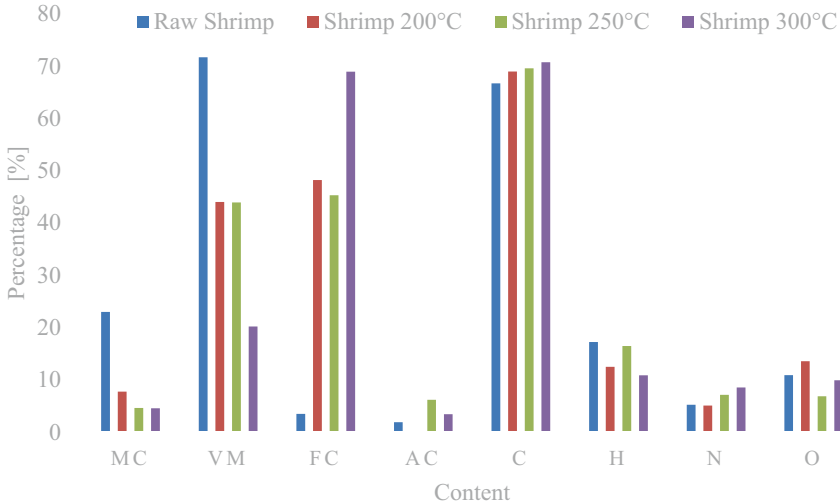


Fig. 2. Ultimate and proximate analysis of raw and torrefied SS.

This reduction can be attributed to the thermal degradation of organic matter and is consistent with a higher yield of biochar than raw SS discussed previously. The FC content increased dramatically to 48.20%, indicating a higher carbon-rich biochar yield. The AC remained minimal, suggesting less formation of inorganic waste products. As the torrefaction temperature increased to 250 °C, the MC reduced further to 4.62%, indicating a continued dehydration process which could increase the energy density of the biochar. The VM showed little change, while FC decreased slightly to 45.30%. However, a notable increase in AC to 6.18% may suggest a higher yield of inorganic compounds due to thermal breakdown. At the highest torrefaction temperature of 300 °C, MC fell slightly to 4.55%, but VM saw a large decrease to 20.19%, indicative of extensive thermal breakdown. The FC content soared to 68.91%, implying a high yield of thermally stable carbon structures. AC fell to 3.42%, suggesting less thermal conversion from organic to inorganic compounds at this temperature. The ultimate analysis revealed that the raw SS were composed of 66.70% carbon (C), 17.21% hydrogen (H), 5.20% nitrogen (N), and 10.89% oxygen (O). After torrefaction at 200 °C, the C content raised to 68.94% while the H content decreased to 12.48%. This shift suggests the initiation of thermal decomposition and devolatilization processes, translating organic matter into carbon-rich structures. The N content minimally decreased to 5.05%, while the O content slightly rose to 13.53%. At a higher torrefaction temperature of 250 °C, the C content further increased to 69.58%, while the H content increased to 16.46%. This increase in hydrogen content might be due to the rearrangement or reformation of hydrogen-containing compounds under increased thermal conditions. Notably, the nitrogen content

rose to 7.13%, implying thermal stability and lower volatility of nitrogenous compounds during torrefaction. The O content experienced a significant drop to 6.84%, possibly due to intensified decarboxylation and other oxygen-releasing reactions. At the maximum torrefaction temperature of 300 °C, the C content reached a high of 70.71%, while the H content decreased to its lowest at 10.86%. The declining hydrogen content suggests an enhanced thermal breakdown of hydrogen-rich compounds, releasing hydrogen as a gaseous product. The N content continued to rise, reaching 8.52%, further substantiating its thermal stability. The O content pattern remained complex, with a slight rise to 9.91%, which could be due to the restructuring of the remaining biomass, causing a relative increase in the O content. The reduction in MC and VM, variation in FC and AC, increase in C, and decrease in H content with temperature are consistent with the thermal degradation and carbonization processes reported in the literature [8–10]. The complex trends observed for N and O suggest more intricate reactions and transformations taking place during torrefaction. These results, alongside the high C in biochar, suggest potential applications of this biochar as a soil amendment to improve carbon sequestration and as a feedstock for energy production given its high FC content and reduced VM.

3.3 FTIR Analysis

FTIR analysis was carried out to determine the functional groups and structural changes in the SS before and after torrefaction. Figure 3 presents the FTIR spectra of raw and torrefied SS, revealing several well-defined peaks associated with different functional groups. In the case of raw SS, peaks corresponding to O–H stretching ($3600\text{--}3000\text{ cm}^{-1}$) were observed for hydrogen bonds of the surface hydroxyl and H_2O . Aliphatic C–H stretching vibrations were also noticeable in the $2900\text{--}2800\text{ cm}^{-1}$ range. Other peaks within the $1470\text{--}1750\text{ cm}^{-1}$ range were assigned to C=O and C=C stretching vibrations of aromatic groups. Additionally, the C–O stretching for alcohol compounds was detected within the $1200\text{--}950\text{ cm}^{-1}$ range. Upon torrefaction, the spectra revealed significant structural changes. At 250 and 300 °C, the O–H bond disappeared, suggesting due to dehydration reactions [11]. The loss or reduction of hydroxyl groups in SS during torrefaction contributes to the dehydration observed in the proximate analysis, where MC decreases with increasing torrefaction temperature. At 200 °C, the C–H peaks in the $2900\text{--}2800\text{ cm}^{-1}$ range vanished, suggesting the breakdown of aliphatic C–H bonds. However, the intensity of these peaks increased at 250 and 300 °C, possibly due to the recombination of C–H compounds at higher temperatures. This phenomenon correlates with the fluctuating H content seen in the ultimate analysis. The appearance of peaks in the $2250\text{--}2300\text{ cm}^{-1}$ range after torrefaction can be attributed to the C≡N stretching, suggesting that the nitrogen in raw SS transformed into nitrile groups during torrefaction. This change in nitrogenous compounds corresponds to the observed increase in N in the ultimate analysis as the torrefaction temperature increases.

Other than that, the peaks indicating the existence of C=O, C=C, and C–O in the raw SS either reduced in intensity or disappeared after torrefaction, indicating the deoxygenation, and decarboxylation of the torrefied SS, aligning with the changes in C and O reported in the ultimate analysis. Overall, the FTIR results complement the findings from the proximate and ultimate analyses, providing a deeper understanding of the structural and compositional changes occurring during the torrefaction process.

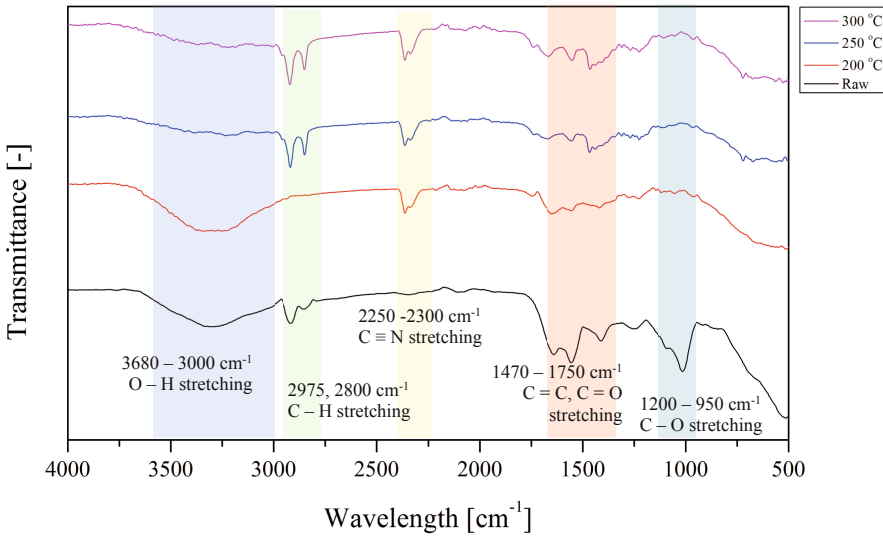


Fig. 3. FTIR spectra of raw and torrefied SS.

4 Conclusions

This study demonstrated the characterization of the torrefaction process of SS, focusing on its impact on the yield and composition of solid biochar. The torrefaction temperature emerged as a crucial factor in biochar, bio-oils, and biogas yield, with a decrease in biochar yield and an increase in bio-oils and biogas yield observed as the temperature increased. Proximate and ultimate analyses indicated notable shifts in the SS's composition during torrefaction, with MC and VM content decreasing, FC increasing, and intricate variations observed for AC, C, H, N, and O contents. Further, FTIR analysis affirmed these findings by illustrating significant structural changes in the SS, including dehydration, thermal breakdown of aliphatic C-H bonds, and transformation of nitrogenous compounds. These findings provide a basis for optimizing the production of biochar from SS, which holds the potential for use in carbon sequestration and energy generation. Future research should delve into these applications and evaluate the associated environmental impacts.

Acknowledgements. The supports by Universiti Malaysia Terengganu are highly acknowledged.






References

1. Prakash Nirmal, N., Santivarangkna, C., Singh Rajput, M., Benjakul, S.: Trends in shrimp processing waste utilization: an industrial prospective. *Trends Food Sci. Technol.* **103**, 20–35 (2020)
2. Elango, D., Packialakshmi, J.S., Manikandan, V., Jayanthi, P.: Sustainable synthesis of carbon quantum dots from shrimp shell and its emerging applications. *Mater. Letter* **312**, 131667 (2022)

3. Yang, C., et al.: Efficient removal of Tris (2-chloroethyl) phosphate by biochar derived from shrimp shell: adsorption performance and mechanism study. *Ecotoxicol. Environ. Saf.* **254**, 114728 (2023)
4. Huang, S., Ding, Y., Li, Y., Han, X., Xing, B., Wang, S.: Nitrogen and sulfur co-doped hierarchical porous biochar derived from the pyrolysis of mantis shrimp shell for supercapacitor electrodes. *Energy Fuels* **35**, 1557–1566 (2021)
5. Wu, M., Teng, X., Liang, X., Zhang, Y., Huang, Z., Yin, Y.: Supporting nanoscale zero-valent iron onto shrimp shell-derived N-doped biochar to boost its reactivity and electron utilization for selenite sequestration. *Chemosphere* **319**, 137979 (2023)
6. Vandecasteele, B., et al.: Chemically versus thermally processed brown shrimp shells or Chinese mitten crab as a source of chitin, nutrients or salts and as microbial stimulant in soilless strawberry cultivation. *Sci. Total. Environ.* **771**, 145263 (2021)
7. Shamsuddin, N.A., Munajat, N.F.: Characteristics of biochar from fish wastes pyrolysis in a fixed-bed reactor. In: *AIP Conference Proceedings*, p. 40007. AIP Publishing (2023)
8. Jifara Daba, B., Mekuria Hailegiorgis, S.: Torrefaction of corncob and khat stem bio-mass to enhance the energy content of the solid biomass and parametric optimization. *Bio-resource Technol. Rep.* **21**, 101381 (2023)
9. Mei, Y., et al.: Effect of temperature oscillation on torrefaction and pyrolysis of elm branches. *Energy* **271**, 127055 (2023)
10. Cardarelli, A., Pinzi, S., Barbanera, M.: Effect of torrefaction temperature on spent coffee grounds thermal behaviour and kinetics. *Renewable Energy* **185**, 704–716 (2022)
11. Zhao, A., Liu, S., Yao, J., Huang, F., He, Z., Liu, J.: Characteristics of bio-oil and biochar from cotton stalk pyrolysis: effects of torrefaction temperature and duration in an ammonia environment. *Biores. Technol.* **343**, 126145 (2022)



Hybrid Fiber/Filler Reinforced Vegetable Oil-Based Composites: A Short Review

Rohani Mustapha¹ , Azrul Nazif Adnan¹ , Siti Noor Hidayah Mustapha² ,
Che Mohd Ruzaidi Ghazali¹ , and Mohamad Awang¹ 

¹ Faculty of Ocean Engineering Technology and Informatics, Universiti Malaysia Terengganu, Kuala Nerus, 21030 Kuala Terengganu, Terengganu, Malaysia

rohani.m@umt.edu.my

² Advanced Biopolymer Group, Faculty of Industrial Sciences and Technology, Universiti Malaysia Pahang, Lebuhraya Tun Razak, Gambang, 26300 Kuantan, Pahang, Malaysia

Abstract. The development of filler- and fibre-reinforced vegetable oil composites has received considerable attention in recent years due to their environmental friendliness and potential to replace synthetic composites. Vegetable oil composites can be reinforced with either natural or synthetic fillers/fibres, resulting in partially or fully green composites. However, synthetic fibers have the disadvantage of being non-renewable and unsustainable due to their production from petroleum-based sources. To address this limitation, there is a growing trend toward hybridizing two or more types of filler/fibers as a hybrid reinforcement system, which can improve the supporting properties of the composites. Therefore, this review article specifically focuses on the use of hybrid filler/fibers in vegetable oil-based composites, including the various types of hybrid fiber/fibers, vegetable oils used, and their potential applications. Additionally, the mechanical and thermal properties of these composites are also being reviewed.

Keywords: Hybrid · Composites · Vegetable Oil · Mechanical Properties · Thermal Properties

1 Introduction

In recent years, plant oils have gained attention as a potential source for creating resins and pre-polymers that could replace petroleum-based resources. Vegetable oils such as soybean, linseed, cottonseed, and castor oils have shown promise in the development of composite materials due to their abundance, low cost, and renewable nature [1]. These oils can be functionalized through the addition of crosslinking agents to create crosslinked functionalized oils, which can then be reinforced with natural fibers to enhance their mechanical and thermophysical characteristics.

The utilization of natural or synthetic fillers/fibers in vegetable oil-based composites can make them partly or fully eco-friendly. There are two categories of fillers/fiber reinforcements: natural and synthetic. Natural fibers comprise cotton, flax, hemp, coconut, flaxseed, kenaf, and jute, while synthetic fibers include glass, carbon, nylon, rayon,

acrylic, and Lycra [2]. Figure 1 demonstrates the classification of fibers, while Table 1 provides annual statistics on natural fiber production. Industrial applications typically use glass fibers because of their strength and stiffness compared to natural fibers [3].

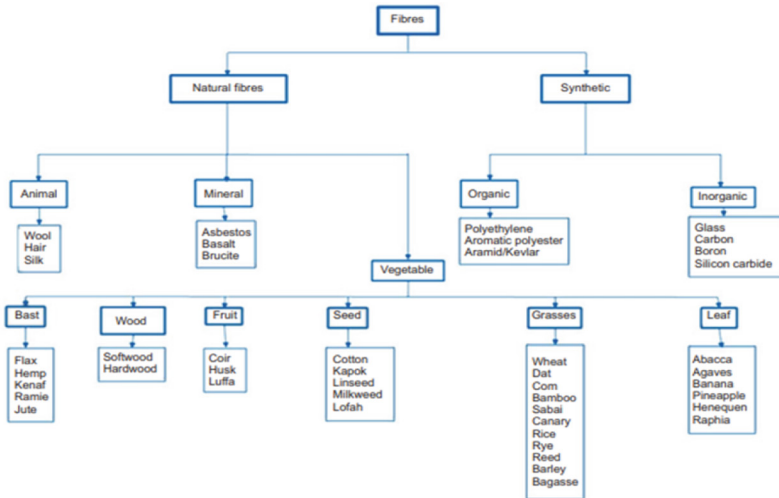


Fig. 1. Classification of the fibers [4]. Open access.

However, synthetic fibers have certain drawbacks such as poor renewability, high production cost, poor recyclability, high energy consumption, machine abrasion, and health risks [4, 5].

In recent times, natural fibers have emerged as a promising alternative to petroleum-based fiber products owing to their eco-friendliness and renewability, providing an edge over synthetic materials [4]. Despite these advantages, natural fiber composites have some disadvantages, including poor chemical and fire resistance, low liquefaction point, weak interaction between the matrix and the fibers, and low moisture absorption [4, 6]. As a result, plant fibers must undergo surface treatment using chemical or physical methods before being used in composites. Surface properties should be modified to reduce flammability and water absorption for best results [7]. Alkali and silane are commonly used chemical treatments [8].

Hybridization is an active area of research because combining two or more fillers/fibres to produce composites can create sustainable materials with improved properties. Hybrid fillers/fibres can compensate for the disadvantages of one type of reinforcement with another, resulting in composites with higher stiffness and strength than single reinforced polymer composites [5]. The three types of fillers/fibres used in hybridization are fiber-fiber, filler-fiber, and filler-filler. Hybrid composites have gained significant attention compared to single reinforced fillers/fibres composites, such as natural fiber composites or glass fiber compounds. The concept of hybridization is prevalent in various fields of study, including mechanics, polymer and chemical chemistry, metallurgy, physics, science and technology, and energy sources, with the main goal

Table 1. The yearly manufacture of natural fiber [9].

Natural fiber	Origin	World production (x 10 ³ Tons)
Coir	Fruit	100
Banana	Stem	200
Bamboo	Stem	10.000
Jute	Stem	2500
Hemp	Stem	215
Flax	Stem	810
Abaca	Leaf	70
Kenaf	Stem	770
Roselle	Stem	250
Ramie	Stem	100
Sisal	Leaf	380
Sun hemp	Stem	70
Cotton lint	Fruit	18.500
Wood	Stem	1.750.000
Broom	Stem	Abundant
Elephant Grass	Stem	Abundant
Linseed	Fruit	Abundant
Oil Palm Fruit	Fruit	Abundant
Rice Husk	Fruit/grain	Abundant

of mixing three or more elements to produce superior performance or qualities for the intended purposes.

In this context, the present study aims to provide an overview of hybrid filler- and fibre- reinforced vegetable oil-based composites and their mechanical and thermal properties. By understanding the properties and potential applications of these materials, we hope to pave the way for their wider use in various industries while reducing the environmental impact of the manufacturing processes.

2 Hybrid Fiber-Fiber Reinforced Vegetable Oil Composites

Hybrid fiber-reinforced thermoset composites offer many possibilities, and natural fibers, organic-synthetic fibers, and synthetic-synthetic fibers can be used, as shown in Fig. 2. In various applications, including medical devices, furnishings, structural elements, and vehicle parts, vegetable oil reinforced with hybrid natural fiber can replace synthetic fibers. However, creating these hybrid composites can be challenging, as their varied characteristics and cross-sectional adhesion must be considered [10]. Different processing techniques, such as simple mixing, lattice structures, and segmented sandwich

laminates, can be used [11]. Natural fibers can be combined with other natural fibers or incorporated into a polymer matrix to balance cost while improving functionality and quality [10].

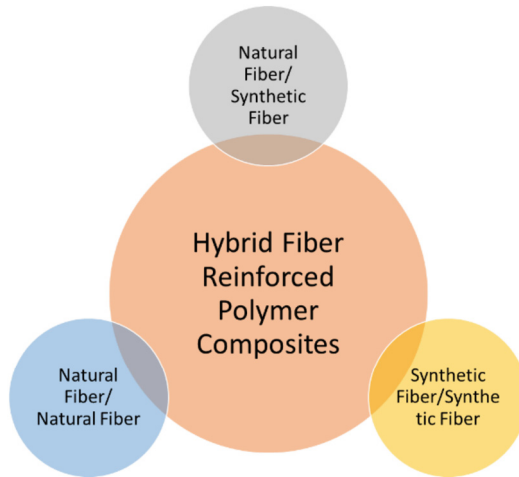


Fig. 2. An overview of natural fiber hybridization.

While research on natural-natural fiber reinforced hybrid composites as alternatives to synthetic fibers is ongoing, limitations exist when hybridizing natural-natural fibers due to factors such as fiber arrangement, matrix selection, interfaces tension, and permeability, which can affect natural fiber performance [4, 5].

For instance, in an experiment conducted by Hanan et al. [12], the tensile and flexural properties of oil palm empty fruit bunch (EFB) composites improved significantly when kenaf fiber content was increased, while pure EFB composites had better impact characteristics than hybrid composites. When natural-natural fiber reinforced hybrids are subjected to high strain, their tensile strength is maximized.

Furthermore, Uriquiza et al. [13] found that the hybridization of Henequen and ixtle yarn fibers as a reinforcement for bio-laminates improved viscoelasticity and increased fabric compaction compared to henequen laminate alone. The post-curing process of all the laminates investigated in this study was aided by an increase in the glass transition temperature.

Queiroz et al. [14] investigated the differences in reinforcement between interlaminar jute/glass fiber hybrids and pure jute and discovered that the mechanical properties of jute fiber-based composites were significantly improved by macroscopic hybridization of the interaction. The improvements in flexural strength were attributed to the higher interlaminar shear strength of the outer plastic layers.

Finally, Darshan et al. [15] conducted a study on silk fiber reinforced epoxy composites and basalt and hybrid fiber reinforced epoxy composites. Hybridization of silk/basalt

fibers outperformed silk fiber-reinforced epoxy composites because the two reinforcing fibers act synergistically, resulting in an epoxy matrix with exceptional hardness, strength, modulus, and toughness.

In recent years, several researchers have conducted research on hybrid fiber reinforced vegetable oil composites. The development of vegetable oil composites using hybrid fibers as reinforcement in vegetable oil-based resins are still in progress owing to their potential as a sustainable and eco-friendly alternative to conventional thermoset resins/composites. There is limited literature available regarding hybrid fiber reinforced composites that utilize vegetable oil as a base. Few researchers have reported on this topic.

For example, a study conducted by Lascano et al. [16] carried out a comparative study on the flexural and impact strength of hybrid basalt-flax fiber reinforced vegetable oil-based epoxy composites made from basalt/basalt, basalt/flax, and flax/flax. According to their findings, the composite materials that utilized hybrid basalt/basalt exhibited superior properties compared to other composites. However, when one of the basalt fabrics in the face sheets was replaced with a flax fabric, it had a significant impact on the overall properties, particularly the flexural strength and modulus, while the impact strength remained largely unaffected.

On the other hand, Mustapha et al. [17] investigate the effects of hybrid kenaf and glass fiber reinforced acrylated epoxidized palm oil (AEPO)/epoxy filled nanoclay composites on water absorption properties. They found that using glass fibers as the outer layer of the composites (GKKG, G- glass, K- kenaf) and alternated layer KGKG exhibited the lowest water uptake than other layering sequences.

Motoc et al. [18], investigated the dynamic mechanical and thermal decomposition properties of flax/basalt hybrid laminates, which were made from an epoxidized linseed oil-polymer composite. The researchers examined the impact of maleinized linseed oil (MLO) and glutaric anhydride (GA) as crosslinking agents, analyzed the effects of stacking order as the primary factor, and assessed the dynamic mechanical and thermal decomposition properties of the composites. The findings showed that incorporating glutaric anhydride (GA) led to the production of relatively brittle flax and flax/basalt laminates with high hardness. The loss moduli decreased as the number of basalt layers increased. In addition, the glass transition temperatures (T_g) shifted from 70 °C to 59 °C and 56 °C with increasing MLO content in the GA:MLO curing agent system, resulting in lower brittleness of the crosslinked resin.

In the study by Santhosh and Rao [19], the mechanical and thermal behavior of cotton/nylon fiber hybrid composites were compared with and without the addition of castor oil. The results showed that the composites with castor oil exhibited higher tensile, flexural and impact strength than the composites without castor oil. The thermal properties of the composites were analyzed by DMA, which indicated an improvement in the damping properties of the composites with castor oil. In addition, the decrease in glass transition temperature for the composites with castor oil indicated improved damping performance at higher temperatures.

3 Hybrid Fiber-Filler Reinforced Vegetable Oil Composites

Another type of hybrid composites are filler-and fiber-reinforced vegetable oil composites, which are made by mixing several types of fillers and fibers with resins derived from vegetable oil. These composites are versatile and can be used in a variety of industries, including automotive, aerospace, construction, and consumer goods. The fillers used in these composites serve to improve their mechanical properties and can be either organic or inorganic. Some commonly used organic fillers include cellulose, lignin, and starch, while inorganic fillers can be made from materials like silica, clay, or calcium carbonate. Fibers are incorporated into the composites to reinforce and strengthen them. Natural fibers such as jute, hemp and flax are commonly used, but synthetic fibers such as glass and carbon are also used.

In a study by Arun Prakash and Viswanthan [20], researchers investigated the mechanical and thermal properties of a neem oil-blended epoxy composite reinforced with sea urchin tips and kenaf tissue fibers with surface modifications. The addition of neem oil to the epoxy resin degraded the mechanical and thermal properties, but transformed the epoxy composite into a bioform. Incorporation of surface-modified kenaf fibers into the epoxy-neem bio-mixture resulted in improved mechanical properties, while the use of surface-modified sea urchin particles further improved both mechanical and thermal properties compared to the starting material. In addition, water uptake results showed that the designations of the surface-modified composites remained unchanged after immersion.

Yang et al. [21] studied the tensile test, water resistance, and thermal analysis of bioplastic composites reinforced with epoxidized oils based on hybrid starch and empty fruit grapes. The researchers found that low epoxidized oil content (EO) resulted in smoother composite surfaces, while high EO content resulted in voids and discontinuities due to phase separation. The addition of epoxidized soybean oil (ESO) increased the thermal stability of the bioplastics due to its strong interaction with starch/EFB. In addition, a small amount of EO acted as a compatibilizer and improved the mechanical properties of the bioplastic composites, while a higher content of EO had a negative effect on the mechanical properties. The introduction of EO resulted in a moderate decrease in water absorption and solubility, but increased water vapour permeability.

Khandelwal et al. [22] conducted a study to evaluate the electrical, morphological, thermal, and mechanical properties of epoxy linseed oil (ELO) composites. These composites were composed of biobased materials and were filled with carbon nanotubes (CNTs) and polyaniline (PANI). Through morphological analyses, it was confirmed that both CNTs and PANI were distributed uniformly within the ELO matrix. Results showed that the tensile strength and elastic modulus of the composite increased considerably upon incorporating CNTs, indicating that the composite was reinforced. Furthermore, the toughness of the ELO/PANI5 composite improved when 0.1% CNTs were added, demonstrating an increase in the composite's impact strength.

4 Hybrid Filler-Filler Reinforced Vegetable Oil Composites

One of the options for hybrid composites is the hybrid filler-fiber reinforced vegetable oil-based composites. These composites are made by combining two different types of fillers with resins based on vegetable oil. The primary objective of using two types of fillers is to achieve a synergistic effect that enhances the mechanical properties compared to using a single type of filler.

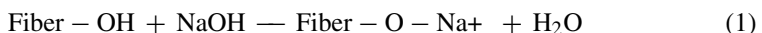
The fillers used in these composites can be organic or inorganic, and common organic fillers include cellulose, lignin, and starch. Meanwhile, inorganic fillers can be made from materials like silica, clay, or calcium carbonate. Using two different types of fillers can enable the composite to benefit from the unique properties of each filler, which can result in a combination of properties that cannot be achieved using only one type of filler.

Kaatabi et al. [23] investigated an environmentally friendly method to improve the mechanical properties of soybean oil-based composites reinforced with flaxseed and aluminium tris hydroxide (ATH), as well as with an ethylene-methyl acrylate (EMA)-based polyamide nanocomposite. The inclusion of ATH particles into the organic polymer enabled the composites to maintain stiffness without sacrificing durability, while also improving barrier and material characteristics. The researchers conducted mechanical tests, such as tensile and impact strength, using the conventional ASTM test plan. The study's results highlight the possibility of achieving best-practice designs that maximize constituent interactions, thereby broadening the spectrum of microbiologically polymer nanocomposites.

Dutta et al. [24] investigated the potential of epoxidized soybean oil (ESO) as a compatibilizer and plasticizer in a nanocomposite of polyvinyl chloride (PVC)/rice husk ash and modified montmorillonite (OMMT). The team fabricated several composites, keeping the optimized ESO constant and varying the OMMT content. The composites were characterized and their properties studied using sophisticated instrumentation. The results showed that the addition of 1 phr OMMT significantly improved the tensile, flexural and hardness properties by 97%, 90% and 91%, respectively. In addition, the addition of OMMT increased the hydrophobicity of the composites, making them suitable for outdoor applications.

5 Disadvantages of Hybrid Fiber/Fiber Reinforced Vegetable Oil Composites

Most natural fiber, including kenaf fibers, must undergo chemical modification because they are highly polar, which makes them incompatible with non-polar polymers and leads to lower composite performance. Alkali treatments are a common method of modifying and treating cellulose fibers such as kenaf fiber. This is because alkali treatments are an inexpensive and relatively effective method of removing lignin and other soluble substances from the cellulose surface, increasing the roughness of the fiber surface and improving adhesion at the fiber-matrix interface [25]. The reaction for alkali treatment using sodium hydroxide (NaOH) is shown below:



Although NFRPs have the potential to replace synthetic fibers, they have two major issues that limit their widespread application. First, they have a low processing temperature. Second, natural fibers have a poor mechanical strength that cannot rival the strength of synthetic fibers.

Therefore, recent studies have focused on developing hybrid composites with two or more types of reinforcing filler/fiber in a single matrix. Hybrid reinforced polymer composites are very attractive materials for high performance applications because they have the ability to develop products with better mechanical properties, environmental performance, and cost effective. There is a growing interest in enhancing polymer properties by employing hybrid natural-synthetic filler/fibers to replace existing natural fiber or glass fiber composites. Hybrid composites have properties that could not be attained by mono-fiber composites. They offer more advanced composites with reduced cost, acceptable corrosion resistance, good mechanical properties i.e. flexural modulus, good strength properties, and good thermal stability.

Natural fiber/filler reinforced vegetable oil-based composites also are susceptible to water absorption, which can lead to swelling and degradation over time. This can be a major issue in applications where the composite is exposed to water or high humidity levels, as it can result in a loss of mechanical properties and reduced lifespan.

To mitigate this issue, researchers have been investigating different strategies to improve the water resistance of these composites. These include modifying the vegetable oil-based resins to enhance their water resistance, applying water-resistant coatings or treatments to the natural fibers and fillers, and blending natural fibers with hydrophobic synthetic fibers or fillers to create composites that are more resistant to water absorption. While some progress has been made in improving the water resistance of vegetable oil-based composites reinforced with natural fibers/fillers, there remains a need for further optimization to enhance their suitability for various applications.

6 Current Application on Hybrid Fiber-Reinforced Vegetable Oil Composites

The extensive mechanical properties exhibited by NFRP composites render them well-suited for various structural applications. These properties include impact strength, tensile strength, flexural strength, compressive strength, creep resistance, and fatigue resistance. Hybrid NFRPs are particularly attractive due to their low production cost, high strength-to-weight ratio, and ease of fabrication [26]. However, natural fibers have certain drawbacks, such as inconsistent raw material and property characteristics, poor water barrier capabilities, and unfavorable bonding behavior with the matrix. The variability in characteristics due to factors such as the plant section, climate, and plant age makes it difficult to utilize natural fibers in industrial applications, which has led to the development of hybrid biocomposites. Despite the common use of hybrid fiber as a reinforcer, little research has been conducted on composites made of vegetable oil.

Recently, researchers have been exploring the use of plant oils, such as soybean, linseed, cottonseed, and castor oils, as a replacement for petroleum-based resources in the creation of resins and pre-polymers. However, crosslinked functionalized oils have inferior mechanical and thermophysical characteristics, which can be improved

by reinforcing them with renewable bio-fibers. Although fully biocomposites (matrix and filler of natural origin) are still in the research stage, hybrid materials already have a wide range of uses. For instance, Kamarudin et al. [27] discovered that composite materials made by epoxidizing fiber and resins derived from soybean oil are employed in the walls, floors, and roofs of residential and low-rise commercial buildings. These panels were produced using a resin vacuum infusion method or vacuum-assisted resin transfer moulding.

O'Donnell et al. [28] also produced panels from acrylated epoxidized soybean oils (AESO) and natural fiber mats (flax, cellulose, pulp and recycled paper, hemp) for indoor uses such as housing, building components, furniture, and vehicle parts. These materials exhibited good mechanical properties compared to woven AESO composites reinforced with E-glass fibers, although the flexural modulus values varied depending on the type of fibers used, although the latter exhibited higher strength. Guna et al. [29] mentioned that hybrid composites are used in the automotive, construction, sports, and medical industries. Many hybrid biocomposites, such as tanks, piping, and vessels, are being investigated as alternatives to glass- and fiber-reinforced composites.

7 Conclusion

In summary, the field of hybrid filler/fiber reinforced vegetable oil composites is relatively new, with ongoing studies exploring the use of multiple fillers and fibers with vegetable oil-based resins. There is still much to be learned about the benefits and limitations of these materials. As the demand for environmentally friendly materials in applications such as automotive and housing construction continues to rise, there is a need to develop compatible composites that are sustainable and eco-friendly. The properties of these composites depend on the types of resin, vegetable oil, fiber/filler, as well as the chemical and physical modifications used. Developing fully green composites is a challenging task, but further research can lead to innovative ways of creating high-performance composites with commercial viability and increased bio-based content. Therefore, future studies should focus on developing composites with higher mechanical performance and bio-based contents to meet the demand for eco-friendly materials.

References






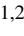

1. Krishnasamy, S., et al.: Recent advances in thermal properties of hybrid cellulosic fiber reinforced polymer composites. *Int. J. Biol. Macromolecules*. **141**, 1–13 (2019)
2. Gholampour, A., Ozbakkaloglu, T.: A review of natural fiber composites: properties, modification and processing techniques, characterization, applications. *J. Mater. Sci.* **55** (3), 829–892 (2020). <https://doi.org/10.1007/s10853-019-03990-y>
3. Santhosh, G., Rao, R.N.: Effect of castor oil on mechanical and thermal behaviours of hybrid fibers reinforced epoxy based polymer composites. *Mater. Today Proceed.* **46**, 2787–2790 (2021)
4. Mochane, M.J., et al.: Recent progress on natural fiber hybrid composites for advanced applications: a review. *Express Polym. Lett.* **13**(2), 159–198 (2019)
5. Safri, S.N.A., Sultan, M.T.H., Jawaid, M., Jayakrishna, K.: Impact behaviour of hybrid composites for structural applications: a review. *Compos. B Eng.* **133**, 112–121 (2018)

6. Gieparda, W., Rojewski, S., Różanska, W.: Effectiveness of silanization and plasma treatment in the improvement of selected flax fibers' properties. *Mater.* **14**(13), 3564 (2021)
7. Halip, J.A., Hua, L.S., Ashaari, Z., Tahir, P.M., Chen, L.W., Uyup, M.K.A.: Effect of treatment on water absorption behavior of natural fiber-reinforced polymer composites. In: *Mechanical and Physical Testing of Biocomposites, Fiber-Reinforced Composites and Hybrid Composites*, pp. 141-156 (2018)
8. Sepe, R., Bollino, F., Boccarusso, L., Caputo, F.: Influence of chemical treatments on mechanical properties of hemp fiber reinforced composites. *Compos. B Eng.* **133**, 210–217 (2018)
9. Sanjay, M.R., Madhu, P., Jawaid, M., Senthamaraiannan, P., Senthil, S., Pradeep, S.: Characterization and properties of natural fiber polymer composites: a comprehensive review. *J. Clean. Prod.* **172**, 566–581 (2018). <https://doi.org/10.1016/j.jclepro.2017.10.101>
10. Neto, J., Queiroz, H., Aguiar, R., Lima, R., Cavalcanti, D., Banea, M.D.: A review of recent advances in hybrid natural fiber reinforced polymer composites. *J. Renew. Mater.* **10**(3), 561–589 (2022)
11. Nurazzi, N.M., et al.: A review on mechanical performance of hybrid natural fiber polymer composites for structural applications. *Polym.* **13**(13), 1–47 (2021)
12. Hanan, F., Jawaid, M., Md Tahir, P.: Mechanical performance of oil palm/kenaf fiber-reinforced epoxy-based bilayer hybrid composites. *J. Nat. Fibers* **17**(2), 155–167 (2018)
13. Franco-Urquiza, E.A., Saleme-Osornio, R.S., Ramírez-Aguilar, R.: Mechanical properties of hybrid carbonized plant fibers reinforced bio-based epoxy laminates. *Polym.* **13**(19), 3435 (2021)
14. Queiroz, H.F.M., Banea, M.D., Cavalcanti, D.K.K.: Adhesively bonded joints of jute, glass and hybrid jute/glass fibre-reinforced polymer composites for automotive industry. *Appl. Adhes. Sci.* **9**(1), 1–14 (2021). <https://doi.org/10.1186/s40563-020-00131-6>
15. Darshan, S.M., Suresha, B.: Effect of basalt fiber hybridization on mechanical properties of silk fiber reinforced epoxy composites. *Mater. Today Proceed.* **43**, 986–994 (2021)
16. Lascano, D., Valcárcel, J., Balart, R., Quiles-Carrillo, L., Boronat, T.: Manufacturing of composite materials with high environmental efficiency using epoxy resin of renewable origin and permeable light cores for vacuum-assisted infusion molding. *Ingenius* **23**, 62–73 (2020)
17. Mustapha, R., Mustapha, S.N.H., Suriani, M.J., Ruzaidi, C.M., Awang, M.: Water Absorption Behaviour of Epoxy/Acrylated Epoxidized Palm Oil (AEPO) Reinforced Hybrid Kenaf/Glass Fiber Montmorillonite (HMT) Composites. *J. Phys. Conf. Ser.* **2080**(1), 012013 (2021)
18. Motoc, D.L., Ferri, J.M., Ferrandiz-Bou, S., Garcia-Garcia, D., Balart, R.: Dynamic–mechanical and decomposition properties of flax/basalt hybrid laminates based on an epoxidized linseed oil polymer. *Polymers* **13**(4), 1–11 (2021)
19. Santhosh, G., Rao, R.N.: Effect of castor oil on mechanical and thermal behaviours of hybrid fibres reinforced epoxy based polymer composites. *Mater. Today Proceed.* **46**, 2787–2790 (2021)
20. Arun Prakash, V.R., Viswanthan, R.: Fabrication and characterization of echinoidea spike particles and kenaf natural fibre-reinforced Azadirachta-Indica blended epoxy multi-hybrid bio composite. *Compos. Part A Appl. Sci. Manuf.* **118**, 317–326 (2019)
21. Yang, J., Ching, Y.C., Chuah, C.H., Liou, N.S.: Preparation and characterization of starch/empty fruit bunch-based bioplastic composites reinforced with epoxidized oils. *Polymers* **13**(1), 1–15 (2021)
22. Khandelwal, V., Sahoo, S.K., Kumar, A., Sethi, S.K., Manik, G.: Bio-sourced electrically conductive epoxidized linseed oil based composites filled with polyaniline and carbon nanotubes. *Compos. Part B Eng.* **172**, 76–82 (2019)
23. Kaatubi, K.M., et al.: Investigate the mechanical properties of soybean oil reinforced with ATH-filled polyester-based hybrid nanocomposites. *J. Nanomaterials* **2022**, 1–7 (2022)

24. Dutta, N., Bhadra, B., Gogoi, G., Kumar Maji, T.: Development of polyvinyl chloride/waste rice husk ash/modified montmorillonite nanocomposite using epoxidized soybean oil as green additive substituting synthetic plasticizer and compatibiliser. *Clean. Mater.* **2**, 100033 (2021)
25. Faruk, O., Bledzki, A.K., Fink, H.P., Sain, M.: Biocomposites reinforced with natural fibers: 2000–2010. *Prog. Polym. Sci.* **37**(11), 1552–1596 (2012)
26. Fairlie, G., Njuguna, J.: Damping properties of flax/carbon hybrid epoxy/fiber-reinforced composites for automotive semi-structural applications. *Fibers* **8**(10), 64 (2020)
27. Kamarudin, S.H., Abdullah, L.C., Aung, M.M., Ratnam, C.T., Jusoh Talib, E.R.: A study of mechanical and morphological properties of PLA based biocomposites prepared with EJO vegetable oil based plasticiser and kenaf fibers. *Mater. Res. Express* **5**(8), 085314 (2018)
28. O'Donnell, A., Dweib, M.A., Wool, R.P.: Natural fiber composites with plant oil-based resin. *Compos. Sci. Technol.* **64**(9), 1135–1145 (2004)
29. Guna, V., Ilangovan, M., Ananthaprasad, M.G., Reddy, N.: Hybrid Biocomposites. *Polym. Compos.* **39**, 30–57 (2017)



A Review on the Effect of Extrusion Parameter on 3D Printing Filament Diameter

Krishna Kumar Nitiyah^{1,2} , Musa Luqman^{1,2} ,
Mohamad Rasidi Mohamad Syahmie^{1,2} , Ahmad Khairul Rafezi¹ ,
Abd Rahim Shayfull Zamree^{3,4} , Rozyanty Rahman^{1,2} ,
and Ahmad Azrem Azmi^{1,2} 

- ¹ Faculty of Chemical Engineering Technology, Universiti Malaysia Perlis, Jejawi, Taman Muhibbah, 02600 Perlis, Arau, Malaysia
nietieyah15@gmail.com
- ² Advanced Polymer Group, Center of Excellence Geopolymer and Green Technology (CEGeoGTech), University Malaysia Perlis, 02600 Jejawi, Perlis, Malaysia
- ³ Faculty of Mechanical Engineering Technology, University Malaysia Perlis, 02600 Perlis, Arau, Malaysia
- ⁴ Green Design and Manufacture Research Group, Center of Excellence Geopolymer and Green Technology (CEGeoGTech), University Malaysia Perlis, 02600 Perlis, Arau, Malaysia

Abstract. Over the years, the extrusion technique has captured the attention of polymer industries by meeting the demand for polymer processing and fabrication of final products. Extrusion is a continuous process, and it has a lot of potential in the increasing polymer sector, especially in the three-dimensional (3D) printing sector. 3D printing is popular because the feedstock filament form is accessible and produce able. The properties of the filament used influence the printed part qualities regardless of the FDM parameters. This study provides information on how extrusion parameters affect the diameter of extruded filaments. This study reviews previous studies on the effect of varied extrusion settings on filament diameter. The review will serve as a resource for researchers in the 3D printing sector to fabricate their filaments for 3D printing. Overall, this paper will provide solutions to overcome issues in obtaining optimal filament diameters for future research projects.

Keywords: Extruder · Extrusion · Filament · Barrel Temperature · Extrusion Speed · Diameter

1 Introduction

One of the most well-known polymer processing methods is extrusion. The extrusion method applies to melt blending, homogenizing of material, forming finished goods, and pelletizing polymeric melt [1–6]. Single-screw extruders and twin-screw extruders are two kinds of extruders available in polymer processing.

The major components of the extruder are the heating barrel, screw profile along the barrel, motor for screw rotation, and die for the shaping of extrudates [7, 8]. There are

three sections in the extruder's flow channel of the barrel: the feed zone, the transition zone, and the metering zone. The feed material enters the feed zone from the hopper, and the melted polymer is conveyed to the transition zone through pressure and shear generated within the barrel. Here is where the mixing and intermixing occur. Then, the molten polymer flows towards the die and out of the nozzle [9, 10]. The extruded filament solidified through a water bath or a cooling fan [11].

The source material for the 3D printer is filament form. Many kinds of thermoplastic filament materials are available in the 3D printing industry [12, 13]. Regardless of the material availability, the research interest in producing new filament material is rising to fabricate diverse 3D printing feedstock materials. Filament fabrication covers a range of materials, such as thermoplastic elastomer, composite, blend, and recycled filament. Each filament fabrication has different processing requirements. They standardised the filament diameter, with typical sizes of 1.75 mm, 2.85 mm, and 3 mm [14]. The diameter and quality of the filament are affected by extrusion processing factors, such as extrusion temperature, extrusion speed, nozzle diameter, spindle speed, and cooling conditions. Extrusion parameters are crucial for forming filaments with consistent roundness and dimensional precision while manufacturing filaments.

2 Effect of Extrusion Parameter on Filament Properties

Extrusion parameters are crucial for forming filaments with consistent roundness and dimensional precision while manufacturing filaments. The dimensional accuracy affects the quality of the filament. Diameter tolerance refers to the variance in the filament dimension during extrusion. To achieve a uniform diameter and continuous filament with optimum form, 3D printer filaments are typically generated using a single screw extruder, and adjusting the filament extruder settings is required. The quality of the filament influences the properties of 3D-printed components [14]. This section discusses the influence of filament extruder settings on filament diameter. Table 1 presents the summary of the research works for filament diameter.

Nassar et al. (2019) [11] performed filament fabrication using high-density polyethylene (HDPE) by varying extrusion speed and cooling method while maintaining constant extrusion temperature. Table 2 represents the reading of filament diameter under different extrusion parameters. The researcher focused on the cooling effect of filament to ensure the roundness of filament with a consistent diameter. Based on the results, a higher extrusion rate did not melt feed materials completely to form uniform dimensions. The solidification happens at a faster pace by using a cold air gun. Thus, these studies reveal the filament does not have sufficient time to extend to achieve the ideal diameter under tension between the nozzle and the spooler. At a lower extrusion rate, the material has adequate time to melt to the desired stage, and the melt flow rate is in a controlled condition. Cooling of filament using a water bath allows the filament to extend further upon tension and form a smaller-diameter filament. A slower extrusion rate and solidification via a cold air gun produced the preferred filament size [11].

Mirón et al. (2017) [15] conducted research work to manufacture filament for a 3D printer with a diameter of 2.85mm. They implemented an extrusion temperature range of 175 °C to 195 °C for processing polylactic acid (PLA) pellets into filaments

Table 1. A summary type of extruder and processing parameters

No	Author	Extruder Type	Input Parameter	Variable	Material	Findings
1	Nassar et al., (2019) [11]	Filament extruder	<ul style="list-style-type: none"> Extrusion speed (rpm) Cooling method 	<ul style="list-style-type: none"> 18,22 Cold air gun, water bath 	High density polyethylene	Filament fabrication under slower extrusion speed with a hot air gun cooling method is effective in producing filament in the required range
2	Mirón et al., (2017) [15]	Filabot EX2 extruder	<ul style="list-style-type: none"> Extrusion temperature (°C) 	<ul style="list-style-type: none"> 165,1700,175,180,185,190 	Polylactic acid	Larger diameter filament fabricated under lower extrusion temperature and vice versa. The optimum extrusion temperature for PLA is between 175 °C-180 °C
3	Herianto et al., (2020) [16]	Single screw extruder	<ul style="list-style-type: none"> Spooler speed (rpm) Extrusion speed (rpm) Extrusion temperature (°C) 	<ul style="list-style-type: none"> 2,4 40,50 180,190,200 	Recycled polypropylene	The spooler speed and extrusion speed need to work parallelly to achieve consistent filament diameter
4	Kuo et al., (2021) [17]	Welzoom desktop extruder	<ul style="list-style-type: none"> Extrusion temperature (°C) Extrusion speed (rpm) Cooling distance (mm) 	<ul style="list-style-type: none"> 182,184,186 480,490,500 52,5,55,57,5 	Recycled Polylactic acid	Under higher extrusion temperatures and faster speed, the structural stability of the filament reduces which causes a smaller diameter of the filament
5	Liu et al., (2018) [18]	Welzoom desktop extruder	<ul style="list-style-type: none"> Extrusion temperature (°C) Extrusion speed (rpm) 	<ul style="list-style-type: none"> 185,190,195,200 2,3,4,5,6 	Polylactic acid	A larger diameter of filament fabricated due to die swell behaviour under higher temperatures with faster extrusion speed

Table 2. Error! No text of specified style in document..Filament diameter under different extrusion parameters.

Run	Extrusion temperature (°C)	Extrusion speed (rpm)	Cooling method	Filament diameter (mm)
1	180	22	Cold air gun	1.81 ± 0.02
2	180	22	Water bath	1.68 ± 0.02
3	180	18	Cold air gun	1.74 ± 0.02
4	180	18	Water bath	1.65 ± 0.02

under automatic extrusion speed. Extruding at a lower temperature of 165 °C produces filament with a high diameter. In addition, a smaller diameter with a blister on the surface of filaments was obtained at a high extrusion temperature of 185 °C to 190 °C. Their findings highlight issues with manufacturing filaments under various temperatures, and troubleshooting methods are shown in Table 3 below. Based on their studies, the ideal extrusion temperature is 175 °C-180 °C for the extrusion of PLA. However, further analysis regarding the effect of extrusion speed and observations on the roundness of the filament is required to understand the impact of extrusion speed. Since the extrusion speed of the screw profile along the barrel affects torque and shear, that influences transition behaviour and flow output.

Table 3. Extrusion parameters and troubleshooting methods

Extrusion temperature (°C)	Extrusion speed	Troubleshooting	Solutions
165	Very slow	High diameter	Increase temperature
170	Slow	High diameter	Increase temperature
175	Good	-	-
180	Good	-	-
185	Fast	Filament with blister and small diameter	Decrease temperature
190	Too fast	Filament with blister and small diameter	Decrease temperature

Another research by Herianto et al., (2020) [16] focused on optimizing extrusion parameters such as spooler speed, extrusion rate, and temperature to achieve a consistent filament diameter using recycled polypropylene. The target diameter of the filament was 1.75mm with 0.05mm tolerance. As per the findings, they obtained the desired filament diameter with an extrusion temperature of 200 °C, 4 rpm spooler speed, and extrusion

Table 4. Filaments diameter obtained under various extrusion temperatures and screw speeds

Screw speed (rpm)	Extrusion temperature (°C)			
	185	190	195	200
2	1.756	1.680	1.620	1.448
3	1.760	1.721	1.680	1.575
4	-	1.791	1.727	1.665
5	-	1.831	1.810	1.747
6	-	1.946	1.888	1.857

speed at 40 rpm. Under a slower spooler speed of 2 rpm and an extrusion speed of 40 rpm, the diameter of the filament is larger. The faster setting for the spooler and screw speed causes the filament to have a smaller diameter. According to the Analysis of Variance (ANOVA) result, the spooler and extrusion speed highly influence the filament diameter. They found that the filaments produced have rougher textures. The rougher filament produces printed parts with irregular surfaces. Thus, the researchers are required to focus on enhancing the filament quality, roundness and smoothness to achieve good printing quality.

Kuo et al. (2021) [17] conducted research to fabricate filaments made from PLA by manipulating extrusion variables, such as extrusion temperature, extrusion speed, and cooling distance between the nozzle and the spooler. The findings show that a rise in barrel temperature from 176 °C to 182 °C leads to an increase in filament diameter. Extrusion temperature at 182 °C is optimal to achieve a filament diameter of 1.75mm. Further temperature rise above the ideal temperature reduces the filament diameter. The filament diameter gets smaller with faster extrusion speed. Extrusion speed at 490 mm/min produced filament with 1.7 mm with smaller standard deviations, while 480 mm/min produced filament with 1.65 mm with minimal variations. Solidification is necessary for fabricating filament. A cooling distance of 55 mm fabricates a filament with the target diameter. The research highlighted that filament size accuracy is highly affected by extrusion temperature compared to other parameters. The variations in filament diameter reflect how minor changes in variables can affect the output filaments. In the future, the researchers should perform melt flow index testing to understand rheological behaviour, which reveals the structural stability of filament in maintaining the desired shape and diameter in filament fabrication.

Liu et al. 2018 [18] studied the effect of filament extruder parameters that affect the diameter of the filament. Table 3 shows the filament diameter achieved under various extrusion temperatures and screw speeds. The researcher reported that, as temperature increases, the diameter decreases. This phenomenon shows melting viscosity behaviour. Higher extrusion temperature reduces die swelling and improves the volume flow rate. However, a rise in extrusion rate shows an increasing trend in filament diameter because of the high volume of material extruded. The data revealed that, with an extrusion speed of 5 rpm and 200 °C, a satisfied filament diameter of 1.75 mm was produced. However, the research study could have added the study factor of spooler speed in filament fabrication.

The spooler speed matching the extrusion speed is necessary to produce a filament with a constant diameter. An imbalanced speed between the spooler and screw will cause higher tension, which causes variations in filament diameter.

3 Conclusion

In summary, the filament diameter relies on multiple settings of the filament extruder. The primary motive is to achieve a consistent filament diameter by optimizing the extruder's parameters and ensuring the prepared filament has good printing ability and denotes good properties in printed parts. Based on the findings above, the temperature setting depends on the material melting point, glass transition temperature, and degradation temperature, and it highly affects the material rheological behaviour. Besides, the speed of the spooler has a high effect on filament diameter as it determines the output of material flow, which eventually influences the filament size. The winding process causes tension in the filament. Thus, speed optimization is necessary. The process needed to be smooth to avoid the coiling effect and stretching of the filament. On the last note, cooling assists in solidifying a filament into the desired shape and size. Less cooling affects the filament quality, where the roundness is inconsistent, and the size will be non-uniform.

Acknowledgement. The authors would like to acknowledge the facilities provided by Universiti Malaysia Perlis (UniMAP) and the Ministry of Higher Education (MOHE) of Malaysia for financial support of this research through the Fundamental Research Grant Scheme (FRGS) under a grant number of FRGS/1/2020/TK0/UNIMAP/02/90.

The authors also like to extend their great gratitude to Research Management Center (RMC UniMAP), Universiti Malaysia Perlis (UniMAP), for the publication incentive grant and all the support given.








References

1. Snowdon, M.R., Mohanty, A.K., Misra, M.: Effect of compatibilization on biobased rubber-toughened poly (trimethylene terephthalate): miscibility, morphology, and mechanical properties. *ACS Omega* **3**(7), 7300–7309 (2018)
2. Abdullah, N.A.S., Mohamad, Z.: The effect of dynamic vulcanization on themorphological and mechanical properties of the toughened poly (lactic acid)/epoxidized natural rubber. *Malaysian J. Fundam. Appl. Sci* **14**(3), 348–352 (2018)
3. Abdullah, N.A.S., Mohamad, Z., Man, S.H.C., Baharulrazi, N., Majid, R.A., Jusoh, M., Ngadi, N.: Thermal and toughness enhancement of poly (lactic acid) bio-nanocomposites. *Chem. Eng. Trans* **72**, 427–432 (2019)
4. Tanrattanakul, V., Jaratrotkamjorn, R., Juliwanlee, W.: Effect of maleic anhydride on mechanical properties and morphology of poly (lactic acid)/natural rubber blend. *Songklanakarin J. Sci. Technol.* **42**(3), 697–704 (2020)
5. Mohammad, N.N.B., Arsad, A., Sani, N.S.A., Basri, M.H.: Effect of compatibilisers on thermal and morphological properties of polylactic acid/natural rubber blends. *Chem. Eng. Trans* **56**, 1027–1032 (2017)
6. Kijjaroun, W., Chuayjuljit, S., Chaiwutthinan, P., Boonmahitthisud, A.: Green composites of poly (Lactic acid)/epoxidized natural rubber filled with coir fibers. *Key Eng. Mater.* **845**, 39–44 (2020)

7. Campbell, G.A., Spalding, M.A.: Single-Screw Extrusion: Introduction and Troubleshooting. Anal. Troubl. Single-Screw Extruders. 2nd edn. Hanser, Liberty Twp, Ohio (2013)
8. Tadmor, Z.: Principles of Polymer Processing, 2nd edn. Wiley, Hoboken, New Jersey (2006)
9. Hyvärinen, M., Jabeen, R., Kärki, T.: The modelling of extrusion processes for polymers—a review. *Polymers (Basel)* **12**, 1–14 (2020)
10. Lin, T.A., Lin, J.H., Bao, L.: Polypropylene/thermoplastic polyurethane blends: mechanical characterizations, recyclability and sustainable development of thermoplastic materials. *J. Mater. Res. Technol* **9**(3), 5304–5312 (2020)
11. Nassar, M.A., Elfarahaty, M., Ibrahim, S., Hassan, Y.: Design of 3D filament extruder for Fused Deposition Modeling (FDM) additive manufacturing. *Int. Des. J* **9**(4), 55–62 (2019)
12. Clifton, W., Clifton, W., Damon, A., Damon, A., Martin, A.K.: Considerations and cautions for three-dimensional-printed personal protective equipment in the COVID-19 crisis. *3D Print. Addit. Manuf* **7**(3), 97–99 (2020)
13. Kim, G., Barocio, E., Pipes, R.B., Sterkenburg, R.: 3D printed thermoplastic polyurethane bladder for manufacturing of fiber reinforced composites. *Addit. Manuf.* **29**, 100809 (2019)
14. Ravichandran, P., Anbu, C., Poornachandran, R., Shenbagarajan, M., Yaswahnthan, K.S.: Design and development of 3D printer filament extruder for material reuse. *Int. J. Sci. Technol. Res.* **9**(1), 3771–3775 (2020)
15. Mirón, V., Ferrándiz, S., Juárez, D., Mengual, A.: Manufacturing and characterization of 3D printer filament using tailoring materials. In: *Manufacturing Engineering Society International Conference 2017, Procedia Manuf*, pp. 888–894. Elsevier, Ponte-vedra, Spain (2017)
16. Herianto, Atsani, S.I., Mastrisiswadi, H.: Recycled polypropylene filament for 3D printer: extrusion process parameter optimization. In: *3rd International Conference on Engineering Technology for Sustainable Development 2019*, pp. 1–7. IOP Publishing, Yogyakarta, Indonesia (2020)
17. Kuo, C.C., Chen, J.Y., Chang, Y.H.: Optimization of process parameters for fabricating polylactic acid filaments using design of experiments approach. *Polymers (Basel)* **13**(8), 1222 (2021)
18. Liu, W., Zhou, J., Ma, Y., Wang, J., Xu, J.: Fabrication of PLA filaments and its printable performance. In: *5th Annual International Conference on Material Science and Engineering (ICMSE2017)*, p. 012033. IOP Publishing, Fujian (2018)



Mechanical Performance of Coal Ash - Mine Tailings Blended Geopolymer Designed by Taguchi Method

Petrica Vizureanu^{1,2} , Dumitru-Doru Burduhos-Nergis¹ ,
Andrei Victor Sandu^{1,3} , Dragos-Cristian Achitei¹ ,
Diana-Petronela Burduhos-Nergis¹ , Madalina-Simona Baltatu¹ ,
and Manuela-Cristina Perju¹ 

¹ Faculty of Materials Science and Engineering, “Gheorghe Asachi”
Technical University of Iasi, 67 Prof. D. Mangeron Blvd., 700050 Iasi, Romania
dumitru-doru.burduhos-nergis@academic.tuiasi.ro

² Technical Sciences Academy of Romania, 26 Dacia Blvd., 030167 Bucharest, Romania

³ Academy of Romanian Scientists, 54 Splaiul Independentei St., Sect. 5, 050094 Bucharest,
Romania

Abstract. Geopolymers are emerging as an eco-friendly alternative to conventional building materials. These materials exhibit enormous potential as a substitute for traditional technologies like concrete, but more applied studies are needed to evaluate their practicality on an industrial scale. Moreover, each type of raw material needs to be optimized in terms of parameters that influence the properties of the final product. In order to optimize geopolymers in terms of mechanical performance, the obtaining parameters and the possibilities offered by the Taguchi method were considered to design a series of geopolymers suitable for civil engineering applications. The optimization was conducted considering: (i) three blends comprising a different percentage of fly ash (FA), fly ash with S (FS) and red mud (RM), (ii) three different liquids to solid ratios (0.70, 0.75 and 0.80), (iii) three different Na₂SiO₃ to NaOH ratios (1.0, 1.25 and 1.5) and (iv) three different molar concentrations of NaOH solution (3, 6.5 and 10 M). The mechanical strength tests showed that the mixture with the best compressive strength is the one consisting of 35 wt.% FA, 15 wt.% FS and 50 wt.% RM, with liquid: solid ratio (L/S) of 0.7, Na₂SiO₃: NaOH of 1.5 and 10 M NaOH, respectively. In terms of flexural strength, the mixture with the same amounts of raw materials, but the following parameters exhibited the highest value after 28 days of curing: L/S of 0.75, Na₂SiO₃:NaOH of 1 and 7M NaOH.

Keywords: Mine tailings · Circular economy · Geopolymers · Taguchi design · Fly ash · Liquid to solid ratio · Na₂SiO₃ to NaOH ratio · NaOH concentration

1 Introduction

A crucial component of the circular economy is the reduction of waste by substituting non-renewable raw materials with recycled by-products that have similar characteristics [1]. Moreover, to associate with this concept, the manufacturing technologies must

include proper management of the resulted by-products, including recycling and reuse stages [2]. The circular economy's primary mission is to ensure the transition to a low-carbon economy while maintaining the quality of the final products [3]. Therefore, finding new, efficient, and innovative techniques for enhancing the usage of different types of materials that are now categorized as waste and primarily end up in landfills is a priority in multiple manufacturing sectors. The term "waste valorisation" refers to any industrial processing operations that try to reuse, recycle, or compost wastes, therefore transforming them into useful goods or energy resources [4, 5].

When it comes to raw material consumption and high CO₂ emissions, the construction materials sector is a priority since the production of Ordinary Portland Cement (OPC) is responsible for more than 8% of the total CO₂ emissions worldwide, along with a significant consumption of limestone [6]. To overcome these limitations and integrate the circular economy concept into this sector, in the last few years many studies have aimed to find sustainable solutions for replacing OPC [7, 8]. Therefore, they focus on both developing techniques that use low processing temperatures and identifying wastes that are suitable to replace cementitious materials. Accordingly, different types of waste have been identified that partially substitute for OPC in concrete. However, to totally replace it, an innovative method of manufacturing concrete with similar properties was developed, i.e., geopolymers. Geopolymers are oxide materials with similar properties to those of OPC-based materials but that can use aluminosilicate wastes instead of natural limestone [9]. Along with the most commonly used raw materials (metakaolin, coal ash, slags, etc.) for geopolymers, mine tailings (MT) are identified as a sustainable resource that can boost the transition of the construction sector toward sustainable development [10–12].

Waste from extractive activities (i.e., waste from mineral resource extraction and processing) is one of the EU's main waste streams [13]. Mining and quarrying branches (exploration, prospecting, extraction, and processing of ores) produced large amounts of wastes in last decades. Re-processing and valorising such waste can result in the recovery and production of "clean" secondary tailings, as well as a cost reduction and an increased environmental benefit. Although new construction designs of tailing dumps have been developed, the waste facilities are filled to capacity due to the constantly increasing amounts of mine tailings generated as lower grades of ore must be processed [14]. Accordingly, by introducing and encouraging the use of mine tailings in geopolymerization, a conveyable source of raw materials for building materials will be developed. Moreover, the foundation of circular economy for mining industry will be obtained.

Currently, close to 55 billion cubic meters of mine tailings are stored worldwide, and the amount is expected to increase by up to 23% until 2025 [15]. Moreover, many tailings Storage Facilities are also very fragile structures, with well over 100 major tailings dam failures recorded since 1960, some with dramatic casualties and all with important environmental impacts [14]. Considering the consumption of virgin raw materials due to concrete manufacturing, the use of mine tailings as a substitute can support the conservation of virgin resources for 4 to 5 years. The use of mine tailings as raw materials for geopolymers has also been analysed by Zhang et al. [16]. In their study, a partial replacement of fly ash with molybdenum tailings has been researched to obtain a cost-effective method of waste valorisation. However, the authors observed that a substitution of FA

with MT higher than 20 wt.% will result in a decrease in mechanical performance due to the increase in macropore volume fraction. Orozco et al. [17] obtained sustainable bricks using gold mine tailings activated with NaOH or Ca(OH)₂ and a low curing temperature of 80 °C. In another study [18], an enhancement of the mechanical properties of gold mine tailings-based geopolymer bricks was obtained by introducing 10% palm oil fuel ash. Moreover, due to the addition of fuel ash, the samples could be cured at room temperature, promoting even further reductions in costs and CO₂ emissions. Since obtaining geopolymers with good mechanical properties using MT as raw materials is challenging because of the high content of nonreacting phases, especially quartz, Qing et al. [19] obtained geopolymer concrete with a compressive strength of 47.6 MPa by applying alkali-hydrothermal activation at 300 °C to the quartz powder. Yet, despite the fact that the material meets the requirements of 42.5 cement, such high temperatures could drive this technology away from the sustainability concept. The low reactivity of MT was also identified by Krishna et al. [20] when assessing the use of mine tailings as aggregates or precursors for geopolymers manufacturing. Moreover, they concluded that due to the heterogeneity of the MT, a tailored processing technique should be researched for each region and the available MT. Moreover, the performance of the final products will be affected by multiple parameters, such as the characteristics of the raw materials, the type and concentration of the activator, and curing conditions.

Despite the fact that obtaining good mechanical properties and room temperature curing is challenging, the biggest issue in the integration of mine tailings into geopolymer manufacture is related to the containment of heavy metals and leaching possibilities during the operation of the developed products. Wang et al. [9] conducted a comprehensive literature analysis on the possible applications of geopolymers containing wastes with high levels of heavy metals. According to their study, the products developed by this method are safe and durable due to the physical encapsulation, covalent bonding, ion exchange, and compound formation mechanisms used by the geopolymerization reaction to solidify and stabilize heavy metals. The production of tailings and the related issues, together with Greenhouse Gas Emissions from mineral and metal production, are the two main environmental challenges for the future of the construction materials industry. At the same time, mineral production is expected to further grow rapidly in the coming decades to meet the material demand for the energy transition [21].

Although multiple studies focus on finding different parameters to increase the reactivity of MT to achieve room temperature curing, there is a major research gap regarding developing blended mixtures that can integrate MT as raw materials for geopolymerization. In this study, coal ash and mine tailings blended geopolymers have been designed considering the advantages of the Taguchi method in order to find the optimum mixing combination to achieve good mechanical performance and room temperature curing.

2 Materials and Methods

Any material rich in silicon and aluminium that can be dissolved by an alkaline solution is a source of raw material for obtaining geopolymers. Globally, several wastes with potential for geopolymerization have been identified, such as power plant ash, red mud, blast furnace slag, etc. However, the rationale for choosing the type of waste is related to

the type of product that will be manufactured along with the availability and alternatives for the valorisation of that residue. For example, if the raw material can be further processed to extract high-value minerals or elements, it shouldn't be used as raw material for concrete, but if the waste cannot be processed through another method or the other methods don't use relevant quantities, i.e., a low rate of recycling, the mineral waste should be seen as a candidate for construction materials.

2.1 Materials

In this study, two types of coal ashes (fly ash and flue gas desulfurization fly ash - noted as fly ash with sulphur) have been used as an aluminosilicate component in order to obtain geopolymers suitable for civil engineering applications. Both coal ashes are by-products available in high amounts and deposited in land fields by a local thermal power plant (S.C. Holboca C.E.T. II S.A., Iasi, Romania). As mine tailings, the residues resulted from the extraction of alumina from bauxite, i.e., red mud, was used. This was collected from the dumps of Alum S.A., Tulcea, Romania. The chemical composition of the used raw materials has been analysed by X-ray fluorescence (XRF) using an XRF S8 Tiger (Bruker GmbH, Karlsruhe, Germany) in order to establish a suitable activation method. Also, to assure experiment repeatability, the collected wastes have been dried until a constant weight (as described in [12]).

As activators, commercially available sodium silicate solution (S.C. KYNITA S.R.L., Valcea, Romania) and sodium hydroxide flakes (98% purity) from the same supplier were chosen. Prior to mixing with the Na_2SiO_3 solution, the NaOH flakes were dissolving in tap water at the desired concentration. The sodium silicate solution had a density of 1.52 g/cm^3 and a pH of 11.5. Also, according to its quality certificate, the solution contains sodium silicate min. 44.8%, min. 31.10% SiO_2 , min. 13.70% Na_2O and additives.

2.2 Sample Design and Preparation

Designing material parameters aims to optimize quality features while being least sensitive. The Taguchi technique is a systematic process for determining the best combination of parameters. Orthogonal networks allow for exploration of multiple influencing elements with a reduced number of tests, minimizing research techniques and applying essential discoveries to various investigations.

Table 1. Solid component mixture.

		Raw material, wt. %		
		FA	FS	RM
Mixture code	B1	45	5	50
	B2	40	10	50
	B3	35	15	50

Based on preliminary experiments and literature, the following geopolymer design factors (parameters) were chosen in this study: (i) three mixtures comprising a different percentage of fly ash (FA), fly ash with sulphur (FS) and red mud (RM) designated as B1 = 45% FA + 5% FS + 50% RM, B2 = 40% FA + 10% FS + 50% RM and B3 = 35% FA + 15% FS + 50% RM (Table 1), (ii) three different liquid to solid ratios (0.70, 0.75, and 0.80), (iii) three different $\text{Na}_2\text{SiO}_3/\text{NaOH}$ ratios (1.0, 1.25, and 1, 5) and (iv) three different molar concentrations of NaOH solution (3, 6.5 and 10). The design of experiments with three factors and three levels is shown in Table 2. Consistent with the L9 orthogonal matrix Taguchi method (36), 9 different mixtures were required to establish the influence of all factors involved, as presented in Table 3. The casting procedure of the obtained geopolymers consisted of the following steps: first, the dry materials (FA, FS and RM) were mixed for 3 min (until a homogeneous mixture was obtained).

Table 2. Experimental factors and levels.

Experimental factor	Level 1	Level 2	Level 3
A. Solid component mixture	B1	B2	B3
B. Liquid to solid ratio (L/S), wt.%	0.7	0.75	0.8
C. Na_2SiO_3 to NaOH ratio, wt.%	1	1.25	1.5
D. Molar concentration of NaOH solution	3	6.5	10

Table 3. The coal ash-mine tailings blended geopolymers mixtures.

Experimental factor		Sample code								
		S1	S2	S3	S4	S5	S6	S7	S8	S9
A	B1	B1	B1	B1	B2	B2	B2	B3	B3	B3
	B	0.7	0.75	0.8	0.7	0.75	0.8	0.7	0.75	0.8
	C	1	1.25	1.5	1.25	1.5	1	1.5	1	1.25
	D	3	10	6.5	6.5	3	10	10	6.5	3

During the process, sodium silicate and sodium hydroxide solution were mixed according to the composition. Afterwards, the liquid component (activator) was added over the solid component (raw materials) and mixed for 3 min to obtain a homogeneous mixture. The mixing of the components was done with the help of a planetary mixer with variable speed, according to the EN 196–1:2016 standard, and the flow of obtaining them is presented in Fig. 1.

After the mixing stage, the obtained binder was poured into moulds with sample dimensions of 40 mm \times 40 mm \times 160 mm and their vibration was applied in order to

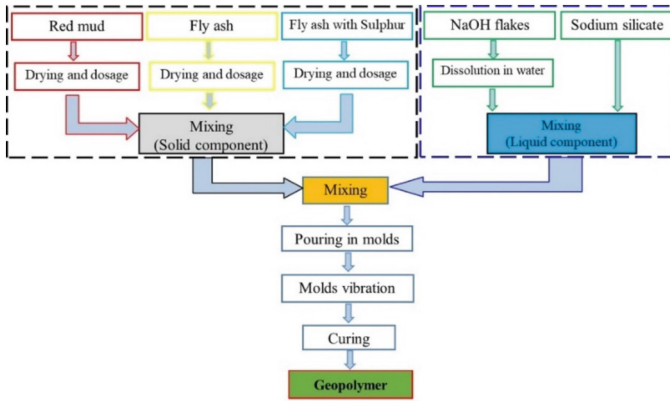


Fig. 1. Schematic representation of the technological flow for obtaining geopolymers.

obtain a uniform mixture with reduced air bubbles. The filled moulds were then cured at room temperature (22 ± 2 °C), the upper surface of the mould was covered with a plastic sheet in order to reduce the evaporation rate of the liquid. The samples were unwrapped after 24 h and kept under laboratory conditions until the day of testing.

The most energy-efficient raw materials and processing procedures were examined to ensure that the developed technology is eco-friendly and has a low CO₂ footprint.

2.3 Methods

Both the compressive and flexural strengths of the developed materials have been tested at 14 and 28 days, respectively. The sample size and testing conditions have been followed according to SR EN 196–1:2016 requirements. The microstructural analysis of the obtained geopolymers was conducted on the fracture surface after the mechanical tests using a scanning electron microscope (SEM) type FEI Quanta FEG 450 (FEI Company, Washington, DC, USA).

3 Results and Discussions

3.1 Raw Materials Characterization

Coal Ash. Two types of coal ashes have been used in the manufacture of the geopolymer samples. The chemical composition of the collected fly ash (Table 4) shows a high content of chemical elements that can contribute to the geopolymerization reaction. As can be seen, the fly ash meets the requirements of ASTM C 618 for class F fly ash since the sum of the main three oxides (SiO_2 , Al_2O_3 and Fe_xO_y) is above 75wt.%. However, the fly ash with sulphur (FS) has a high content of Ca and sulphur oxides and insignificant quantities of other elements that are present in FA. This type of waste results from the desulfurization process of flue gases contains hydrated calcium sulphate ($\text{CaSO}_4 \cdot 2\text{H}_2\text{O}$), calcium sulphites ($\text{CaSO}_3 \cdot 1/2\text{H}_2\text{O}$), anhydrous calcium sulphate and sulphite (CaSO_4 and CaSO_3), other calcium compounds ($\text{Ca}(\text{OH})_2$, CaCO_3 , CaCl_2), as well

as unbound water (H_2O) mixed with fly ash and its mineral components. Considering the chemical composition of the coal ashes, it is expected that the FA will contribute to the sodium aluminosilicate hydrate (N-A-S-H) or aluminium-modified calcium silicate hydrate (C-A-S-H) formation, while the FS addition will promote calcium silicate hydrate (C-S-H), which will result in lower setting time and higher content of ettringite and gypsum [22, 23].

Table 4. Oxide chemical composition of the collected coal ashes.

	Oxide content, wt. %										
	SiO ₂	Al ₂ O ₃	Fe _x O _y	CaO	K ₂ O	MgO	TiO ₂	Na ₂ O	P ₂ O ₅	SO ^x	oth
FA	50.16	27.02	8.40	6.49	1.60	1.59	1.54	0.65	1.16	0.78	< 0.3
FS	4.86	0.01	0.01	68.22	–	–	0.02	–	0.01	26.87	< 0.01

The SEM analysis of the collected coal ashes shows the morphology of the particles from the composition of the fly ash (Fig. 2, a) as well as structural particularities of the FS (Fig. 2, b). As can be seen, the fly ash is a mix of spherical particles with different diameters, ranging from a few micrometers to some that exceed 50 μ m. Compared to FA, FS shows a finer composition consisting mostly of irregular-shaped particles mixed with spherical particles with diameters lower than 5 μ m.

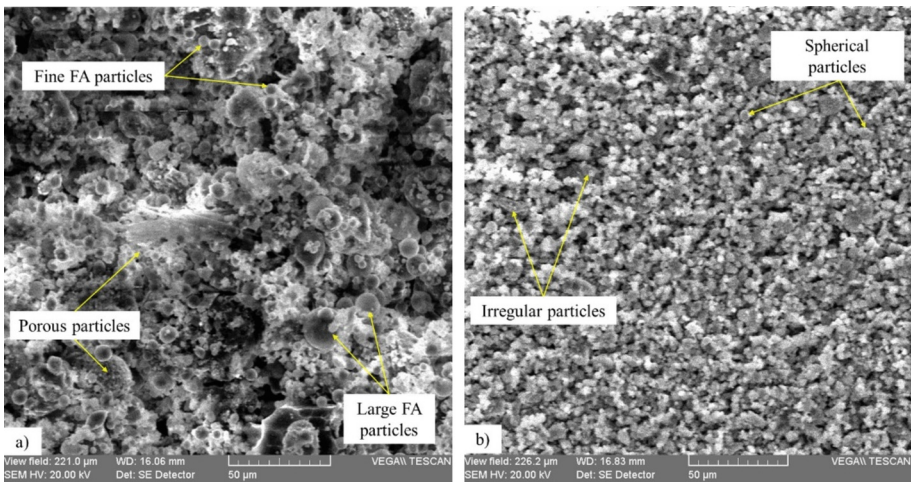


Fig. 2. The morphology of collected coal ashes: a) fly ash; b) fly ash with sulphur.

Red Mud. This waste is a byproduct of the Bayer process used to process bauxite. Its chemical composition is presented in Table 5. The characteristics of alumina mining residues vary depending on the type of bauxite and the alumina production process.

However, the resulting red mud is mainly composed of a mixture of coarse and fine particles. Through the comparative analysis of the SEM micrographs obtained at different magnifications (Fig. 3), it can be seen that the collected material consists of a mixture of millimeter-sized particles but also a considerable fraction of micrometric-sized particles. Also, the microstructural analysis highlights a mixture with high homogeneity and porosity.

Figure 4 shows the distribution of chemical elements on the surface of the studied red mud sample. As can be seen, if we exclude the particle with a high silicon content, this residue shows a homogeneous chemical distribution. However, by correlating the EDAX results with those obtained by SEM analyses, it can be stated that the collected material has a high content of sand particles dispersed relatively uniformly throughout the volume of the material.

Table 5. Oxide chemical composition of red mud.

	Oxide content, wt. %										
	SiO ₂	Al ₂ O ₃	Fe _x O _y	CaO	K ₂ O	MgO	TiO ₂	Na ₂ O	P ₂ O ₅	SO ^x	oth
RM	12.74	16.05	47.33	5.31	0.03	–	3.60	13.86	0.61	0.37	< 0.30

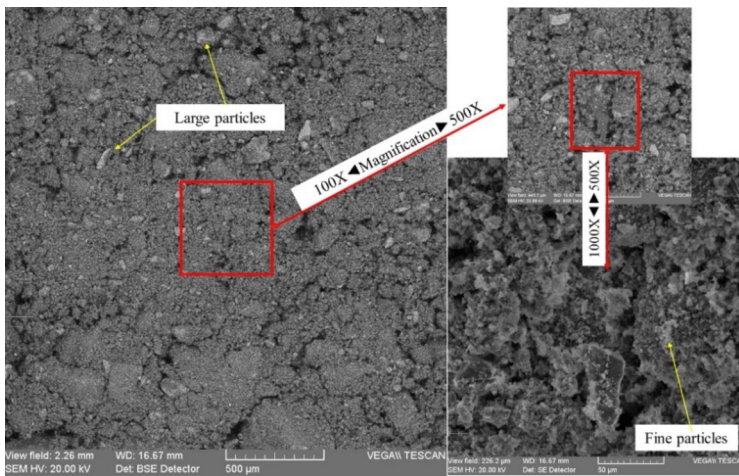


Fig. 3. The morphology of collected red mud particles.

Moreover, among the chemical elements identified, O, Al, and Fe are uniformly distributed over the entire surface, but Ca, Ti, Na, and S present significant concentrations only at the level of small, randomly dispersed particles.

3.2 Mechanical Performance Evaluation

Flexural Strength. The flexural strength of the obtained geopolymers increased in most of the cases from 14 days to 28 days (Fig. 5). Except for sample S2, where a slight

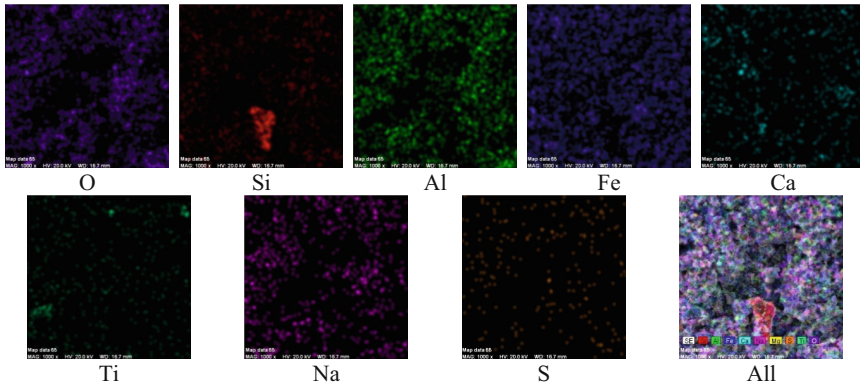


Fig. 4. The distribution of chemical elements on the surface of the analyzed red mud.

decrease can be observed when the age of the samples increases, most of the samples showed a significant improvement in flexural strength. For example, from 14 to 28 days, the value of S3 increased 48 times, the value of S4 increased 10 times, and the lowest increase was that of S1, which increased almost two times. This behavior is related to the NaOH concentration; as also observed in previous studies, higher concentrations will result in better mechanical properties at earlier stages. The high distribution of the flexural strength values confirms that the obtaining parameters are interdependent, i.e., they affect each other. The highest flexural strength at 14 days was presented by the sample S2, which was activated with NaOH (10 M), a Na_2SiO_3 to NaOH ratio of 1.25, and a L/S of 0.75. However, at 28 days, S8 showed the optimum mixture to achieve the highest flexural strength.

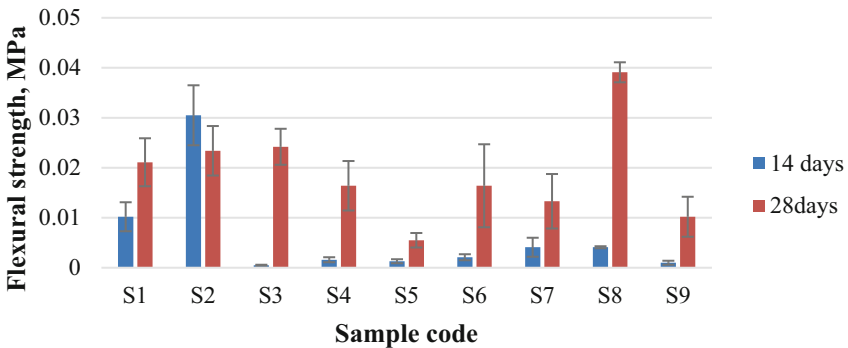


Fig. 5. The flexural strength of the obtained geopolymers.

Compressive Strength. Figure 6 shows the evolution of compressive strength from 14 to 28 days. As can be seen, the mixture specific to S2 didn't perform too well at this test, being one of the samples with almost the same lost value at 28 days. In this case, S7 exhibited the optimum composition despite the aging time, while S4 showed a slight

decrease after 28 days of curing. The increase in compressive strength was in the range of 10 to 130%; the highest evolution was presented by S3, while the lowest was shown by S2. Overall, most of the samples showed an increase of almost 50%. Moreover, the tested mixtures showed a low deviation value, which confirm that the obtained samples had a homogenous structure and composition.

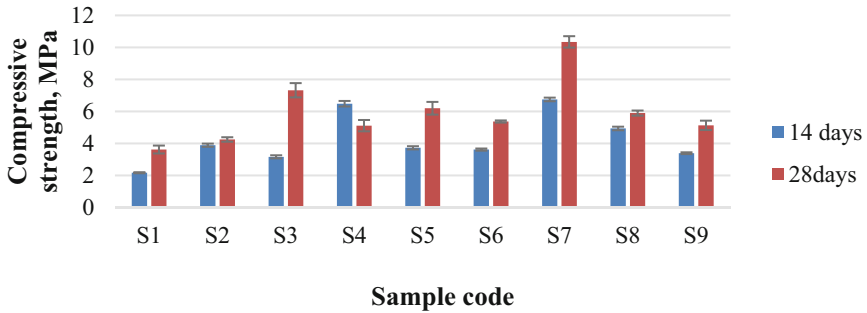


Fig. 6. The compressive strength of the obtained geopolymers.

To better understand the influence of the obtained parameters on the mechanical properties of the obtained geopolymers, 3D plots were drawn.

Figure 7, shows the influence of FS content and $\text{Na}_2\text{SiO}_3/\text{NaOH}$ ratio on the compressive strength value. As can be observed, the sodium silicate to sodium hydroxide ratio has a high influence on the compressive strength; lower ratios will result in poor mechanical properties. Moreover, FS content will also affect the performance of the blended geopolymers. As depicted in Fig. 8, a 10 wt.% addition will show almost constant mechanical properties despite the $\text{Na}_2\text{SiO}_3/\text{NaOH}$ ratio, while an addition of 5 or 15 wt.% will improve the compressive strength depending on this ratio.

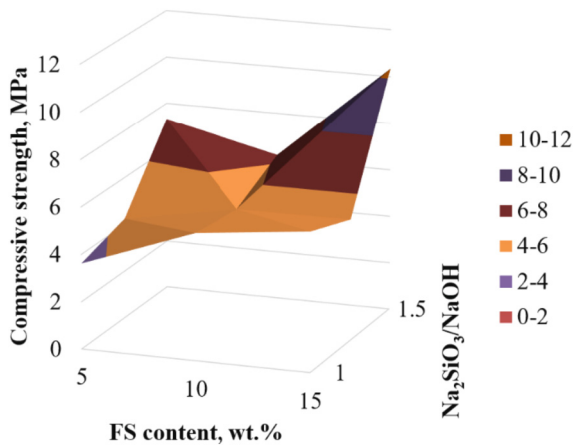


Fig. 7. The influence of FS content and $\text{Na}_2\text{SiO}_3/\text{NaOH}$ ratio on the compressive strength.

L/S is another parameter that can influence the performance of geopolymers. As presented in Fig. 8, at low NaOH concentrations, i.e., 3 or 6.5 M, higher ratios of L/S will promote better compressive strength, while for 10M NaOH, the mixture with L/S of 0.7 showed the optimum composition.

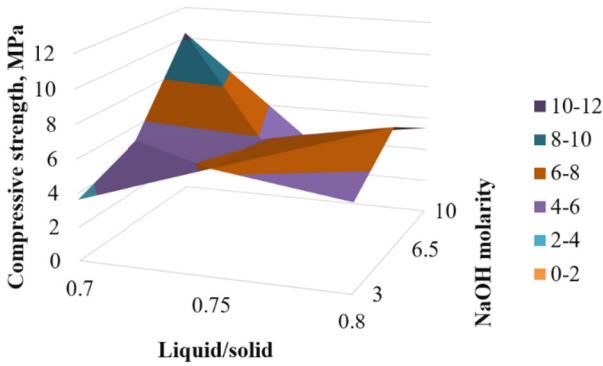


Fig. 8. Influence of liquid/solid ratio and NaOH molarity on compressive strength.

This behavior could be related to activator loss during curing. The OH^- from the activator, especially from the NaOH solution, is responsible for the leaching process of Si^{4+} and Al^{3+} ions; therefore, a loss of activator will also result in a loss of the necessary ions to assure the dissolution of the aluminosilicate material.

Considering the influence of NaOH concentration and FS content (Fig. 9), it can be observed that a combination of high FS and sodium hydroxide solutions will show increased mechanical properties. Moreover, the 3D plot shows that for 5 wt.% of FS, a 6.5M solution of NaOH would be optimum; at 10 wt.% addition, the 6.5 M solution showed higher compressive strength, while for 15 wt.% addition of FS, the NaOH solution with a 10 M concentration showed higher compressive strength.

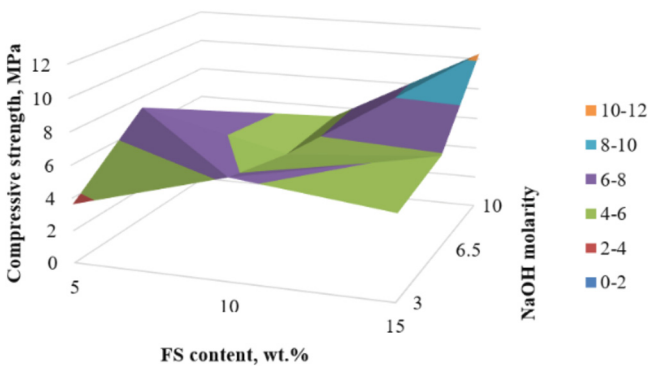


Fig. 9. Influence of FS content and NaOH molarity ratio on compressive strength.

3.3 Microstructural Analysis of the Obtained Geopolymers

In order to highlight the relationship between the morphological particularities of the developed materials and their mechanical performances, the mixture with the lowest compressive strength, i.e., S1, was compared with the one with the highest value for this property, i.e., S7. As can be seen from Fig. 10, the microstructure of the S1 geopolymer (Fig. 10, a) shows multiple unreacted coal ash particles, especially those with high dimensions.

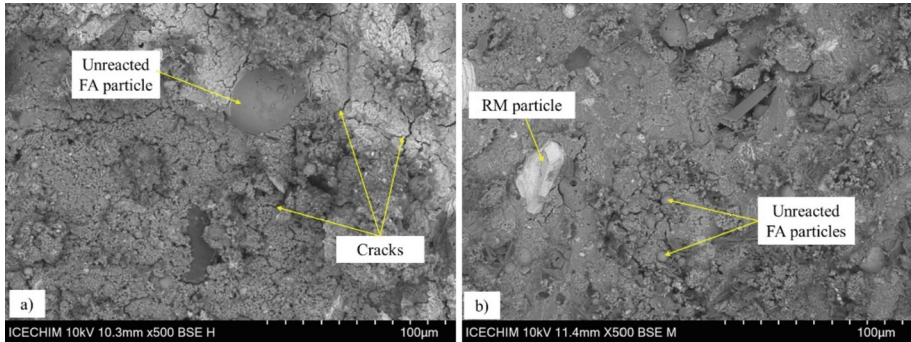


Fig. 10. Microstructural analysis of the obtained geopolymers: a) sample S1; b) sample S7.

Moreover, the entire matrix shows interconnected cracks and a large zone with a high number of pores and voids. Compared to S1, the microstructure of S7 geopolymer shows a much more compact matrix, a low number of cracks, and unreacted particles only in small zones. Moreover, most of the unreacted particles are embedded in the compact matrix.

Considering the composition of the compared mixture, it can be stated that higher NaOH concentrations and Na_2SiO_3 to NaOH ratios will increase the dissolution of the aluminosilicate source and increase the compactness of the matrix, promoting higher mechanical properties.

4 Conclusions

- This study evaluates the influence of liquid-to-solid ratios, $\text{Na}_2\text{SiO}_3/\text{NaOH}$ ratios, and NaOH molarity on the mechanical properties of coal ash-red mud blended geopolymers. According to the obtained results, the following conclusions can be drawn:
- The analysed parameters influence each other. Therefore, it cannot be stated that one parameter will promote better mechanical properties despite the values of the other.
- The addition of 5 wt.% and 15 wt.% of flue gas desulfurization fly ash (fly ash with sulphur) improved the compressive strength of the geopolymers. However, a 10% addition keeps the mechanical properties of the tested materials almost constant despite the fluctuations of the other parameters.

- The mechanical strength tests showed that the mixture with the best compressive strength is the one consisting of 35 wt.% FA, 15 wt.% FS, and 50 wt.% RM, with a liquid to solid ratio (L/S) of 0.7, a Na₂SiO₃ to NaOH ratio of 1.5, and 10 M NaOH, respectively. In terms of flexural strength, the mixture with the same amounts of raw materials exhibited the highest value after 28 days of curing: L/S of 0.75, Na₂SiO₃ to NaOH of 1, and 7M NaOH.

Acknowledgment. This work was supported by a grant of the Ministry of Research, Innovation and Digitization, CNCS/CCCDI -UEFISCDI, project number COFUND-ERAMIN-3-RecMine, contract no. 307/2022, within PNCDI III.

References

1. Salmenperä, H., Pitkänen, K., Kautto, P., Saikku, L.: Critical factors for enhancing the circular economy in waste management. *J. Clean.* **280**, 124339 (2021)
2. Ferronato, N., Rada, E.C., Gorrity Portillo, M.A., Cioca, L.I., Ragazzi, M., Torretta, V.: Introduction of the circular economy within developing regions: a comparative analysis of advantages and opportunities for waste valorization. *J. Environ. Manage.* **230**, 366–378 (2019)
3. Yang, M., et al.: Circular economy strategies for combating climate change and other environmental issues. *Environ. Chem. Lett.* **21**(1), 55–80 (2022)
4. Kumar, V., et al.: Bioengineering of biowaste to recover bioproducts and bioenergy: a circular economy approach towards sustainable zero-waste environment. *Chemosphere* **319**, 138005 (2023)
5. Hemati, S., et al.: Thermal transformation of secondary resources of carbon-rich wastes into valuable industrial applications. *J. Compos. Sci.* **7**(1), 8 (2023)
6. Martinez, D.M., Horvath, A., Monteiro, P.J.M.: Comparative environmental assessment of limestone calcined clay cements and typical blended cements. *Environ. Res. Commun.* **5**, 055002 (2023)
7. Burduhos Nergis, D.D., Vizureanu, P., Lupescu, S., Burduhos Nergis, D.P., Perju, M.C., Sandu, A.V.: Microstructural analysis of ambient cured phosphate based-geopolymers with coal-ash as precursor. *Arch. Metall. Mater.* **67**, 595–600 (2022)
8. Mohamed, O.A., Najm, O., Ahmed, E.: Alkali-activated slag & fly ash as sustainable alternatives to OPC: Sorptivity and strength development characteristics of mortar. *Cleaner Materials* **8**, 100188 (2023)
9. Wang, S., et al.: Application of geopolymers for treatment of industrial solid waste containing heavy metals: state-of-the-art review. *J. Clean. Prod.* **390**, 136053 (2023)
10. Zhang, L., Ahmari, S., Zhang, J.: Synthesis and characterization of fly ash modified mine tailings-based geopolymers. *Constr. Build. Mater.* **25**, 3773–3781 (2011)
11. Moukannaa, S., Loutou, M., Benzaazoua, M., Vitola, L., Alami, J., Hakkou, R.: Recycling of phosphate mine tailings for the production of geopolymers. *J. Clean. Prod.* **185**, 891–903 (2018)
12. Burduhos-Nergis, D.D., Vizureanu, P., Sandu, A.V., Burduhos-Nergis, D.P., Bejinariu, C.: XRD and TG-DTA study of new phosphate-based Geopolymers with coal ash or Metakaolin as Aluminosilicate source and mine tailings addition. *Materials* **15**, 202 (2022)
13. Mancini, S., Casale, M., Rossi, P., Faraudello, A., Dino, G.A.: Operative instruments to support public authorities and industries for the supply of raw materials: a decision support tool to evaluate the sustainable exploitation of extractive waste facilities. *Resour. Policy* **81**, 103338 (2023)

14. Vizureanu, P., Nergis, D.D.B., Sandu, A.V., Nergis, D.P.B., Baltatu, M.S.: The physical and mechanical characteristics of geopolymers using mine tailings as precursors. In: Vizureanu, P. and Krivenko, P. (eds.) *Advances in Geopolymer-Zeolite Composites*. IntechOpen, Rijeka (2021)
15. GRID-Arendal: Global Tailings Dam Portal | GRID-Arendal. <https://www.grida.no/publications/472>
16. Zhang, J., Fu, Y., Wang, A., Dong, B.: Research on the mechanical properties and microstructure of fly ash-based Geopolymers modified by molybdenum tailings. *Constr. Build. Mater.* **385**, 131530 (2023)
17. Orozco, C.R., Castro, K.D.L.T., De Boda, M.M.T.: Valorization of waste mill tailings from small-scale mining through Geopolymerization: strength, durability, and heavy metal leaching potential. *J. Soils Sediments* **23**, 1985–1997 (2023)
18. Opiso, E.M., Tabelin, C.B., Maestre, C.V., Aseniero, J.P.J., Arima, T., Villacorte-Tabelin, M.: Utilization of palm oil fuel ash (POFA) as an admixture for the synthesis of a gold mine tailings-based Geopolymer composite. *Minerals* **13**, 232 (2023)
19. Qing, L., Chuanming, L., Huili, S., Junxiang, W., Xianjun, L.: Use of activated quartz powder as an alkaline source for producing one-part Ca-rich slag based cementitious materials: activation mechanism, strength, and hydration reaction. *J. Build. Eng.* **64**, 105586 (2023)
20. Krishna, R.S., Shaikh, F., Mishra, J., Lazorenko, G., Kasprzhitskii, A.: Mine tailings-based Geopolymers: properties, applications and industrial prospects. *Ceram. Int.* **47**, 17826–17843 (2021)
21. Marinova, S., Deetman, S., van der Voet, E., Daioglou, V.: Global construction materials database and stock analysis of residential buildings between 1970–2050. *J. Clean. Prod.* **247**, 119146 (2020)
22. Faradilla, F.S., Nugroho, D.T., Hidayati, R.E., Nurlina, Bayuaji, R., Hartanto, D., Fansuri, H.: Optimization of SiO₂/Al₂O₃ ratio in the preparation of Geopolymer from high calcium fly ash. *IOP Conference Series: Earth and Environmental Science*, vol. 616, p. 12051 (2020)
23. Amran, M., et al.: Long-term durability properties of Geopolymer concrete: an in-depth review. *Case Stud. Constr. Mater.* **15**, e00661 (2021)



Densification Behavior and Mechanical Performance of Nepheline Geopolymer Ceramics: Preliminary Study

Nur Bahijah Mustapa¹ , Romisuhani Ahmad^{1,2} ,
Mohd Mustafa Al Bakri Abdullah² , Wan Mastura Wan Ibrahim^{1,2} ,
Andrei Victor Sandu³ , Christina Wahyu Kartikowati⁴ , Puput Risdanareni⁵ ,
and Wan Hasnida Wan Mohamed Saimi¹

- ¹ Faculty of Mechanical Engineering Technology, Universiti Malaysia Perlis (UniMAP), 01000 Perlis, Malaysia
romisuhani@unimap.edu.my
- ² Center of Excellence Geopolymer and Green Technology (CEGeoGTech), Faculty of Chemical Engineering; Technology, Universiti Malaysia Perlis (UniMAP), 01000 Perlis, Malaysia
- ³ Faculty of Material Science and Engineering, Gheorghe Asachi Technical University of Iasi, 700050 Iasi, Romania
- ⁴ Department of Chemical Engineering, Universitas Brawijaya, Malang, Indonesia
- ⁵ Department of Civil Engineering, Faculty of Engineering, Universitas Negeri Malang, 65145 Malang, Indonesia

Abstract. Nepheline geopolymer ceramics have emerged as a promising sustainable alternative to traditional cementitious materials in various applications. As the sintering mechanism plays a crucial role in the densification and mechanical performance of ceramics, therefore, in this paper, a preliminary study was conducted to examine the effects of densification towards mechanical properties of geopolymer-based nepheline ceramics upon sintering. The said innovative geopolymer technology can convert raw materials of aluminosilicate activating with alkaline activator into ceramic-like materials requiring low temperatures. The experimental procedure includes the synthesis of nepheline geopolymer ceramics through the geopolymerization method, then sintered at different temperatures to explore the sintering behavior and its impact on the materials' microstructure and mechanical performance. The densification behavior of nepheline geopolymer ceramics during sintering was analyzed by evaluating the changes in density, shrinkage, and porosity. The microstructural evolution and are determined by using SEM. The relationships between sintering conditions, microstructure, and mechanical performance were investigated to understand the underlying mechanisms affecting the material's strength and durability. The geopolymer exhibited its highest flexural strength of 54.93 MPa when sintered at 1200 °C, while the lowest strength of 6.07 MPa was observed at a sintering temperature of 200 °C. The findings demonstrate a positive correlation between the sintering temperature and the flexural strength of the geopolymer ceramics, indicating that higher temperatures lead to increased strength. Ultimately, this knowledge can facilitate the broader utilization of nepheline geopolymer ceramics as sustainable materials in various engineering and construction applications.

Keywords: Geopolymer · Geopolymer-based Ceramics · Ceramics · Sintering Mechanism

1 Introduction

In the production of high-strength ceramics, the conventional method often involves high processing temperatures exceeding 1600 °C. However, this high temperature can have adverse effects on the resultant materials, particularly on pore size and distribution, which are critical factors influencing mechanical properties. Methods like Hot Isostatic Pressing (HIP) and Spark Plasma Sintering (SPS) have been utilized to produce high-density ceramics. However, these methods often pose challenges in terms of cost and complexity, making them inaccessible to many industries and research institutions that lack the necessary equipment and expertise to carry out the intricate sintering process and control requirements [1]. Conventionally, sintering of glass-ceramics typically involved two main steps. Firstly, the raw materials are heated to high temperatures, reaching up to 1500 °C, to achieve vitrification, followed by the processes of nucleation and crystal growth [2]. Besides, the requirement for high sintering temperature, the resulting ceramics also suffer from various complications such as agglomeration, abnormal grain growth, and furnace contamination. Therefore, the novel method of using geopolymer in producing ceramic materials is introduced.

In the 1970s, a researcher Davidovits introduced geopolymer firstly as an alternative to developing inorganic polymer materials. Geopolymers, classified as ceramic-like inorganic polymers, are synthesised at temperatures below 100 °C. These materials consist of interconnected mineral molecules bonded by covalent links. The composition of geopolymers typically involves aluminosilicates, including rock-forming minerals, amorphous silica, and aluminosilicate-rich industrial by-products like coal fly ash and blast furnace slag. These raw materials offer ample sources of aluminosilicates for geopolymer production. By mixing the aluminosilicate sources into a strong alkali activator such as sodium hydroxide (NaOH), geopolymers were synthesised by the dissolution and polycondensation of aluminosilicate materials in alkali-activated solutions [3, 4]. Geopolymers offer numerous desirable characteristics, including low weight, impressive thermal and mechanical properties, strong resistance to chemicals, and good permeability. These advantageous traits make geopolymers suitable for various applications, such as high-temperature-resistant ceramics, heat-resistant coatings and adhesives, containment of radioactive waste, and as cementitious components in construction materials [5]. Moreover, geopolymers are gaining recognition as suitable matrices for reinforced composites, various refractory applications, corrosion-resistant coatings, and as precursors for the formation of ceramics [6].

In contemporary times, there has been a burgeoning interest in innovative ceramic materials based on geopolymers, owing to their remarkable mechanical characteristics and ecological compatibility. These materials have garnered significant attention and are poised to exhibit substantial applicability in the times ahead. Geopolymer exposed to high temperatures by the sintering process produces ceramic materials. This is due to the effect of the sintering mechanism when heat is applied to the geopolymer body. For example,

geopolymer was used to produce high-flexural strength ceramics and one-part-mixing GP [7]. Nevertheless, the utilization of high-temperature sintering alone can induce undesirable shrinkage and cracking, consequently compromising the overall strength of the end products. The utilization of low-temperature geopolymer-based ceramics offers convenience in the production of diverse and intricately shaped products. Moreover, these ceramics exhibit commendable fire resistance, environmental friendliness, and exceptional thermal properties [8]. Furthermore, the exploration of porous geopolymer-based ceramic materials has gained significant attention in current research due to their notable stability, high surface area, and permeability. These materials hold promise for various applications in lightweight structural components, filters, and other relevant areas.

The characteristics of the pores, such as their shape, volume, and distribution, in porous geopolymer-based ceramics are influenced significantly by the manufacturing technique and the composition of the composites. Research has demonstrated that by altering the chemical composition of the geopolymer-based ceramics, it is possible to control the water retention and adjust the porosity accordingly [9]. The progression of phase formation subsequent to the sintering process is contingent upon multiple variables, including the composition of the raw materials, the preparation of the ceramic mixtures, and the specific optimum temperature at which the ceramic structure is subjected to the sintering procedure [10]. However, there is a lack of studies investigating how the sintering mechanism affects the densification and crystallisation of geopolymer-based ceramics as it correlates with the mechanical properties of the end product. Therefore, in this paper, the sintering mechanism of geopolymer-based ceramics is studied. Effects on the densification of ceramics products and the mechanical performance are analysed when heat is applied during the sintering process.

2 Experimental Method

2.1 Geopolymer-Based Ceramic Sample Preparation

The aluminosilicate used in this study was kaolin supplied by Associated Kaolin Industries Sdn. Bhd, Petaling Jaya, Selangor, Malaysia. Kaolin has a chemical formula of $\text{Al}_2\text{Si}_2\text{O}_5(\text{OH})_4$, where SiO_2 and Al_2O_3 contribute a large amount to its composition. The alkali activator was prepared by mixing liquid sodium silicate (Na_2SiO_3) and sodium hydroxide (NaOH) solution. The NaOH solution was prepared by mixing distilled water with caustic soda pellets from Formosoda-P, Taiwan. The liquid sodium silicate was supplied by South Pacific Chemicals Industries Sdn. Bhd. (SPCI), Pahang, Malaysia. It is composed of 30.1% SiO_2 , 9.4% Na_2O , and 60.5% H_2O .

A fully dissolved 12 M NaOH solution was mixed with Na_2SiO_3 with a molar ratio of 0.24. Geopolymer-based nepheline ceramic is prepared by mixing kaolin raw materials with an alkali activator, producing a slurry geopolymer paste. The paste then being cured at 80 °C for 24 h before the geopolymer sample was milled and sieved using a 150 μm sieve to obtain a fine geopolymer powder. The fine powder was compressed at 4.5 tons for 2 min. The geopolymer was sintered at six different temperatures of 200 °C, 400 °C, 600 °C, 800 °C, 1000 °C, and 1200 °C, soaking time of 180 min and 5 °C/min heating rate. Later, the nepheline geopolymer-based ceramics produced were characterized to

study the density behaviour and its mechanical properties upon the increment of sintering temperature.

2.2 Characterization of Geopolymer Ceramic

The flexural strength of the geopolymer-based ceramics was evaluated as a measure of their mechanical properties. The testing was conducted using a three-point bending fixture with dimensions of 7 mm x 5 mm x 52 mm, following the ASTM C-1163b standard. To determine the flexural strength of kaolin geopolymer ceramic samples, an Instron-500 tester is utilized. The specimens are subjected to a three-point bending test using a fixture with a span length of 30 mm, and the crosshead speed is set at 0.3 mm/min. The density of geopolymer-based ceramics was determined by applying Archimedes' Rule. The percentage of shrinkage of the geopolymer-based ceramics after sintering at high temperatures was calculated by knowing the dimension before and after the sintering process. The JSM-6460LA model Scanning Electron Microscope (JEOL, Peabody, MS, USA) was utilized to examine the microstructural changes in the nepheline geopolymer-based ceramic. Prior to imaging, the samples were coated with a layer of gold using the JEOL JFC 1600 Auto Fine Coater (Peabody, MS, USA).

3 Results and Discussion

3.1 Physical and Mechanical Properties of Geopolymer-Based Ceramic

Figure 1 presents the changes in the density of unsintered and sintered geopolymer-based ceramics. It is observed that the sintering mechanism for geopolymer sintered at 1200 °C has the highest density (2.254 g/cm³) compared to geopolymer sintered at 200 °C (1.396 g/cm³) and unsintered geopolymer (1.349 g/cm³). As the sintering temperature increase, the bulk density shows an increment. The sintering mechanism facilitates the increase in viscous flow as a result of the presence of a dissolved glassy phase. The highest density, indicating the completion of the densification process, was achieved at a temperature of 1200 °C. Upon sintering to 1200 °C, the water vapour liberates from the pores, of the geopolymer structure [11], lead to the pore formation. This outcome is due to the thermal influence, which facilitates the expansion of the geopolymer matrix [12]. As the sintering process takes place, the application of higher temperatures encourages the densification of kaolin geopolymer-based ceramics. This process involves the migration, rearrangement, and shrinkage of particles, which leads to changes in the bulk density of the ceramics. When the temperature is increased, the diffusion of grains near each other is enhanced, causing a decrease in the distance between alumina grains and promoting grain growth. Consequently, the ceramics become more compact and denser in structure [13, 14].

The sintering temperature plays a significant role in determining the flexural strength of the kaolin-based geopolymer. Figure 2 shows the trend of flexural strength for kaolin-based geopolymer when the sintering temperature increased. The flexural strength of geopolymer-based ceramics sintered at 1200 °C recorded the highest reading (54.932 MPa), while the unsintered geopolymer had the lowest flexural strength

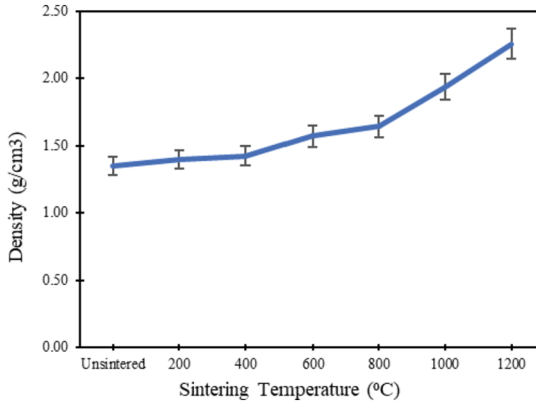


Fig. 1. Density of unsintered and sintered geopolymer-based nepheline ceramics at various temperatures.

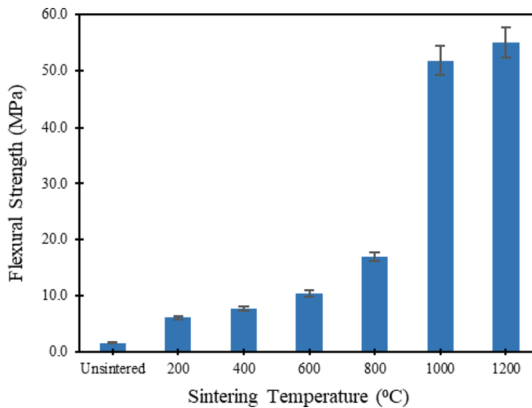


Fig. 2. Flexural strength of unsintered and sintered geopolymer-based nepheline ceramics at various temperatures.

(1.588 MPa). The geopolymer-based ceramics happen to increase a drastic strength when sintered at 1000 °C as the geopolymer matrices start to densify.

Overall, the flexural strength of geopolymer-based ceramics exhibited an upward trend as the exposure temperature increased. The observed enhancement in strength can be attributed to exothermic reactions that facilitated the continued geopolymerization of unreacted precursor materials. This led to the generation of additional reaction products, contributing to the overall strength improvement. Additionally, the densification of the geopolymer structure, facilitated by the solidifying melt and the development of refractory phases within thin geopolymers, contributed to enhanced flexural strength [18]. The elevated temperature played a crucial role in promoting the densification process within the geopolymer matrix, allowing it to fill voids and cracks, ultimately leading to

improved strength. The formation of a more compact structure played a significant role in enhancing the overall strength performance [19].

The enhanced strength observed at 1200 °C can be attributed to the effective diffusion and coalescence of particles, forming large sintered area and a uniform geopolymer matrix. The exposure to elevated temperatures facilitated the sintering process, leading to increased strength by promoting stronger interparticle bonding and effectively mitigating thermal damage at high temperatures. The synergy of polymerization and sintering mechanisms likely contributes to the observed enhancement in geopolymer strength. By subjecting the sample to high temperatures, not only did it solidify, but it also underwent crystallization, leading to enhanced mechanical properties. The flexural strength of the materials improves as the sintering temperature increases, primarily due to the promotion of densification and the suppression of significant grain growth [20].

3.2 Microstructural Evolution of Geopolymer-Based Ceramic

Figure 3 illustrates the results of morphological analyses conducted on kaolin geopolymer ceramics subjected to high-temperature sintering.

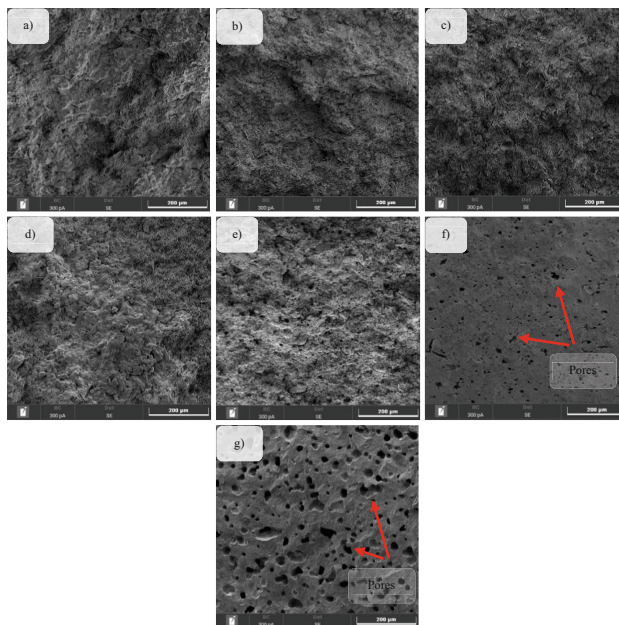


Fig. 3. SEM images of unsintered and sintered geopolymer-based nepheline ceramics at various temperatures.

SEM images of kaolin geopolymer ceramics sintered at temperatures between 200 °C and 400 °C, display the scanning image that closely resembles the unsintered samples.

These images depict a network of amorphous geopolymers with visible cracks, which may be associated with the mechanical strength tests or the evaporation of water during sintering.

Distinct morphological variations are observed when comparing the sintered samples at 800 °C, 1000 °C and 1200 °C with the unsintered geopolymers. These differences signify the crystallization of geopolymers beyond 800 °C, resulting in the elimination of surface irregularities and the formation of a crystalline structure. The transformation from an amorphous network to a crystalline in kaolin geopolymers thereby enhancing their resistance to high temperatures. Although the porosity remains relatively steady above 1000 °C, the open pores decrease due to the partial melting of the geopolymer matrix and the release of gases [21].

The presence of small pores indicates the occurrence of a phase transition from amorphous to crystalline. At higher temperatures, there is a notable expansion of pores as liquid water undergoes a transformation into vapour. This transformation applies pressure on the walls of the pores and creates connections between neighbouring pores, leading to the elimination of smaller pores.

The elevated sintering temperature contributes to the formation of a uniform and smooth microstructure. Densification occurs as fine particles are eliminated, leading to the entrapment of certain pores within the grains and the development of irregular pore sizes [22]. These phenomena arise from thermal expansion due to the release of residual water content, oxidation, and crystallization processes occurring within the geopolymer. Consequently, pore formation and the initiation of cracks are observed.

4 Conclusion

The preliminary results indicate that the sintering mechanism significantly influences the densification behavior and mechanical properties of nepheline geopolymer-based ceramics. Higher sintering temperatures led to enhanced densification, resulting in increased density and reduced porosity. The microstructural analysis revealed that sintering promoted grain growth, leading to the formation of denser and more interconnected microstructures. The presence of well-developed interparticle bonding contributed to the improved mechanical properties of the sintered ceramics.

The findings from this study contribute to the fundamental understanding of sintering processes in nepheline geopolymer ceramics, aiding in the development of optimized manufacturing techniques and improved mechanical properties. Ultimately, this knowledge can facilitate the broader utilization of nepheline geopolymer ceramics as sustainable materials in various engineering and construction applications.

Acknowledgements. This research was funded by Fundamental Research Grant Scheme (FRGS) under grant number FRGS/1/2021/TK0/UNIMAP/02/17 from the Ministry of Education, Malaysia.







References

1. Cho, D.G., Yang, S.K., Yun, J.C., Kim, H.S., Lee, J.S., Lee, C.S.: Effect of sintering profile on densification of nano-sized Ni/Al₂O₃ composite. *Compos. B Eng.* **45**(1), 159–164 (2013)
2. Jamil, N.H., Abdullah, M.M.A.B., Pa, F.C., Mohamad, H., Ibrahim, W.M.A.W., Chairapra, J.: Influences of SiO₂, Al₂O₃, CaO and MgO in phase transformation of sintered kaolin-ground granulated blast furnace slag geopolymer. *J. Market. Res.* **9**(6), 14922–14932 (2020)
3. Yuan, J., et al.: Effects of kinds of alkali-activated ions on geopolymerization process of geopolymer cement pastes. *Construct. Build. Mater.* **293** (2021)
4. Zakka, W.P., Lim, N.H.A.S., Khun, M.C.: A scientometric review of geopolymer concrete. *J. Clean. Prod.* **280**, 124353 (2021)
5. Shen, J., Li, Y., Lin, H., Lv, J., Feng, S., Ci, J.: Early properties and microstructure evolution of alkali-activated brick powder geopolymers at varied curing humidity. *J. Build. Eng.* **54**, 104674 (2022)
6. Sankar, K., Stynoski, P., Al-Chaar, G.K., Kriven, W.M.: Sodium silicate activated slag-fly ash binders: Part I-Processing, microstructure, and mechanical properties. *J. Am. Ceram. Soc.* **101**(6), 2228–2244 (2018)
7. Liew, Y.M., et al.: Formation of one-part-mixing geopolymers and geopolymer ceramics from geopolymer powder. *Constr. Build. Mater.* **156**, 9–18 (2017)
8. Singh, N.B., Middendorf, B.: Geopolymers as an alternative to Portland cement: an overview. *Constr. Build. Mater.* **237**, 117455 (2020)
9. Wu, Y., et al.: Geopolymer, green alkali activated cementitious material: synthesis, applications and challenges. *Constr. Build. Mater.* **224**, 930–949 (2019)
10. Ramli, M.I.I., et al.: The influence of sintering temperature on the pore structure of an alkali-activated kaolin-based geopolymer ceramic. *Materials* **15**(7), 2667 (2022)
11. Yuan, J., et al.: Thermal evolution of lithium ion substituted cesium-based geopolymer under high temperature treatment, part I: effects of holding temperature. *Ceram. Int.* **44**(9), 10047–10054 (2018)
12. Shaikh, F.U.A., Vimonsatit, V.: Compressive strength of fly-ash-based geopolymer concrete at elevated temperatures. *Fire Mater.* **39**(2), 174–188 (2015)
13. Chen, X., et al.: Low sintering temperature and high piezoelectric properties of Li-doped (Ba, Ca)(Ti, Zr) O₃ lead-free ceramics. *J. Alloy. Compd.* **632**, 103–109 (2015)
14. Khattab, R.M., Wahsh, M.M.S., Khalil, N.M.: Preparation and characterization of porous alumina ceramics through starch consolidation casting technique. *Ceram. Int.* **38**(6), 4723–4728 (2012)
15. Yong-Sing, N., et al.: Improvements of flexural properties and thermal performance in thin geopolymer based on fly ash and ladle furnace slag using borax decahydrates. *Materials* **15**(12), 4178 (2022)
16. Yong-Sing, N., et al.: Thin fly ash/ladle furnace slag geopolymer: effect of elevated temperature exposure on flexural properties and morphological characteristics. *Ceram. Int.* **48**(12), 16562–16575 (2022)
17. Kavakeb, K., Balak, Z., Kafashan, H.: Densification and flexural strength of ZrB₂-30 vol% SiC with different amount of HfB₂. *Int. J. Refract Metal Hard Mater.* **83**, 104971 (2019)
18. Badanoiu, A.I., Al Saadi, T.H.A., Stoleriu, S., Voicu, G.: Preparation and characterization of foamed geopolymers from waste glass and red mud. *Construct. Build. Mater.* **84**, 284–293 (2015)

19. Chen, Y., Song, S., Zhu, S., Cui, X., Zhao, F.: Selective laser remelting of in-situ Al_2O_3 particles reinforced AlSi10Mg matrix composite: densification, microstructure and microhardness. *Vacuum* **191**, 10365 (2021)
20. Payakaniti, P., Chuewangkam, N., Yensano, R., Pinitsoontorn, S., Chin-daprasirt, P.: Changes in compressive strength, microstructure and magnetic properties of a high-calcium fly ash geopolymer subjected to high temperatures. *Constr. Build. Mater.* **265**, 120650 (2020)



The Properties of Crumb Rubber Loading on Fly Ash Based Geopolymer Mortar

Reshikesan Ravi¹ , Ahmad Azrem Azmi^{1,2} ,
Mohd Mustafa Al Bakri Abdullah¹ , Lokman Hakim Ibrahim^{1,2} ,
Romisuhani Ahmad³ , and Che Mohd Ruzaidi Ghazali⁴ 

¹ Faculty of Chemical Engineering and Technology, Universiti Malaysia Perlis,
01000 Perlis, Malaysia

ahmadazrem@unimap.edu.my

² Center of Excellence Geopolymer and Green Technology (CEGeoGTECH), Universiti
Malaysia Perlis, 01000 Perlis, Malaysia

³ Faculty of Mechanical Engineering and Technology, Universiti Malaysia Perlis,
01000 Perlis, Malaysia

⁴ Faculty of Ocean Engineering Technology and Informatics, Universiti Malaysia Terengganu,
21030 Terengganu, Malaysia

Abstract. By replacing traditional Portland cement (OPC) with crumb rubber in fly ash-based geopolymer mortar, waste tyre disposal and natural mineral aggregate use can be reduced, resulting in lower CO₂ emissions. Crumb rubber geopolymer mortar is formed when sodium hydroxide (NaOH) and sodium silicate (Na₂SiO₃) are mixed with fly ash (class F) to make aluminosilicate gel. All of the fly ash geopolymer preparations followed the same ratio of solid to liquid (2:1) and the same ratio of NaOH solution (12M) to Na₂SiO₃ solution (2.5). Different amounts of crumb rubber (0%, 5%, 10%, 15%, and 20% by weight of solid) were added to the mixture. The results show that the compressive strength of the geopolymer mortar decreased with increasing crumb rubber loading. The results of the analysis show that the compressive strengths of CR-0%, CR-5%, CR-10%, CR-15%, and CR-20% are 25,59,14,31,11.19,10.38, and 8.16 MPa. The strength is diminished because of inadequate interfacial adhesion between the crumb rubber and geopolymer paste. As the sample weight fell, the percentage of crumb rubber in the geopolymer mortar in-creased, but the density decreased.

Keywords: Crumb Rubber · Fly Ash · Geopolymer Mortar · Compressive · Density · Water absorption

1 Introduction

Geopolymer mortar uses the same materials as traditional mortar, with the exception of cement, which is completely substituted by industrial products like fly ash from coal-fired power plants [1]. Fly ash, an ingredient in geopolymer mortar, reduces carbon emissions by as much as 80% compared to ordinary mortar while maintaining all of its structural integrity [2]. Geopolymer is created by activating aluminosilicate materials

by using an alkaline solution known as ‘geopolymerization’ process [3]. The geopolymerization process is aided by a concentrated solution of alkali-based chemicals like sodium hydroxide (NaOH) and sodium silicate (Na_2SiO_3).

Due to rising vehicle numbers, economic growth, and the automotive industry, tire production has grown worldwide [4]. Population expansion, urbanization, higher incomes, and better roads have increased tire consumption. Tire production has increased waste, posing environmental issues [5]. Tire stockpiles, caused by tire landfilling and unlawful dumping, take up precious area and generate mosquitoes and pests [6]. Tire stacks can burn for long periods, creating harmful smoke and chemicals that harm air quality and public health. Decomposing tires can pollute soil and water. Tires also release microplastics, adding to microplastic contamination. These microscopic particles can penetrate ecosystems, threatening aquatic life and the food chain [7]. One of the solutions to reduce waste tires is processing this waste into alternative aggregates such as shredded, chipped or crumb rubber through the incorporation in manufacturing of geopolymer construction composites (binders, mortar, concrete) [8].

Considering the above, there have been several studies conducted on both geopolymer mortar as well as rubberized mortar or concrete [9–13]. It improves geopolymer matrix ductility [14, 15], crack resistance [16] and impact resistance [17]. It also reduces thermal sound properties [18] and increases the elevated temperature exposure of crumb rubber geopolymer mortar [2, 19]. However, challenges such as optimizing rubber content, understanding long-term behavior, and establishing standardization remain areas for further research. Overcoming these obstacles can unlock the potential of crumb rubber in geopolymer to enhance environmental sustainability and the performance of cementitious materials [20].

2 Materials and Samples Preparation

The low calcium class F fly ash was taken from the Sultan Abdul Aziz Power Station in Kapar, Selangor, Malaysia. The fly ash is used as a source material in the geopolymer mortar mixture. X-Ray Fluorescence (XRF) used to determine the composition of fly ash (Table 1).

Table 1. The composition of fly ash.

Elements	% Mass
Al_2O_3	23.40
SiO_2	50.00
SO_3	0.08
K_2O	1.41
CaO	5.06
TiO_2	1.60
MnO	0.22
Fe_2O_3	17.29

Meanwhile, the crumb rubber from Gcycle Factory Sdn. Bhd. in Sungai Petani, Kedah. The used of crumb rubber is used to replace fine aggregates. Crumb rubber has particles size ranging from 73 μm to 375 μm in order to reduce the unit weight of the geopolymer mortar mixture.

NaOH was obtained from Formosa Plastic Corporation, Taiwan. The 480 g of NaOH powder were dissolved in 1L distilled water and allowed to cool down at room temperature to make 12M NaOH solution. Musbash Resources Sdn. Bhd., located in Kuala Lumpur, was the company that provided the Na_2SiO_3 .

The NaOH and Na_2SiO_3 are combined with the ratio of Na_2SiO_3 to NaOH was fixed at 2.0 and agitated for at least 5 min, or until a homogeneous solution is obtained. The alkali activator solution is combined with fly ash raw materials at least 24 h before use. The NaOH/ Na_2SiO_3 ratio employed for the alkali activator solution was 2.5.

The manufacturing process of producing crumb rubber geopolymer mortar involves several processes. The processes include the preparation of fly ash geopolymer mortar, which is the mixing, molding and curing process. The crumb rubber geopolymer mortar was molded into the shape of a cube with dimensions of 50 mm on each side, as specified by ASTM C109. The proportions of the mix for the crumb rubber geopolymer mortar are shown in Table 2.

The crumb rubber aggregate was employed to replace sand aggregate at replacement of 5%, 10%, 15%, and 20% by weight of the solid. These percentages refer to the total mass of the mortar. The control mixture is the one that simply has fly ash in it and does not have any crumb rubber added to it.

Table 2. Mix proportion of Crumb rubber geopolymer mortar.

Samples	Fly ash (g)	Crumb rubber (g)
CR-0%	800	0
CR-5%	760	40
CR-10%	720	80
CR-15%	680	120
CR-20%	640	160

In the beginning, fly ash and crumb rubber are combined and blended in a large mixing container until they form a consistent mixture. It is necessary to give the alkali activator solution a good shake before adding it to the hand mixer that is already carrying the combination of fly ash and crumb rubber. In accordance with the specifications of the ASTM C109 standard, the geopolymer mortar mixture with variable crumb rubber loadings is poured into steel cube molds measuring 50mm x 50mm x 50mm. During the curing process, the samples are either hermetically sealed or coated with a thin coating of plastic to avoid contamination and loss of moisture. This covering helps to maintain a regulated atmosphere for the curing process, and it also stops the samples from drying out too soon. The curing time lasts for a total of 28 days.

3 Testing

3.1 Water Absorption Test

The water absorption test was carried out in line with ASTM C1585 as part of the study of crumb rubber geopolymer mortar. After 28 days, the cubes were then submerged in room-temperature water for a whole day (24 H). In this way, the mortar may absorb water in a contained manner. Before (W_1) and after (W_2) immersion, the weight of each mortar cube was recorded (W_2). A precise weighing scale or balance was used for the measurements. The Eq. 1 was used to determine the crumb rubber geopolymer mortar's ability to absorb water:

$$\text{Percentage absorbent of water} = ((W_2 - W_1)/W_1) \times 100\% \quad (1)$$

3.2 Density Measurement

ASTM C138 was used to determine the density of the samples used in the study of crumb rubber geopolymer mortar. Density, a measure of the mass contained inside a given volume, may be calculated with relative ease. Each sample of crumb rubber geopolymer mortar was weighed on a precision balance or scale to determine its mass. This equation was used to determine the density (Eq. 2).

$$\text{Density (kg/m}^3\text{)} = \text{Mass (kg)}/\text{Volume (m}^3\text{)} \quad (2)$$

3.3 Compressive Strength Test

The compressive strength test was carried out using a Shimadzu UH-1000kN Universal Testing Machine in accordance with the standard established by the ASTM C109. In this instance, a loading rate of 1.0 MPa per second was applied to the system. After curing for a total of 28 days, a test of the material's compressive strength was carried out.

3.4 Scanning Electron Microscopy (SEM)

In accordance with ASTM B748, the SEM has been used to perform a morphological study. After compression testing, the microscopic images of crumb rubber geopolymer mortar were captured and this image was used to analyze the distribution of stress and failure mechanisms in crumb rubber geopolymer mortar samples.

4 Discussion

4.1 Water Absorption Analysis

Analysed the amount of water that can be absorbed following a 24-h of immersion with the cure duration of 28 days is shown in Fig. 1. Figure 1 demonstrates that when the crumb rubber loading rises, the water absorption capacity of the resulting geopolymer mortar increases as well. The percentages of water absorption capacity are as follows: CR-1% had 1.18%, CR-5% had 5.56%, CR- 10% had 9%, CR-15% had 14.52%, and CR-20% had 19.12%.

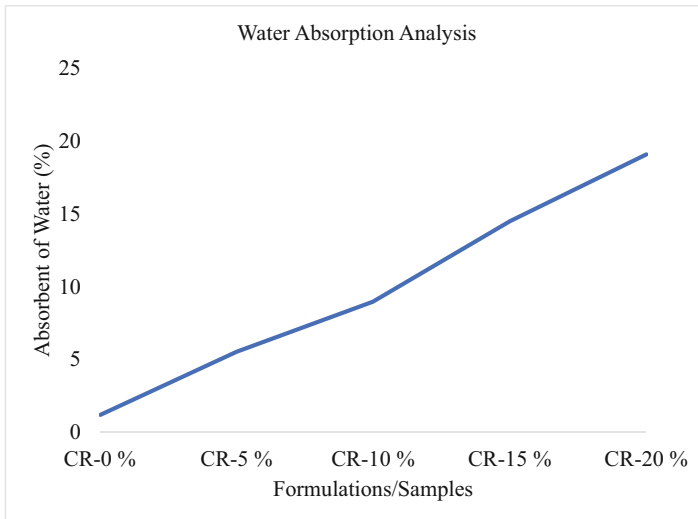


Fig. 1. The percentage of water absorption analysis at 28 days of curing time with 24 h of immersion.

When examining water absorption, consider crumb rubber's impact on mortar density, porosity, and surface. Crumb rubber's water-absorbing ability increases with the mortar's crumb rubber content. Crumb rubber particles allow air to enter and weaken mortar. These spaces allow water to permeate and absorb the material more, enhancing its water-holding capacity. Crumb rubber also makes mortar less dense. Crumb rubber particles are lighter than the geopolymer matrix, causing the density reduction. Crumb rubber particles make mortar lighter. If the material is less dense, it may absorb more water. Crumb rubber geopolymer mortar's water absorption may be modified by other variables. Changing the mixture's ingredients can change its water-absorbing properties. Crumb rubber's porous nature, reduced mortar density, and increased surface area promote water absorption at higher percentages.

4.2 Density Analysis

The density study of various mixes of crumb rubber geopolymer mortar of curing period for 28 days is shown in Fig. 2. According to Fig. 2, there was a rise in the percentage of crumb rubber found in geopolymer mortar, while there was a drop in the density also recorded when the weight of sample decreased. According to the findings, mixes including CR-5%, CR-10%, CR-15%, and CR-20% all demonstrated a decreased density in comparison to CR-0% for the same amount of crumb rubber loading. CR-0% had a density of 2040 kg/m^3 , CR-5% had a density of 1872 kg/m^3 , CR-10% had a density of 1688 kg/m^3 , CR-15% had a density of 1488 kg/m^3 , and CR-20% had a density of 1366 kg/m^3 .

Crumb rubber absorbs water better than other geopolymer mortar components. After absorbing water, crumb rubber expands, reducing mortar density. Crumb rubber has a lower density than usual aggregates, which reduces mortar density when applied. Crumb

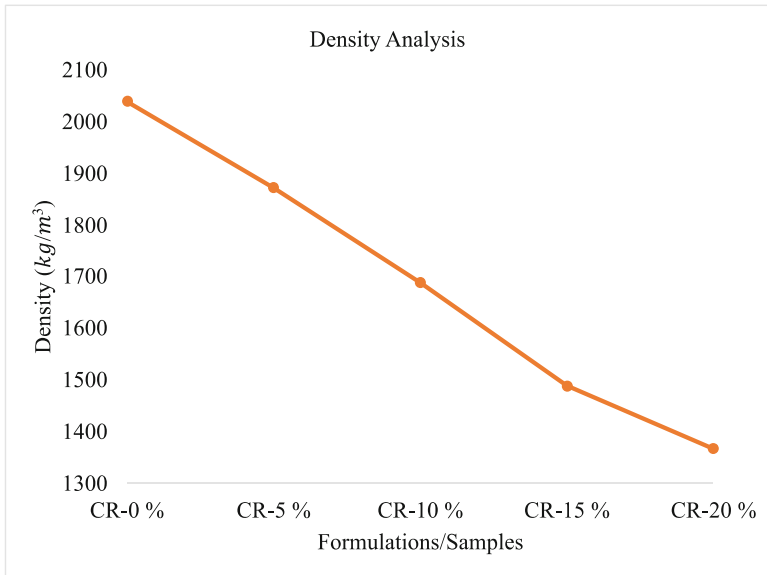


Fig. 2. The density analysis for 28 days of curing time.

rubber geopolymer mortar density decreases as crumb rubber concentration increases. Mortar density decreases with weight. Since mortar density is directly connected to weight, lighter mortars have lower densities, suggesting a relationship between the two. Research found that rubberized geopolymer mortar with more crumb rubber was less dense. Larger-particle crumb rubber may increase mortar pore volume. These additional pores may affect mortar density. Crumb rubber's insulating properties may reduce heat transfer. This attribute may reduce the mortar's density by affecting its mass and thermal conductivity.

4.3 Compressive Strength Analysis

Figure 3 shows the compressive strength of the five crumb rubber geopolymer mortar ratios. Figure 3 indicates that crumb rubber geopolymer cement compressive strength decreased as crumb rubber loading increased. According to the analysis, the compressive strength of CR-0% was 25.59 MPa, CR-5% was 14.31 MPa, CR-10% was 11.19 MPa, CR-15% was 10.38 MPa, and CR-20% was 8.16 MPa.

Crumb rubber enhances geopolymer mixtures and achieves specific goals. Recycled tyres yield crumbs. However, crumb rubber may reduce the compressive strength of the geopolymer mortar made from it. Crumb rubber particles can disrupt the formation and structure of the geopolymer matrix. Rubber particles may not bond with the geopolymer binder, resulting in weak interfaces or voids. This may reduce crumb rubber geopolymer mortar strength. Entrapped air in geopolymer mortar mixes creates voids and weak spots. Alkaline activators prevent crumb rubber and fly ash bonding. Geopolymer mortar compressive strength decreases as void content increases.

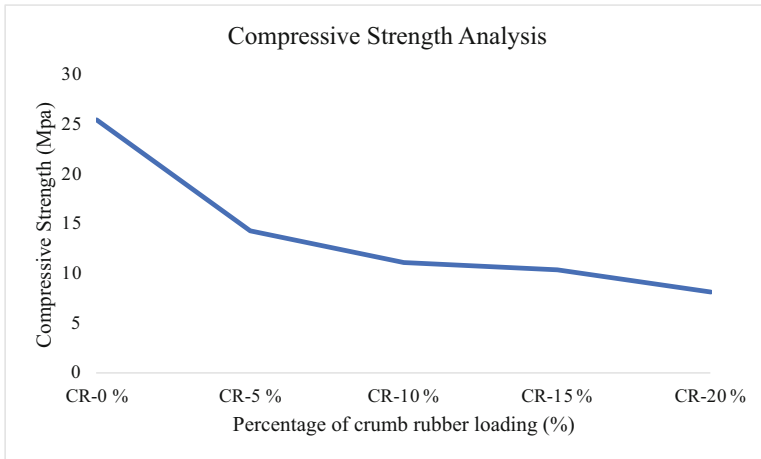


Fig. 3. The compressive strength of crumb rubber geopolymer mortar for 28 days of curing time.

Additionally, the crumb rubber geopolymer mortar decreased because it was more elastically malleable than the matrix. Loaded mortar specimens' fracture in porous areas. In other words, crumb rubber in concrete indicates internal flaws that reduce compressive strength. Solution as crumb rubber is added, it replaces geopolymer binder. Rubber's non-cementitious nature dilutes the geopolymer binder. The drop in binder availability for binding and forming a strong matrix decreases compressive strength. Inability to bond, shredded rubber particles differ in composition and surface features from the geopolymer binder. This may cause weak surfaces and decreased interparticle cohesion due to an insufficient link between the rubber particles and the geopolymer matrix. Poor bonding weakens the load transmission mechanism inside crumb rubber geopolymer mortar, lowering its compressive strength. Distribution that is not uniform may make crumb rubber particle dispersion and distribution homogeneous throughout the geopolymer matrix difficult. Inhomogeneous rubber particle distribution may weaken crumb rubber geopolymer mortar's compressive strength.

4.4 Scanning Electron Microscopy

The SEM micrograph of crumb rubber geopolymer mortar were compare under magnification of 500x as shown in Fig. 4.

These images show the crumb rubber geopolymer mortar interfaces in each sample. The matrix in CR-0% has become a highly compressed paste, as seen in (a). The matrix contains the semispherical imprints of some of the grains that did react, and the non-reacted fly ash particles are lodged within this matrix. They are incorporated into the sodium aluminosilicate gel that is created as a result of the reaction. When the percentage of crumb rubber in the geopolymer mortar is 10%, as shown in (c), the interfacial zones became denser as the number of voids rises. The microstructure of the mortar reveals that the matrix looked to have much larger porosity as the crumb rubber content increased to

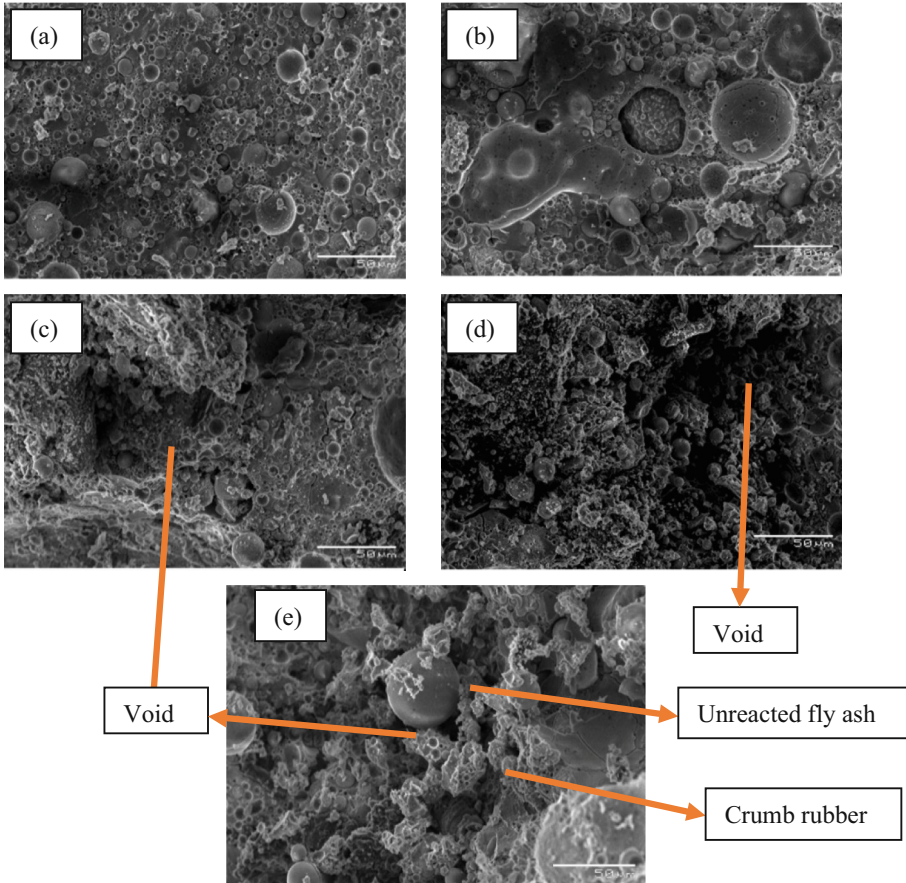


Fig. 4. SEM micrographs of (a) CR-0%, (b) CR-5%, (c) CR-10%, (d) CR-15%, and (e) CR-20% under magnification of 500x.

15% and 20% as in (d) and (e), which led to relatively poor adhesion between the crumb rubber and geopolymer paste.

5 Conclusion

After the investigation, geopolymer mortar was tested with crumb rubber instead of fine aggregate. Loading with 0%, 5%, 10%, 15%, and 20% crumb rubber was examined. The compressive strength, density, and water absorption of crumb rubber geopolymer mortar were significantly affected by increasing the amount of crumb rubber employed. The crumb rubber geopolymer's mechanical performance was assessed using specimen compressive strength. As crumb rubber increased, compressive strength presumably decreased. Crumb rubber's flexibility may have lowered the mortar's strength. Crumb rubber particles may have caused this decline by stress concentration effects, particle packing disruption, and geopolymerization interference.

Density affects weight and lifespan. As crumb rubber quantities changed, researchers presumably noted density changes. Crumb rubber, a lighter fine aggregate, may have made the geopolymer mortar less dense. Water absorption capacity is a material's ability to absorb water. As crumb rubber loading increased, the geopolymer mortar with crumb rubber probably absorbed more water. Crumb rubber is porous; therefore water may have penetrated deeper, causing the observed outcome.

In conclusion, substituting crumb rubber for fine aggregate in geopolymer mortar significantly affected its compressive strength, density, and water absorbing capacity. When crumb rubber loading increased, compressive strength, density, and water absorption capacity decreased.



References

1. Castillo, H., Collado, H., Droguett, T., Vesely, M., Garrido, P., Palma, S.: State of the art of geopolymers: a review. *e-Polymers* **22**(1), 108–124 (2022)
2. Luhar, S., Chaudhary, S., Luhar, I.: Thermal resistance of fly ash based rubberized geopolymer concrete. *J. Build. Eng.* **19**, 420–428 (2018)
3. Ween, O.S., Cheng-Yong, H., Abdullah, M.M.A.B., Ho, L.N., En, O.W.: Geopolymer via pressing method: Aluminosilicates/Alkaline solution ratio as the determining factor. *IOP Conf. Ser. Mater. Sci. Eng.* **864**(1), 012164 (2020)
4. Graham, I.: Automotive industry: trends and reflections. In: ILO, *The Global Economic Crisis Sectoral Coverage WP*, vol. 278, pp. 1–217 (2010)
5. Oliveira Neto, G.C.D., Chaves, L.E.C., Pinto, L.F.R., Santana, J.C.C., Amorim, M.P.C., Rodrigues, M.J.F.: Economic, environmental and social benefits of adoption of pyrolysis process of tires: a feasible and ecofriendly mode to reduce the impacts of scrap tires in Brazil. *Sustainability* **11**(7), 2076 (2019)
6. Park, Y., Abolmaali, A., Kim, Y.H., Ghahremannejad, M.: Compressive strength of fly ash-based geopolymer concrete with crumb rubber partially replacing sand. *Constr. Build. Mater.* **118**, 43–51 (2016)
7. Aslani, F.: Mechanical properties of waste tire rubber concrete. *J. Mater. Civil Eng.* **28**(3) (2016)
8. Luhar, I., Luhar, S.: Rubberized geopolymer composites: value-added applications. *J. Compos. Sci.* **5**(12), 312 (2021)
9. Azrem Azmi, A., Abdullah, M.M.A.B., Mohd Ruzaidi Ghazali, C., Ahmad, R., Musa, L., Sheau Rou, L.: The effect of different crumb rubber loading on the properties of fly ash-based geopolymer concrete. *IOP Conf. Ser. Mater. Sci. Eng.* **551**(1) (2019)
10. Abd-Elaty, M.A.A., Ghazy, M.F., Khalifa, O.H.: Mechanical and thermal properties of fibrous rubberized geopolymer mortar. *Constr. Build. Mater.* **354**, 129192 (2022)
11. Zhao, J., Xie, J., Wu, J., Zhao, C., Zhang, B.: Workability, compressive strength, and microstructures of one-part rubberized geopolymer mortar. *J. Build. Eng.* **68**, 106088 (2023)
12. Luhar, S., Chaudhary, S., Luhar, I.: Development of rubberized geopolymer concrete: strength and durability studies. *Constr. Build. Mater.* **204**, 740–753 (2019)
13. Kuang, F., Long, Z., Kuang, D., Guo, R., Sun, J.: Experimental study on preparation and properties of low content rubberized geopolymer mortar. *Constr. Build. Mater.* **352**, 128980 (2022)
14. Dong, M., Elchalakani, M., Karrech, A., Hassanein, M.F., Xie, T., Yang, B.: Behaviour and design of rubberised concrete filled steel tubes under combined loading conditions. *Thin-Walled Struct.* **139**, 24–38 (2019)

15. Elghazouli, A.Y., Bompa, D.V., Xu, B., Ruiz-Teran, A.M., Stafford, P.J.: Performance of rubberised reinforced concrete members under cyclic loading. *Eng. Struct.* **166**, 526–545 (2018)
16. Li, L.J., Tu, G.R., Lan, C., Liu, F.: Mechanical characterization of waste-rubber-modified recycled-aggregate concrete. *J. Clean. Prod.* **124**, 325–338 (2016)
17. Sukontasukkul, P., Jamnam, S., Rodsin, K., Banthia, N.: Use of rubberized concrete as a cushion layer in bulletproof fiber reinforced concrete panels. *Constr. Build. Mater.* **41**, 801–811 (2013)
18. Pongsopha, P., Sukontasukkul, P., Zhang, H., Limkatanyu, S.: Thermal and acoustic properties of sustainable structural lightweight aggregate rubberized concrete. *Res. Eng.* **13**, 100333 (2022)
19. Azmi, A.A., et al.: Crumb rubber geopolymer mortar at elevated temperature exposure. *Arch. Civil Eng.* **68**(3) (2022)
20. Gill, P., Jangra, P., Roychand, R., Saberian, M., Li, J.: Effects of various additives on the crumb rubber integrated geopolymer concrete. *Cleaner Mater.* **8**, 100181 (2023)



Phosphate Conversion Coatings for Biomaterials: A Bibliometric Analysis

Diana-Petronela Burduhos-Nergis¹ , Andrei Victor Sandu^{1,2,3} ,
Dumitru-Doru Burduhos-Nergis¹ , Carmen Nejneru¹ , Petrica Vizureanu^{1,4} ,
and Costica Bejinariu¹ 

¹ “Gheorghe Asachi” Technical University of Iasi, 41, “D. Mangeron” St., 700050 Iasi, Romania
peviz2002@yahoo.com, costica.bejinariu@yahoo.com

² Romanian Inventors Forum, Str. Sf.P.Movila 3, 700089 Iasi, Romania

³ Academy of Romanian Scientists, 54 Splaiul Independentei St., Sect. 5,
050094 Bucharest, Romania

⁴ Technical Sciences Academy of Romania, 26 Dacia Blvd, 030167 Bucharest, Romania

Abstract. Finding solutions regarding the promotion of the biological response of metallic implants became thoroughly researched, especially by surface modification treatments, due to the high number of clinical demands and the advantageous commercial context. Most of the researchers focused on hydroxyapatite or metal oxide coatings deposited by different methods (electrodeposition, sol-gel, physical vapor deposition, etc.). However, in the last few years, chemical conversion coatings have increased attention in the field of biomaterials. The phosphate layers obtained by this technology have multiple benefits, among which are high adherence to the substrate, similar morphology with the bone, high corrosion resistance, etc. Also, the phosphate coatings present chemical stability and good wear resistance and don't have an impact on the mechanical properties of the substrate. Therefore, this paper aims to analyze the evolution of research in the field of coatings for metallic biomaterials, focusing on conversion coatings deposited on biomaterials, using bibliometric analysis. The results show an increase in the number of publications regarding the chemical conversion process since 2012, many of which are about the layers deposited on magnesium and titanium alloys.

Keywords: conversion coatings · biocompatibility · biomaterials · bibliometric analysis

1 Introduction

In 2020, USD 49.02 billion was spent on orthopaedic implants worldwide, anticipating brisk growth of 5.1% in the coming period. This development is mainly due to the increase in osteoporosis and osteoarthritis cases [1].

In the case of products made from biocompatible materials, worldwide, medical technology manufacturers are continuing to develop their products [2]. His evolution is due, first of all, to the significant increase in demand for these products but also to

unprecedented technological progress. Thus, a growing number of companies focus their activity on the design, development, production, and marketing of human implants and prostheses [3].

Biomaterials can be classified according to several criteria, including material type such as: metallic, polymeric, ceramic, and composite [4].

Regarding the value of the global market for implants made of metallic biomaterials, it was valued at \$86.3 billion in 2020 and is expected to grow by 5.4% by 2030 [5]. This data is based on reports of the number of people living with musculoskeletal diseases [6]. For example, according to the Romanian statistics office, in 2020, 15% of the population needed orthopaedic implants. This can be attributed to the increasing number of road accidents and trauma cases across the globe. In addition, there is an increasing demand for minimally invasive surgery among people [7]. Therefore, there is a lot of research on continuously improving the biological response of existing biomaterials on the market through surface treatments [8].

Biomaterials have diverse applications [9] and can be classified according to the systems in the body where they are used:

- For bone systems: bone prosthesis, implant;
- Muscular and digestive system: stitches;
- Circulatory system: valves or artificial vessels;
- Respiratory system: a device for artificial respiration;
- Urinary system: catheters, renal dialysis devices;
- Nervous system: hydrocephalic drain, cardiac pacemaker;
- Endocrine system: groups of encapsulated pancreatic cells;
- Reproductive system: mammoplasty, etc.

Regarding the metallic materials, which are used to replace joints, bone screws, and implants, they are based on titanium [10], stainless steel [11], Co-Cr alloys [12] and gold [13]. Their advantages are represented by superior mechanical properties (high mechanical resistance, elasticity), but the biggest disadvantage is represented by low resistance to corrosion when interacting with substances in the body (NaCl, HF, H₂O₂ etc.) [14].

Due to the low corrosion resistance properties that can eliminate toxic corrosion products in the body, as well as the bio-inert surface of the material, there is the possibility of an inflammatory reaction in the body, and this aspect often leads to the failure of the implant [14, 15]. Therefore, among the key conditions necessary for the efficient functioning of the implant are, among others, biocompatibility, biofunctionality, and biodegradability [16].

Therefore, there is a need to develop high-performance materials or coatings aimed at obtaining characteristics suitable for the human body.

Biomaterials can be encapsulated by depositing a thin film layer on their surface. This will enable the material to be accepted by the body after implanting it, due to its improved characteristics. Several techniques are used to coat bio-metallic material surfaces, including hydroxyapatite coatings, glass-ceramic coatings with tricalcium phosphate, oxide coatings, composite coatings, etc. [17, 18].

The most common metallic materials for biomedical uses in the world are titanium alloys. They are utilized in medicine for implants that replace damaged bones and tissues.

Examples include artificial hip joints, knee joints, and bone plates. In addition, artificial hearts, prosthetic heart valves, pacemakers, and screws for fracture fixation are also made from titanium and its alloys. [19, 20].

They show superior mechanical properties, chemical and mechanical stability, and favorable biocompatibility, having been used for many years as implant materials [21]. Due to corrosive properties and bio-inert surfaces, significant problems have arisen, including long-term failures and tissue necrosis as a result of them. Therefore, these defects must be substituted by surface treatments [19–21].

This paper analyzes the evolution of research in the field of coatings for metallic biomaterials, focusing on conversion coatings.

2 Methods

The evolution of research in the field of coatings used to improve biomaterial properties was carried out with the help of bibliometric analysis, with the implementation methodology being presented in Fig. 1.

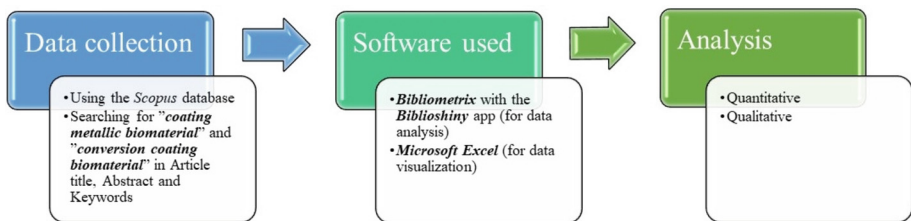


Fig. 1. The methodology of the study.

The data were extracted from Scopus, resulting in 978 research types published worldwide. This was done following the search for “coating metallic biomaterial” with the search query “Article Title, Abstract, Keywords”. The papers published were written in English (95%), Chinese (1.84%), German and Spanish (0.51%), Russian (0.41%), Italian, Czech, Japanese, and Portuguese (0.31%), and Hungarian (0.2%). In terms of research on conversion coatings, the search was conducted for “conversion coating biomaterial” thus obtaining 202 papers, of which 96.04% are written in English, 2.97% in Chinese, and 1% in Japanese and Spanish.

The software chosen for the bibliometric analysis was Bibliometrix, with the Biblioshiny application [22]. Also, the data was visualized and verified in Microsoft Excel. The results were analyzed quantitatively and qualitatively. Publication years, types of research, writing languages, types of journals, and research constituent information (authors, countries, etc.) were analyzed quantitatively. Keyword mapping and thematic areas were considered in the qualitative analysis.

3 Results and Discussion

3.1 Data Obtained for “Coating Metallic Biomaterial”

The bibliometric analysis presents statistical information about publications, sources, citations, authors, frequency, etc. Table 1 presents a summary of the information related to research publications. Also, the number of sources from which publications were extracted is 455, and the number of documents is 978. This is with an average citation per document of 29.42 and 49878 references. The documents were articles (670), books (5), book chapters (58), conference papers (128), conference reviews (9), letters (1), retracted (1), and reviews (106).

Table 1. The main information about the data obtained between 1977 and 2022.

Document contents	
Keywords Plus	7595
Author's Keywords	2014
Authors	
Authors	3791
Authors of single-authored docs	54
Authors collaboration	
Single-authored docs	73
Co-Authors per Doc	4.8
International co-authorships %	23.72%

In Fig. 2, it is shown how interest in coatings used for metallic biomaterials has evolved over time. It can be observed that the annual growth rate is 8.72% in 2022. As can also be seen in the figure, the first research was published in 1977, and the number of studies increased exponentially from 2000 onward.

Regarding the first 10 sources according to the number of publications, these are presented in Table 2. As can be seen, most articles were published in top journals, with their impact factor exceeding 4. Also, these sources are significant journals in the fields of materials and bioengineering.

Regarding the distribution of publications according to the corresponding author's country of affiliation, it can be observed that research on improving biomaterial properties through surface treatments has been carried out on all continents. However, little research has been carried out in certain parts of South America, Northern and Eastern Europe, as well as Africa.

Table 3 shows the first 10 countries that produced scientific publications in the field of metallic biomaterial coatings. Over the years, 59 countries have been interested in this field, and 20 have published at least 10 articles in the field.

Among these countries, China and the USA are among the first to produce medical devices, explaining researchers' high interest.

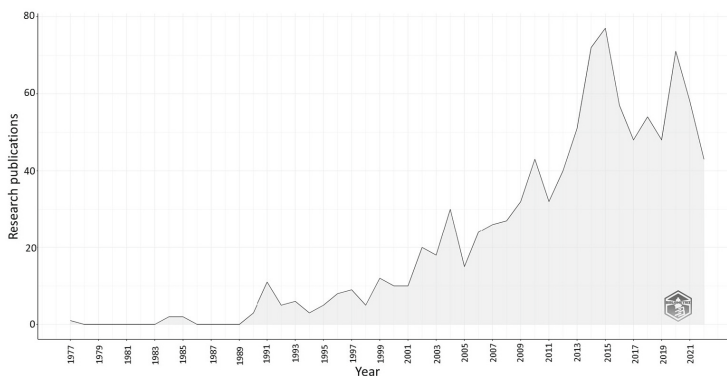


Fig. 2. Annual scientific production on coatings used for metallic biomaterials.

Table 2. Top 10 most relevant sources.

Sources	Publisher	Number of publication	IF 2021
Materials Science and Engineering C	Elsevier	46	7.328
Surface and Coatings Technology	Elsevier	27	4.865
Journal Of Biomedical Materials Research - Part A	Wiley	26	4.854
Biomaterials	Elsevier	23	15.304
Journal of Materials Science: Materials in Medicine	Springer Science + Business Media	19	4.727
Acta Biomaterialia	Elsevier	18	10.633
Acs Applied Materials and Interfaces	American Chemical Society (United States)	16	10.383
Colloids and Surfaces B: Biointerfaces	Elsevier	15	5.999
Journal of Biomedical Materials Research	Wiley	14	4.854
Applied Surface Science	Elsevier	13	7.392

The worldwide distribution of authors with publications in “coating metallic biomaterial” is shown in Fig. 3. The countries that don’t have any authors affiliated with them are colored gray. The intensity of the blue color is related to the number of publications associated with that country. Joint publications by authors from different countries are

Table 3. Top 10 countries regarding the number of publications according to the corresponding author's country of affiliation on coatings used for metallic biomaterials.

Country	Number of publications	Frequency
USA	136	0.105
China	98	0.100
India	57	0.058
Germany	47	0.048
Brazil	41	0.042
Poland	41	0.042
Japan	37	0.038
France	34	0.035
Italy	33	0.034
United Kingdom	32	0.033

indicated with pink lines. Furthermore, no publication appears to be associated with authors from Russia or multiple African countries. European countries have at least one publication in this field.

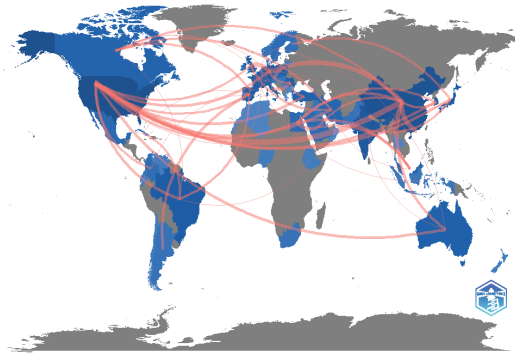


Fig. 3. The collaboration worldmap of authors with publication in the field of “coating metallic biomaterial”.

Regarding the top 50 words as keywords, they are represented in Fig. 4. It can be observed that the subjects of the articles focus on the modification of biomaterial surfaces through biocompatible coatings. As a result, the most commonly used coatings are those based on hydroxyapatite. It also appears that most studies investigate corrosion resistance properties as well as antibacterial or toxicity properties. The most widely used biocompatible materials for research are titanium-based alloys, magnesium-based alloys, and stainless steels.

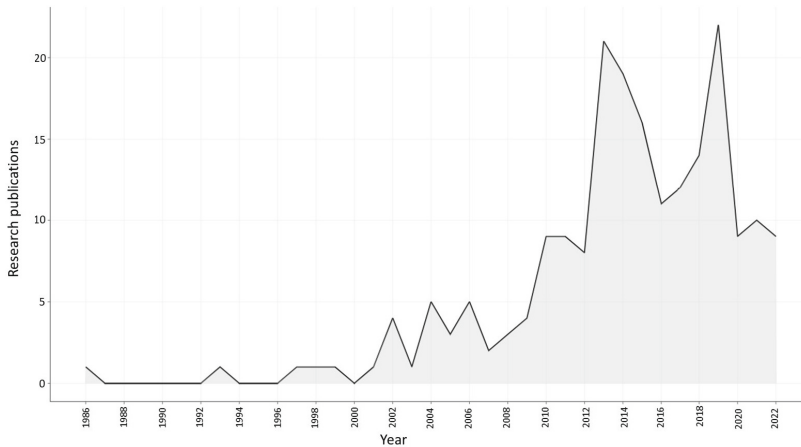


Fig. 5. Annual scientific production on conversion coatings.

Table 6 shows the first 10 countries with the most publications in the field of biomaterial conversion coatings.

Table 5. Top 10 most relevant sources.

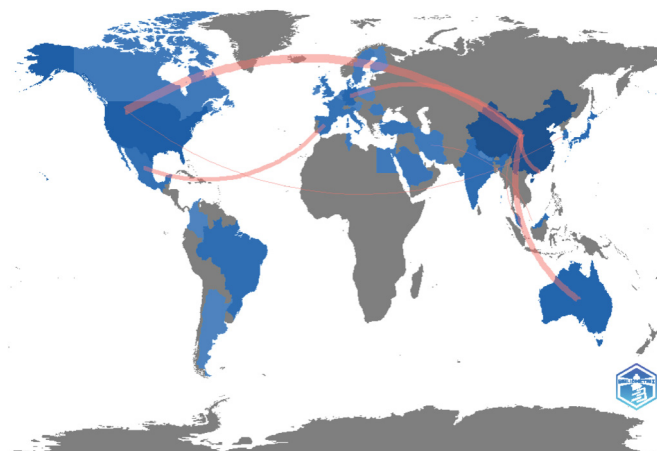
Sources	Publisher	Number of publications	IF 2021
Acs Applied Materials and Interfaces	American Chemical Society (United States)	16	10.383
Biomaterials	Elsevier	9	15.304
Materials Science and Engineering C	Elsevier	9	7.328
Journal of Applied Polymer Science	Wiley	7	3.057
Acta Biomaterialia	Elsevier	6	10.633
Advanced Materials Research	Trans Tech Publications Ltd	6	0
Key Engineering Materials	Trans Tech Publications Ltd	4	0
Advanced Healthcare Materials	Wiley	3	9.933
Applied Surface Science	Elsevier	3	7.392
Acs Biomaterials Science and Engineering	American Chemical Society (United States)	3	14.310

Over the years, 30 countries have been interested in this field, and 9 of them have published at least 5 articles in the field.

Table 6. Top 10 countries regarding the number of publications according to the corresponding author's country of affiliation on conversion coatings.

Country	Number of publications	Frequency
China	76	0.376
USA	23	0.114
Australia	9	0.045
Germany	9	0.045
Brazil	7	0.035
Japan	7	0.035
Korea	6	0.030
India	5	0.025
Malaysia	5	0.025
United Kingdom	4	0.020

An analysis of the worldwide distribution of authors with publications in this field is presented in Fig. 6. The countries that do not have any publications in the analyzed field are presented in gray. While, depending on the number of publications, the blue color intensifies. Also, collaboration links between countries are indicated with pink lines. Regarding the distribution of publications according to the country of affiliation of the corresponding author, it can be observed that research on improving biomaterial properties through chemical conversion deposition has been carried out on all continents. However, not much research has been carried out in certain parts of Asia, Africa, and Eastern Europe.

**Fig. 6.** The collaboration worldmap of authors with publication in the field of “conversion coating biomaterial”.

on this type of coating. These studies were trying to improve the properties of the hydroxyapatite layer being deposited on various biomaterials.

Also, the bibliometric analysis shows that in the last few years, phosphate chemical conversion coatings have steadily drawn a lot of interest when it comes to the surface modification of biomaterials, especially magnesium alloys but also titanium and zinc alloys, and are one of the methods suitable for medical devices due to their advantages.

Acknowledgement. This paper was realized with the support of COMPETE 2.0 project nr.27PFE/2021, financed by the Romanian Government, Minister of Research, Innovation and Digitalization. This paper was also supported by “Gheorghe Asachi” Technical University from Iași (TUIASI), through the Project “Performance and excellence in postdoctoral research 2022”.

References

1. Polaris market research: Orthopedic Implants Market Share, Size, Trends, Industry Analysis Report, By Application (Spinal, Hip, Knee, Dental, Craniomaxillofacial, S.E.T); By Region; Segment & Forecast, 2021–2028 (2021)
2. Javaid, M., Haleem, A., Singh, R.P., Suman, R.: 3D printing applications for healthcare research and development. *Global Health J.* **6**, 217–226 (2022)
3. Harun, W.S.W., Kamariah, M.S.I.N., Muhamad, N., Ghani, S.A.C., Ahmad, F., Mohamed, Z.: A review of powder additive manufacturing processes for metallic biomaterials. *Powder Technol.* **327**, 128–151 (2018)
4. Koons, G.L., Diba, M., Mikos, A.G.: Materials design for bone-tissue engineering. *NatRM* **5**, 584–603 (2020)
5. Metallic Biomaterial Market – Global Industry Trends and Forecast to 2028 | Data Bridge Market Research. <https://www.databridgemarketresearch.com/reports/global-metallic-biomaterial-market>
6. Prodoehl, J., Kraus, S., Buros Stein, A.: Predicting the number of physical therapy visits and patient satisfaction in individuals with temporomandibular disorder: a cohort study. *J. Oral Rehabil.* **49**, 22–36 (2022)
7. Chen, F.M., Liu, X.: Advancing biomaterials of human origin for tissue engineering. *Prog. Polym. Sci.* **53**, 86–168 (2016)
8. Campoccia, D., Montanaro, L., Arciola, C.R.: A review of the biomaterials technologies for infection-resistant surfaces. *Biomaterials* **34**, 8533–8554 (2013)
9. Velez-Cruz, A.J., Farinas-Coronado, W.: Review-bone characterization: mechanical properties based on non - destructive techniques. *Athenea Eng. Sci. J.* **3**, 16–29 (2022)
10. Elias, C.N., Lima, J.H.C., Valiev, R., Meyers, M.A.: Biomedical applications of titanium and its alloys. *JOM* **60**, 46–49 (2008)
11. Shafiee, B.M., et al.: Surface modification of 316L SS implants by applying Bio-glass/Gelatin/Polycaprolactone composite coatings for biomedical applications. *Coatings* **10**, 1220 (2020)
12. Acharya, S., Soni, R., Suwas, S., Chatterjee, K.: Additive manufacturing of Co–Cr alloys for biomedical applications: a concise review. *JMatR.* **36**, 3746–3760 (2021)
13. Gupta, A., et al.: ^{99m}Tc-Methionine gold nanoparticles as a promising biomaterial for enhanced tumor imaging. *J. Pharm. Sci.* **110**, 888–897 (2020)
14. Eliaz, N.: Corrosion of metallic biomaterials: a review. *Materials* **12** (2019)
15. Prasad, K., et al.: Metallic biomaterials: current challenges and opportunities. *Materials* **10** (2017)

16. Ratner, B.D.: The biocompatibility of implant materials. Host Response to Biomaterials: The Impact of Host Response on Biomaterial Selection 37–51 (2015)
17. Dehghanghadikolaei, A., Fotovvati, B.: Coating techniques for functional enhancement of metal implants for bone replacement: a review. *Materials* **12**, 1795 (2019)
18. Mosas, K.K.A., Chandrasekar, A.R., Dasan, A., Pakseresht, A., Galusek, D.: Recent advancements in materials and coatings for biomedical implants. *Gels* **8**, 323 (2022)
19. Sarraf, M., Rezvani Ghomi, E., Alipour, S., Ramakrishna, S., Liana Sukiman, N.: A state-of-the-art review of the fabrication and characteristics of titanium and its alloys for biomedical applications. *Biodes Manuf.* **5**, 371–395 (2022)
20. Sidambe, A.T., Oh, J.K.: Biocompatibility of advanced manufactured titanium implants-a review. *Materials* **7**, 8168–8188 (2014)
21. Jung, H.D.: Titanium and its Alloys for biomedical applications. *Metals* **11**, 11, 1945 (2021). <https://doi.org/10.3390/MET11121945>
22. Aria, M., Cuccurullo, C.: Bibliometrix: an R-tool for comprehensive science mapping analysis. *J. Informetr.* **11**, 959–975 (2017)
23. Liu, B., Xiao, G., Lu, Y.: Effect of pH on the phase composition and corrosion characteristics of Calcium Zinc Phosphate conversion coatings on Titanium. *J. Electrochem. Soc.* **163**, C477–C485 (2016)
24. Zhao, D.W., et al.: Strontium-zinc phosphate chemical conversion coating improves the osseointegration of titanium implants by regulating macrophage polarization. *Chem. Eng. J.* **408**, 127362 (2021)
25. Zhao, D.W., et al.: Interleukin-4 assisted calcium-strontium-zinc-phosphate coating induces controllable macrophage polarization and promotes osseointegration on titanium implant. *Mater. Sci. Eng. C Mater. Biol. Appl.* **118** (2021)

Author Index

A

Abas, Mohamad Aizat 62
Abdullah, Junaidah 22
Abdullah, Mohd Mustafa Al Bakri 45, 116,
184, 193
Achitei, Dragos-Cristian 170
Achitei, George 1
Adnan, Azrul Nazif 152
Ahmad, Mohd Azmier 62
Ahmad, Normadyzah 116
Ahmad, Romisuhani 184, 193
Ali, Nazri 89, 100
Aminnudin 134, 145
Awang, Mohamad 152
Ayub, Khairul Rahmah 22
Azam, Syuhaidah 100
Aziz, Mohd Sharizal Abdul 22
Aziz, Nurhanani Abd 62
Azmi, Ahmad Azrem 163, 193
Azizan, Nor Ariza 22

B

Baltatu, Madalina-Simona 170
Bejinariu, Costica 9, 203
Benchea, Marcelin 9
Burduhos-Nergis, Diana-Petronela 9, 170,
203
Burduhos-Nergis, Dumitru-Doru 9, 31, 170,
203

C

Chiriac, Bogdan 1
Cimpoesu, Nicanor 9

D

Dontu, Andrei Ionut 1

F

Fitriadhy, Ahmad 134

G

Ghazali, Che Mohd Ruzaidi 134, 145, 152,
193
Ghazali, Farah Nurhikmah Che 62

H

Hamed, Alia Syafiqah Abdul 145
Hisham, Asmawi 89, 100
Hussin, Hamzah 89, 100

I

Ibrahim, Lokman Hakim 193
Ibrahim, Wan Mastura Wan 184
Ishak, Siti Aisyah 45
Istrate, Bogdan 31

J

Juiani, Siti Fairuz 22

K

Kartikowati, Christina Wahyu 184
Khan, Muhammad Nasri Nasehir 62

L

Leemsuthep, Anusha 77
Luqman, Musa 163

M

Masa, Abdulhakim 77
Mokhtar, Nor Aieni 134
Munajat, Nur Farizan 145
Murshed, Mohamad Fared 45
Mustapa, Nur Bahijah 184
Mustapha, Rohani 152
Mustapha, Siti Noor Hidayah 152

N

Nazer, Nor Shahidah Mohd 89, 100
Nejneru, Carmen 203

Nitiyah, Krishna Kumar 163
 Nofal Firhat, Adlina Alia 116

O

Osman, Hakimah 77

P

Perju, Manuela-Cristina 170
 Popa, Mihai 9
 Popescu, Aristotel 1

R

Radzi, Mohd Rashid Mohd 62
 Rafezi, Ahmad Khairrel 163
 Rahim, Afikah 89, 100
 Rahman, Fakhurrrazi 134
 Rahman, Rozyanty 163
 Rahmat, Norhasyimi 116
 Ravi, Reshikesan 193
 Riduan, Muhammad Zulfaiz Hilmi 116
 Risdanareni, Puput 184

S

Saimi, Wan Hasnida Wan Mohamed 184
 Sandu, Andrei Victor 9, 31, 170, 184, 203
 Sapawie, Nurfirdaus 89
 Smail, Mohammad Syahrin 77
 Suriani, Mat Jusoh 134
 Syahmie, Mohamad Rasidi Mohamad 163

T

Tanggara, Deddy 89, 100

V

Vizureanu, Petrica 31, 170, 203

W

Winarno, Agus 89, 100

Y

Yusof, Mohd Fazly 22
 Yusof, Nurul Iffah Farhah Mohd 145

Z

Zahari, Nazirul Mubin 62
 Zainal Abidin, Hanafiah 116
 Zainol, Mohd Remy Rozainy Mohd Arif 22,
 45, 62
 Zakaria, Zunaida 77
 Zamree, Abd Rahim Shayfull 163
 Zawawi, Mohd Hafiz 62